Gravity Waves, Turbulence and Rotors in the Lee of Mountains

by

Rita Margarida A. P. Cardoso

Submitted in accordance with the requirements for the degree of Doctor of Philosophy.

University of Leeds

School of Earth and Environment

January 2005.

Acknowledgements

I would like to thank my supervisor, Prof. Stephen Mobbs, for his guidance and support throughout this work and without whom this thesis would not have been possible. I also wish to express my gratitude to Simon Vosper for his comments, guidance and interest in this work.

I would like to thank my colleagues Alexandru Rap, Dominick Spracklen, Richard Ellis and Steve Arnold for the friendly environment that made my time here more enjoyable.

I also wish to express my gratitude to:

Andrew Ross for his comments and help with the numerical simulations.

Volker Horlacher for his help with the data calibration.

Steve Dobbie for enabling me to work with the radiation model.

To everyone at the School of the Environment who was involved in the Falklands field campaign and made the data available.

All the members of the School of the Environment for all their support.

I would also like to thank my friends Mafalda, Mags, JJ, Pedro and Quim for all their support and helping me keep my sanity during these four years.

A special thanks goes to Luís for his support, understanding and encouragement throughout these four years.

I would like to express a special thanks to my family, in particular to my parents and brother for their love and encouragement without which this thesis would not have been feasible.

Finally, I would like to acknowledge the financial support form the Fundacao para a Ciencia e Tecnologia in the form of the grant: $SFRH/BD/1229/2000$.

Abstract

This thesis has focussed on analysing the influence of a temperature inversion in the upstream profile of flow over ridges.

Under northerly conditions, a temperature inversion is commonly observed in the Falkland islands radiosonde launches and severe turbulence is usually coupled with it. The turbulence is presumed to be linked to gravity wave activity and is associated with high temporal and spatial variability in wind speed and direction. Recirculation zones are commonly found under the crest of the waves and their three dimensional structure pose a significant hazard to air traffic. The data obtained from a field campaign aimed at observing the flow field downwind of a mountain ridge in the vicinity of Mt. Pleasant airport in the Falkland islands is analysed. From the data analysis, a correlation between the temperature inversion and the difference in temperature between the sea surface and air is established. The seasonal distribution of these phenomena is also explained.

Due to logistic constraints, there were no radiosonde launches performed upstream during the campaign. To obviate that problem, a one–dimensional boundary layer model with a 1.5–order closure scheme, radiation and cloud parameterisations was developed. The model was then used to simulate the upwind characteristics of some particular case studies during which strong downwind flow was observed.

The influence of temperature inversions on the dynamics of trapped lee–waves was simulated through a series of two–dimensional simulations of flow over idealised ridges. The analysis focussed on the effects of topography composed by two ridges and on the effects of an inversion below the ridge summit. These simulations show that the effects of the second ridge can significantly alter the downstream flow and that a temperature inversion below the summit can also induce strong downwind phenomena.

A two–dimensional simulation using the one–dimensional vertical profile from the boundary layer model was performed. The results were in reasonable agreement with the observed data for that day.

Contents

List of Figures

List of Tables

List of Acronyms

ECMWF	European Centre for Medium–Range Weather Forecasts
IAS	Institute of Atmospheric Sciences
MPA	Mount Pleasant Airfield
MWD	Mountain Wave Drag
SST	Sea Surface Temperature
TKE	Turbulent Kinetic Energy
UMIST	University of Manchester Institute of Science and Tecnology

List of Symbols

c	sound speed, $c^2 = \gamma RT$
$\vec{c_g}$	group speed
$\vec{c}$	speed of a line of constant phase
c_i	phase speed
c_p	specific heat of moist air, $c_p = c_{pd} + r_t c_{pv}$
c_{pd}	specific heat of dry air
c_{pv}	specific heat of water vapour
e	turbulent kinetic energy
f	Coriolis parameter, $f = 2\Omega \sin \phi$
F	total radiative flux
$\mathbf{g}$	acceleration due to gravity, $\mathbf{g} = (\mathbf{0}, \mathbf{0}, \mathbf{g})$
$\vec{i}$	unit vector along the vertical
K_m	momentum eddy diffusivity
K_h	heat eddy diffusivity
K_q	humidity eddy diffusivity
k, l, m	x, y, z, components of the wave number vector
$\vec{k}$	horizontal component of the wave number vector
L	latent heat of vaporisation
L_s	latent heat of sublimation
L_{MO}	Monin–Obukhov length
M	molecular mass of dry air, $M = 28.966$ g mole^{-1}
N	Brunt Väisälä frequency
p	pressure
q_*	surface layer humidity scale
q_t	total water specific humidity
q	specific humidity
q_l	specific humidity for liquid water
Q_{rad}	divergence of the radiation flux
Q	saturation deficit
R	gas constant for dry air, $R = R* /M = 287$ J kg^{-1} K^{-1}
R*	Universal gas constant, $R* = 8.3145$ J mole^{-1} K^{-1}

r_t	total water mixing ratio, $r_t = r + r_l$
r	water vapour mixing ratio
r_l	liquid water mixing ratio
r_i	ice mixing ratio
T	temperature
t	time
u_*	surface layer velocity scale
$\vec{v}$	wind speed vector
$\vec{v}_g$	geostrophic wind speed vector
u, v, w	x, y, z components of the wind
$\mathbf{V}$	ensemble average of the wind speed vector
Z	impedance
γ	c_p/c_v
$\vec{\kappa}$	wave number vector, $\vec{\kappa} = (k, l, m)$
Ω	rotation rate of the Earth, $\Omega = 7.292 \times 10^{-5}$ s^{-1}
ω	frequency
ϕ	latitude
ρ	density
ρ_0	density of a reference horizontally averaged state
ρ'	density deviation from a basic state
$\overline{\rho}$	density of the reference state
θ	potential temperature
θ_l	liquid water potential temperature
θ_*	potential temperature surface scale

1. Introduction

1.1 Motivation

Under northerly flow conditions, it is common to observe severe turbulence in the lee of the ridges (Mt. Simon and Mt. Wickham) that span the island of East Falkland. This turbulence is presumed to be linked to gravity wave activity and is associated with high temporal and spatial variability in wind speed and direction. Recirculation zones are commonly found under the crest of the waves and their three dimensional structure pose a significant hazard to air traffic. Forecasters refer to them as "rotor streaming".

For northerly flow, the air field in East Falkland is located downwind of the mountains and the Met. Office forecasters often issue warnings of severe low–level turbulence. The three–dimensional characteristics of the phenomenon and its temporal variability enhance the difficulty of a forecast. At the present there is no reliable forecasting tool for such conditions. In order to explore the atmospheric conditions that lead to the formation of such rotors and to study their characteristics a field campaign was conducted by the Institute for Atmospheric Sciences (IAS) of the University of Leeds and by the University of Manchester Institute of Science and Technology (UMIST). A substantial part of this thesis is occupied with the analysis of the data obtained during the campaign.

The work performed by Doyle and Durran (2002) on the dynamics of mountain wave induced rotors and by Vosper (2004) on the inversion effects on mountain lee–waves suggest that rotors are associated with trapped lee–waves and that a temperature inversion in the upwind profile can be related to severe turbulence, rotors and strong downslope winds. In fact, an ubiquitous feature in the radiosonde data for the severe weather phenomenon was the occurrence of a temperature inversion in the first 600 m. Since this temperature inversion is missing from the forecast profiles and the radiosonde launch was always performed at the airfield, which lies downstream under northerly flow conditions; the question of whether the inversion exists in the atmosphere upstream and what is its strength

and height is addressed in this thesis. Another aim of this thesis was the development of a one–dimensional boundary layer model which would be able to simulate the upwind profile.

The third part of the thesis was partially motivated by the work done by Vosper (2004) on the influence of temperature inversions in the dynamics of trapped lee–waves. Vosper analyses a range of flows with temperature inversions above a single ridge. In the radiosonde data, the temperature inversion occurs below the height of Mt. Wickham's summit and although it is reasonable to assume that the contraction of the isentropes due to the downslope flow would lower its height, the influence of inversions located below the summit warranted some investigation.

Although simulations over a single ridge provide some insight into what might be expected from the influence of temperature inversions on the downstream flow, East Falkland's orography is composed by two ridges. As will be found in the present study, the effects of the second ridge can significantly alter the downstream flow. This further justified an extension of the simulations from one ridge to two ridges.

1.2 Outline of the Thesis

The thesis is organised as follows. Chapter 2 derives a few standard results of linear theory for internal gravity waves and presents a summary of relevant results. Chapter 3 provides a description of the Falkland's field campaign and a description of the data calibration procedures. Chapter 4 describes the one dimensional boundary layer model and the simulations performed in its validation. Chapter 5 provides a climatological analysis of the field data and attempts to link the seasonality of the extreme events with the sea surface temperature and prevailing winds. An analysis of six cases which are representative of the conditions observed at MPA during northerly flows is also presented in this chapter. Chapter 6 presents four one dimensional simulations for the four case studies in which turbulent flow or strong downwind acceleration occurred. Chapter 7 presents the results of two dimensional simulations, performed with the Met. Office BLASIUS model, for a two layer atmosphere with temperature inversions at the summit height and below the summit for flow over one and two ridges. In this chapter, two dimensional simulations of a case study is also presented. This simulation uses the one dimensional model results as

the upwind profiles. Lastly, chapter 8 includes a summary and conclusions.

2. Internal Gravity Waves

This chapter analyses a simplified set of equations of motion, whose solutions are three dimensional non–hydrostatic inertial gravity waves and determines the appropriate solutions for flow over topography. A summary of relevant results are also presented.

2.1 Linear Theory

The dynamics of a compressible, inviscid, rotating atmosphere in which the undisturbed state is in hydrostatic and geostrophic equilibrium is described by the following equations (cf List of Symbols for meaning of symbols):

- The momentum equation:

$$\frac{D\vec{v}}{Dt} + f\vec{i} \times \vec{v} + g\vec{i} = -\frac{1}{\rho}\nabla p; \tag{2.1}$$

- The continuity equation:

$$\frac{1}{\rho}\frac{D\rho}{Dt} + \nabla \cdot \vec{v} = 0; \tag{2.2}$$

- The thermodynamic equation:

$$\frac{Dp}{Dt} - c^2\frac{D\rho}{Dt} = 0; \tag{2.3}$$

- The ideal gas equation for dry air:

$$p = R\rho T. \tag{2.4}$$

Assuming that all the thermodynamic processes are adiabatic and that the undisturbed state has pressure P, density $\overline{\rho}$ and constant wind speed $(U, V, 0)$ the relevant variables can be decomposed into:

$$\begin{aligned} u(x,y,z,t) &= U + u'(x,y,z,t), & p(x,y,z,t) &= P(x,y,z) + p'(x,y,z,t), \\ v(x,y,z,t) &= V + v'(x,y,z,t), & \rho(x,y,z,t) &= \overline{\rho}(x,y,z) + \rho'(x,y,z,t), \\ w(x,y,z,t) &= w'(x,y,z,t). \end{aligned} \tag{2.5}$$

where the perturbations are denoted by a prime.

The equations for the reference state are, then, depicted by:

$$\frac{\partial P}{\partial x} = \overline{\rho} f V, \tag{2.6}$$

$$\frac{\partial P}{\partial y} = -\overline{\rho} f U, \tag{2.7}$$

$$\frac{\partial P}{\partial z} = -\overline{\rho} g. \tag{2.8}$$

Note that if $\left|\frac{\rho'}{\overline{\rho}}\right| << 1$ a Taylor expansion of the density yields:

$$\frac{1}{\rho} = \frac{1}{\overline{\rho} + \rho'} \approx \frac{1}{\overline{\rho}} \left(1 - \frac{\rho'}{\overline{\rho}}\right) \tag{2.9}$$

Finally, the linearised equations describing the perturbed flow become (please note that partial derivation is indicated by the use of subscripts):

$$u'_t + U u'_x + V u'_y - f v' = -\frac{1}{\overline{\rho}} p'_x, \tag{2.10}$$

$$v'_t + U v'_x + V v'_y + f u' = -\frac{1}{\overline{\rho}} p'_y, \tag{2.11}$$

$$w'_t + U w'_x + V w'_y + \frac{\rho'}{\overline{\rho}} g = -\frac{1}{\overline{\rho}} p'_z, \tag{2.12}$$

$$\delta_1(\rho'_t + U\rho'_x + V\rho'_y) + \delta_2(u'\overline{\rho}_x + v'\overline{\rho}_y) + \delta_3 w'\overline{\rho}_z = -\overline{\rho}(u'_x + v'_y + w'_z), \tag{2.13}$$

$$\begin{aligned} &\delta_4(p'_t + Up'_x + Vp'_y) + \delta_5(u'P_x + v'P_y) + w'P_z = \\ &\quad = c^2(\rho'_t + U\rho'_x + V\rho'_y) + c^2\left[\delta_6(u'\overline{\rho}_x + v'\overline{\rho}_y) + w'\overline{\rho}_z\right]. \end{aligned} \tag{2.14}$$

The δ_i can adopt two values, either zero (if the term is to be discarded) or one (if the term is to be kept). In the following, $\delta_i = 0$ for all i. This is equivalent to a Bousinesq type approximation, where compressibility and density perturbations are deemed negligible everywhere except in the evaluation of the buoyancy term ($\overline{\rho}$ is replaced by ρ_0, except in $\overline{\rho}_z$ in (2.14)).

The final aim is to obtain a single equation for w'. First, the curl and the divergence of the horizontal momentum equations, (2.10) and (2.11), are determined:

$$\left(v'_x - u'_y\right)_t + U\left(v'_x - u'_y\right)_x + V\left(v'_x - u'_y\right)_y + f\left(u'_x + v'_y\right) = 0, \tag{2.15}$$

$$\left(u'_x + v'_y\right)_t + U\left(u'_x + v'_y\right)_x + V\left(u'_x + v'_y\right)_y - f\left(v'_x - u'_y\right) = -\rho_0^{-1}(p'_{xx} + p'_{yy}). \tag{2.16}$$

An equation in w' can be obtained by eliminating the vertical vorticity between previous equations, (2.15) and (2.16), and using the continuity equation (2.13) to replace the horizontal divergence. The outcome of this procedure is:

$$(w'_z)_{tt} + 2\left[U(w'_z)_x + V(w'_z)_y\right]_t + U^2(w'_z)_{xx} + 2UV(w'_z)_{xy} + V^2(w'_z)_{yy} + \\ + f^2 w'_z = \rho_0^{-1}\left[(p'_{xx} + p'_{yy})_t + U(p'_{xx} + p'_{yy})_x + V(p'_{xx} + p'_{yy})_y\right]. \quad (2.17)$$

Another equation relating the pressure perturbation to the vertical wind speed perturbation is required, and this is obtained by eliminating the density perturbation between the vertical momentum equation (2.12) and the thermodynamic equation (2.14). The ensuing equation is:

$$\left[w'_{tt} + 2(Uw'_x + Vw'_y)_t + U^2 w'_{xx} + 2UVw'_{xy} + V^2 w'_{yy}\right] + \\ + N^2 w' = -\rho_0^{-1}\left[p'_t + Up'_x + Vp'_y\right]_z \quad (2.18)$$

where:

$$N^2 = -g\left[\frac{g}{c^2} + \frac{\overline{\rho}_z}{\rho_0}\right]. \quad (2.19)$$

Ultimately, an equation just in w' is obtained by adding the horizontal laplacian of (2.18) to the vertical derivative of (2.17), i.e.,

$$(w'_{xx} + w'_{yy} + w'_{zz})_{tt} + 2\left[U(w'_{xx} + w'_{yy} + w'_{zz})_x + V(w'_{xx} + w'_{yy} + w'_{zz})_y\right]_t + \\ + U^2(w'_{xx} + w'_{yy} + w'_{zz})_{xx} + 2UV(w'_{xx} + w'_{yy} + w'_{zz})_{xy} + V^2(w'_{xx} + w_{yy} + w'_{zz})_{yy} + \\ + N^2(w'_{xx} + w'_{yy}) + f^2 w'_{zz} = 0. \quad (2.20)$$

The dispersion relation for internal gravity waves in a rotating fluid with uniform background buoyancy frequency and wind speed is obtained by assuming that w' can be replaced by its Fourier transform, i.e.,

$$w'(x,y,z) = \iiint_{\infty} \tilde{w} e^{i(kx+ly+mz-\omega t)}\, dkdldm, \quad (2.21)$$

where ω is the flow's frequency and $\vec{\kappa} = (k,l,m)$ is its wave number vector. Thus, (2.20) yields:

$$\omega = (Uk + Vl) \pm \sqrt{\frac{N^2(k^2+l^2) + f^2 m^2}{k^2 + l^2 + m^2}}. \quad (2.22)$$

Apart from the Doppler Effect, this dispersion relation is the same that Gill (1982) obtained for a continuously stratified incompressible rotating fluid.

The former equation can be rewritten as:

$$\omega = \vec{k} \cdot \vec{U} \pm \hat{\omega}, \tag{2.23}$$

where $\vec{k}$ represents the horizontal component of the wavenumber vector, $\vec{U}$ designates the horizontal component of the wind speed vector and $\hat{\omega}$ denotes the intrinsic frequency, i.e., the frequency of an air parcel moving at the same speed as the undisturbed flow. According to Gill (1982), the intrinsic frequency is independent of the magnitude of the wavenumber vector; it is only a function of the angle that this vector makes with the horizontal. The dispersion of surfaces ($\omega = 0$) on the other hand, depend on the magnitude of the wavenumber vector due to the Doppler Effect. Both quantities are highly dependent on the relative values of the two frequencies, N and f. Typically, N/f is of the order of 100, so unless the horizontal scale exceeds the vertical scale by a factor of 14 the dispersion relation is within 1% of the dispersion relation for a non–rotating atmosphere (Gill, 1982).

The group velocity, $\vec{c_g}$, is by definition the gradient of ω in the wavenumber space and therefore is normal to surfaces of constant ω.

$$\vec{c_g} = (U, V, 0) \pm \frac{m\left(N^2 - f^2\right)}{\left(k^2 + l^2 + m^2\right)^{3/2} \sqrt{N^2\left(k^2 + l^2\right) + m^2 f^2}} \left(km, lm, -k^2 - l^2\right). \tag{2.24}$$

For a zero vertical wavenumber there is no vertical propagation of energy, since the group velocity relative to the mean flow is also zero. According to Gill (1982), for $N^2 \gg f^2$ and increasing m, the group velocity has a maximum, $\frac{2N}{3^{3/2}\sqrt{k^2+l^2}}$, which corresponds to a 35° propagation with the vertical $\left(m = \sqrt{\frac{k^2+l^2}{2}}\right)$. As $m \to \infty$ the group velocity also tends to zero. For $N^2 \ll f^2$ the inverse reasoning applies.

The phase speed of the wave or the speed of phase propagation in the direction of $\vec{\kappa} = (k, l, m)$ is given by:

$$c = \frac{\omega}{|\vec{\kappa}|} = \left[\vec{\kappa} \cdot \vec{U} \pm \left(\frac{N^2(k^2 + l^2) + f^2 m^2}{k^2 + l^2 + m^2}\right)^{1/2}\right] \frac{1}{\sqrt{k^2 + l^2 + m^2}}. \tag{2.25}$$

The speed with which the phase advances along a certain axis or the rate at which the

intersection of the phase lines with that axis advances along it is:

$$c_i = \frac{\omega}{\vec{\kappa}_i}. \tag{2.26}$$

Note that the phase speed does not satisfy the rules of vector composition, in fact $\frac{1}{c^2} = \frac{1}{c_x^2} + \frac{1}{c_y^2} + \frac{1}{c_x^2}$. Note that, when $N^2 > f^2$ the vertical phase speed and the group velocity have opposing signs, which indicates that there is upwards transfer of energy when phase propagation is downward and vice versa. When $N^2 < f^2$ upwards transfer of energy occurs when the phase propagation is upwards. Note that, since the equations for the group velocity and phase speed are different these are dispersive waves.

The speed of the phase lines along the direction of $\vec{\kappa} = (k, l, m)$ is determined by the phase velocity:

$$\vec{c} = \frac{\omega}{|\vec{\kappa}|^2} = \left[\vec{\kappa} \cdot \vec{U} \pm \left(\frac{N^2(k^2 + l^2) + f^2 m^2}{k^2 + l^2 + m^2}\right)^{1/2}\right] \frac{\vec{\kappa}}{k^2 + l^2 + m^2}. \tag{2.27}$$

If the horizontal advection is omitted the group velocity and the phase velocity are perpendicular vectors with oppositely directed vertical components when $N^2 > f^2$.

2.1.1 Polarisation Relations

The incompressibility condition imposes an important restriction on the properties of plane waves. From it:

$$\vec{\kappa} \cdot \vec{v} = 0 \tag{2.28}$$

i.e., any motion is confined to a plane normal to the wave number vector or to planes parallel to surfaces of constant phase. For progressive plane waves the relationship between each variable and how they vary in space and time is given by the polarisation relations. They are obtained by assuming that p', ρ', u' and v' can be replaced by their Fourier transform:

$$p'(x, y, z) = \iiint_{\infty} \tilde{p} e^{i(kx+ly+mz-\omega t)}\, dkdldm, \tag{2.29}$$

$$\rho'(x, y, z) = \iiint_{\infty} \tilde{\rho} e^{i(kx+ly+mz-\omega t)}\, dkdldm, \tag{2.30}$$

$$u'(x, y, z) = \iiint_{\infty} \tilde{u} e^{i(kx+ly+mz-\omega t)}\, dkdldm \tag{2.31}$$

and

$$v'(x, y, z) = \iiint_{\infty} \tilde{v} e^{i(kx+ly+mz-\omega t)}\, dkdldm. \tag{2.32}$$

By replacing (2.29) and (2.21)in (2.18) it follows:

$$\tilde{p} = -\rho_0 \frac{(N^2 - f^2)m}{\omega(k^2 + l^2 + m^2)}\tilde{w}. \tag{2.33}$$

By replacing (2.30) and (2.21)in (2.14) the polarisation relation for density becomes:

$$\tilde{\rho} = \frac{i\rho_0}{g}\frac{N^2}{\omega - (Uk + Vl)}\tilde{w}. \tag{2.34}$$

After applying $\frac{\partial}{\partial t} + U\frac{\partial}{\partial x} + V\frac{\partial}{\partial y}$ to (2.10) and using (2.31), (2.21) and (2.33) the polarisation equation for u' is given by:

$$\tilde{u} = -\frac{[((Uk + Vl) - \omega)k - ifl]\left[N^2 - (\omega - (Uk + Vl))^2\right]}{m[\omega - (Uk + Vl)]\left[(\omega - (Uk + Vl))^2 - f^2\right]}\tilde{w}. \tag{2.35}$$

Lastly, after applying $\frac{\partial}{\partial t} + U\frac{\partial}{\partial x} + V\frac{\partial}{\partial y}$ to (2.11) and using (2.32), (2.21) and (2.33) the polarisation equation for v' is given by:

$$\tilde{v} = -\frac{[((Uk + Vl) - \omega)l + ifk]\left[N^2 - (\omega - (Uk + Vl))^2\right]}{m[\omega - (Uk + Vl)]\left[(\omega - (Uk + Vl))^2 - f^2\right]}\tilde{w}. \tag{2.36}$$

The velocity vector rotates anticyclonically with time and since the continuity equation implies that particle movement is confined to planes perpendicular to the wave number vector, these have elliptical orbits due to the balance between the Coriolis and gravitation forces. (2.33) implies that the pressure perturbations are in quadrature with density perturbations and in phase with vertical velocity perturbations. This last assertion means that these waves produce an energy flux.

Note that the polarisation relations are obtained after the inverse Fourier transform is performed on the preceding equations.

2.1.2 Energy Flux

The perturbation energy flux is defined as (Gill (1982)):

$$\vec{F'} = \int_{-\infty}^{+\infty} \tilde{p}\vec{\tilde{v}}^* \, dkdldm = \overline{p'\vec{v}'} \tag{2.37}$$

For periodic waves in a medium of uniform properties the mean can be used instead of the integral. Since the integral over each wavelength is the same, the mean over a large volume becomes equal to the mean over one wavelength as the volume tends to infinity.

Each component of the energy flux is given by:

$$\overline{p'u'} = \frac{\rho_0}{2} \frac{[((Uk+Vl)-\omega)k - ifl]\left[N^2 - (\omega-(Uk+Vl))^2\right]^2}{m^2[\omega-(Uk+Vl)]^2\left[(\omega-(Uk+Vl))^2 - f^2\right]} \tilde{w}^2, \tag{2.38}$$

$$\overline{p'v'} = \frac{\rho_0}{2} \frac{[((Uk+Vl)-\omega)l + ifk]\left[N^2 - (\omega-(Uk+Vl))^2\right]^2}{m^2[\omega-(Uk+Vl)]^2\left[(\omega-(Uk+Vl))^2 - f^2\right]} \tilde{w}^2, \tag{2.39}$$

and

$$\overline{p'w'} = -\frac{\rho_0}{2} \frac{(N^2-f^2)m}{(\omega-(Uk+Vl))(k^2+l^2+m^2)} \tilde{w}^2. \tag{2.40}$$

Note that as long as $f < N$, the vertical energy flux component has the opposite sign from that of the vertical component of the phase velocity which confirms that there is upward energy transport when the phase propagation is downward and vice versa.

2.2 Internal Gravity Waves Generated at a Boundary

Suppose, now, that the lower boundary is a small isolated mountain. The non–linear effects can be disregarded by presuming that the mountain acts as a small perturbation. Therefore, it can be assumed that each wave can be represented by a superposition of waves (each with its wavelength). Given that the problem is linear, the influence of each wavelength can be evaluated independently from the others, hence the orography can be represented by a Fourier integral:

$$h(x,y) = \iint_{\infty} \tilde{h} e^{i(kx+ly)}\, dkdl. \tag{2.41}$$

By considering stationary waves $\omega = 0$, the intrinsic frequency which the air particles

intersect the orography is: $\hat{\omega} = -\vec{U} \cdot \vec{k}$. Now, the group velocity becomes:

$$\vec{c_g} = \frac{m\left(N^2 - f^2\right)}{\left(k^2 + l^2 + m^2\right)^{3/2}\sqrt{N^2\left(k^2 + l^2\right) + m^2 f^2}}\left(-km, -lm, k^2 + l^2\right). \tag{2.42}$$

and the phase speeds are denoted by:

$$c_i = -\frac{1}{k_i}\sqrt{\frac{N^2(k^2 + l^2) + f^2 m^2}{k^2 + l^2 + m^2}}. \tag{2.43}$$

The condition that for $N^2 > f^2$, upward energy transport occurs when the phase speed is downwards.

According to Smith (1980), if η is the vertical displacement of a isentropic surface in relation to its position upstream where the fluid is not disturbed by the mountain, the lower kinematic boundary condition for a stationary and inviscid flow is:

$$w' = \frac{d\eta}{dt} \approx U\frac{\partial \eta}{\partial x} + V\frac{\partial \eta}{\partial y}. \tag{2.44}$$

The appropriate lower boundary condition is that the flow normal to the boundary should be zero for $z = h(x, y)$, i.e. the flow follows the orography's contours:

$$\eta(x, y, 0) = h(x, y). \tag{2.45}$$

Following Smith (1980) and replacing η by a Fourier integral:

$$\eta(x, y, z) = \iint_{\infty} \tilde{\eta}(k, l, z) e^{i(kx + ly + mz)}\, dkdl. \tag{2.46}$$

then:

$$\tilde{\eta}(k, l, 0) = \tilde{h}(k, l), \tag{2.47}$$

which implies:

$$\tilde{\eta}(x, y, z) = \tilde{\eta}(k, l, 0) e^{imz}. \tag{2.48}$$

Now, by introducing (2.46) into (2.44) the polarisation relations will be written as:

$$\tilde{w} = i(Uk + Vl)\tilde{\eta}. \tag{2.49}$$

$$\tilde{u} = -i\frac{[(Uk + Vl)k - ifl]\left[N^2 - (Uk + Vl)^2\right]}{m\left[(Uk + Vl)^2 - f^2\right]}\tilde{\eta}, \tag{2.50}$$

$$\tilde{v} = -i\frac{[(Uk + Vl)l + ifk]\left[N^2 - (Uk + Vl)^2\right]}{m\left[(Uk + Vl)^2 - f^2\right]}\tilde{\eta}, \tag{2.51}$$

$$\tilde{p} = i\rho_0[N^2 - (Uk + Vl)^2]\frac{\tilde{\eta}}{m}, \tag{2.52}$$

$$\tilde{\rho} = \frac{\rho_0}{g}N^2\tilde{\eta}, \tag{2.53}$$

As before, air particles have elliptical orbits for an observer that moves with the reference flow. In the southern hemisphere, air particles are deflected to the right of the summit, by moving towards low pressure (due to the geostrophic wind relations). The pressure and the vertical wind component perturbations remain in phase which means that upstream of the mountain, where upward flow is observed, an area of high pressure is found. Inversely, an area of low pressure is observed in the lee, where there is downward flow. This implies that there is a net force on the mountain in the direction of the flow.

The vertical energy flux is now:

$$\overline{p'w'} = \frac{\rho_0}{2}\frac{N^2 - (Uk + Vl)^2}{m}(Uk + Vl)\tilde{\eta}^2. \tag{2.54}$$

As long as $N^2 \geq (Uk + Vl)^2$ (hydrostatic flow) there is upward propagation if and only if m has the same sign as $Uk + Vl$. By equating (2.22) to zero and solving for the vertical wave number, m is denoted by:

$$m = \pm\left[\frac{\left(k^2 + l^2\right)\left[N^2 - (Uk + Vl)^2\right]}{(Uk + Vl)^2 - f^2}\right]^{\frac{1}{2}} \tag{2.55}$$

If m is imaginary, it could be either have a positive imaginary part and the solution is an evanescent wave, or negative imaginary part and the solution is an exponentially increasing perturbation which must be regarded as non–physical. Vertical propagation occurs if and only if m is real, i.e., when:

$$f^2 < (Uk + Vl)^2 < N^2 \tag{2.56}$$

or

$$f^2 > (Uk + Vl)^2 > N^2 > 0 \tag{2.57}$$

This solution corresponds to upstream sloping waves and that m must have the same sign as the horizontal wavenumber component in the direction of the background wind. When $f^2 = (Uk + Vl)^2$, m is infinite and hence the perturbation velocities are also infinite; the separation of mean flow and wave perturbation used in this section breaks down. In practice, friction would tend to remove this wave component and/or nonlinear effects would become important.

If the flow is two dimensional, i.e. $V = 0$, then the conditions for vertical propagating waves become:

$$f < Uk < N \tag{2.58}$$

or

$$f > Uk > N > 0. \tag{2.59}$$

Rotation effects become important when the horizontal wavenumber is of the same order of f/U. Following Smith (1980) by assuming that the horizontal wave number can be approximated by the mountain width in the direction of the flow (L), then rotation effects become important when:

$$\frac{U}{fL} \gg 1 \tag{2.60}$$

which is that the horizontal scale of the mountain must be much larger than the distance of the downwind drift during an inertial oscillation.

If rotation effects are ignored, m is reduced to:

$$m = \frac{N}{U}\frac{\sqrt{k^2 + l^2}}{k} - 1. \tag{2.61}$$

For upward propagation to occur $Uk < N$; hence for a mountain of width L, the flow is hydrostatic when:

$$\frac{U}{NL} \gg 1 \tag{2.62}$$

which is that the horizontal scale of the mountain is much larger than the distance of the downwind drift during a buoyancy oscillation.

For linear theory to be valid all the flow must go over the mountain and not be diverted around it. In this case, if it is further assumed that the mountain is two–dimensional, the vertical wave number has to be much smaller than the height of the mountain (h), i.e., during a buoyancy oscillation $Nh/U \ll 1$.

In all the previous definitions of m it has been assumed that the waves propagate without being reflected, which is not always true.

2.2.1 Wave Reflection

If the atmosphere is assumed to be piecewise–uniform with a flow of uniform wind speed of U and a buoyancy frequency given by:

$$N = \begin{cases} N_1, & 0 < z < H \\ N_2, & z > H \end{cases} \tag{2.63}$$

then wave reflection and refraction can occur at the buoyancy discontinuity. Assuming that propagating waves occur in both layers then at the boundary between the layers, the pressure perturbation and the vertical velocity must be continuous. Following Gill (1982), this condition implies that the impedance:

$$Z = \frac{p'}{\rho_0 w} \tag{2.64}$$

must be the same on both sides of the boundary. For a two–dimensional flow, the wave on the top layer is unbounded and has the form:

$$w = w_2 e^{i(kx + m_2 z - \omega t)} \tag{2.65}$$

then the impedance for a plane wave becomes:

$$Z = -\frac{\omega m_2}{k^2} \tag{2.66}$$

where m_2 is the vertical wave number for the upper layer with $N = N_2$. Below $z = H$, the propagating wave has an upward component as well as a downward component due to the reflection at the boundary. Then:

$$w = w_1 \left[e^{im_1(z-H)} + re^{-im_1(z-H)} \right] e^{i(kx-\omega t)}. \tag{2.67}$$

The impedance is now given by:

$$Z = \frac{\omega m_1}{k^2} \frac{-e^{im_1(z-H)} + re^{-im_1(z-H)}}{e^{im_1(z-H)} + re^{-im_1(z-H)}} \tag{2.68}$$

where the reflection coefficient r is the ratio between the amplitudes of the upward and downward moving waves. At the boundary this is obtained by equating the expressions for the impedance for both layers:

$$r = \frac{m_1 - m_2}{m_1 + m_2} \tag{2.69}$$

Below $z = H$ the velocity amplitude oscillates between extreme values spaced at intervals of a quarter wavelength ($\pi/2m_1$). According to Gill (1982), the amplitude at even multiples of $\pi/2m_1$ below $z = H$ is the same as at $z = H$ and at odd multiples the amplitude is:

$$\frac{1-r}{1+r} = \frac{m_2}{m_1} \tag{2.70}$$

times the value at $z = H$. When $N_1 > N_2$ ($m_1 > m_2$) the extremum is at a maximum and depending on the number of quarter of wavelengths the discontinuity is above the ground it is the most efficient generation of waves on the upper layer. For $N_1 < N_2$ ($m_1 < m_2$) the extremum is at a minimum. At the ground the reflection coefficient is obtained by considering zero vertical velocity at the ground,

$$r = -e^{-2im_1H} \tag{2.71}$$

with,

$$w = w_0 e^{i(kx-\omega t)} \tag{2.72}$$

where,

$$w_0 = w_1 \left[e^{-im_1H} + re^{im_1H} \right]. \tag{2.73}$$

The vertical energy flux is independent of height and is given by:

$$\overline{p'w'} = \frac{U m_2 \rho_0 w_0^2}{2k \left[1 + ((m_2/m_1)^2 - 1) \sin^2(m_1 H) \right]} \tag{2.74}$$

If the discontinuity is at an even number of quarter wavelengths above the ground, then $\sin(m_1 H) = 0$, and:

$$\overline{p'w'} = \frac{U m_2 \rho_0 w_0^2}{2k} \tag{2.75}$$

which is the same result as if there was no lower layer. If the number of wavelengths between the ground and the discontinuity is an odd integer, then $\sin(m_1 H) = 1$, and:

$$\overline{p'w'} = \frac{U m_1^2 \rho_0 w_0^2}{2 m_2 k}. \tag{2.76}$$

The flux is enhanced when $m_1 > m_2$.

2.3 Background on Internal Gravity Waves

Comprehensive reviews on the flow of stratified fluids over orography can be found in Gill (1982) and Baines (1995). This section will only present a brief summary of a few results and observations that will help to put in perspective the work done in later chapters.

A first attempt to model flow over orography was performed by Long (1953) using hydraulic theory. The transition from subcritical to supercritical flow is used to explain the emergence of strong downwind flows in the lee of mountains. The advantage of Long's model is that analytical solutions for two dimensional, non–linear, mountain waves can be obtained. A disadvantage of the use of this approach is that it assumes that the fluid must be bounded by a rigid lid or a free surface impeding the possibility of vertical propagation of energy which is observed in the real atmosphere.

Queney (1948) was the first to circumvent that problem by using linear theory of internal gravity waves to study inviscid stratified flows, with uniform wind and stability, over a two dimensional isolated mountain. His results showed that the nature of the flow depended critically on the horizontal scale of the mountain or on rotation effects. As noted by Queney, linear theory allows for vertical transport of energy.

The extension of Queney's work to non–homogeneous atmospheres was first presented by Scorer (1949). Scorer established the necessary condition to explain the trapping of gravity waves. Klemp and Lilly (1975) studied gravity wave propagation in multilayered atmospheres with discontinuities in static stability. They found that the mechanism which leads to strong downslope winds is associated with partial reflection of upward propagat-

ing gravity waves by the variations in static stability.

If the static stability varies slowly with height the WKB method yields that the amplitude of the wave is proportional to $\rho^{-1/2}$ and the phase change with height as the vertically propagating gravity wave transverses the different layers is proportional to N.

According to Smith (1989), a vertically propagating wave is partially reflected with a phase shift of π by a sudden increase in static stability. The downward reflected wave is again reflected upwards by the lower boundary with another phase shift of π. If the reflected wave is in phase with the original wave generated by the topography so that the phase shift is near $2\pi n$, with $n = 1, 2, 3, \ldots$, then the atmosphere can produce much stronger mountain waves than an atmosphere with constant N These are resonant waves, often called lee–waves. If the phase shift is $\pi + 2\pi n$ then the results will be the inverse.

2.3.1 Non–Linear Effects

Non–linear effects on the generation of strong downslope winds has been extensively studied by numeric simulations. Durran (1986) and Wang and Lin (2000) have demonstrated the importance of temperature inversion on wave breaking. Durran (1986) simulated flows in a two layer atmosphere where the layer with highest stability was either near the surface or the top layer. He found that the largest differences between linear and non–linear simulations occur when the static stability in the lower layer was higher than in the upper layer. He also demonstrates that the hydrostatic part of the flow is the forcing mechanism for the lee–waves and that the non–linear effects are responsible for the dislocation of the maximum of the downslope wind to the base of the mountains. Another important result from his simulations is that hydraulic theory can be used to explain the amplification of the surface wind.

Nevertheless Vosper's (2004) non-linear numerical simulations determined that linear theory provides an accurate measure of the lee–waves' wavelength even when rotors occur below the wave crests. However, linear theory is unable to predict the wave amplitude for large hills.

2.3.2 Effects of Mountain Shape

Most of the analytical work and numerical simulations of flow over orography presume that the flow is over a single, symmetrical, smooth mountain; yet, the mountain's shape and/or the number of mountains in the domain has a significant impact on the flow downstream.

Lilly and Klemp (1979) found that the wave amplitude and wave drag are significantly enhanced for mountains with gentle windward slope and steep leeward slopes. Miller and Durran (1991) in their work on the influence of the asymmetry on downslope windstorms also established that steep lee slopes produce an increased response and that the sensitivity is significantly enhanced by surface friction. In their simulations with friction and a two layered atmosphere, they also found that a rotor occurred in the lee for all mountain profiles.

Experiments by Pratt (1984) with flow of a homogeneous layer with a free surface, over two obstacles identified four main regimes which depend on the relative heights of the obstacles. When the height of the first obstacle is significantly higher than the second, the flow is controlled by the first obstacle and is either subcritical or supercritical over the second. If the height of the second obstacle is smaller than the first's, nonlinear wavetrain with breaking waves occurs in the region between the obstacles. When the obstacle heights are comparable a laminar wavetrain is observed in the region between the obstacles. The amplitude of the waves increases with an increase in the upstream Froude number. For a higher second obstacle the flow is dominated by it and the flow over the smaller first obstacle is subcritical.

In simulations with three dimensional mountains, Vosper (1996) notes that the interference between waves generated by flow over two obstacles is significantly enhanced when there are trapped waves in the lower layers of the atmosphere.

2.3.3 Rotors

Although rotors have been observed as a result of theoretical (*e.g.* Queney *et al.* (1960) and Lyra (1943) and experimental studies (*e.g.* Baines and Hoinka (1985) and Hunt and Snyder (1980)), there are very few results dedicated to the investigation of rotor dynamics. Doyle and Durran (2002), Vosper (2004) and Doyle and Durran (2004) are the only

exceptions.

Doyle and Durran (2002) found that realistic rotors develop only in the presence of surface friction and are a boundary layer separation phenomenon that develops in association with large amplitude trapped lee waves. They performed simulations in which the friction at the surface was increased and determined that the point of boundary layer separation shifts upstream with increasing friction. An increase in the surface heat fluxes increases the depth of the rotor but decreases its strength.

There are few observational studies which are dedicated to rotors. Initial observations were made by Manley (1945), Kuettner (1939) and Lester *et al.* (1974). More recently, the observation of a rotor cloud over the Penny Ice Cap was reported by Ozawa *et al.* (1998). Ozawa also reports the occurrence of a temperature inversion downstream and associates it to a possible temperature inversion upstream (his radiosondes were launched 400 km south of the ice cap). Ralph *et al.* (1997) using remote sensing techniques have also investigated trapped mountain waves but their studies focused on the nonstationary characteristics of the flow. The only major field project dedicated to the exclusive observation of rotors and hydraulic jumps was deployed over the Sierra Nevada (Holmboe and Klieforth, 1957).

3. The Falklands Experiment

During the autumn and summer months the Met Office forecasters at the Falkland Islands often issue warnings of severe low-level turbulence when the winds have a predominant northerly direction. This low-level turbulence is often associated with the presence of trapped gravity waves generated by the flow of the winds over the mountains and the emergence of rotors under the crest of these waves. Since the scale of this phenomenon is smaller than the subgrid scale of weather forecasting models, such forecasts are unable to represent the formation of rotors or the presence of severe turbulence. To obviate that problem, the School of the Environment (University of Leeds) and the University of Manchester Institute of Science and Technology (UMIST) set up a field experiment in the Falkland Islands. In the experiment 24 weather stations were deployed from November 2000 to October 2001.

In this chapter a brief description of the Falklands climatology is provided as well as a description of the field campaign and the data calibration procedures.

3.1 Climatology

The Falklands are an archipelago located in the South Atlantic Ocean between 51°S and 53°S, at longitudes between 57° 43'W and 61° 30'W (figure 3.1). The archipelago consists of two major islands, East Falkland and West Falkland, and other minor islands. During the summer months the region lies on the Southwest corner of the South Atlantic high, which means that the prevailing winds at the surface are North-westerly, and in the winter the Antarctic vortex is the dominant circulation pattern so that the predominant surface winds are westerlies. A northward cold current – the Falklands Current, dominates the ocean currents in that area of the South Atlantic.

The monthly average temperature (figure 3.2a) oscilates between 9.3° C in February and 2° C in July. The average daily temperature amplitude is around 8° C from October

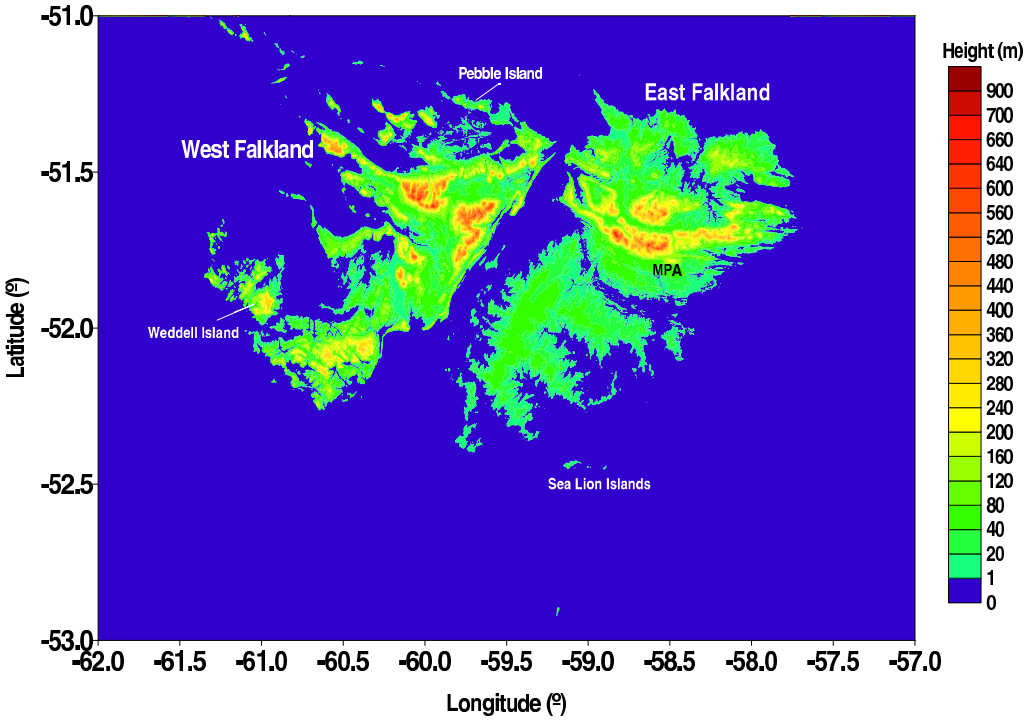

Figure 3.1: The Falklands Archipelago. Terrain heights are shown in meters with a contour interval of 20 m. Also shown is the location of Mount Pleasant Airfield (MPA) and of Pebble, Weddell and Sea Lion Islands.

to February (spring and summer) and around 5° C during winter (June to August). Since the average temperature of the warmest month is below 10° C and greater than 0° C the Falkland's climate is, according to Köppen's Climatic Classification System, a Tundra Polar Climate. This is consistent with the type of vegetation observed in the archipelago.

The percentage of sunshine per percentage of day length (figure 3.2b) is never greater than 42 % (observed in September). During spring and summer the percentage of sunshine varies between 36.7 % and 41 % and is 28.9 % in June. The low value for this parameter along with a high relative humidity (figure 3.2e) is indicative of a high percentage of cloud cover for the whole year. Although there is a high percentage of cloud cover the precipitation (figure 3.2f) is low. The highest amounts occur in January and December and in the remaining months it is always less than 50 mm. The number of days with precipitation greater than 0.1 mm (figure 3.2g)is fairly uniform and low, it fluctuates between 12.8 (January) and 8.5 (September).

During the winter months the percentage of days with ground frost is greater that 57 %. The number of days with ground frost rises steadily from February (7.8 days) to July

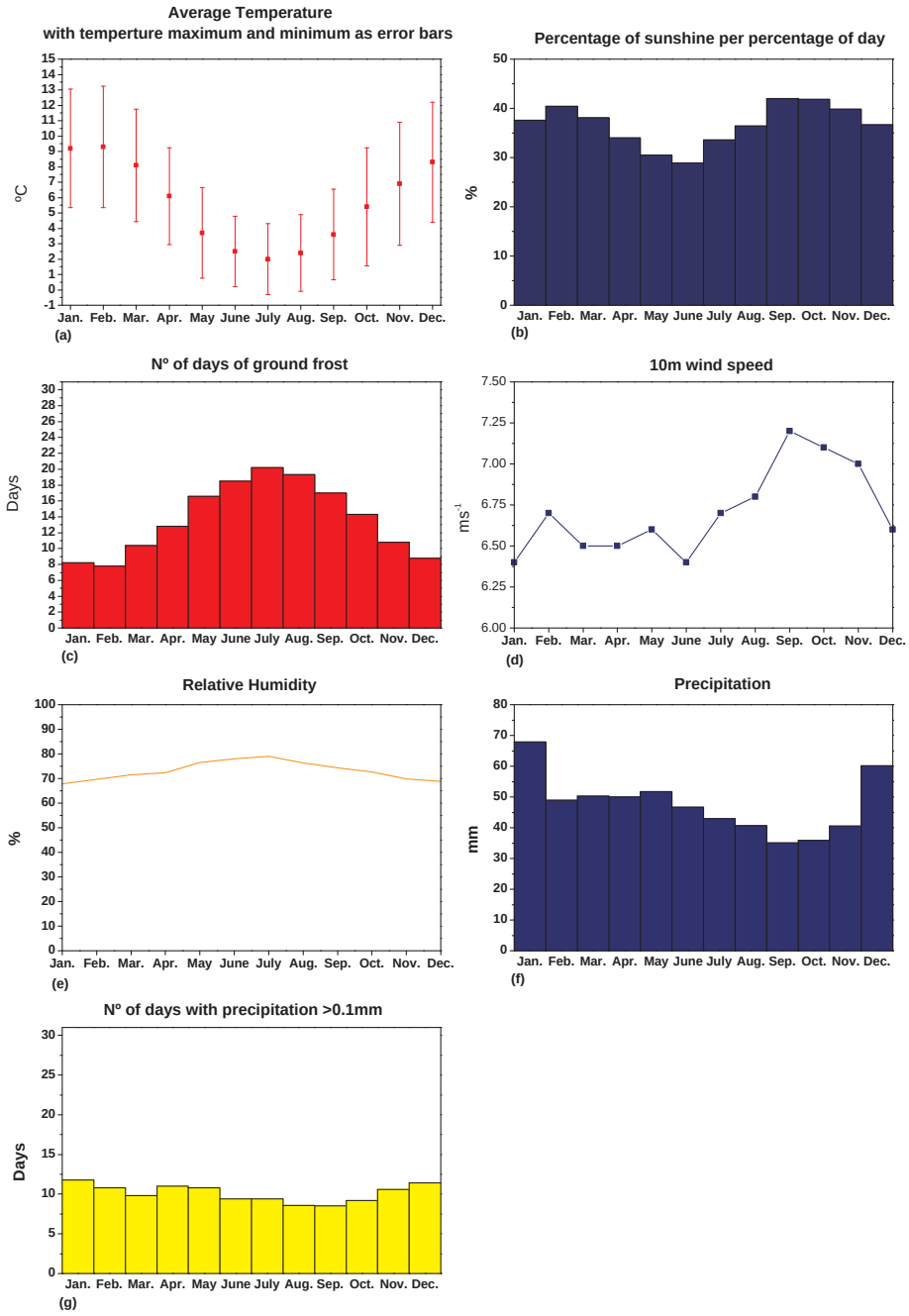

Figure 3.2: 1961 to 1990 climatology for $-51.75°$ S and $-58.47°$ E. (a) monthly average temperature with temperature amplitude as error bars, (b) percentage of sunshine per percentage of day length, (c) number of days of ground frost, (d) 10 m wind speed, (e) relative humidity, (f) precipitation (mm), (g) number of days with precipitation greater than 0.1 mm.

(20.2 days) after which decreases to the minimum observed in February.

The wind speed through out the whole year is not very strong. The highest average monthly wind speeds are observed during late winter and spring, where for the months of September to November the wind speed is greater than 7 ms^{-1}. For the remaining months the wind speed is around 6.5 ms^{-1}.

This climatology data was obtained from the IWMI Climate Atlas (New *et al.*, 2002).

3.2 The Field Experiment

One of the advantages of carrying out such a campaign on an island is that the orography is isolated and the flow in its vicinity is undisturbed by any other topographical features. The topography of East Falkland is also very well defined, i.e., it does not have intricate features that may render the use of simple models or parameterisations impossible. The Falklands have also tundra like vegetation, which reduces the difficulty of parameterising the surface drag.

The relevant topography of East Falkland is comprised of a small mountain (Mount Simon) north of a East/West orientated ridge (Wickham Heights) which has a maximum height of about 640m. To the south of this ridge, is a small hill (Mount Pleasant) of about 220m high (figure 3.3). In the lee of Mount Pleasant lies Mount Pleasant Airport (MPA).

Under northerly winds severe turbulence presumably associated to gravity waves is commonly observed. Under certain conditions, the turbulence is associated to high temporal and spatial variability in wind speed and direction with recirculation zones. The Met Office forecasters refer to these recirculation zones as "rotor streaming". These rotors pose a significant hazard to air traffic and the location of MPA in the lee of Mt. Pleasant enhances the need for a forecasting tool. The main objectives of the campaign were:

- Investigate resonant gravity waves and hydraulic jumps;
- Study the relationship between mountain waves and rotor streaming;
- Develop a rotor streaming prediction system;
- Validate mountain wave forecasts for the Falklands.

The measurements in East Falkland were made in the vicinity of Mount Pleasant Airport where nine stations (2 – 9 and 13) were deployed in a grid so that the turbu-

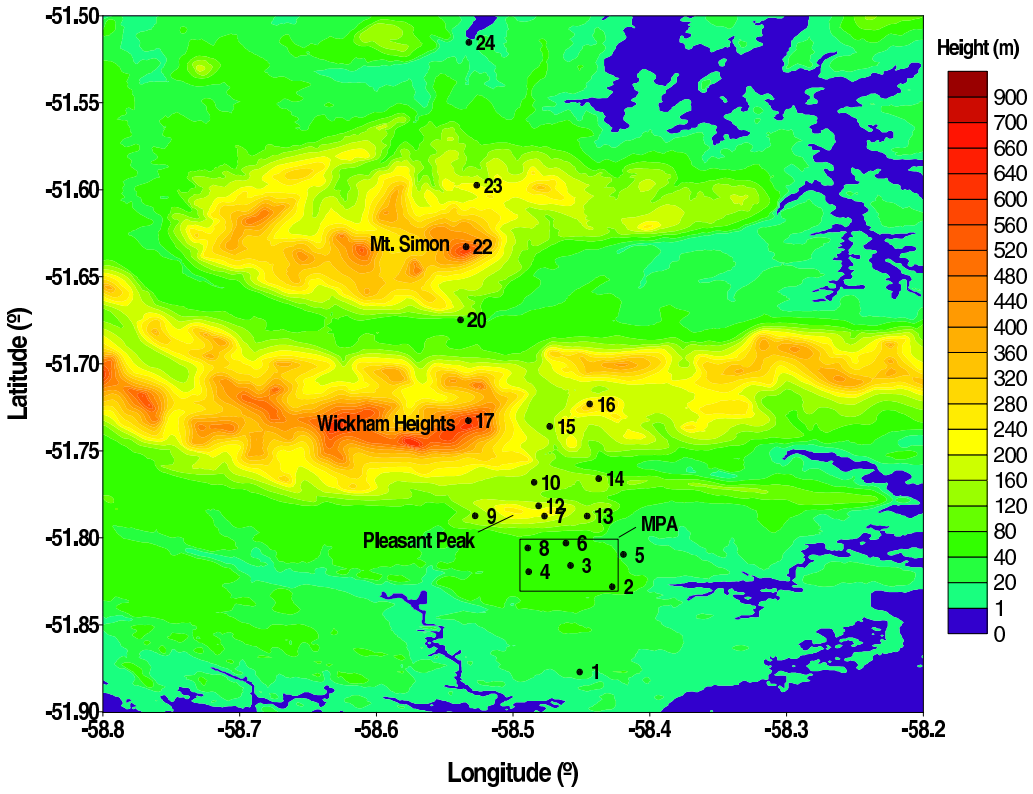

Figure 3.3: Location of the automatic weather stations on East Falkland as well as detailed view of the terrain. Also shown is the approximate location of MPA.

lent phenomena would be captured and well characterised (figure 3.3). Stations were also deployed along a North/South transect across the two ridges, so that under northerly conditions the upstream conditions might be related to the downstream flow. For the cases that we are interested in, station 24 is considered to be upwind and should represent the surface characteristics of the atmospheric flow undisturbed by the mountains. Stations 22 and 17 are located on top of Mt. Simon and Mt. Wickham respectively and should provide an idea of the flow at the summits and how the different mountains influence it. The station in the valley between Mt. Simon and Mt. Wickham (station 20) is most probably sheltered from the main flow and should have different features.

The location and height, relative to a base station at Mount Pleasant Airport (MPA), of each station is described in table (3.1).

Each automatic weather station (figure 3.4) consisted of a RM Young propeller anemometer; a temperature sensor housed in a radiation shield and a relative humidity sensor, all mounted on a two-meter mast. At the base of the mast a microbarograph was placed. The

Station	Latitude	Longitude	Altitude (m)
1	51° S 52' 37.72"	58° W 27' 4.83"	−26.335
2	51° S 49' 41.59"	58° W 25' 39.12"	−20.477
3	51° S 48' 57.27"	58° W 27' 28.76"	−4.609
4	51° S 49' 10.55"	58° W 29' 18.99"	9.510
5	51° S 48' 34.70"	58° W 25' 9.55"	−28.662
6	51° S 48' 10.92"	58° W 27' 41.12"	−8.509
7	51° S 47' 14.76"	58° W 28' 37.18"	67.686
8	51° S 48' 20.77"	58° W 29' 21.00"	−3.368
9	51° S 47' 14.76"	58° W 31' 39.86"	58.928
10	51° S 46' 5.74"	58° W 29' 4.51"	66.771
12	51° S 46' 54.23"	58° W 28' 52.98"	134.590
13	51° S 47' 15.12"	58° W 26' 44.71"	51.576
14	51° S 45' 57.63"	58° W 26' 14.81"	76.204
15	51° S 44' 9.76"	58° W 28' 23.36"	67.893
16	51° S 43' 32.55"	58° W 26' 38.46"	228.830
17	51° S 43' 57.74"	58° W 31' 57.74"	547.372
20	51° S 40' 29.21"	58° W 32' 18.61"	−15.947
22	51° S 37' 57.91"	58° W 32' 3.45"	524.070
23	51° S 35' 50.66"	58° W 31' 35.80"	162.876
24	51° S 30' 55.20"	58° W 31' 56.12"	−47.306
Pebble	51° S 18' 45.72"	59° W 36' 28.16"	−52.498
Weddell	51° S 53' 42.03"	60° W 55' 3.54"	−48.442
Sea Lion	52° S 25' 41.49"	59° W 4' 36.07"	−57.330

Table 3.1: Location and height of each of the stations deployed in the campaign. The station height is relative to a base station which is about 80 m high.

sampling rate of all instruments was 3s that was stored as 30s averages. Turbulence measurements were also made at site 3 and 7. At each of these two sites, two sonic anemometers were mounted on 15 m masts, at 7.5 and 15 m high. At Mt. Pleasant Airport, two Sodars were deployed at the beginning of the campaign (these did not remain for the whole duration of the experiment) and a WebCam pointing North towards the mountains was also set up. The Met Office released radiosondes twice a day at approximately 1100 UTC and 2300 UTC and on days when high turbulence or rotors were present they released an extra sonde. Unfortunately the radiosondes were released at Mt. Pleasant Airport, which means that they were not representative of the upwind profiles for the days of interest.

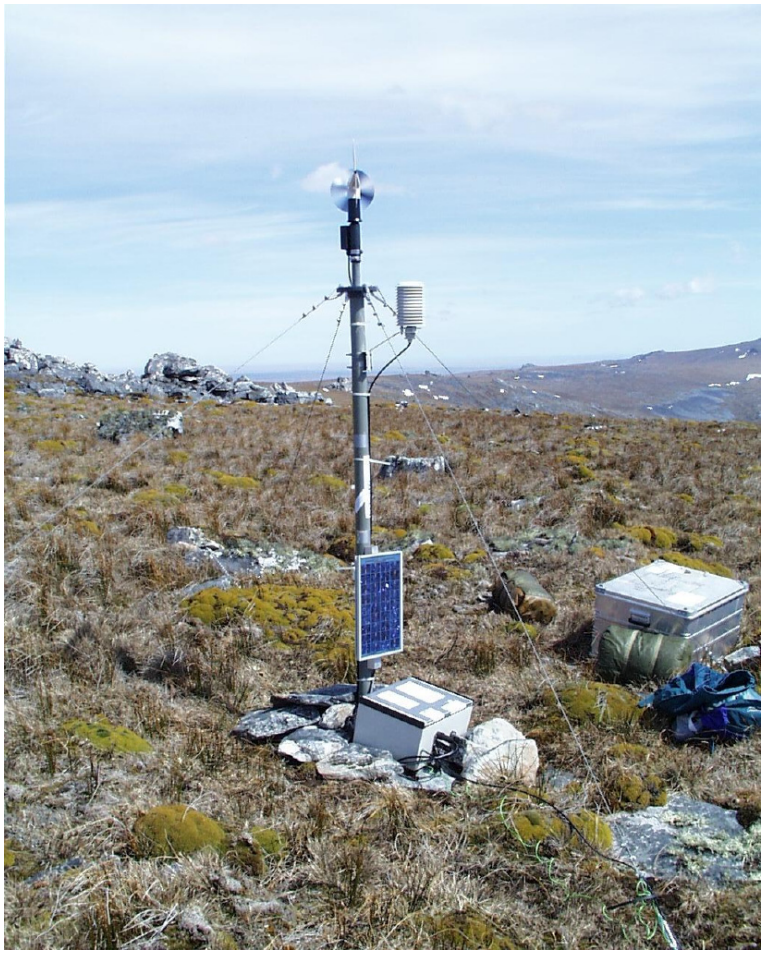

Figure 3.4: Weather Station with microbarograph

The sites were revisited at the end of April 2001. During this visit the temperature sensor of site 22 had to be replaced by a new one and the mast had to be returned to the upright position (it had been thrown down by a bull — this rendered the wind data

useless from that moment). The microbarograph and the anemometer of site 16 had also to be replaced. At the end of the experiment the static head of the microbarograph from site 1 had become unattached, the anemometer from site 10 was loose and site 16 was flooded so all the data after about Julian day 170 was lost. On both occasions, the other stations did not have any major problems.

3.3 Sensor Calibration

A description of the sensors used and of their calibration will be the focus of this section. Since the author did not participate in the calibration procedures only a summary of the proceedings will be described. For a detailed description see Horlacher (2003).

The microbarographs were designed and constructed by Martin Hill, the Senior Experimental Officer at the School of the Environment. Each unit consisted of a self–contained data acquisition system constituting of A–D converters for pressure, temperature, humidity and wind, along with data storage. The data from each station was stored on a PCMCIA flash card.

3.3.1 Calibration Setup

The calibration of 22 of the instruments was performed in an undisturbed location in Martin Hill's fields, in the Pennines. The other two microbarographs were calibrated in the Falklands. The setup was the same in both sites. At Martin Hill's field the temperature and humidity sensors were setup in a wooden beam about 1 m from the ground at a distance of circa 50 cm from each other. The pressure sensors were all connected to a porous garden hose (static head) about 2 cm thick that was laid out as a 10 m diameter ring. This set-up ensures that all instruments are subjected to the same atmospheric conditions and since the pressure is measured as an average of the pressure on the whole ring, the local fluctuations in wind speed won't influence the pressure signal (Vosper and Mobbs, 1997). On a separate post, a Vaisala PT100 1/3B was mounted to serve as a reference for the temperature sensor and a digiquartz barometer from Paroscientific Inc. was set up inside Martin's house connected to the same static head(it was not set–up near the other instruments because it needed a 240 V AC power supply).

3.3.2 Calibration of the Temperature and Humidity Sensors

The calibration of the temperature and humidity sensors was done by linear regression between data from the calibrated reference sensor and raw data obtained during a field experiment that took place in 2000, on Arran. The reference sensor used was a Vaisala PT100 1/3B, borrowed from the University of Innsbruck and its calibration is described in the next section.

Calibration of the Reference Temperature/Humidity Sensor

The reference sensor was placed in a container filled with water. The container had an adjustable temperature unit (Haake DC5) and a Testoterm Testo 781 Quartz Temperature Sensor. Obviously, this last temperature sensor was a calibrated sensor and was used as reference. The water in the container was heated from -10° C to 30° C. Readings were made every 5° C, but because the water temperature could not be maintained for a long period, several readings were made for each temperature. The calibration was obtained by linear regression between the reference sensor and the average of the readings for the appropriate temperature. The standard deviation of the difference between the reference sensor and the calibrated sensor was 0.03 (Pippan 2000).

The calibration of the humidity sensor was performed by University of Munich. They placed the sensor in an airtight box connected to a constant air stream of known pressure and humidity. A regulating unit adjusted the humidity. According to Pippan (2000), for relative humidity values near saturation, the sensor overestimated relative humidity by about 10 % to 15%, which was due to the fact that the University of Munich calibrated it only up to 65% relative humidity. The University of Innsbruck, subsequently, made an attempt to correct the offset. When the correction was applied to the uncalibrated time series from Martin's fields the changes in the overall values was only of about 1 % (Horlacher, 2003) and the maximum value achieved was 95 % although the site is generally exposed to high relative humidity values. To obviate this problem Horlacher (2003) ignored the University of Innsbruck's correction and applied an offset so that the maximum of 95 % became 100%. He notes that this is not a proper calibration as no standard was involved, but it allows qualitative analysis of the field values as long as they are compared with each other.

Calibration of the Field Temperature Sensors

In the field experiment, two types of sensors were used. Microbarographs b11, b20 and b26 were equipped with a Honeywell HIH-3602-C sensor and the other microbarographs were equipped with a Beta Therm 100 K 6A1. Both sensors are semiconductors, which change resistance with temperature. The first type of sensor was initially deployed on all microbarographs on Arran and is a temperature as well as humidity sensor. The whole sensor is housed in a sintered stainless steel can and the temperature sensor is located beneath the humidity sensor. During the Arran 2000 experiment water got into the sensor casing and they started to fail (Martin Hill's personal communication). These temperature sensors were then replaced with the Beta Therm 100K 6A1, which were, then, soldered directly onto the connectors from the old sensors. Only five sensors survived, three of which were used in the Falklands.

For each temperature sensor, the conversion from resistance to temperature is calculated with:

$$R_t = R_r \quad e^{((B/T_t)-(B/T_r))} \tag{3.1}$$

where R_t is the resistance of the temperature T_t, R_r is the resistance of the sensor at 25° C (T_r) and B is a characteristic constant of the material (these values were obtained from the manufactor). After the conversion from resistance to temperature was conducted, a linear least squares fit between the data from the reference sensor and the data from the calibration period was performed. All the slopes from the least squares fit range between 1.003 and 1.03 and the offsets vary between $-0.003°$ C and $-0.2°$ C. The only exceptions were microbarographs b19 and b22 where high noise level has influenced the temperature signal. The correlation coefficient was greater than 0.999 for all sensors (Horlacher, 2003).

During the Falkland's experiment the temperature sensor from microbarograph b14 (station 22) stopped working and had to be replaced by a new uncalibrated sensor. Since that at the end of the experiment no precision instrument was available, one of the other calibrated sensors had to be used as reference. Microbarograph b01 was chosen as the reference sensor. This choice was based on the following criteria (Horlacher, 2003):

- The smallest standard deviation from the difference between the data from the precision instrument and the data from the sensor;

- A high number of records involved in the calibration.

Calibration of the Relative Humidity Sensors

The relative humidity is measured through a change in capacity between two electrodes. The water vapour present in the air acts as a dielectric and its variation changes the capacity between the electrodes. According to the manufacturers, the relationship between the output signal and the relative humidity is:

$$rh = \frac{rh_{measured}}{1.0546 - 0.0026t} \tag{3.2}$$

where $rh_{measured}$ is the output signal from the capacitor and t is the temperature in degrees centigrade. So, only when temperature and humidity values are available can the relative humidity data be compensated using the previous equation.

As with the temperature sensors, a linear least square fit was performed between the data and the reference sensor. For these sensors, the correlation coefficients were between 0.97 and 0.999 and the standard deviation for the difference between the reference sensor and the field values was less than 1 %, except for microbarographs b01 and b19 (Horlacher, 2003). Both the reference sensor and the field sensors have a problem for high humidity values. When the surface temperature of the sensor is only slightly above the ambient dew point, the rate at which water evaporates is longer than the sensor time response, so the output values remain constant (at or above 100 %) regardless of the ambient relative humidity (http://content.honeywell.com). The company also suggests that exposure to humidity values greater than 95 % for longer than 24 hours leads to an upwards drift of 2 % to 3 %. The shift is repeatable but only when the sensor is put in an environment of 10 % relative humidity for up to ten hours. Since the instruments were deployed for one year in the Falklands this renders the data for high relative humidity values useless.

3.3.3 Calibration of the Pressure Sensors

The reference sensor for the pressure calibration was a Field Barometric Standard Model 760, which is a resonant quartz crystal barometer. The sensor is a dual beam load–sensitive resonator (Busse 1987) which is driven piezoelectrically in 180° phase opposition. The atmospheric pressure is transformed into a torque that acts onto the two beams changing

the frequency of the resonator beam. The change in frequency produces an electric signal, which allows the pressure to be measured. The quartz crystal used in the pressure sensor besides being sensitive to pressure is also sensitive to temperature. Another quartz crystal, which is only sensitive to temperature, is used to correct the signal for temperature changes. The resolution of the barometer is 0.1 hPa for all environmental conditions and has a precision of 0.01 % per reading. According to Paroscientific the drift rate per year is estimated to be 0.007 hPa.

The pressure sensor used (SENSYM SX15AD2) is a box that is separated into two parts by a diaphragm. The diaphragm separates a nearly evacuated part and the other is exposed to the atmosphere. A silicone layer on both sides also, covers it. A change in atmospheric pressure induces changes in pressure difference across the diaphragm. This, in turn, deforms it and the attached silicone layers as well. The compression or stretching of the silicone layers changes their resistance. This change in resistance can be transformed into a voltage difference through a Wheatstone Bridge. The resistance of the silicone is in the range of 1 to $10k\Omega$, which is a compromise between obtaining the highest resistance, minimising power consumption and maintaining similarities between the resistors. The voltage output of the Wheatstone Bridge is transformed into a digital signal through a 24 bit analog–to–digital converter (Burr–Brown AD1210). The converter works on the basis of a second order sigma delta conversion. The use of a 24 bit converter enables measurements of pressure between 0 and 1100 hPa with high resolution without the use of amplifiers or comparators. These would be an extra source of temperature dependence. The bits are then transformed into pressure through the calibration equation.

The Calibration Equation

Imperfections in the silicone are what transforms it from an insulator into a semi-conductor, but also introduce a temperature dependency. So for a given pressure, the voltage output of the Wheatstone Bridge (which is also temperature dependent) will change with temperature changes even if the pressure remains constant. To solve this problem, two Beta Therm 100 K 6A1 temperature sensors were attached to the circuit board next to the pressure sensor. So, at each time step, two internal temperatures are measured as well as the pressure. This way, if one of the temperature sensors fails the pressure time series can still be calibrated. These two temperature sensors do not need to be calibrated, as only the relative change in temperature is needed.

Previous experiments determined that for an accuracy of 0.05 hPa a third or fourth order polynomial is needed for the calibration. These experiments had used another type of microbarograph and when a forth order polynomial was used in the least squares fit between the reference sensor and the data that accuracy couldn't be achieved (Horlacher, 2003). The problem was due to the different time responses of the silicon and the temperature sensors. The temperature sensors have a faster reaction time. A fifth term was introduced into the equation. The four terms of the equation are determined by a best fit between the bits and temperatures. The fifth term is related to the temperature behaviour 30 minutes earlier time. This is obtained through an iterative method (see Horlacher (2003) for more details). The calibration equation is as follows:

$$P[b(t), T(t)] = a_1 + a_2 b(t) + a_3 b(t) T(t) + a_4 b(t) T(t)^2 + a_5 T(t - t_i) \tag{3.3}$$

where $P[b(t), T(t)]$ is the calibrated pressure for time step t, with an internal average temperature $T(t)$. $b(t)$ is the output signal from the 24 bit analog to digital converter and $T(t - t_i)$ is the shifted temperature in time. The a_j are the estimated coefficients.

3.4 Quality Control

In this section a description of the quality control procedures is described. Each time a station was visited the stored data was retrieved and a new file was created. The first step was, then, joining all the files for each station, so that there was only one file per station.

Although the timekeeping of the microbarographs was usually accurate (drift of up to 2 min. after a year) there were some inaccuracies in the time steps and some data was missing. If the error in the time step was smaller than 15 s the time was corrected, otherwise it was considered that data was missing. The missing data was considered to be -999.0. At this stage the date was also changed. The Julian days for the year 2000 were transformed into negative days and the 31^{st} of December became day zero. The next step was to visually check the pressure sets for obvious wrong data, i.e. the data from two sets was plotted, compared and obvious differences were checked for plausibility. Subsequently the data was calibrated and automatically checked for sudden increases or decreases in just one time step. The steps in temperature should not be greater than 0.5° C. For relative humidity, the threshold was 5 % and the pressure could not increase or decrease for more than 0.5 Pa. The sets were also automatically checked for "spikes" (a sudden

increase (decrease) followed by a decrease (increase)). The sets were then plotted and all the suspicious time steps were checked. These time steps were, then, flagged according to the type of error and a flag file was constructed. The flags were:

- 0 for good data;
- 1 when the value was slightly outside physical or instrument range (e.g. humidity $> 100\%$, wind < 1 m/s). This value was not changed (and thought suitable for use in lower resolution data generation);
- 2 for a suspect value. The was value not changed but should be used with caution (not to be used in the generation of lower resolution data);
- 3 for values slightly outside physical or instrument range (e.g. small negative wind speeds). The values were corrected into the physical range;
- 4 when the value was outside physical range or an outlier – value disregarded;
- 5 bad data (e.g. transmission error, external influence) – value disregarded;
- 6 no value available i.e. bad in raw data – value disregarded.

The spikes were all flagged as bad data, with flag 5. The data after a big step was usually flagged with flag 2. All relative humidities between 100% and 110% were flagged with flag 1 and for values greater than 110% or negative the flag was 4. Flag 1 was also used for wind speeds less than 1ms^{-1}. Negative wind speeds were flagged as 4. The files were, subsequently, set into files with the same range and length. It was decided that all the files should start on the 29^{th} of October 2000 and end on the 7^{th} of November 2001 The final set of data is a ten minute average of the thirty—second data. For this data, new flags were introduced.

- 0 for good data;
- 1 if two thirds of the data was good;
- 2 if less than two thirds of the data was good. The values for this data were changed to -999.0.

The final step was to correct the pressure for altitude. The heights of all of the stations relative to a base station at MPA were surveyed using a differential GPS. This gave the altitude to ± 1 m, hence the error of the reference pressure was approximately ± 0.15 hPa.

The stations on East Falkland were split into three groups. The first group included stations 1 to 17, the second group was made up from stations 17, 20 and 22 and the third group had the remaining stations. For each group, whenever possible, a vertical temperature profile was constructed. As a first approximation, the temperature values are fitted into a straight line using linear regression by assuming that the uncertainty associated with each measurement is unknown and that the measurement errors are normally distributed. The maximum likelihood parameters are obtained by minimising the chi–square function (this is a simple least squares fit). The assumption of normally distributed errors can lead to significant errors in the parameter estimation if outliers are present, so a more robust technique was used for the section which includes stations 1 – 17. For the other two sections, each containing only three microbarographs, the least square fit was assumed to be a good estimate. The line fitting for stations 1 – 17 was done by minimising the absolute deviation, i.e., the function that is minimised is:

$$\sum_{i=1}^{N} |y_i - a - bx_i| \tag{3.4}$$

instead of the χ^2. This is simplified by the fact that the median of a set of numbers is the value which minimises the sum of absolute deviations (the subroutines used were obtained from Press *et al.* (2001)). When it was impossible to determine a vertical profile, the atmosphere was considered isothermal. The pressure was, then, corrected using the hydrostatic equation, i.e.:

$$p_{ref} = p_{sta} \left[\frac{T_0 + T_1 z_{sta}}{T_0 + T_1 z_{ref}} \right]^{\frac{g}{RT_1}} \tag{3.5}$$

where T_1 is the slope determined by either method, z_{ref} is sea level, z_{sta} is the station height relative to sea level (height from table (3.1) plus the height of the reference station).

After the height correction, a small temporal trend was found between the pressure time series. The difference between the stations in East Falkland and station 4 was determined for wind speeds less than 3 ms^{-1} in an attempt to reduce this trend. The microbarograph of station 4 was chosen since during the calibration procedures it had very few errors and was not too close to the ridges. Linear regression was then used to determine the temporal evolution of the differences. A first order fit was used for all stations except station 3, 5 and 8. For station 3 a fifth order fit had to be used, for station 8 a third order fit gave the best approximation and for station 5 an exponential decay was the best fit.

4. 1–D Model

Severe turbulence at the surface and strong winds are often observed downstream of the two ridges that span East Falkland under northerly flow conditions. This turbulence is presumed to be associated with trapped gravity waves and the wind speed and direction at Mt. Pleasant Airfield (which lies downstream) exhibit high temporal and spatial variability. Recirculation zones are commonly found underneath the wave crests. During these events, which pose a significant hazard to air traffic, a temperature inversion is observed in the radiosonde vertical profiles. Since the radiosonde launches are performed at MPA, there is no upstream profile.

This chapter describes a one dimensional model developed to emulate the evolution of the marine boundary layer in the vicinity of the Falkland Islands. The main aim was to have a fast and simple model that would reproduce the major processes and since most of the relevant parameterisations in weather prediction models have a one dimensional structure, the construction of a 1–D model seemed an appropriate way to address the problem.

In boundary layer models turbulence parameterisation plays a significant role, and so substantial consideration has to be given to the type of turbulence closure, structure of the mixing length and dissipation. According to Brasseur *et al.* (1998), a greater weight should be imposed on the formulation of the mixing length and the dissipation than on the type of the turbulence closure. They show that a diagnostic treatment of the dissipation produced the best results and that a one-and-a-half closure model with a mixing length dependant on the turbulent kinetic energy and potential temperature profiles performed very similarly to a second order model. In view of that, a one–and–a–half order closure was chosen as well as a diagnostic treatment for the dissipation.

Due to the important feedbacks on the temperature profile, moisture was also included. Water vapour plays an important role in the radiative budget of the atmosphere, accounting for most of the longwave absorption and a modest amount of shortwave absorption as

well. In addition it is also strongly associated with the distribution of stratiform clouds, which themselves have a strong influence on the radiative flux.

4.1 Basic Equations

The dynamics of an incompressible, viscous, rotating atmosphere is described by applying the Bousinesq approximation and Reynolds averaging to the Navier–Stokes equations. The mean values of the wind speed are given by the equation:

$$\frac{d\mathbf{V}}{dt} = -\frac{1}{\rho_0}\nabla p + \frac{\rho'}{\rho_0}g\vec{i} - f\vec{i} \times \mathbf{V} - \frac{\partial}{\partial x}\overline{\mathbf{V}'u'} - \frac{\partial}{\partial y}\overline{\mathbf{V}'v'} - \frac{\partial}{\partial z}\overline{\mathbf{V}'w'}, \tag{4.1}$$

where $\mathbf{V} = (u, v, w)$ is the ensemble average of the wind speed in the (x, y, z) directions, respectively, ρ_0 is a standard value of the density representing a basic horizontally averaged state. It is also assumed that the influence of the viscous stress is negligible when compared with the other forces.

For both moist and dry adiabatic processes with no precipitation, the conserved variables are the total water specific humidity, $q_t = q + q_l$ (with q as the specific humidity for water vapour and q_l as the specific humidity of liquid water), and liquid water potential temperature, θ_l:

$$\theta_l = \theta\left(1 - \frac{Lq_l}{c_pT}\right). \tag{4.2}$$

L designates the latent heat of vaporisation (function of temperature), c_p is the specific heat of moist air ($c_p = c_{pd} + r_t c_{pv}$, c_{pd} represents the specific heat of dry air, c_{pv} indicates the specific heat of water vapour and r_t denotes the total water mixing ratio).

Thus, the water content and the thermodynamic state are represented by:

$$\frac{dq_t}{dt} = -\frac{\partial}{\partial x}\overline{q_t'u'} - \frac{\partial}{\partial y}\overline{q_t'v'} - \frac{\partial}{\partial z}\overline{q_t'w'} \tag{4.3}$$

and

$$\frac{d\theta_l}{dt} = -\frac{\partial}{\partial x}\overline{\theta_l'u'} - \frac{\partial}{\partial y}\overline{\theta_l'v'} - \frac{\partial}{\partial z}\overline{\theta_l'w'} + Q_{rad} \tag{4.4}$$

where Q_{rad} denotes the divergence of the radiation flux. The divergence of the infrared flux is mostly important in stable nocturnal boundary layer and near the surface where it can be of the same order as the divergence of the turbulent heat flux (Deardorff (1971) and Izumi and Barad (1963)).

4.1.1 Governing Equations

Assuming horizontal homogeneity of the mean variables, except for pressure and potential temperature, the effects of the horizontal turbulent fluxes are neglected. This also implies that, for a non-sloping boundary layer, the mean vertical momentum equation is reduced to the hydrostatic equation.

The mean geostrophic wind is used to represent the pressure gradient force and baroclinicity is allowed by permitting the geostrophic wind to change with height. Thus the horizontal temperature gradients are replaced by the thermal wind:

$$\frac{\partial \theta_l}{\partial x} = \frac{f}{g}\theta_0 \frac{\partial v_g}{\partial z}, \tag{4.5}$$

$$\frac{\partial \theta_l}{\partial y} = -\frac{f}{g}\theta_0 \frac{\partial u_g}{\partial z}. \tag{4.6}$$

The model equations become:

$$\frac{\partial u}{\partial t} = f(v - v_g) - \frac{\partial}{\partial z}\overline{u'w'}, \tag{4.7}$$

$$\frac{\partial v}{\partial t} = -f(u - u_g) - \frac{\partial}{\partial z}\overline{v'w'}, \tag{4.8}$$

$$\frac{\partial q_t}{\partial t} = -\frac{\partial}{\partial z}\left[\overline{q'w'} + \overline{w'q'_l}\right], \tag{4.9}$$

$$\frac{\partial \theta_l}{\partial t} = \frac{f}{g}\theta_0\left(v\frac{\partial u_g}{\partial z} - u\frac{\partial v_g}{\partial z}\right) - \frac{\partial}{\partial z}\left[\overline{\theta'w'} - \frac{\overline{\theta}}{\overline{T}}\frac{L}{c_p}\overline{w'q'_l}\right] - \frac{\theta_{l_0}}{T_0 c_p}\frac{1}{\rho_0}\frac{\partial F}{\partial z}, \tag{4.10}$$

with $F = F\uparrow - F\downarrow$ is the total radiative flux ($F\uparrow$ is the upward flux and $F\downarrow$ is the downward flux) and the subscript 0 denotes reference profiles which are horizontal averages, i.e. they are only height dependant.

4.2 Water Parameterisation

The problem of representing clouds in a model is coupled with the irregular distribution of water within the cloud, since the air inside clouds is not uniformly saturated. It may contain unsaturated air due to entrainment and the merging of adjacent clouds. The cloud boundaries are also highly irregular, so each grid volume cannot be assumed to be either saturated or unsaturated. To alleviate this problem it is assumed that the conserved variables for non precipitating processes, θ_l and q_t, have joint normal probability distributions within any grid volume (Sommeria *et al.*(1977), Bechtold *et al.* (1995), Chaboureau *et al.* (2002)).

Initially, a Gaussian probability function was used to parameterise the cloud fraction and liquid water content (Sommeria *et al.*(1977)). Later, Bougeault (1981) noted that the skewness factor of the distribution is important in the development of cloud convection due to the updrafts of moist and cold air. The skewness of the distribution becomes important below a cloud cover of about 20% (Cuijpers *et al.* (1995)). Thus, the choice of the distribution function is of paramount importance for the appropriate representation of clouds. Cuijpers *et al.* (1995) parameterised the distribution function for boundary layer clouds, from small cumulus to stratocumulus. Recently Chaboureau *et al.* (2002) extended this parameterisation to all cloud types. It is this parameterisation that is described here.

The properties of moist adiabatically ascending air are determined by assuming that there is no precipitation, so that the total water mixing ratio (or specific humidity) is conserved. A liquid temperature is defined from the potential liquid temperature and the ice mixing ratio:

$$T_l = \theta_l \left(\frac{p}{p_0} \right)^{R_d/c_{pd}} - \frac{L_s r_i}{c_p} \tag{4.11}$$

where L_s designates the latent heat of sublimation and r_i denotes the ice mixing ratio.

Following Mellor (1977), the liquid temperature is combined with moisture into one

single variable $s = ar_t - bT_l$. The parameters a and b are defined as:

$$a = \left(1 + \frac{Lr_{sl}}{c_p}\right)^{-1}; \qquad b = ar_{sl}; \qquad r_{sl} = \frac{Lr_{sat}(T_l)}{R_v T_l^2}. \tag{4.12}$$

r_{sl} as the saturation mixing ratio.

When the temperature falls inside the glaciation interval $253 < T < 273.16$ K, the parameterisation assumes that a fraction of the cloud is composed of ice particles. The fraction of solid condensate is estimated by:

$$\chi = \frac{273.16 - T}{273.16 - 253}. \tag{4.13}$$

The latent heat and the saturation mixing ratio are then determined as a weighted average of their respective fraction for liquid water and ice.

The saturation deficit, $Q = r_t - r_{sat}$, is then normalised by the variance of s and are both expressed as:

$$Q = a[r_t - r_{sat}(T_l)]/\sigma_s \tag{4.14}$$

and

$$\sigma_s = 0.2l\left[a^2\left(\frac{\partial r_t}{\partial z}\right)^2 - 2abc_p^{-1}\frac{\partial h_l}{\partial z}\frac{\partial r_t}{\partial z} + b^2c_p^{-2}\left(\frac{\partial h_l}{\partial z}\right)^2\right]^{1/2}. \tag{4.15}$$

l is a length scale which is assumed to be equal to 600m, h_l denotes the liquid water static energy and $c_p^{-1}\partial h_l/\partial z = \partial T_l/\partial z + g/c_p(1 + r_t)$.

Finally, the cloud fraction is defined at every model level where the liquid mixing ratio ($r_L = r_l + r_i$) is greater than zero, through:

$$N = max\{0, min[1, 0.5 + 0.36\tan^{-1}(1.55Q)]\} \tag{4.16}$$

and the liquid mixing ratio is obtained from the normalised expressions:

$$\begin{cases} \frac{r_L}{\sigma_s} = e^{(1.2Q-1)}, & \text{if} \quad Q < 0, \\ \frac{r_L}{\sigma_s} = e^{-1} + 0.66Q + 0.086Q^2, & \text{if} \quad 0 \le Q \le 2, \\ \frac{r_L}{\sigma_s} = Q, & \text{if} \quad Q > 2. \end{cases} \tag{4.17}$$

Since there is no precipitation the water vapour mixing ratio is obtained from $r = r_t - r_L$ and the individual fractions of water and ice mixing ratios are estimated with the use of χ.

4.3 Radiation Scheme

The radiation scheme is the radiation model developed by Fu and Liou (1992, 1993) which also includes ice radiation parameterisation (Fu, 1996; Fu *et al.*, 1998). This is a broad–band model with six bands in the solar region of the spectrum and twelve in the thermal infrared region where a four–stream solution is obtained for the radiative transfer equations. A detailed description is given in appendix at the end of the chapter.

4.4 Turbulence Closure

In order to close equations (4.7) to (4.9), the turbulent fluxes are expressed as:

$$-\overline{u'w'} = K_m \frac{\partial u}{\partial z}, \tag{4.18}$$

$$-\overline{v'w'} = K_m \frac{\partial v}{\partial z}, \tag{4.19}$$

$$-\left[\overline{\theta'w'} - \frac{\overline{\theta}}{\overline{T}} \frac{L}{c_p} \overline{w'q'_l}\right] = K_h \left(\frac{\partial \theta_l}{\partial z} - \gamma_g\right), \tag{4.20}$$

$$-(\overline{q'w'} + \overline{w'q'_l}) = K_q \frac{\partial q_t}{\partial z}, \tag{4.21}$$

in which K_m is the momentum eddy diffusivity, K_h is the heat eddy diffusivity and K_q is the humidity eddy diffusivity. The moisture eddy viscosity is taken to be equal to that for heat.

The γ_g term in (4.20) is introduced to impose an upward counter gradient heat flux under unstable conditions in those parts of the column where there is a positive potential temperature vertical gradient. Mailhot and Benoit (1982) determined that this term is of the order of $10^{-3}\mathrm{Km}^{-1}$. According to Mahrt (1985), γ_g reflects the effects of larger eddies in the temperature turbulent fluxes, while the term proportional to the temperature gradient represents the contributions of the smaller eddies. Its parameterisation follows Deardorff (1977) and Therry and Lacarrère (1983):

$$\gamma_g = \begin{cases} 5\dfrac{Q_0}{w_* H} & \text{unstable} \\ 0 & \text{stable} \end{cases} \tag{4.22}$$

where Q_0 is the surface kinematic heat flux (to be defined later), H is the height of the boundary layer and w_* is Deardorff's (1970) convective velocity scale which will also be defined later.

The eddy diffusivity coefficients are taken as (Mailhot and Benoit (1982)):

$$K_m = c_k^{\frac{1}{4}} l e^{\frac{1}{2}}, \tag{4.23}$$

$$K_h = \alpha_h K_m, \tag{4.24}$$

$$K_q = \alpha_q K_m, \tag{4.25}$$

where e is the turbulent kinetic energy l represents a mixing length which will be defined later and c_k, α_h and α_q are parameters which will be adjusted after a sensitivity analysis. The set of equations is still not closed due to the dependence of the eddy viscosity coefficients on the turbulent kinetic energy. Another equation is therefore needed.

The temporal evolution of the turbulent kinetic energy given by:

$$\frac{\partial e}{\partial t} = -\overline{u'w'}\frac{\partial u}{\partial z} - \overline{v'w'}\frac{\partial v}{\partial z} - g\frac{\overline{\rho'w'}}{\rho_0} - \frac{\partial}{\partial z}\left(\overline{e'w'} + \frac{\overline{p'w'}}{\rho_0}\right) - \epsilon. \tag{4.26}$$

All the terms on the right-hand side can be parameterised as functions of the previous variables and so the set of equations is finally closed.
The first two terms on right represent the shear production terms and their parameterisation makes use of (4.18) and (4.19).

Assuming that in buoyancy driven motions, the density fluctuations due to pressure changes are small when compared to pressure fluctuations, the buoyancy flux term (term three) may be rewritten as (Holton, 1992):

$$-\frac{\overline{\rho'w'}}{\rho_0} = \frac{\overline{\theta'_{vl}w'}}{\theta_0}, \tag{4.27}$$

where $\theta_{vl} = \theta(1 + 0.61q_t - 1.61q_l)$ is the virtual potential temperature. Following Bechtold *et al.* (1992) and Deardorff (1976) the buoyancy flux must be expressed in terms of the conserved thermodynamic variables.

For unsaturated air, where $q_l = 0$, and ignoring the third order term, it may be expanded as:

$$\overline{\theta'_{vl}w'}|_{clear} = (1 + 0.61q_t)\overline{\theta'_l w'} + 0.61\theta_0\overline{q'_t w'}. \tag{4.28}$$

For saturated air, the derivation follows Cuijpers *et al.* (1993), where:

$$\overline{\theta'_{vl}w'}|_{sat} = E\overline{\theta'_l w'} + \left[\frac{L}{c_p T}E - 1\right]\theta_0 \overline{q'_t w'} \tag{4.29}$$

with

$$E = \frac{1 - q_t + 1.61 q_s \left(1 + 0.622 \frac{L}{R_d T}\right)}{\left(1 + 0.622 \frac{L^2}{R_d c_p T^2} q_s\right)}. \tag{4.30}$$

For partly saturated layers the amount of cloud N is used in a linear interpolation between the saturated and the clear air fractions:

$$\overline{\theta'_{vl}w'} = N\overline{\theta'_{vl}w'}|_{sat} + (1 - N)\overline{\theta'_{vl}w'}|_{clear}. \tag{4.31}$$

The turbulent fluxes in the equations above are parameterised using (4.20) and (4.21). In (4.30), q_s represents the saturation specific humidity.

The transport term (the fourth term) is expressed as:

$$\frac{\partial}{\partial z}\left(\overline{e'w'} + \frac{\overline{p'w'}}{\rho_0}\right) = -K_e \frac{\partial e}{\partial z} \tag{4.32}$$

where $K_e = \alpha_e K_m$. α_e is a parameter that will be set after a sensitivity analysis. The dissipation rate is parameterised following Sun and Ogura (1980):

$$\epsilon = \frac{(2e)^{3/2}}{\Lambda}, \tag{4.33}$$

where $\Lambda = 15.0l$ and l is a length scale:

$$l = \begin{cases} l_u, & \text{if} \quad \dfrac{\partial \theta}{\partial z} \leq 0 \\ \dfrac{1}{\dfrac{1.0}{l_u} + \dfrac{1.0}{l_s}}, & \text{if} \quad \dfrac{\partial \theta}{\partial z} > 0 \end{cases} \tag{4.34}$$

where l_u is the Blackadar (1962) length scale:

$$l_u = \frac{kz}{\left(1 + \dfrac{kz}{l_0}\right)}, \tag{4.35}$$

with,

$$l_0 = 0.1 S_l \frac{\int_0^\infty ez\, dz}{\int_0^\infty e\, dz} \tag{4.36}$$

and l_s is the buoyancy length scale:

$$l_s = \frac{2e^{1/2}}{\left[\frac{g}{\theta_0}\frac{\partial\theta}{\partial z}\right]^{1/2}}. \tag{4.37}$$

In (4.36)

$$S_l = \begin{cases} 0.75 + 1.25z/H, & \text{if} \quad z < H \\ 2.0, & \text{if} \quad z \geq H. \end{cases} \tag{4.38}$$

This allows the length scale of eddies near the ground to be proportional to height and it is also proportional to the penetration depth of a non-mixing parcel in the stable layer.

4.5 Surface Fluxes

The surface fluxes are obtained by assuming that the Monin-Obukhov similarity theory is valid in the lowest model level. The velocity, temperature and humidity scales are obtained form:

$$u_* = \frac{kM(z)}{\ln\frac{z}{z_{om}} - \Psi_m\left(\frac{z}{L_{MO}}\right) + \Psi_m\left(\frac{z_{om}}{L_{MO}}\right)}, \tag{4.39}$$

$$\theta_* = \frac{k\Delta\theta}{0.74\left[\ln\frac{z}{z_{om}} - \Psi_h\left(\frac{z}{L_{MO}}\right) + \Psi_h\left(\frac{z_{oh}}{L_{MO}}\right)\right]}, \tag{4.40}$$

and

$$q_* = \frac{k\Delta q}{0.74\left[\ln\frac{z}{z_{om}} - \Psi_h\left(\frac{z}{L_{MO}}\right) + \Psi_h\left(\frac{z_{oh}}{L_{MO}}\right)\right]}. \tag{4.41}$$

$M(z)$ denotes de wind speed at the first model level, $\Delta\theta = \theta(z) - \theta(z_{oh})$ represents difference between the virtual potential temperature at the first model level and at the surface, $\Delta q = q(z) - q(z_{oh})$, z_{om} designates the aerodynamic surface roughness length and $z_{oh} = 0.1z_{om}$ is the aerodynamic surface roughness length for heat and moisture.

For $z/L_{MO} > 0$ the Ψ_m and Ψ_h functions are given by Beljaars and Holtslag (1991).

$$-\Psi_m = a\frac{z}{L_{MO}} + b\left(\frac{z}{L_{MO}} - \frac{c}{d}\right)exp\left(-d\frac{z}{L_{MO}}\right) + \frac{bc}{d} \tag{4.42}$$

where $a = 0.7$, $b = 0.75$, $c = 5.0$ and $d = 0.35$.

$$-\Psi_h = \left(1 + \frac{2}{3}a\frac{z}{L_{MO}}\right)^{3/2} + b\left(\frac{z}{L_{MO}} - \frac{c}{d}\right) \quad exp\left(-d\frac{z}{L_{MO}}\right) + \frac{bc}{d} - 1.0 \tag{4.43}$$

where $a = 1.0$, $b = 0.667$, $c = 5.0$ and $d = 0.35$.

For $z/L_{MO} < 0$ Grachev's *et al.* (2000) matching between the near neutral and free convection forms is applied. For the near–neutral Buisinger's *et al.* (1971) formula is used:

$$\Psi_{m_{Kansas}} = 2\ln\left(\frac{1+x}{2}\right) + \ln\left(\frac{1+x^2}{2}\right) - 2\tan^{-1}x + \frac{\pi}{2} \tag{4.44}$$

and

$$\Psi_{h_{Kansas}} = 2\ln\left[\frac{1}{2}\left(1 + \sqrt{1 - 16\frac{z}{L_{MO}}}\right)\right] \tag{4.45}$$

with:

$$x = \left(1 - 16\frac{z}{L_{MO}}\right)^{1/4}, \quad \text{for} \quad -2 < \frac{z}{L_{MO}} < 0 \tag{4.46}$$

For free-convection Fairall *et al.* (1996) formula is used:

$$\Psi_{conv} = \frac{3}{2}\ln\left(\frac{y^2 + y + 1}{3}\right) - \sqrt{3}\ln\left(\frac{2y+1}{\sqrt{3}}\right) + \frac{\pi}{\sqrt{3}} \tag{4.47}$$

with:

$$y = \left(1 - \alpha\frac{z}{L_{MO}}\right)^{1/3}, \quad for \quad \frac{z}{L_{MO}} < -0.1 \tag{4.48}$$

where $\alpha = 10.15$ for the momentum equation and $\alpha = 35.15$ for the temperature and moisture equations. The final form for Ψ is:

$$\Psi_\alpha = \frac{\Psi_{\alpha_{Kansas}} + \left(\frac{z}{L_{MO}}\right)^2 \Psi_{\alpha_{conv}}}{1 + \left(\frac{z}{L_{MO}}\right)^2}, \quad \alpha = \text{m,h} \tag{4.49}$$

The kinematic heat and humidity fluxes are defined as:

$$Q_0 = -u_*\left(\theta_* + 0.61\theta_{v_0}q_*\right) \tag{4.50}$$

$$E_0 = -u_* q_* \tag{4.51}$$

and the convective velocity scale is:

$$w_* = \left(\frac{gHQ_0}{\theta_0}\right)^{1/3} \tag{4.52}$$

w_* is a measure of the variance of the horizontal velocity components.

Finally the Monin-Obukhov length is defined as:

$$L_{MO} = \frac{\theta_{v0} {u_*}^3}{kgQ_0} \tag{4.53}$$

It is obtained by solving (4.39), (4.40)and (4.41) iteratively until u_*, θ_* and q_* converge, i.e. when the difference between two iterations is less than 0.1 of either variable. In the rare cases when this does not happen the iteration is stopped when u_* is less than 10^{-5} ms^{-1} and an error message is produced. This signals the failure of the surface layer scheme and the results are not to be trusted.

4.6 Numerical Scheme

4.6.1 Reference Profiles

Two types of reference profiles were considered. In the first, the atmosphere is assumed to be in hydrostatic balance and the temperature decreases with height according to the dry adiabatic lapse rate. The reference temperature profile is determined from the surface temperature at the initial time step from:

$$T_0(z) = T(0) - 0.0065\Delta z \tag{4.54}$$

The reference pressure profile is obtained from the hydrostatic equation, i.e.:

$$p_0(z) = p(0)\left[\frac{T_0(z)}{T(0)}\right]^{\left(\frac{g}{0.0065R_d}\right)} \tag{4.55}$$

Finally, the potential temperature profile is estimated from the two previous profiles and the liquid water potential temperature and virtual potential temperature are assumed to be equal the potential temperature.

In the second type, the reference profile is assumed to be the initial profile. This can either be idealised or a radiosonde profile.

4.6.2 Boundary Conditions

In order to solve the equations (4.7) to (4.9) and (4.26) boundary conditions have to be imposed. At the lowest boundary, Dirichlet boundary conditions are imposed. The wind speed at z_0 is considered to be zero and the wind speed at first model level is determined through:

$$(u_1, v_1) = (u_2, v_2) \left[\frac{\ln \frac{z_1}{z_{om}} - \Psi_m \left(\frac{z_1}{L_{MO}} \right) + \Psi_m \left(\frac{z_{om}}{L_{MO}} \right)}{\ln \frac{z_2}{z_{om}} - \Psi_m \left(\frac{z_2}{L_{MO}} \right) + \Psi_m \left(\frac{z_{om}}{L_{MO}} \right)} \right] \tag{4.56}$$

The potential temperature and the specific humidity are imposed at the surface and their values at the first model level are obtained from:

$$\theta_{l1} = \theta_{l2} \left[\frac{\ln \frac{z_1}{z_{om}}}{\ln \frac{z_2}{z_{om}}} \right] + \theta_{ls} \left[1 - \frac{\ln \frac{z_1}{z_{om}}}{\ln \frac{z_2}{z_{om}}} \right] \tag{4.57}$$

and

$$q_{t1} = q_{t2} \left[\frac{\ln \frac{z_1}{z_{om}}}{\ln \frac{z_2}{z_{om}}} \right] + q_{ts} \left[1 - \frac{\ln \frac{z_1}{z_{om}}}{\ln \frac{z_2}{z_{om}}} \right] \tag{4.58}$$

The turbulent kinetic energy surface boundary condition is a function of u_*, w_* and z_{om}. Following Mailhot *et al.* (1982) it is expressed as:

$$E_0 = \begin{cases} 3.75 u_*^2 & \text{if} \quad L_{MO} > 0 \\ 3.75 u_*^2 + 0.2 w_*^2 + \left(\frac{-z_0}{L_{MO}} \right)^{\frac{2}{3}} u_*^2 & \text{if} \quad L_{MO} \leq 0 \end{cases} \tag{4.59}$$

At the model's top, Neumann conditions are stipulated:

$$\frac{\partial \mathbf{V}}{\partial z} = 0 \, \mathrm{ms}^{-1}, \tag{4.60}$$

$$\frac{\partial \theta_l}{\partial z} = 1. \times 10^{-2} \, \mathrm{Km}^{-1}, \tag{4.61}$$

$$\frac{\partial q}{\partial z} = 0 \, \mathrm{kgkg}^{-1}, \tag{4.62}$$

$$\frac{\partial e}{\partial z} = 0 \, \mathrm{m}^2 \mathrm{s}^{-2}. \tag{4.63}$$

4.6.3 Time Discretisation

A second order in time and space scheme was chosen to discretise the model equations. The scheme is a Crank-Nicolson type scheme, which is semi–implicit. A finite time difference operator and a weighted time average are defined:

$$\Phi_t = \frac{\Phi(t) - \Phi(t - \Delta t)}{\Delta t} \tag{4.64}$$

$$\Phi_\alpha = \mu\Phi(t) + (1 - \mu)\Phi(t - \Delta t) \tag{4.65}$$

For the general variable Φ the equations of the model are written in the following format:

$$\Phi_t = \frac{\partial}{\partial z}\left(K\frac{\partial \Phi_\alpha}{\partial z}\right) + \chi\Phi_\alpha + \upsilon \tag{4.66}$$

Φ is either $u+iv$, θ_l, q_t or e. Table 4.1 identifies each of the parameters in the momentum, liquid potential temperature and specific humidity prognostic equations. Note that a complex equation is created from (4.7) and (4.8) by creating a complex wind speed $(u + iv)$ and complex geostrophic wind speed $(u_g + iv_g)$ to obtain:

$$\frac{\partial(u + iv)}{\partial t} = \frac{\partial}{\partial z}\left(K_m\frac{\partial(u + iv)}{\partial z}\right) - if((u + iv) - (u_g + iv_g)) \tag{4.67}$$

u_g, v_g, θ, T, γ_g and K are evaluated at time $t-\Delta t$. A stability analysis with constant eddy coefficients and constant υ reveals that as long as $\mu \geq 0.5$ this scheme is unconditionally stable. If $\mu = 0.5$, (4.66) reduces to the Crank-Nicolson scheme, if $\mu = 1$ (4.66) is the implicit scheme and when $\mu = 0$ (4.66) represents the forward Euler scheme. Following Mailhot *et al.* (1982) $\mu = 0.75$ was chosen.

4.6.4 Vertical Grid and Finite–Difference Approximation

The parameterisation of the length scale assumes that the eddies length scale is proportional to height near the ground and tends to a constant above it. According to Yamada *et al.* (1975), the computational accuracy is improved if the vertical grid reflects these features. Thus, their vertical coordinate transformation is used. A new coordinate is defined as:

$$x = c_1 z + c_2 \ln\left(\frac{z}{\Gamma}\right) \tag{4.68}$$

Φ	K	χ	υ
$u+iv$	K_m	$-if$	$if(u_g+iv_g)$
θ_l	K_h	0	$\frac{f}{g}\theta_0\left(v\frac{\partial u_g}{\partial z}-u\frac{\partial v_g}{\partial z}\right)-\frac{\theta_{l_0}}{T_0 c_p}\frac{1}{\rho_0}\frac{\partial F}{\partial z}-\frac{\partial}{\partial z}(K_h\gamma_g)$
q_t	K_q	0	0

Table 4.1: Identification of the variable Φ and the parameters K, χ and υ in (4.66) for the mean wind, liquid potential temperature and specific humidity prognostic equations.

where $c_1 = 0.0376$, $c_2 = 0.417$, $\Gamma = 0.01$ and z is in meters. In this new coordinate system, Δx is proportional to $\Delta z/z$ for small z and equivalent to Δz for large z.

In the new coordinate system, (4.66) is rewritten as:

$$\Phi_t = m\frac{\partial}{\partial z}\left(Km\frac{\partial \Phi_\alpha}{\partial z}\right)+\chi\Phi_\alpha+\upsilon \tag{4.69}$$

where all the vertical derivatives obey the following relation:

$$\frac{\partial \Phi}{\partial z} = m\frac{\partial \Phi}{\partial x}, \tag{4.70}$$

and m is the stretch factor,

$$m \equiv \frac{dx}{dz} = c_1 + \frac{c_2}{z}. \tag{4.71}$$

In this formulation $\Delta x = 1$ and the finite–difference expression for (4.66) is:

$$\begin{aligned}\Phi_j^t - \Phi_j^{t-\Delta t} = \frac{m_j \Delta t}{2}\Big[&\left((mK)_{j+1}+(mK)_j\right)^{t-\Delta t}(\Phi_\alpha)_{j+1}^t - \\ &-\left((mK)_{j+1}+2(mK)_j+(mK)_{j-1}\right)^{t-\Delta t}(\Phi_\alpha)_j^t + \\ &+\left((mK)_j+(mK)_{j-1}\right)^{t-\Delta t}(\Phi_\alpha)_{j-1}^t\Big] + \Delta t\left(\chi(\Phi_\alpha)_j^{t-\Delta t}+\upsilon\right)\end{aligned} \tag{4.72}$$

where the index j stands for different model levels.

4.6.5 Treatment of the Kinetic Energy Equation

The prognostic equation for the kinetic energy is highly nonlinear and preliminary tests using the simple discretisation gave solutions that were numerically unstable. To alleviate the problem (4.26) is expressed as:

$$\frac{\partial e}{\partial t} = Be^{\frac{1}{2}} - Ce^{\frac{3}{2}} + \frac{\partial}{\partial z}\left(K_e\frac{\partial e}{\partial z}\right) \tag{4.73}$$

where B represents coefficient for the shear production terms and the buoyancy term and C is the coefficient of the dissipation term. While C is always positive, B can be either positive (when buoyancy dominates – usually during daytime) or negative (when shear dominates – typically during night time).

Following Mailhot *et al.* (1982), (4.73) is solved by the method of fractional steps. First equation (4.73) is solved analytically by omitting the diffusion term. An interim value for the kinetic energy is found analytically.

$$\int_{t-\Delta t}^{t} dt = \int_{e(t-\Delta t)}^{e_*(t)} \frac{dE}{Be^{\frac{1}{2}} - Ce^{\frac{3}{2}}} \tag{4.74}$$

The analytical expression for e_* is given by:

$$e_* = \left|\frac{B}{C}\right| \frac{\left[\sqrt{\frac{e}{|B/C|}} - \tan\frac{\Delta t\sqrt{|B|C}}{2}\right]^2}{\left[1 + \sqrt{\frac{e}{|B/C|}}\tan\frac{\Delta t\sqrt{|B|C}}{2}\right]^2} \quad \text{if} \quad B \leq 0$$

or (4.75)

$$e_* = \frac{B}{C}\frac{\left[\frac{\sqrt{B/C}+\sqrt{e}}{\sqrt{B/C}-\sqrt{e}}e^{\Delta t\sqrt{BC}} - 1\right]^2}{\left[1 + \frac{\sqrt{B/C}+\sqrt{e}}{\sqrt{B/C}-\sqrt{e}}e^{\Delta t\sqrt{BC}}\right]^2} \qquad \text{if} \quad B > 0$$

The kinetic energy equation (4.26) is now solved by reducing it to a diffusion equation and using (4.75) for the value of $e(t - \Delta t)$

$$\frac{e(t) - e_*}{\Delta t} = m\frac{\partial}{\partial x}\left(mK_e\frac{\partial}{\partial x}(\mu e(t) + (1-\mu)e_*)\right) \tag{4.76}$$

4.6.6 Smoothing

Due to numerical instabilities a vertical filter $(1:1:1)$ had to be applied to the mixing length for heights above 200m.

$$\Psi(x) = (\Phi(x-1) + \Phi(x) + \Phi(x+1))/3 \tag{4.77}$$

4.7 Sensitivity Analysis

An analysis of the model's behaviour and the calibration of the unknown parameters is presented through a comparison of the results with observations from the Wangara Experiment (Clark *et al.*, 1971).

This experiment took place in Hay, Australia (34° 30'S, 144° 56'E) between July and August 1967 and a twelve hour period for day 33 (16^{th} of August 1967)was chosen for this analysis.

4.7.1 Observed Conditions

During day time (from 7:00 to 17:45 local time) a thin very unstable layer is observed between the surface and a well mixed layer above (figure 4.1) The mixed layer's height increases up to just above 1200m until 16:00 and remains constant until sunset. Above this layer, the atmosphere remains stable.

During night time a temperature inversion, due to radiative cooling, develops whereas the

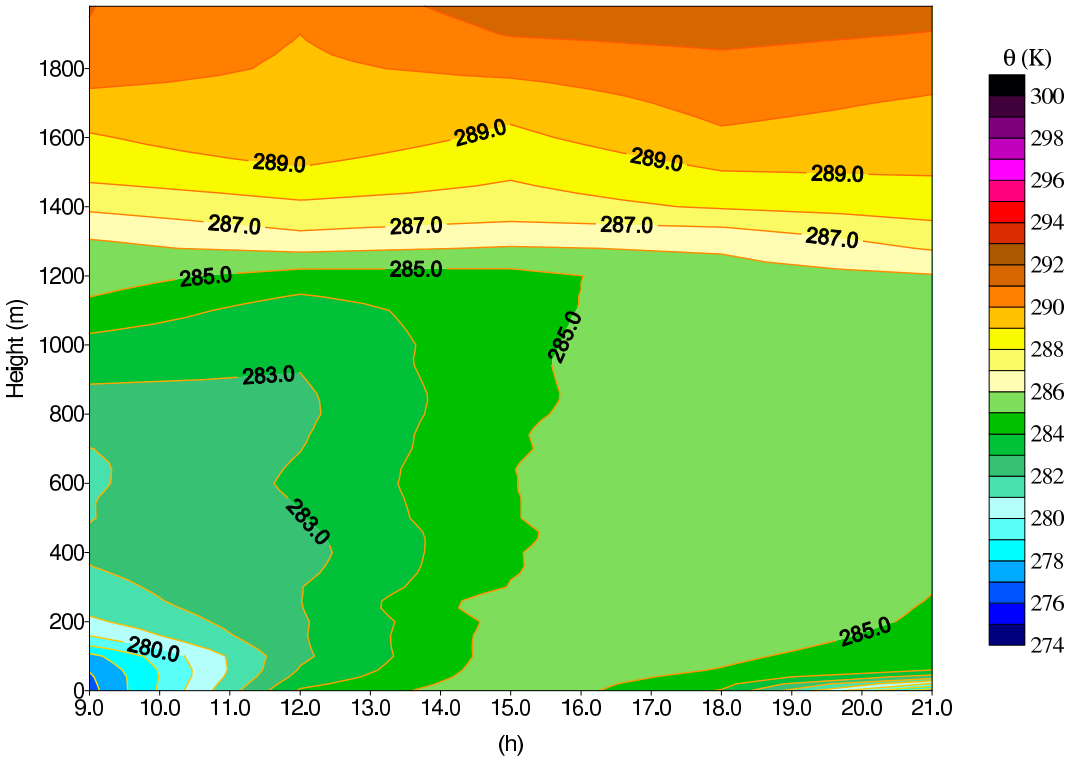

Figure 4.1: Time and space variation of the observed potential temperature observed during day 33 of the Wangara Experiment

mixed layer properties remain constant until 12:00. According to Yamada *et al.* (1975),

the increased temperatures in the layer between 500m and 1500m are due to large scale subsidence of warm air above. The wind speed increases during whole day and a low level jet develops after sunset.

4.7.2 Model Results

In the experiment thermal winds from surface up to 1km in height and from 1km to 2km were estimated twice per day (9:00 and 21:00) from the Bureau of Meteorology synoptic radiosonde network (Yamada *et al.*, 1975) (table 4.2) and parabolic profiles were fitted to these values so that the geostrophic wind is given by:

$$U_g(t,z) = \frac{(\Delta U_g)_2 - (\Delta U_g)_1}{2\times 10^6} z^2 + \frac{3(\Delta U_g)_1 - (\Delta U_g)_2}{2\times 10^3} z + U_{g0}(t) \tag{4.78}$$

and

$$V_g(t,z) = \frac{(\Delta V_g)_2 - (\Delta V_g)_1}{2\times 10^6} z^2 + \frac{3(\Delta V_g)_1 - (\Delta V_g)_2}{2\times 10^3} z + V_{g0}(t) \tag{4.79}$$

The values of the geostrophic wind between observations were linearly interpolated.

In addition to the surface pressure, the temperature and specific humidity were mea-

	U_{g0}	$(\Delta U_g)_1$	$(\Delta U_g)_2$	V_{g0}	$(\Delta V_g)_1$	$(\Delta V_g)_2$
9:00	−5.34	2.98	1.49	−0.43	−0.04	0.26
21:00	−5.99	2.81	1.32	−1.93	−0.67	0.45

Table 4.2: Observed surface geostrophic wind and thermal wind differences (ms^{-1}) at 9:00 and 21:00. The subscript 1 refers to the difference between the geostrophic wind at the surface and 1 km whereas the subscript 2 refers to the height difference between 2 and 1 km.

sured at screen height (1.2m) every hour (table 4.3) and as with the geostrophic wind, the values between observations were linearly interpolated. The surface specific humidity was considered to be the same as the measured at screen height but the value of the surface temperature was extrapolated by assuming neutral flow between the two levels:

$$\theta_0 = \theta_1 \frac{\ln \frac{z_0}{1.2}}{\ln \frac{z_1}{1.2}} + \theta_s \left[1 - \frac{\ln \frac{z_0}{1.2}}{\ln \frac{z_1}{1.2}}\right] \tag{4.80}$$

Time	T (°C)	q (10^{-3} kg kg^{-1})	p (hPa)	Time	T (°C)	q (10^{-3} kg kg^{-1})	p (hPa)
9:00	5.30	4.247496	1023.00	16:00	14.60	3.698817	1019.00
10:00	9.20	4.426648	1023.10	17:00	14.60	3.442070	1018.90
11:00	11.70	4.379618	1022.40	18:00	12.30	3.729911	1018.90
12:00	12.70	3.966487	1021.50	19:00	8.10	3.709394	1019.60
13:00	13.30	3.804893	1020.70	20:00	6.80	3.482635	1019.80
14:00	13.80	3.686724	1019.70	21:00	5.60	3.608018	1019.80
15:00	14.20	3.778295	1019.30				

Table 4.3: Observed hourly surface pressure and screen height temperature and specific humidity for day 33 of the Wangara Experiment.

where the index 0 refers to the surface and the index 1 refers to the first level in the initial profile.

Figure (4.2) shows the initial profiles for the mean wind components, potential temperature and specific humidity.

Three different simulations were performed to determine the different parameters and study the models stability by using different μ. Aditionally, a simulation to test the influence of the grid spacing was conducted with even grid spacing.

The simulations began at 9:00 and ran for 12 hours until 21:00. They should be able to reproduce the diurnal convective boundary layer and the night stable boundary layer. For all simulations a $\Delta t = 20$ s was used.

4.7.3 Assessment of the Variable Coefficients

The temperature profiles replicate reasonably well the observed profiles for the whole day (figure 4.3).

During daytime the unstable surface layer as well as the mixed homogeneous layer are both well reproduced although the model has some difficulty in duplicating the heat fluxes of the boundary layer in the levels below 300 m. A comparison of figure (4.1) and figure (4.6a) shows that between 12:00 and 16:00 the real surface layer is warmer than the modelled and from 16:00 to sunset (17:45) the lowest levels of the surface layer start to cool down and the model is unable to replicate such cooling. That is reflected in the

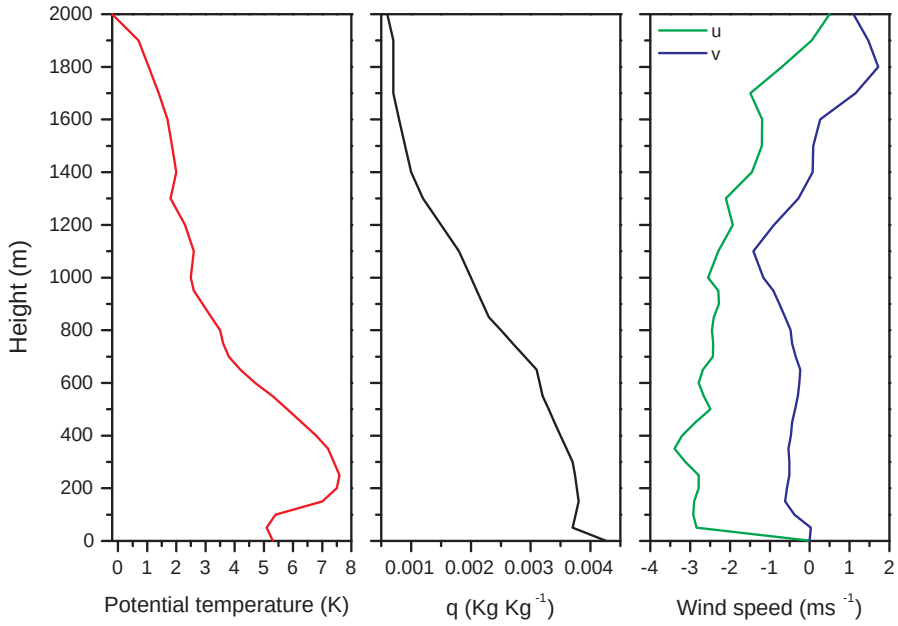

Figure 4.2: Initial profiles for the mean wind components, potential temperature and specific humidity

absolute error in potential temperature (difference between the observed and simulated potential temperatures). At 12:00 and for levels below 1000m it is less than |0.35| K (figure 4.4). By 15:00 the observed boundary layer below 300 m is about 0.4 K warmer than the simulated and by 18:00 (just after sunset) the model's inability to replicate the cooling of the surface layer leads to an absolute error of -0.68 K at 60 m.

After sunset the model develops a low–level inversion which has a sharper temperature gradient than the observed (figures 4.3 and 4.6a). This is reflected in a 2.54 K absolute error at 60m at 21:00.

The model's mixed layer grows to levels above the real mixed layer and the simulated free atmosphere is colder than the observed. This is reflected in the high absolute errors for heights above 1200 m and probably due to the lack of available data for levels above 2000m. The radiation model needs this information to determine the heat fluxes. In this run, the atmosphere above the models top level was considered to be in hydrostatic balance and the models top pressure was used as reference. At these levels, the temperature was assumed to decrease with height according to the global mean lapse rate and the dry and wet specific humidities were kept constant and equal to the humidities at the model's

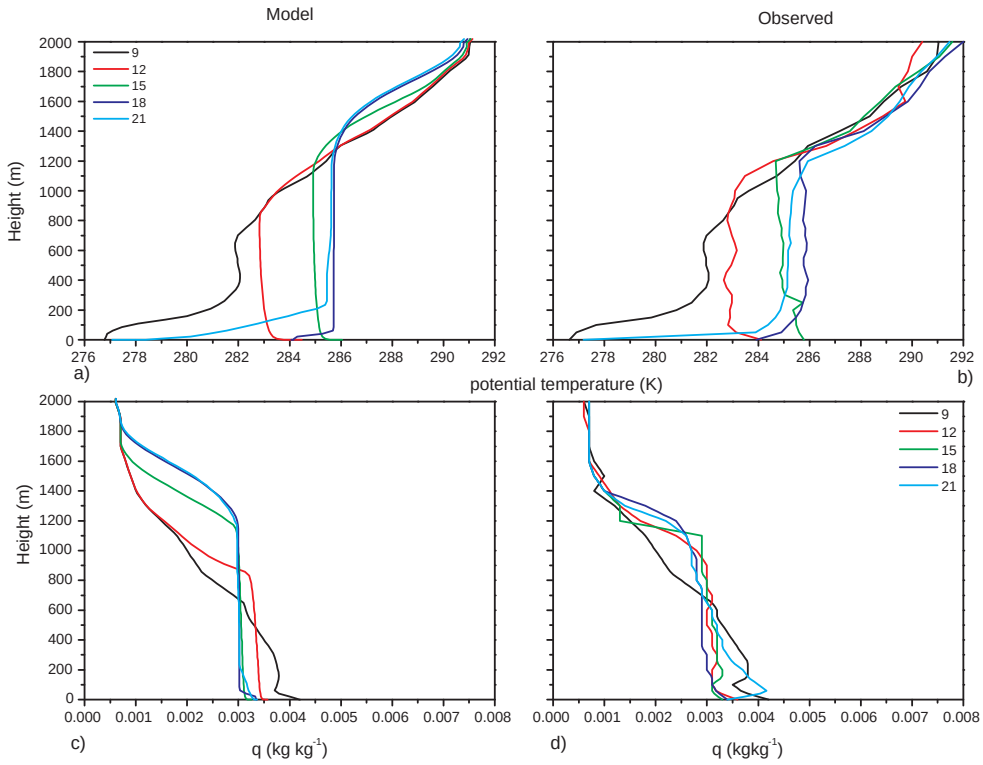

Figure 4.3: Potential temperature and specific humidity profiles for every 3 hours. (a) and (c) simulation with $\mu = 0.75$, (b) and (d) observed conditions.

top level. The use of different profiles can have a significant impact on the heat fluxes at the top of the mixed layer. This was the best compromise available.

The specific humidity profiles have similar characteristics. The most significant differences are observed in the levels above the mixed layer were the simulated atmosphere is considerably wetter than observed and in the nocturnal surface layer were the simulated is dryer than the observed.

The daytime wind profiles (figure 4.5) are nearly constant in the mixed layer due to the turbulent mixing. Above the boundary layer, the turbulent fluxes are negligible and so the departure from the observed values and the modelled inertial motion computed from (4.7) and (4.8) is due to the neglect of the advection terms in both equations (figure 4.5).

The wind speed for the first 3 hours of simulation does not depart significantly from

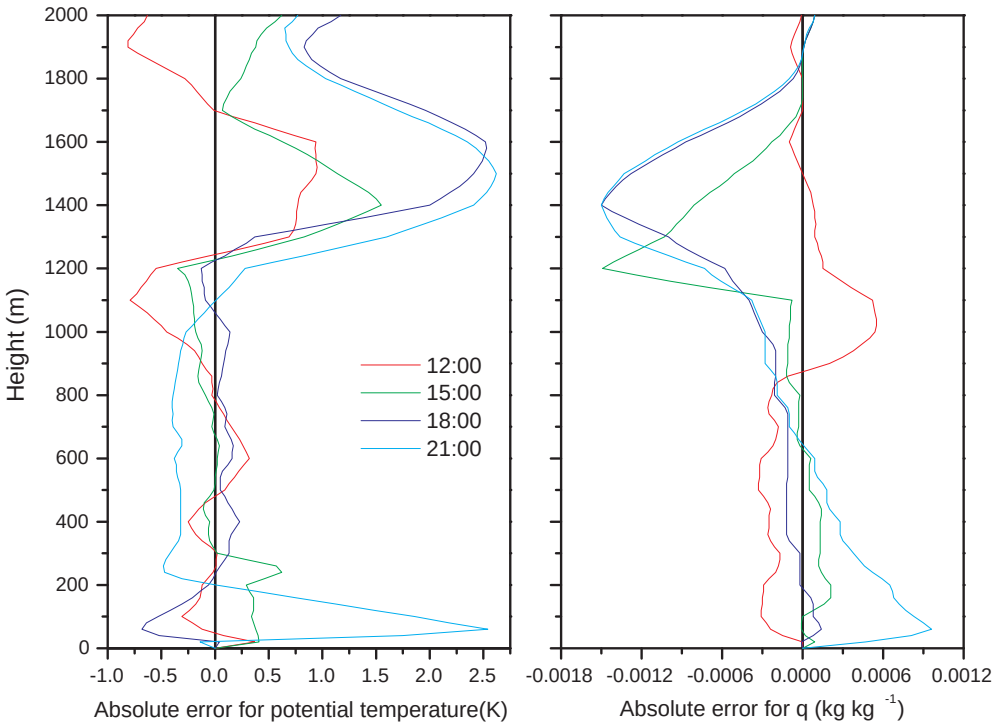

Figure 4.4: Absolute error of Potential temperature and specific humidity profiles every 3 hours

the observed values, but the subsequent intensity is too big. However that is reversed at sunset; now the speed is not strong enough (figure 4.5). This is due to the modelled easterly component since the northerly component almost attains the observed value near the surface (see figure 4 and 6 in Mailhot and Benoit (1982) for a comparison with the measured profiles). After sunset the development of a nocturnal jet as consequence of free inertial oscillations due to the negligible turbulent fluxes is also present and as before it is not strong enough, the modelled wind speed is about $1 ms^{-1}$ weaker than the observed.

The kinetic energy profile follows that of Yamada *et al.* (1975). During daytime, TKE increases as the turbulent boundary layer expands. Above it, the kinetic energy is lower than 0.01 $m^2 s^{-2}$ (figure 4.6 b). Just after sunset the kinetic energy decreases sharply and only the first model levels have values greater than 0.01 $m^2 s^{-2}$. There are some bubbles of kinetic energy above greater than 0.01 $m^2 s^{-2}$ the mixed layer which are due to the presence of a small cloud.

A comparison between the modelled mixing length and Sun and Ogura's (1980) mod-

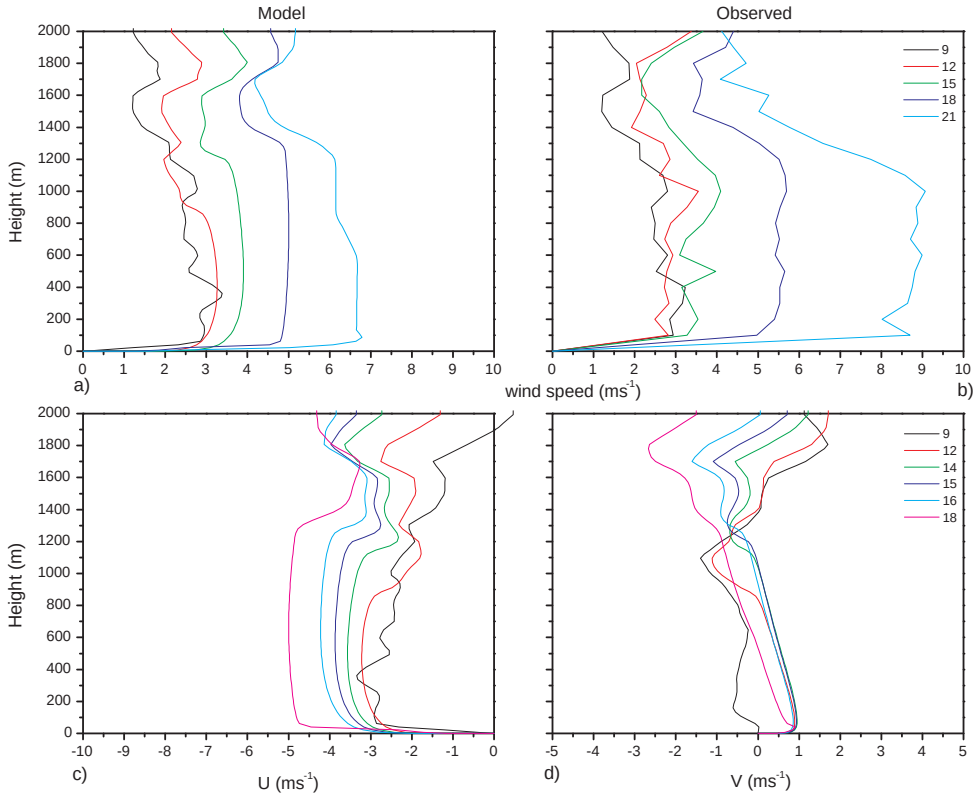

Figure 4.5: (a) Modelled and (b) observed wind speed for day 33 of the Wangara Experiment. Also shown are the modelled easterly (c) and northerly (d) wind components. The simulation was performed with $\mu = 0.75$.

elled mixing length shows reasonable agreement. Although in this case the maximum is not as strong as Sun and Ogura's.

All these results are highly dependant on the tuned coefficients and for this simulation they were chosen to be:

$$c_k = 0.3, \quad \alpha_h = 10, \quad \alpha_q = 10, \quad \alpha_e = 1.$$

An increase in c_k leads to a decrease in the wind speed in the mixed boundary layer and has the opposite effect on the temperature and kinetic energy. An increase or decrease in α_h leads to a similar effect on the temperature without affecting the intensity of the wind speed as long as the mixed layer and the nocturnal stable layer are fully developed.

The model was also run with the two types of reference profiles, no visible change was noticeable between the results.

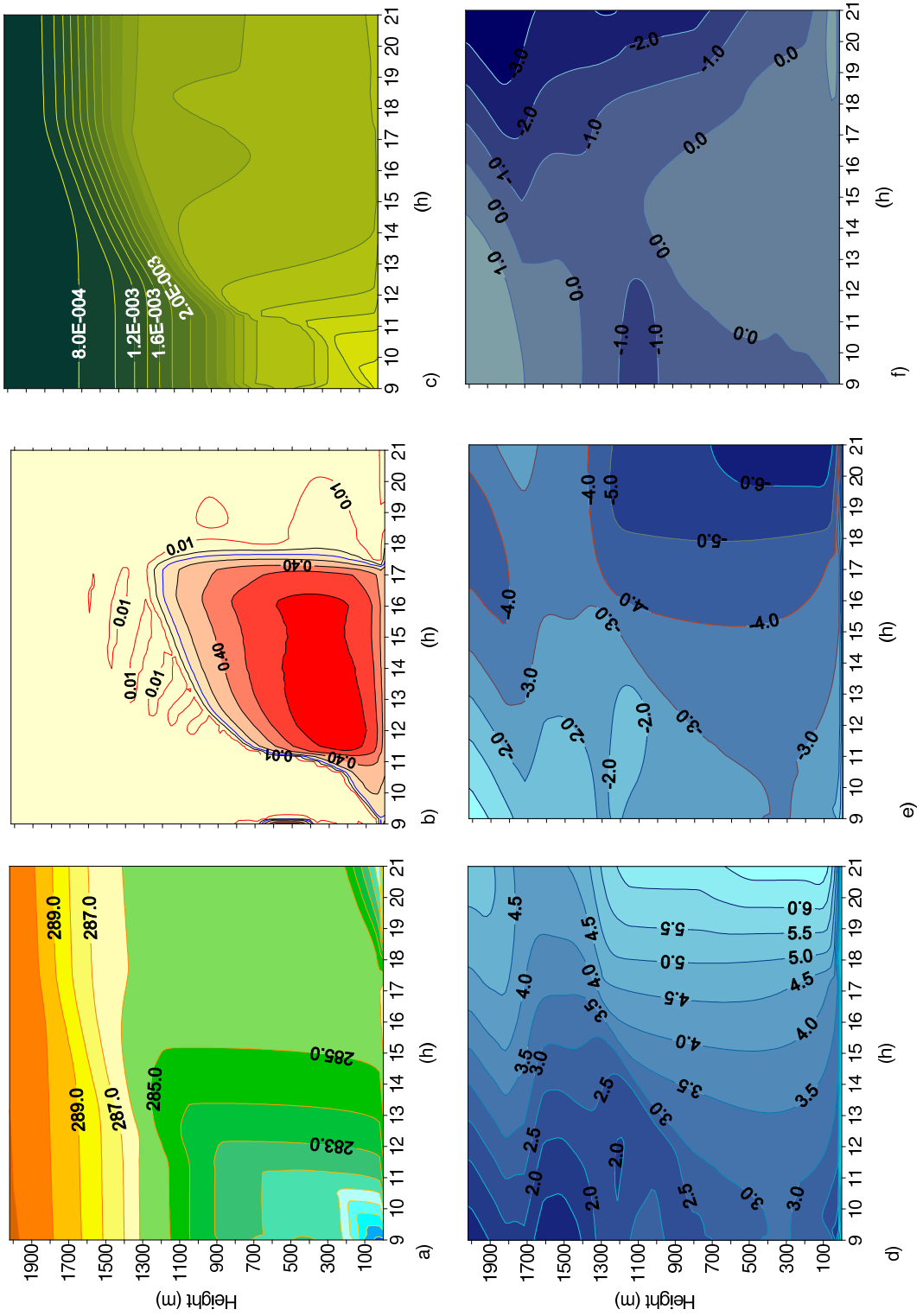

Figure 4.6: Time and space variation of: (a) potential temperature (K); (b) kinetic energy (m^2s^{-2}); (c) specific humidity ($kgkg^{-1}$); (d) wind speed (ms^{-1}); (e) easterly wind component (ms^{-1}) and (f)northerly wind component (ms^{-1}) for a simulation with $\mu = 0.75$.

Counter Gradient Heat Flux (γ_g)

In this section the counter gradient heat flux is turned on. This counter gradient is responsible for a reduction of the TKE in the mixed layer and inside the cloud (figure 4.7). As a consequence, the very small cloud is reduced even further (figure 4.8).

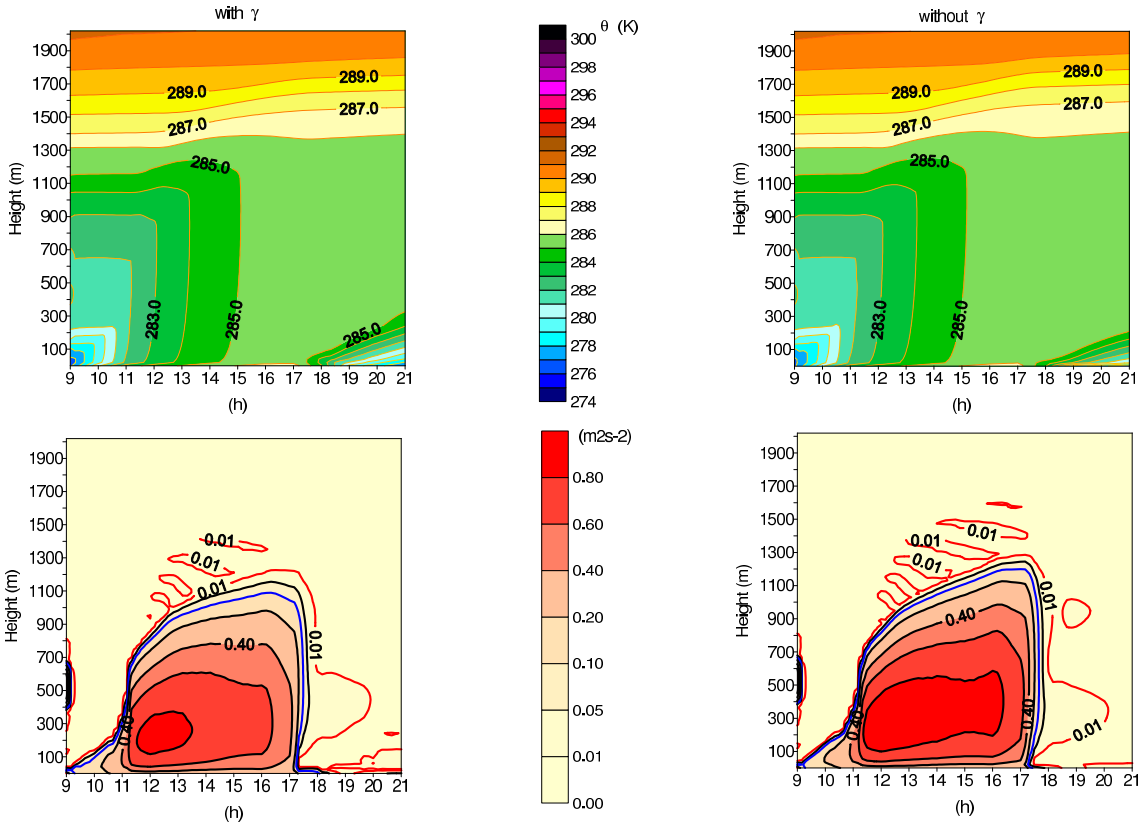

Figure 4.7: Time and space variation of potential temperature (K) and kinetic energy (m^2s^{-2}) for a simulation with $\mu = 0.75$ and γ_g turned on.

Due to the negative heat flux after sunset, this term is turned off but this is when its influence has more significant effects. The drying of the mixed layer leads to the development of a colder nocturnal boundary layer which is 3 K colder than the observed.

Its effects on the wind profiles are negligible except for the lowest levels after sunset. The nocturnal jet is stronger in this run.

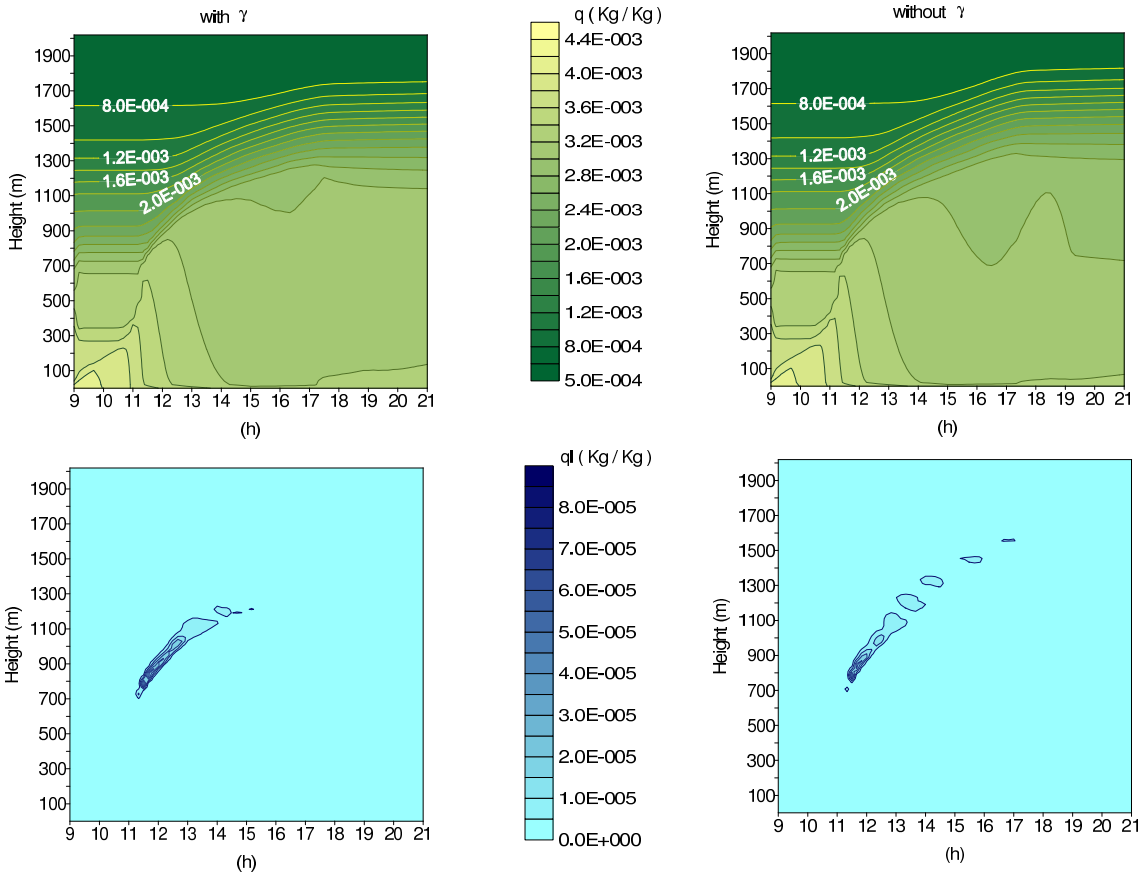

Figure 4.8: Time and space variation of specific humidity ($kgkg^{-1}$) and liquid water specific humidity ($kgkg^{-1}$) for a simulation with $\mu = 0.75$ and γ_g turned on.

4.7.4 $\mu = 1$

For this simulation, μ was changed to one, i.e. the numerical scheme is the implicit scheme, and the coefficients were kept constant. The differences between the results from this experiment and the results from the previous one are not very significant. The potential temperature profiles show a slight increase in intensity but the wind speed near the surface decreases. In figure 4.9 a small increase in the liquid water content in the cloud above the boundary layer can be seen as well as a decrease in specific humidity after sunset in the layers between 700m and 1150m.

4.7.5 $\mu = 0.5$

In this model run μ was changed to 0.5. The model is unstable and will not run with the coefficients used in the previous runs, so α_h and α_q were changed from 10 to 9. The differences between the results from this experiment and the results from $\mu = 0.75$ are not

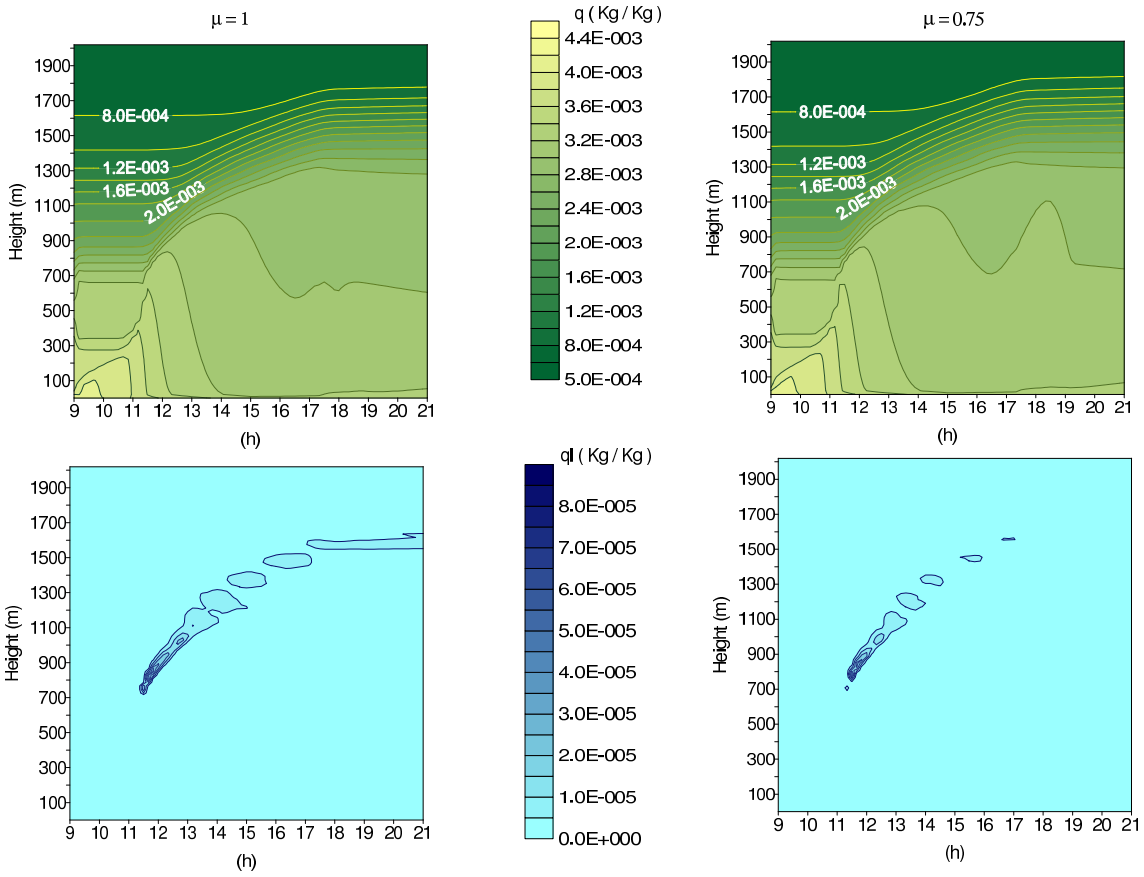

Figure 4.9: Time and space variation of specific humidity ($kgkg^{-1}$) and liquid water specific humidity ($kgkg^{-1}$) for simulations with $\mu = 1$ and $\mu = 0.75$.

very significant, except for the specific humidity. The specific humidity in the nocturnal boundary layer, between the top of the residual layer and the surface stable layer, is lower than in the previous runs. As was seen in the previous run, an increase in the liquid water content is also present above the mixed layer. The potential temperature profiles exhibit a small decrease in intensity and very slight increase in the lowest levels of the wind speed can also be seen.

4.7.6 Vertical Grid with Constant Spacing

The simulation with a constant grid spacing used $\Delta z = 20$m.

In this case the unstable layer in the diurnal temperature profile is also higher than the observed and higher than the simulation with variable grid spacing. In the lower levels the stable boundary layer that develops in the evening is not well resolved (figure 4.10).

The specific humidity is affected in a similar manner by the grid spacing.

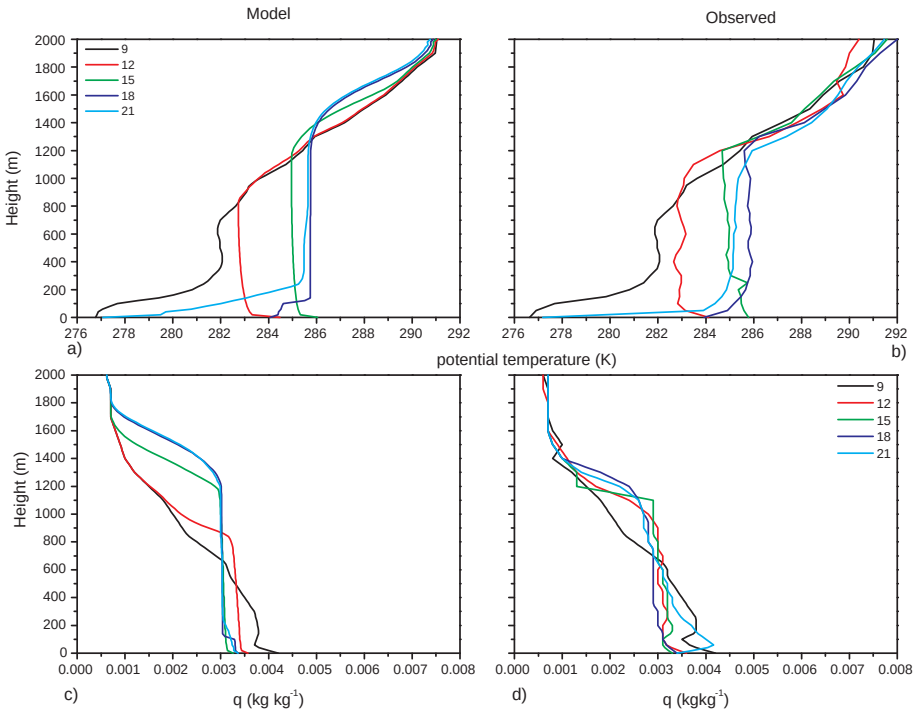

Figure 4.10: Potential temperature and specific humidity profiles for every 3 hours. (a) and (c) simulation with $\mu = 0.75$ and constant grid spacing, (b) and (d) observed conditions.

The wind speed has similar characteristics as the stretched grid. The differences also lie in the lowest levels which are not well resolved after the development of the stable layer (figure 4.11).

4.8 Summary

The model simulates both the mixed layer and the stable nocturnal boundary layer well, as long as the lowest levels are well resolved. The proposed turbulence parameterisations and stretched grid produce results comparable to published results for a 1.5 order closure model of Mailhot and Benoit (1982) and second order Yamada's *et al.*(1975) model.

The differences in stability between values of μ between 0.75 and 1 are not significant.

For the remainder of this thesis $\mu = 0.75$, the counter gradient heat flux will be turned off and the eddy diffusion parameters will be:

$$c_k = 0.3, \quad \alpha_h = 10, \quad \alpha_q = 10, \quad \alpha_e = 1.$$

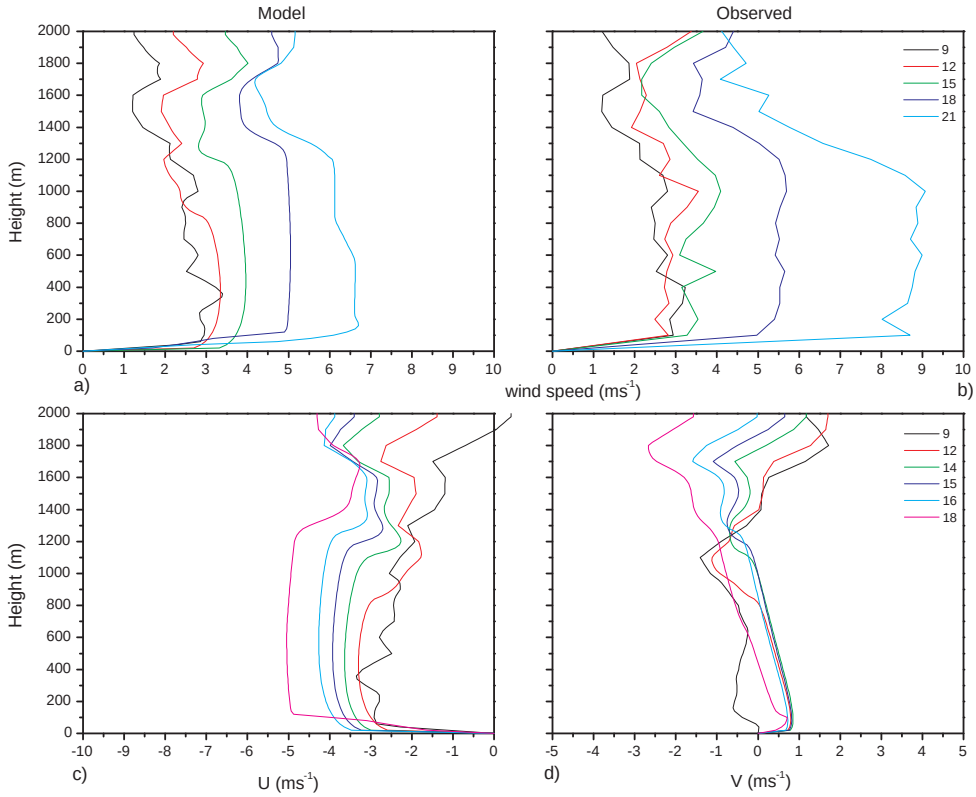

Figure 4.11: (a) Modelled wind speed for a simulation with $\mu = 0.75$ and constant grid spacing (b) observed wind speed during day 33 of the Wangara experiment. (c)Modelled easterly wind component and (d) modelled northerly wind component.

4.9 Appendix: Radiation Scheme

The radiation spectrum of the atmosphere is composed by two peaks; one in the shortwave band which is related to the solar radiation and the second in the longwave region related to the absorbed and emitted radiation by water vapour, carbon dioxide, ozone and the earth's surface. These wavelengths are broadly separated due to the disparate temperatures of the emitters. The spectrum of the shortwave radiation peaks in the visible spectrum near $\lambda = 0.5$ μm and is concentrated at wavelengths shorter than 0.4 μm. Tails of the shortwave spectrum extend into the ultraviolet ($\lambda < 0.3$ μm) and into the near–infrared region of the spectrum ($\lambda > 0.7$ μm). The longwave spectrum peaks at wavelengths of about 10 μm and its tails extend to the microwave region ($\lambda > 100$ μm) and to wavelengths of about (0.5 μm). The overlap of the two spectra is negligible so they can be treated independently.

As radiation passes through the atmosphere it is weakened by its interaction with the different atmospheric constituents. For a particular wavelength, the intensity of a pencil of radiation which crosses an atmospheric section of thickness ds, is reduced due to absorption and scattering by a factor of:

$$dI_\lambda = -k_\lambda \rho I_\lambda ds \tag{4.81}$$

where I_λ represents the intensity of the radiation of wavelength λ, ρ is the density of the section and k_λ the mass extinction cross section (in units of area per mass). The same pencil of radiation can also be reinforced by radiation emitted by the different atmospheric molecules and by radiation scattered from other directions. This can be represented in a similar manner by:

$$dI_\lambda = j_\lambda \rho ds \tag{4.82}$$

where j_λ denotes the source function coefficient. The total intensity change of the radiation pencil is, then, given by the sum of both equations:

$$dI_\lambda = -k_\lambda \rho I_\lambda ds + j_\lambda \rho ds \tag{4.83}$$

which is usually normalised and written in the following manner:

$$\frac{dI_\lambda}{k_\lambda \rho ds} = -I_\lambda + J_\lambda. \tag{4.84}$$

Now the source function is assumed to be:

$$J_\lambda = \frac{j_\lambda}{k_\lambda}. \tag{4.85}$$

For atmospheric modelling it is reasonable to assume that at each grid box, the atmosphere is plane–parallel such that density, temperature, pressure and gaseous constituents are horizontally homogeneous; i.e. only vertical variations are permitted. If z denotes the usual vertical axis, θ the inclination of the pencil of radiation in relation to z and ϕ the azimuthal angle in reference to the x axis, the total intensity change in the pencil's radiation can be written as:

$$\mu \frac{dI_\lambda(\tau, \mu, \phi)}{d\tau} = -I_\lambda(\tau, \mu, \phi) + J_\lambda(\tau, \mu, \phi) \tag{4.86}$$

where $\mu = \cos\theta$ and τ is the normal optical thickness measured downwards from the outer boundary:

$$\tau = \int_z^\infty k\rho \, dz'. \tag{4.87}$$

The scattering of radiation implies that part of the pencil of radiation which has an incident angle of (θ', ϕ') is redirected into the pencil with an angle of (θ, ϕ). This is described by the recurrence to a nondimensional parameter called phase function, $P(\mu, \phi; \mu', \phi')$, which represents the angular distribution of scattered energy as a function of the scattering angle, $\cos\Theta = \mu'\mu + (1-\mu^2)^{1/2}(1-\mu'^2)^{1/2}\cos(\phi' - \phi)$. The source function may, now, be written as:

$$J(\tau, \mu, \phi) = \frac{\tilde{\omega}}{4\pi}\int_0^{2\pi}\int_{-1}^{1} I(\tau, \mu', \phi')P(\mu, \phi; \mu', \phi')\, d\mu' d\phi' + \\ + \frac{\tilde{\omega}}{4\pi}F_0 P(\mu, \phi; -\mu_0, \phi_0)e^{-\tau/\mu_0} + (1-\tilde{\omega})B[T(\tau)] \tag{4.88}$$

where F_0 is the solar flux at the top of the atmosphere, μ_0 is the cosine of the solar zenith angle (the negative sign in μ_0 represents the fact that the direct solar radiation is downward), $\tilde{\omega}$ is the single–scattering albedo and B denotes the emission of radiation by the atmosphere.

The phase function may be obtained in terms of Legendre polynomials:

$$P(\mu, \phi; \mu', \phi') = \sum_{l=0}^{N} \tilde{\omega}_l P_l \cos(\Theta) \tag{4.89}$$

where the moment $\tilde{\omega}_l$ can be determined from the orthogonal property of Legendre polynomials,

$$\tilde{\omega}_l = \frac{2l+1}{2}\int_{-1}^{1} P(\cos(\Theta))P_l(\cos(\Theta))\, d\cos(\Theta), \quad l = 0, 1, ...N \tag{4.90}$$

For azimuthally independent scattering, the equation for diffuse radiative transfer is simplified into the following form:

$$\mu\frac{dI(\tau,\mu)}{d\tau} = I(\tau,\mu) - \frac{\tilde{\omega}}{2}\int_{-1}^{1} I(\tau,\mu')P(\mu,\mu')\, d\mu' + \frac{\tilde{\omega}}{4\pi}F_0 P(\mu, -\mu_0)e^{-\tau/\mu_0} + (1-\tilde{\omega})B[T(\tau)]. \tag{4.91}$$

For the transfer of terrestrial infrared radiation in a scattering atmosphere, in local thermodynamic equilibrium, the term related to the direct solar radiation is removed and for the transfer of solar radiation the emission of radiation by the atmosphere is negligible at the these wavelengths so this term is omitted.

By replacing the integral by summation, using Gauss quadrature, and using (4.89), equation (4.91) can be solved by determining its eigenvalues and eigenvectors.

Fu and Liou's (1992, 1993) model assumes that each layer receives two radiative streams

in the upper and lower boundaries and expand the scattering phase function into four terms ($N = 3$). Each layer is assumed to be homogeneous with an optical depth τ_1 and that there is no diffuse radiation from the top and bottom of this layer. The boundary conditions from the top and bottom of the layer are:

$$I_{-1,-2}(\tau = 0) = 0 \qquad \text{and} \qquad I_{1,2}(\tau = \tau_1) = 0. \tag{4.92}$$

The boundary conditions at the surface are modified to include the surface albedo.

The upward (positive) and total (direct plus diffuse) downward (negative) fluxes at a given level are given by:

$$F^+(\tau) = 2\pi(a_1\mu_1 I_1 + a_2\mu_2 I_2), \tag{4.93}$$

and

$$F^-(\tau) = 2\pi(a_1\mu_1 I_{-1} + a_2\mu_2 I_{-2}) + \mu_0\pi F_0 e^{-\tau/\mu_0}. \tag{4.94}$$

The Gauss quadrature weights in the four–stream approximation are: $\mu_1 = 0.3399810$, $\mu_2 = 0.8611363$, $a_1 = 0.6521452$ and $a_2 = 0.3478548$.

5. Data Analysis

In this chapter, the properties of the flow of a selection of northerly wind cases is analysed and the relationship between the results and gravity wave theory is considered. The time series obtained by the 2 m masts deployed in East Falkland (figure 5.1) are also used to determine a climatology of the campaign.

The choice of the days that might possess interesting features was made by selecting

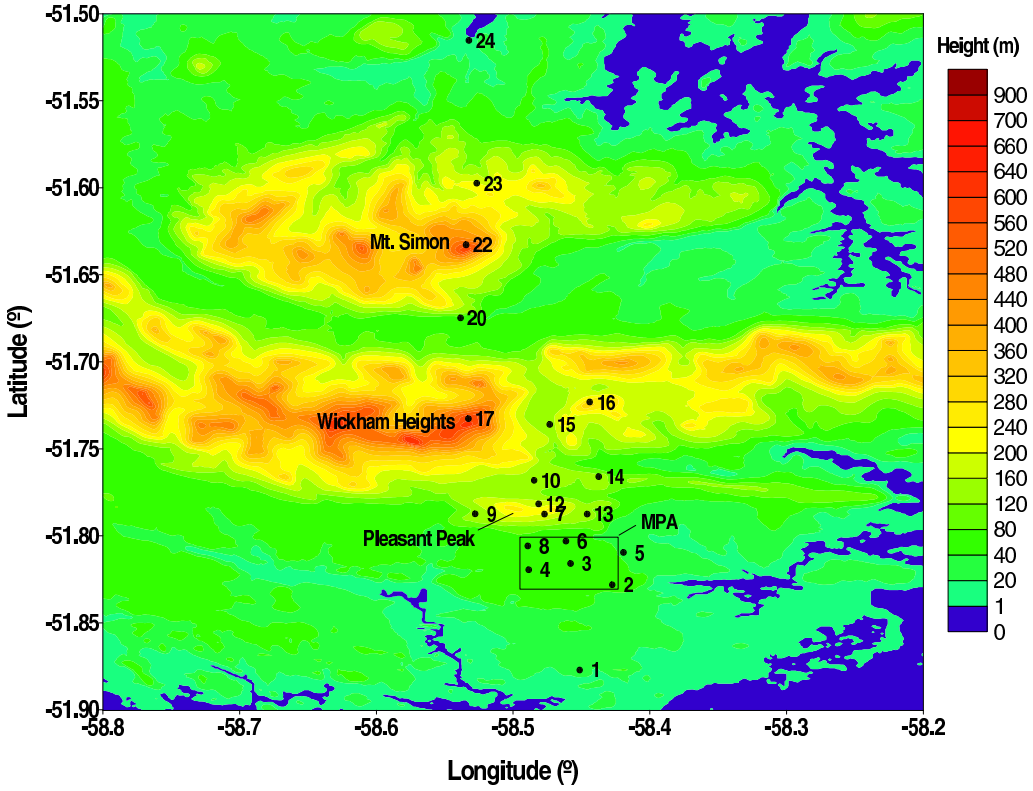

Figure 5.1: Location of the automatic weather stations on East Falkland as well as detailed view of the terrain. Also shown is the approximate location of MPA.

the radiosonde profiles in which the wind direction at 500 m was between 300° and 60°. As a result, 125 days were selected for analysis. From these, a detailed analysis of 6 cases is presented here. These cases fall into the three categories highlighted in Mobbs *et al.* (2005) and are representative of the different flow regimes observed during the campaign.

Here, time refers to time of the experiment in units of Julian day. Note that for clarity the 1^{st} of January 2001 is considered to be day 1, the 31^{st} of December 2000 is day 0 and the remaining days of year 2000 are negative. Times of day will be quoted in UTC and local time is three hours behind UTC from the 9^{th} of September 2000 to the 14^{th} of April 2001 and four hours behind from the 15^{th} of April 2001 to the 1^{st} of September 2001.

5.1 Climatology

5.1.1 Wind

The flow measured at the most northerly station on West Falkland, station 24, is not very strong (figure 5.2a). In fact, 60% of the observed wind speeds are below 6 ms^{-1} and only 2.64% are above 12 ms^{-1}. The maximum speed measured was 21.97 ms^{-1}, for a wind from

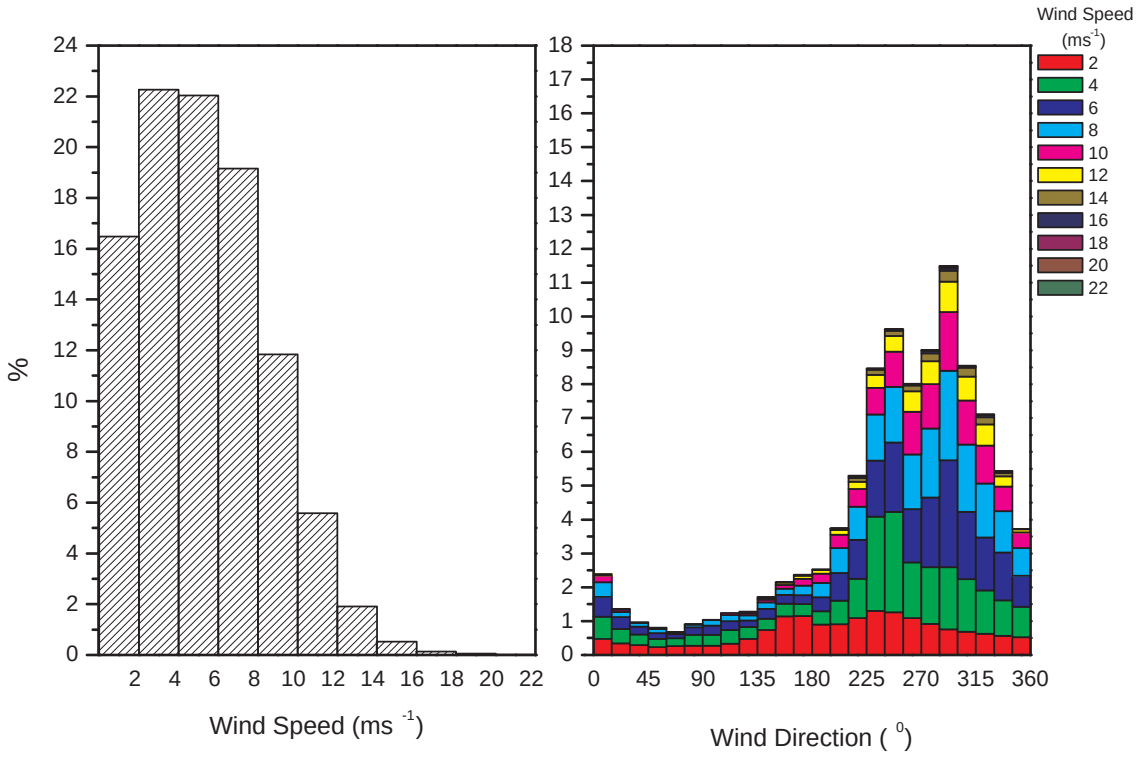

Figure 5.2: Histograms of the 2 m wind data measured at site 24 during the whole campaign. (a) Histogram of wind speed and (b) histogram of wind speed as a function of wind direction.

289.8^o, on the 2^{nd} of March 2001.

The highest wind speeds measured at station 24 are for north–westerly winds (wind direction between 285^o and 300^o). These are wind speeds between 20 and 22 ms^{-1} but

represent only 0.01% of the whole data set. This is illustrated on figure (5.2b).

Other relevant features of the wind at site 24 are:

- Winds speeds between 18 and 20 ms^{-1} represent only 0.05% of the whole data set and are resultant from flow with direction between 270^o and 300^o;

- Northerly flows with wind direction from 315^o to 345^o and wind speeds between 16 and 18 ms^{-1} represent only 0.03% of the total data;

- For wind directions between 30^o and 45^o and 60^o and 120^o the wind speed is never greater than 10 ms^{-1};

- The majority of the flow has a direction between south–westerly and north–westerly (55%);

- 21% of the flow is from north-westerly to north–easterly and only 6% of the wind blows between north–easterly and south–easterly;

- The months of May, June, July and August are months when the wind speed is weakest, around 85% of the observed wind speeds are below 8 ms^{-1} with 20% or more below 2 ms^{-1}. These are months when there is the highest percentage of southerly or south–easterly flow.

The measured flow for a station at MPA (station 4) is represented in figure (5.3). Relatively to the previous site, site 4 has an increase in wind speed. Although the highest percentage of the wind speed is still observed for the bin $4-6$ ms^{-1}, the second highest percentage is now for the bin $6-8$ ms^{-1}. There is also an increase in the percentage in the individual bins for wind speeds greater than 10 ms^{-1}. The wind is also more westerly and the highest percentage in the wind direction is for flow from 270°–285°. There is also a decrease in the percentage of south–westerly flows. The influence of the orography north of MPA is reflected in a 10% increase in the northerly flows and also in the increase in the wind strength. While at site 24 the maximum wind speed for northerly flows was never greater than 18 ms^{-1}, for site 4 the maximum speed falls in the bin 20–22 ms^{-1}. Individual bins for speeds greater than 10 ms^{-1} also show an increase in percentage.

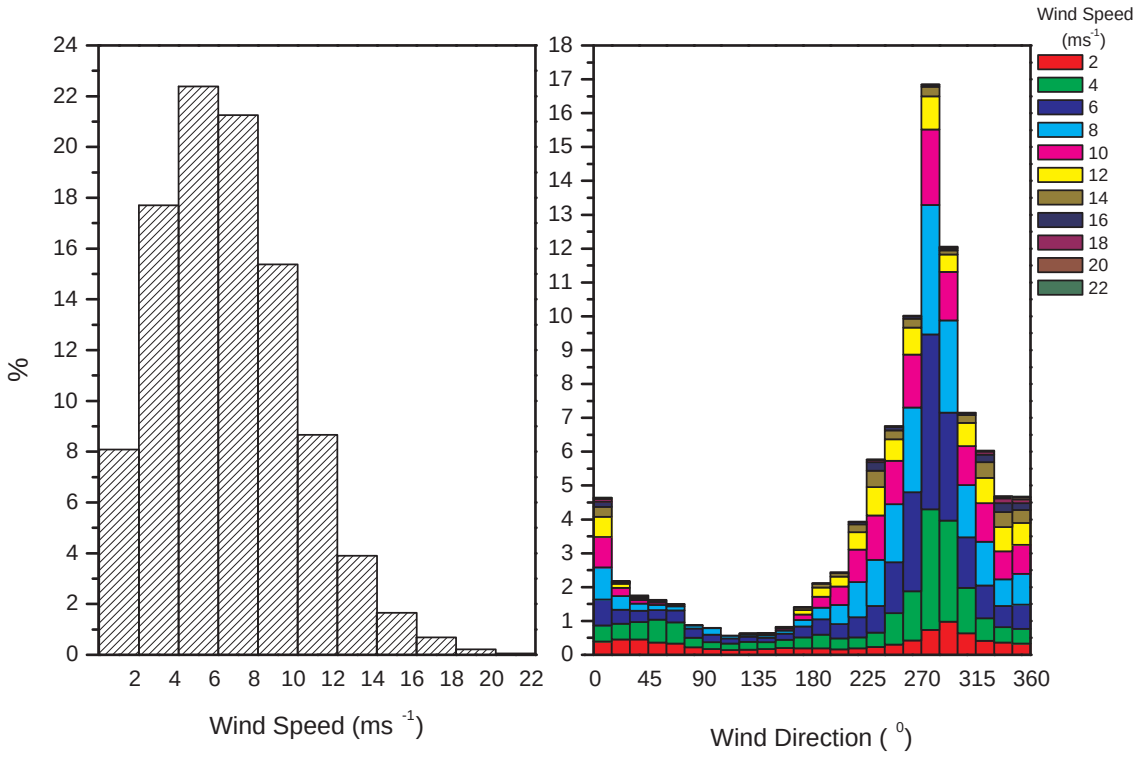

Figure 5.3: Histograms of the 2 m wind data measured at site 4 during the whole campaign. (a) Histogram of wind speed and (b) histogram of wind speed as a function of wind direction.

Relative Acceleration

The influence of the mountains on the flow's acceleration can be accessed by the calculation of the fractional relative acceleration, Δs, where:

$$\Delta s = \frac{U - U_{ref}}{U_{ref}}, \tag{5.1}$$

U_{ref} is the wind speed at station 24 and U is the wind speed at the individual station at MPA. When the wind direction is northerly the relative acceleration is equal to the speed–up. Figure (5.4) shows that there are no considerable differences between stations. Station 3 is the station where the highest percentage of deceleration is observed and station 4 is the one which has the least percentage. The decreased percentage in deceleration is compensated by an increase in the amount of flow that has acceleration less than 1. Flows which are accelerated by more than 100% have the same distribution for the four stations.

South–easterly is the direction from which there is greater flow deceleration for all stations and northerly is the direction which leads to the greatest speed–ups. East and south–east are directions that have the highest percentage of $\Delta s > 6$, this implies that for

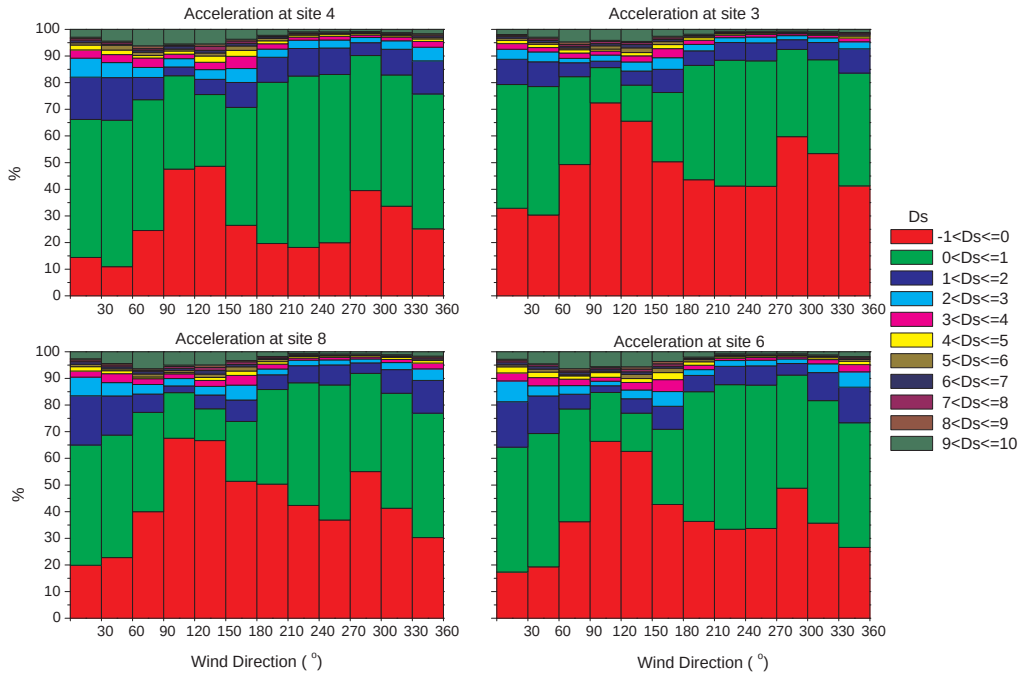

Figure 5.4: (a)Histogram of $\Delta s = \frac{U-U_{24}}{U_{24}}$ as a function of wind direction at station 24, for stations 8, 6, 4 and 3.

easterly wind there is a decoupling between the flow on either side of the mountains.

Gust Factors

A measurement of the gustiness of the flow is achieved by calculating the gust factor. Gust factors were determined by Ágústsson and Ólafsson in their private communication, for 36 automatic weather stations in Iceland. These stations are mostly located along Iceland's coast line and depending on the wind direction they are either upwind or downwind of a ridge. Ágústsson and Ólafsson found that the average gust factor was independent of the stability of the atmosphere, but strongly dependent on the wind speed and on topography.

Here, gust factors are define as $G = U_g/U$, where U represents the 10 min average of the wind speed at each stations and U_g is the 30 s wind speed maximum for that period. Figure (5.5a) shows the average gust factor as a function of wind speed for stations 1–6 and 8 as well as the average at station 24. Ágústsson and Ólafsson found that for every 5 ms^{-1} increase in the mean wind speed there is a reduction of about 0.04 in the gust factor for wind speeds between 10 ms^{-1} and 25 ms^{-1}. Here, if a similar restriction is put on the

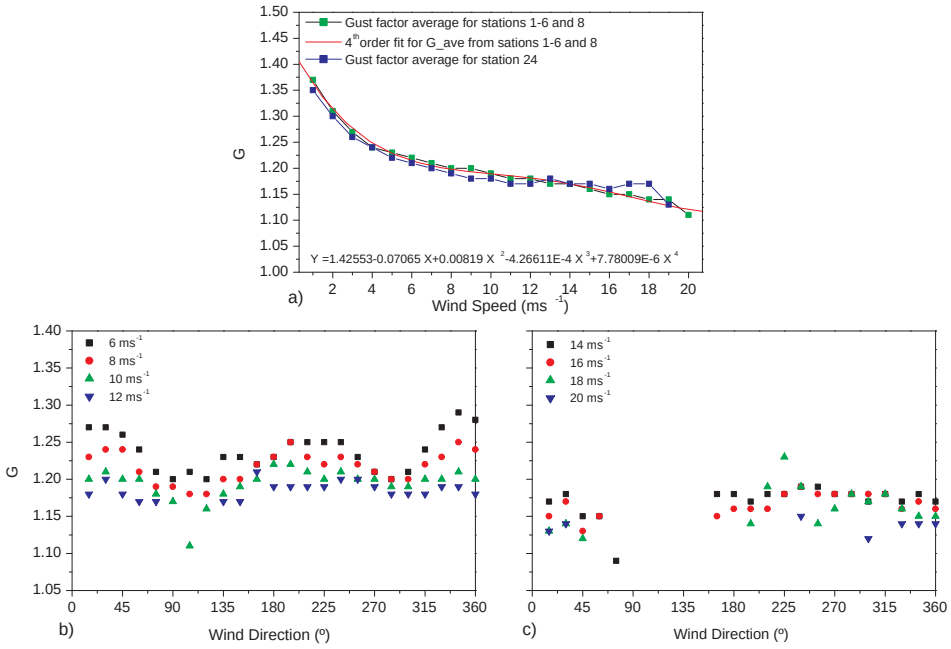

Figure 5.5: (a) Average gust factor for stations 1–6 and 8 and the average gust factor for station 24 as a function of wind speed; (b) and (c) average gust factor for wind speeds greater than 6 ms^{-1} as a function of wind direction for stations $1-6$ and 8.

wind speed, the average gust factor is 1.16 and there is a reduction of 0.034 for every 5 ms^{-1} increase in the mean wind speed. This average is lower than theirs ($G_{av} = 1.4$) due to their use of 3 s data to determine the gust factors.

If the restriction on the lower wind speed the limit is relaxed to 5 ms^{-1} the average increases slightly to 1.18 but the slope remains the same. In fact, a linear fit produces the following result: $G = 1.25956 - 0.00676U$. For wind speeds lower than 5 ms^{-1} the linear fit is no longer possible. A fourth order fit is obtained for the whole range of wind speeds. This fit will be assumed to represent the average gustiness for each individual wind speed and used to assess how turbulent the individual case studies are.

In figure (5.5b and c) the influence of the wind direction is highlighted. For wind speeds greater than 6 ms^{-1} and less than 14 ms^{-1} the gust factors at MPA are highest for northerly wind and are lowest for easterlies and westerlies. For wind speeds greater than 12 ms^{-1} there is not enough data to draw any conclusions.

5.1.2 Temperature

The relationship between the sea surface temperature and the air temperature north of the Falklands is of great importance in determining the vertical temperature profile and the development of a temperature inversion. Due to the large heat capacity of the oceanic mixed layer the sea surface over large areas is relatively uniform and the diurnal forcing of the marine boundary layer is very small; so an air mass that has travelled above a great expanse of sea surface is usually in a near neutral state. This will be the case for northerly conditions. The relationship between the difference between the 2 m air temperature and the sea surface temperature (SST) in the ECMWF's ERA 40 analysis, for a grid box centred at (301° E, −51° N) can be observed in figure (5.6).

For the months from May to September the sea surface temperature (SST) is greater than the 2 m air temperature and the days in which this relationship is reversed are days when there is northerly flow. There are some few isolated instances when this is not true but the temperature difference is very small. The upward heat flux due to a warmer surface produce a well mixed boundary layer and along with the fact that there are fewer northerly winds during the autumn and winter months explains the low frequency of strong rotor events for this period. As was mentioned earlier, the wind speed for these months is usually weak and along with the low surface temperature it will produce blocked flow.

During the summer months (January, February and March) the air temperature is greater than the SST. The periods when this is reversed are periods when southerly or south–westerly are observed at station 24. The lower ocean temperature cools the atmosphere immediately above it and the downward heat flux produces a stable layer in the first hundred meters with a discontinuity above it. The stronger winds, the greater proportion of northerly flow and the larger temperature difference gives rise to the increased frequency of strong rotor events.

Figure (5.7) shows the difference

between the monthly 2 m air temperature at station 24 and the monthly sea surface temperature (SST) of the NOAA Weakly Optimum Interpolation SST global analysis fields, for a grid box centred at (301.5° E, −51.5° N) during the period November 2000 and October 2001. It summarises what was previously said; between October and March the sea surface is on average colder than the air temperature and the reverse is true for the remaining months.

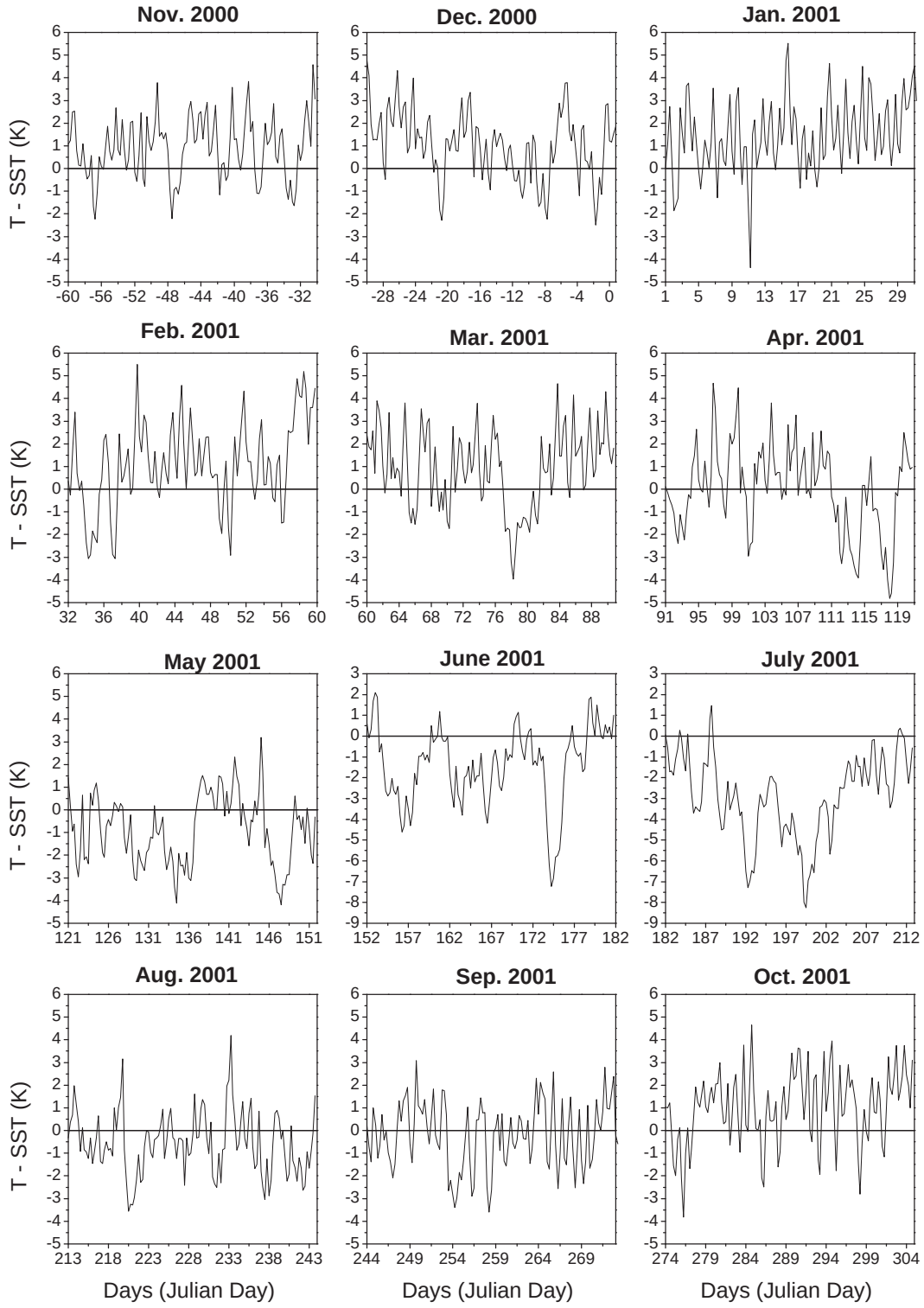

Figure 5.6: Difference between the 2 m air temperature and the sea surface temperature (SST) in the ECMWF's ERA 40 analysis, for a grid box centred at (301◦ E, −51° N) during the period November 2000 and October 2001.

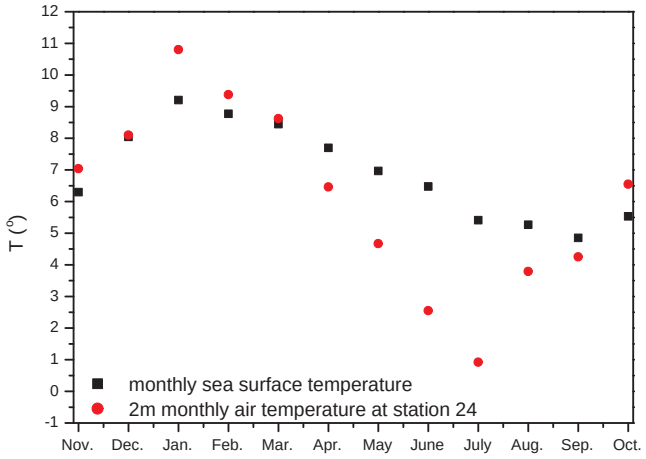

Figure 5.7: Difference between the monthly 2 m air temperature at station 24 and the monthly sea surface temperature (SST) of the NOAA Weakly Optimum Interpolation SST global analysis fields, for a grid box centred at (301.5°E, −51.5° N) during the period November 2000 and October 2001.

Although not shown, an analysis of the relationship between this temperature difference and the wind direction observed at site 24 reveals that the highest negative differences ($t_2 - SST < -4$ K) are only observed for wind directions between 105^o and 285^o and that northerly flow has the highest percentage of high positive temperature difference.

5.1.3 Pressure

The diurnal cycle of solar heating induces a diurnal surface–pressure variation which is linked to different processes:

- The first is related to the heat absorption by ozone and water vapour. Since these components are longitudinally homogeneously distributed they induce a diurnal planetary–scale migrating tide (Lindzen 1967 and Chapman and Lindzen 1970). According to Haurwitz and Cowley (1973), a diurnal and a semi–diurnal signals can be approximated by:

$$S_1(p) \approx 0.629 \sin^3\theta \sin(T + \phi + 12^o), \tag{5.2}$$

and

$$S_2(p) \approx 1.161 \sin^3\theta \sin(2T + 2\phi + 159^o), \tag{5.3}$$

where the amplitude is in hPa, T denotes Greenwich Mean Time, and (θ, ϕ) represent the co–latitude and longitude;

- The second is related to the interaction of the mountain with the atmosphere.

Figure (5.8) shows the result of the application of the two equations (5.2 and 5.3)to the Falklands. The diurnal tide has an amplitude of 0.3 hPa and has a maximum at 9 local time

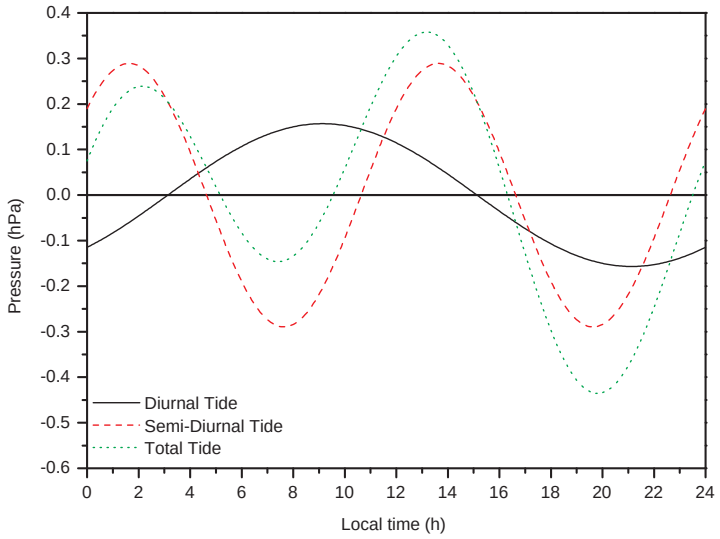

Figure 5.8: Analytical tides for the Falkland Islands obtained from equations (5.2) and (5.3)

and a minimum twelve hours latter. The semi–diurnal tide has an amplitude of 0.56 hPa and has two maxima, the first at 1.6 h and the other at 13.6 h local time. The minimum are located at 7.6 h and 19.6 h local time. Both the diurnal and semi–diurnal tides are centred on 0 hPa. The total tide is the result of the sum of the two previous components and is no longer centred on 0 hPa. Its amplitude in the first twelve hours is of 0.38 hPa and 0.8 hPa in the second twelve hours. The first maximum and minimum are attained at 2 h and 7.4 h respectively. The second maximum and minimum are reached at 13.2 h and 19.8 h respectively.

Davies and Phillips (1985) have also found diurnal and semi–diurnal pressure signal during the ALPEX campaign. Here a similar procedure is used to determine such signals (figure 5.9). The semi–diurnal signal corresponds to the semi–diurnal tidal component and the diurnal relates to the total tide. These two components for $T = 0$ min, were determined

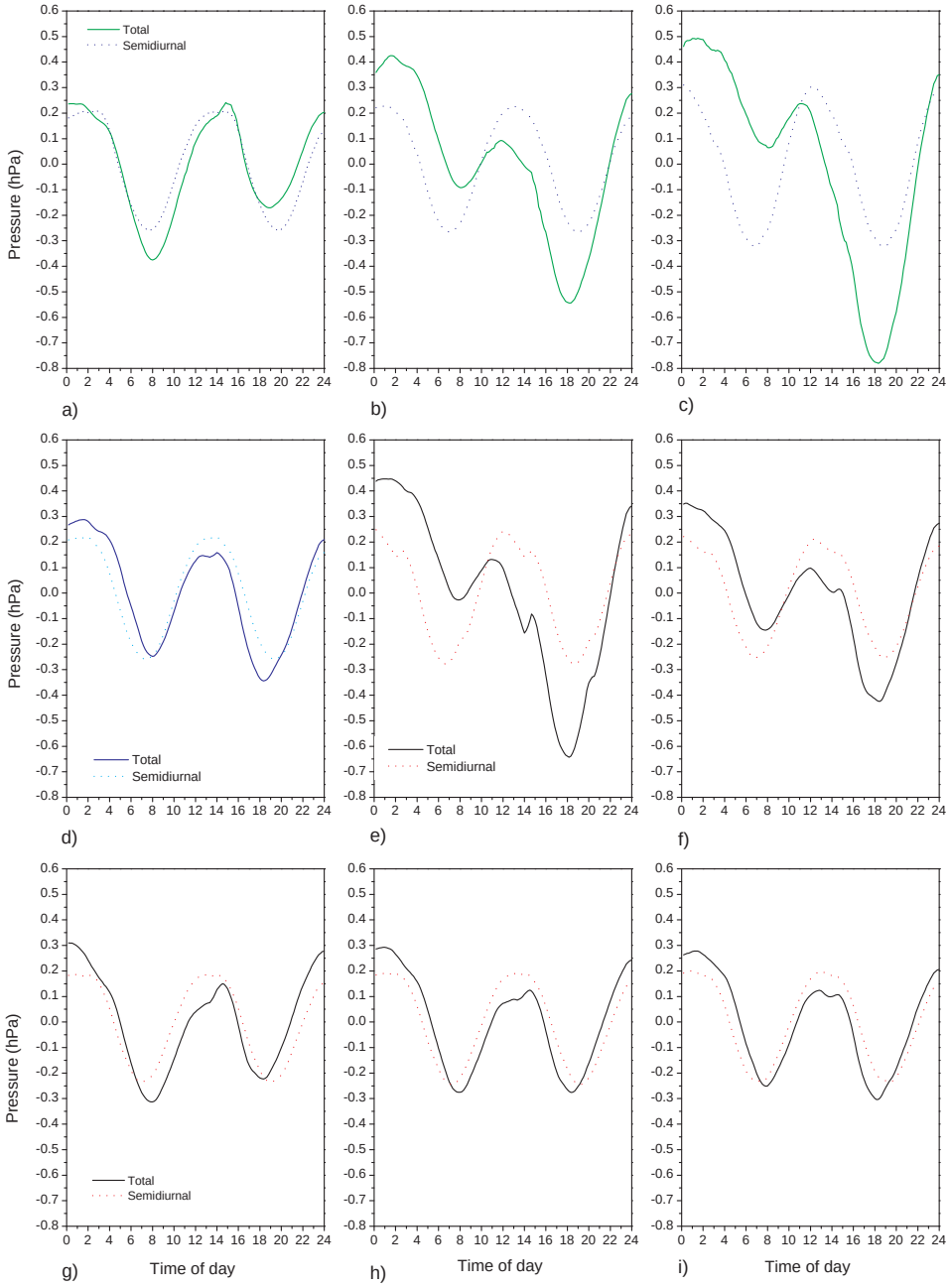

Figure 5.9: Semi–diurnal tide and the total tide amplitude for stations: (a) 24, (b) 23, (c) 22, (d) 20, (e) 17, (f) 12, (g) 8, (h) 4 and (i) 1

using the following formulae:

$$(S_1(p) + S_2(p))|_{T=0} = \frac{1}{N}\sum_{i=1}^{N} p|_{T=0} \tag{5.4}$$

and

$$S_2(p)|_{T=0} = \frac{1}{2N}\sum_{i=1}^{N}(p|_{T=0} + p|_{T=12}) \tag{5.5}$$

where N is the number of days of the campaign. This was performed on the 10 min data (144 records per day). A moving average using eight neighbouring points was performed and the average of the 144 signals was removed from each signal.
Figure (5.9) shows the semi–diurnal tide and the total tides for a transect from north to south across East Falkland. The proximity of the mountains does not alter the shape of the semi–diurnal tide or its amplitude. The amplitude ($\sim$ 0.25 hPa) is slightly reduced in comparison with the analytical which might be due to the averaging processes. The maxima and minima are located at the same times as the predicted by the analytical equations. The total tide, on the other hand, suffers the influence of the proximity of the mountains. Stations 24, 8, 4 and 1 have an almost symmetrical signal centred on 0 hPa, with amplitude around 0.3 hPa and differences between the stations are less than the accuracy of the calibrations hence this signal will not affect the calculation of the pressure differences between these stations. The location of the maxima and minima are also in the same location as determined by the analytical formulae.

As the height of stations increases, the effect of the proximity of the mountain is felt on the first minimum which is significantly reduced and on the first maximum and second minimum which are increased. The height dependence for the amplitude of the total signal has also been observed by Davies and Phillips (1985) in the Gotthard cross–section of the ALPEX campaign. Frei and Davies (1993) propose three types of effects to explain the dissimilarities. The first is related to pseudo-static effects like different exposure of the slopes to shading, albedo variations and asymmetry in the topography or valley geometry. The second is related to the transport of the thermal response and the diurnal variation of the orographic perturbation. The third is related to the interaction of the planetary tides with the mountain. Davies and Phillips (1985) propose that differences in thermal transport as the cause of their variations. It is though possible that changes of the wind speed with height and the consequent thermal transport would be the main cause for the differentiation in the signals. If pressure differences, involving these stations (22, 23, 20, 17 and 12) and the others, are to be determined this signal should be removed from the time series.

5.2 Case Studies

The six cases that will be depicted in this section represent types of flow which are illustrative of the conditions observed under northerly conditions at Mount Pleasant Airport (MPA). They fall into the three categories identified in Mobbs *et al.* (2005):

(i) Strong downwind acceleration ($\Delta s \geq 1.75$);

(ii) Strong downwind acceleration and variable flow ($\Delta s \geq 1.75$ and $\sigma_H / \overline{U} \geq 0.4$);

(iii) Weak downwind acceleration ($\Delta s < 0.5$).

Here Δs is the speed–up, σ_H denotes the spatial standard deviation of the wind vector at stations 1–6 and 8 (to be defined later), $\overline{U}$ represents the mean wind vector for the same stations. Note that in (*ii*) it is the maximum of $\sigma_H / \overline{U}$ which is used.

Alongside the turbulence analysis of the wind field, the temperature and pressure perturbations at the stations in the vicinity of the airport (stations 2, 3, 4, 5, 6 and 8) will also be examined. In particular, emphasis will be put on the correlation between pairs of opposing stations, i.e., pairs 2–5, 3–6 and 4–8 and also on the relationship between these stations and the most northerly station in East Falkland, station 24 (see figure (5.1) for the location of the stations).

All the cases, with the exception of the first, display a temperature inversion near the surface in the radiosonde profile and the connection between the inversion and the temperature difference between the air temperature and the sea surface temperature (SST) will also be scrutinised. The Met Office forecast for the grid point centred at (51.0°S, 59.0°W) will be used to ascertain if inversions are forecasted upstream. When inversions are forecasted, their height and gradient will be compared with the same parameters in the radiosonde.

5.2.1 Weak downwind acceleration

The first two cases fall into category (*iii*), i.e., the flow downstream shows very little variability and is decelerated. The wind direction at the surface is northerly or north–westerly and there is evidence of gravity wave motion in both cases. The pressure difference and

temperature difference between the stations at MPA is negligible for both cases.

The first case departs from the second since it shows no evidence of a temperature inversion in the radiosonde profile.

17^{th} of May 2001

The vertical profiles of temperature, wind speed, wind direction and balloon ascent rate deduced from the radiosondes launched at MPA are presented in figure (5.10). The temperature profiles in both launches (figure 5.10a and d – black line) show no strong inversion in the

lowest 1000 m. There is only a weak inversion ($\sim$ 1.5 K) at about 1800 m in the profile at $1112Z$ (T = 137.47 days). Although the temperature difference between the 2 m air temperature and the sea surface temperature (SST) in the ECMWF's ERA 40 analysis is positive for the whole day, suggesting that there is advection of warm air north of the Falklands, the temperature difference between the 2 m temperature at station 24 and the SST obtained from the NOAA Weekly Optimum Interpolation SST global analysis fields (Reynolds and Smith 1994) reflects the effects of the coastal boundary layer. This difference is negative up to T = 137.2 days and remains positive for the rest of the day, however, it is never greater than 1.5 K which might be the reason for the lack of a temperature inversion downstream, i.e., the inversion at 24, if it ever existed, is either too low or too weak to propagate downstream [1]. The blue line represents the Met Office temperature forecast for $1200Z$ (figure 5.10a) and $0000Z$ on the 18^{th} of May (figure 5.10d). Both profiles agree reasonably well with the radiosonde profiles although the small temperature inversion is absent at $1200Z$. This is probably due to lack of resolution.

The depth averaged Brunt Väisälä frequency in the lowest 500 m reflects the observed stable atmospheric profile; it is 0.011 Hz at T = 134.47 days and 0.012 Hz at T = 137.97 days.

As in all the other cases presented here, the wind direction in both profiles (figure 5.10b and e) is northerly, backing with height through the boundary layer. The ascent rate for the first sonde (figure 5.10c) exhibits an ~ 2 ms^{-1} fluctuations in the lowest 5000

[1] This difference was determined by using three grid points centred at (50.5°S, 59.5°W), (50.5°S, 58.5°W) and (50.5°S, 57.5°W) for the SST and the wind direction at station 24 as the determining factor for the use of either grid point.

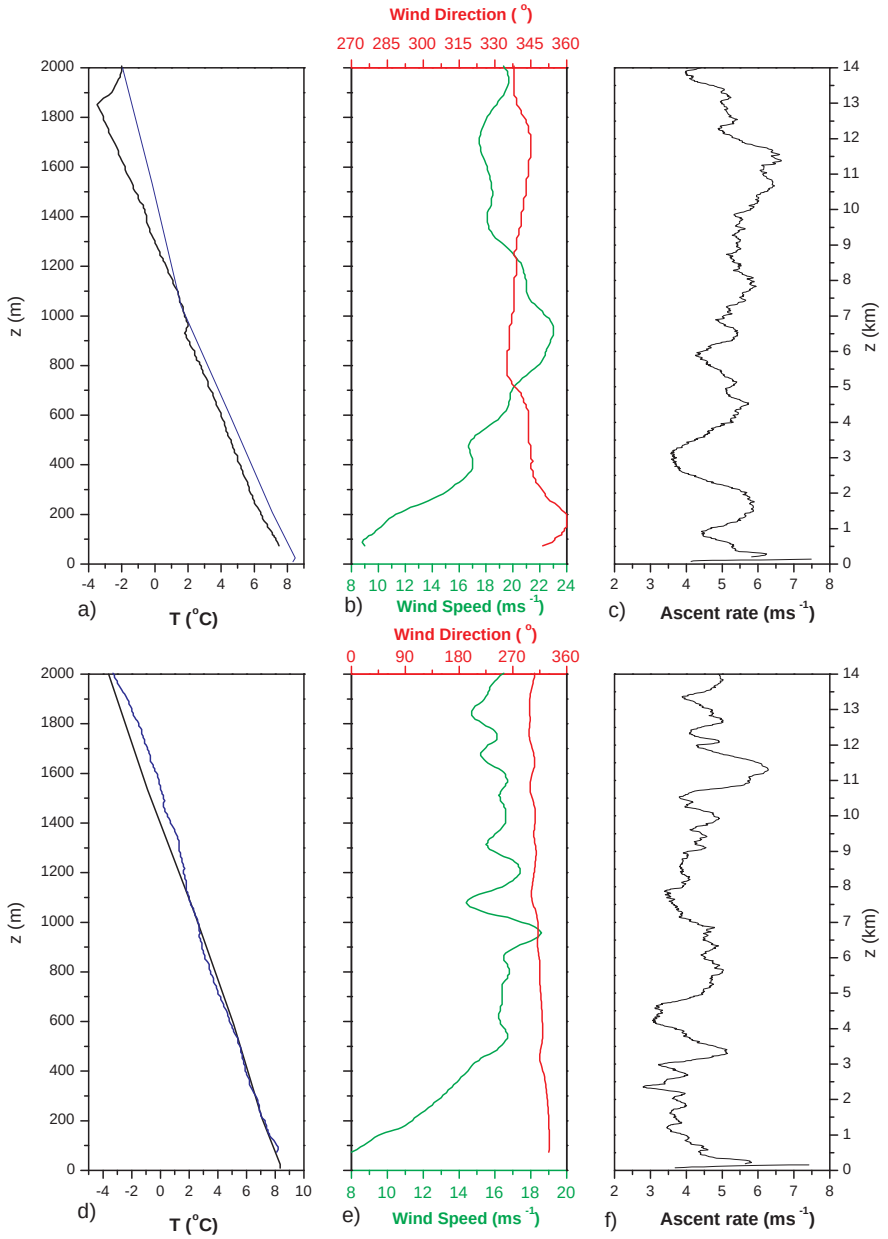

Figure 5.10: MPA radiosonde measurements, on the 17^{th} of May, of (a) temperature (black line), (b) wind speed and direction and (c) ascent rate at $1112Z$ ($T = 137.47$ days) and (d) temperature (black line), (e) wind speed and direction and (f) ascent rate measured at $2317Z$ ($T = 137.97$ days). Met Office temperature forecast for (a) $1200Z$ ($T = 137.5$ days) on the 17^{th} of May and (d) $0000Z$ ($T = 138.0$ days) on the 18^{th} of May (blue line).

m which is evidence of the presence of gravity waves. These oscillations have, however, disappeared by $2317Z$ ($T = 137.97$ days).

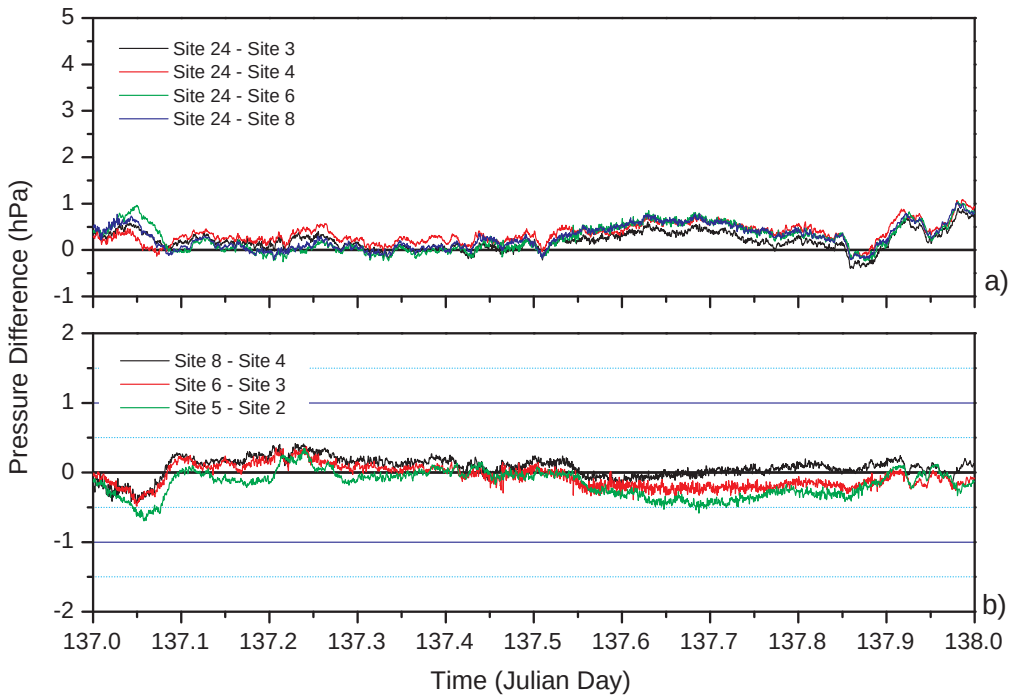

Figure 5.11: The 30sec pressure difference between (a) site 24 and 4 stations at MPA and (b) pressure difference between the stations at MPA on the 17^{th} of May. Stations 4 and 8 are along a line normal to the ridges; stations 6 and 3 and stations 5 and 2 are along two lines approximately parallel to the first and each other.

The pressure difference between site 24 and the stations downstream is negligible as well as the pressure difference between the downstream stations at MPA. Both are fairly uniform throughout the day (figure 5.11).

The 2 h pressure spectrum (cf appendix at the end of the chapter for details) for station 24 has very low energy and no particular frequency stands out (figure 5.12). The spectrum for the downstream stations also has low energy but is significantly different than the previous one. In stations 4 and 8, the spectrum amplitude increases from a frequency of 2.5×10^{-4} Hz up to frequencies of 0.004 Hz and then declines to zero. In Stations 6 and 3 the maximum is shifted to $f \sim 0.006$ Hz. Station 6 is the only one which has a significant energy at $f \sim 0.0069$ Hz and $f \sim 0.0043$ Hz. All these frequencies represent periods of a few minutes.

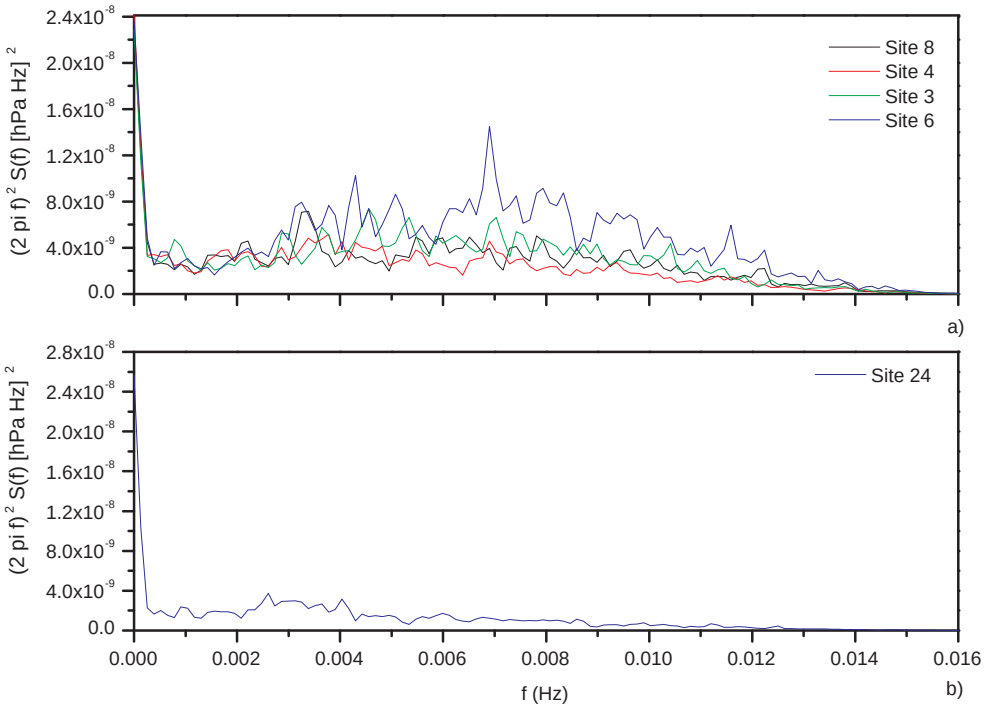

Figure 5.12: 2 h pressure spectrum for stations (a)8, 6, 4 and 3, and (b)24 on the 17^{th} of May.

Examples of the 30 s average wind speeds measured at 2 m by the automatic weather stations are presented in figure (5.13). The wind at station 24 and at MPA is consistently northerly and steady for the whole day.

The flow's temporal variability is emphasized by the 10 minute standard deviation of the wind field, σ.

$$\sigma^2 = \sigma_u^2 + \sigma_v^2 \tag{5.6}$$

where σ_u^2 and σ_v^2 are respectively the standard deviation, at each station, of the westerly and southerly 10 minute average of the wind components measured at stations 1–6 and 8. This parameter can be taken as an estimate of turbulence since it can be taken as an approximation of the horizontal component of the turbulent kinetic energy ($\sigma^2 \sim 2TKE$).

The spatial variations of the flow across MPA are determined by the spatial standard deviation of the wind field, σ_H.

$$\sigma_H^2 = \sigma_{uH}^2 + \sigma_{vH}^2 \tag{5.7}$$

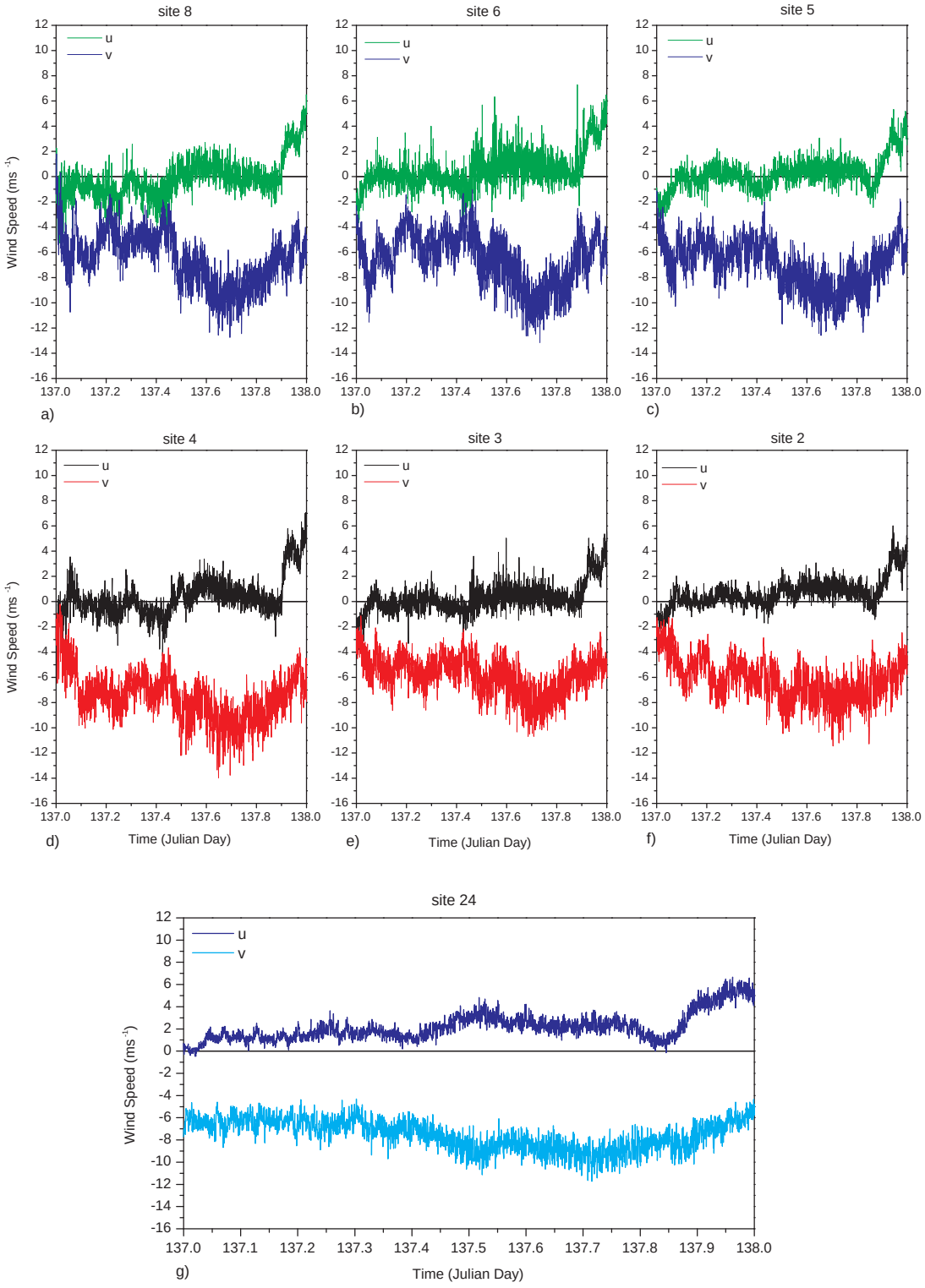

Figure 5.13: 30s wind for stations (a) 8, (b) 6, (c) 5, (d) 4, (e) 3, (f) 2 on the 17^{th} of May. The relative position of each picture is the same as the relative location of the stations. (g) 30s wind for station 24 on the 17^{th} of May.

where σ_{Hu} and σ_{Hv} are respectively the standard deviation of the westerly and southerly component from the average of the wind speed at stations 1–6 and 8 for a single point in time.

The low values and low variability for both parameters (figure 5.14) demonstrate that

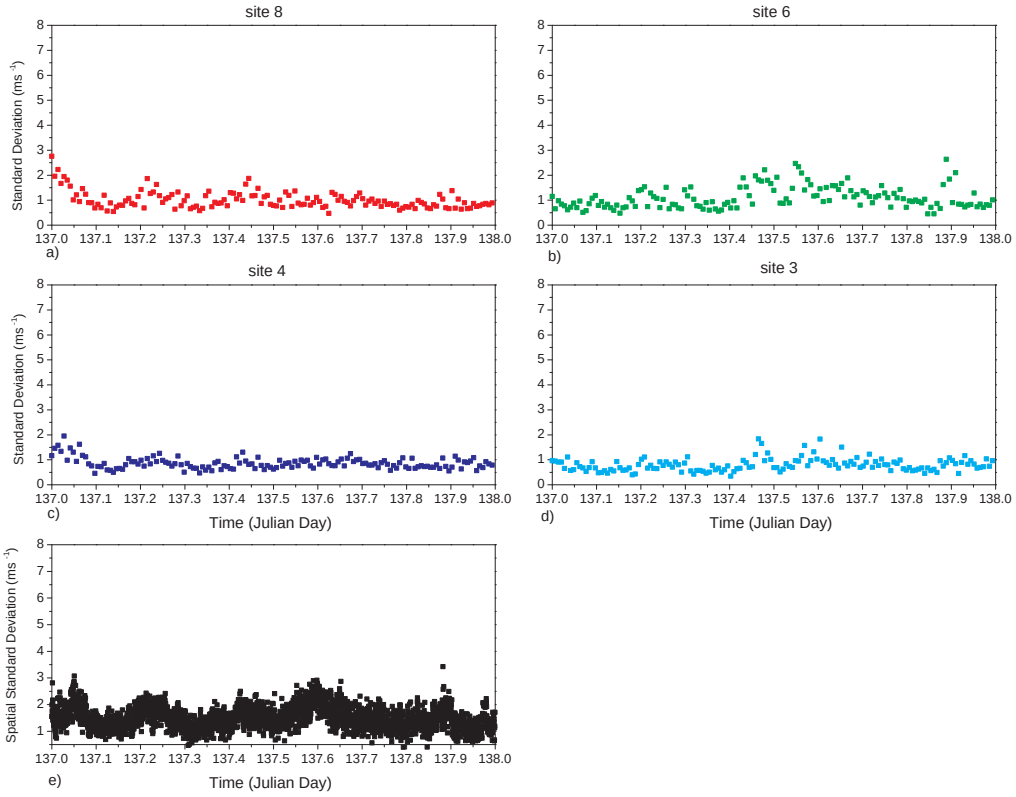

Figure 5.14: 10 min standard deviation for stations (a)8, (b)6, (c)4, (d)3 and (e)horizontal standard deviation on the 17^{th} of May.

the flow across MPA is fairly uniform and relatively uni–directional throughout the day. The uniformity of the flow is highlighted by the gust factors (figure 5.15 a, b, c and d). Except for the first hour in station 4, the gusts in stations 3 and 4 are less than 20% above average for the whole day and for all wind speeds. Stations 8 and 6 show evidence of being more turbulent although the gusts are mostly less than 20% above average.

A typical example of the flow direction is presented in figure (5.16). The flow is consistently northerly for all stations and the flow vectors do not show any significant acceleration downstream of the mountains, in fact, some of the stations show deceleration.

This behaviour is emphasized by the calculation of the speed–up (figure 5.15 e, f,

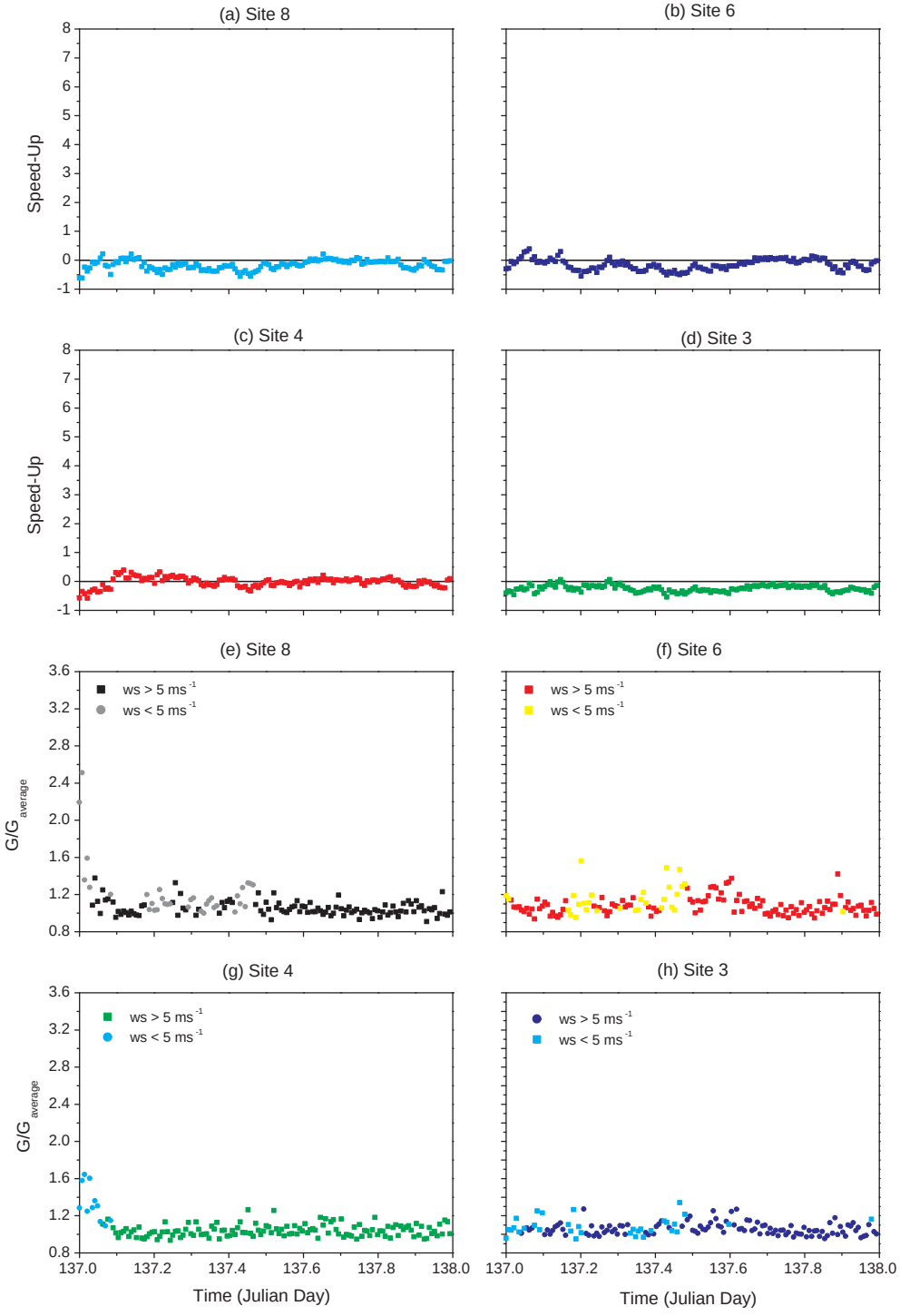

Figure 5.15: Gust factors normalized by the average gust factor for stations (a) 8, (b) 6, (c) 4 and (d) 3 and speed–up for stations (e) 8, (f) 6, (g) 4 and (h) 3 on the 17^{th} of May

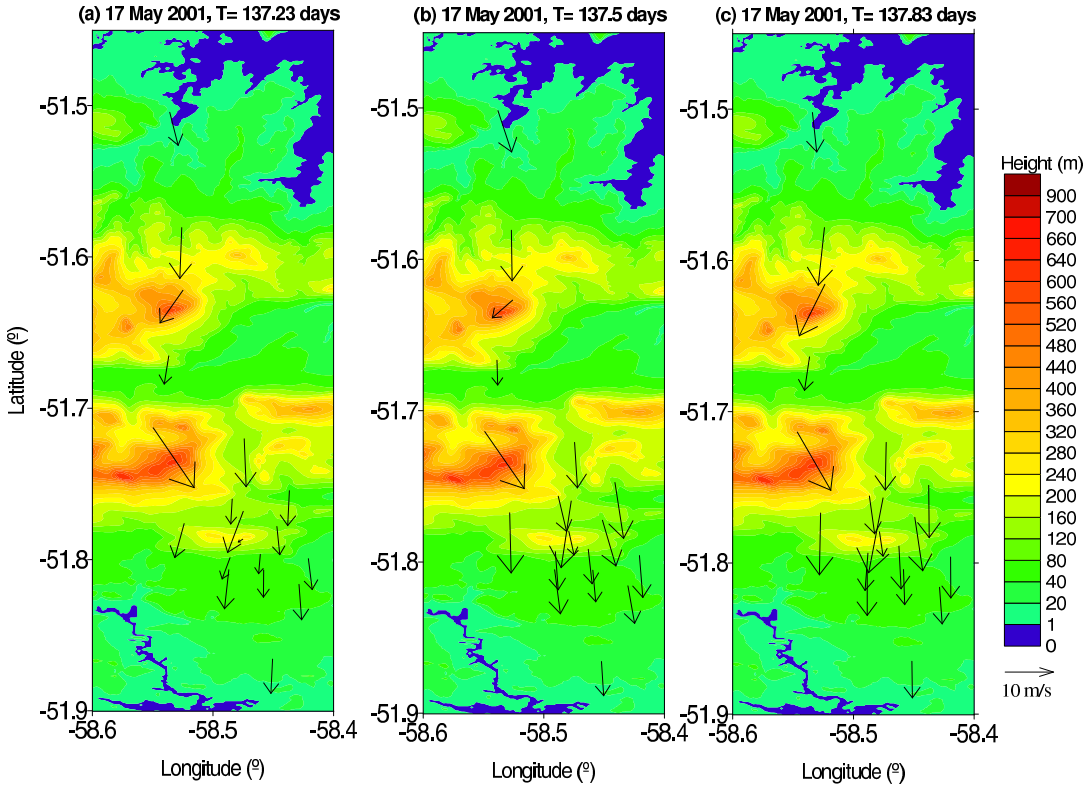

Figure 5.16: The 10 minute average wind field measured at the AWS sites for the 17^{th} of May.

g and h). The speed–up is negligible or negative for all stations which is expected as $0.6 < NH/U < 1.2$ (N is the height average Brunt Väisälä frequency between the ground and 500 m for both radiosondes ascents). Mobbs *et al.* 2005 found that increases in Δs are correlated to increases in NH/U, since the horizontal velocity perturbation can by scaled by NH/U [2].

The evolution of the temperature time series (not shown) reflects the effects of boundary layer warming due to radiative processes. The difference in potential temperature between station 24 and the stations downstream is positive and the difference between the downstream stations is negative, although very small, for the pairs 6–3 and 8–4 and is negligible between stations 5 and 2. These differences remain relatively uniform for the whole day, which is also an indication of low variability.

[2] Assuming that the topography is a streamline, the vertical velocity perturbation can be scaled by: $w' \sim U\frac{DH}{Dx} \sim UH/L$, and $\frac{\partial w}{\partial z} \sim NH/L$. It is assumed that the vertical scale of the forced motion is equal to the vertical wavenumber of two dimensional hydrostatic mountain wave, N/U, and that the hill's height is H and its with is L. The continuity equation implies that $\frac{\partial u'}{\partial x} \sim NH/L$, so $|u'|/U \sim NH/U$. (u' is the horizontal velocity perturbation)

In summary, the flow is northerly and has very low variability remaining relatively uniform for the whole day. Pressure and temperature differences between the stations downstream are negligible as well as the pressure differences between station 24 and the stations at MPA.

Another sign of the low variability is the low energy of the pressure spectrum and the small gust factors.

7^{th} of August 2001

Throughout this day, the temperature difference between the 2 m air temperature and the sea surface temperature (SST) in the ECMWF's ERA 40 analysis is positive. In contrast, the temperature difference between station 24 and the weekly averaged SST at $0000Z$ ($T = 219.0$ days) is -2 K and decreases to -0.5 K at $0300Z$ ($T = 219.125$ days). It, then, remains reasonably constant until after sunrise when boundary layer heating also plays a role in turning it positive (air temperature greater than the SST). Note that August is a winter month and that the air temperature is usually lower than the sea surface for the whole day. So it is reasonable to assume of that there is advection of warm air from north of the Falklands. Boundary layer processes would, then, lead to the formation of a temperature inversion near the surface. In fact, a temperature inversion with a temperature increase of 3.6^o C is observed between 389 m to 701 m in the $1110Z$ ($T = 219.47$ days) radiosonde (figure 5.17a – black line). This is reflected in the high Brunt Väisälä frequency in its vicinity. At the base of the inversion $N = 0.0174$ Hz and reaches a maximum of 0.0178 Hz at 411 m. At the top of the inversion it has been reduced to 0.0125 Hz and reaches a minimum at 1420 m ($N = 0.0048$ Hz).

Although the evidence ($T_{air} - SST > 0$ and top of the radiosonde's inversion is above Mt Wickham's summit) points to the formation of a temperature inversion in the upstream temperature profile the Met Office forecast in unable to produce one, since such inversion is absent from its profile (figure 5.17a – blue line). Figure (5.17b) shows a northerly wind direction near the ground which backs with height up to 640 m to then veer with height.

The balloon ascent rate deduced from the ascent at MPA, shows a 3 ms^{-1} fluctuation between 1000 m and 2000 m, and 1.3 ms^{-1} oscillations in the lowest 1000 m, which is

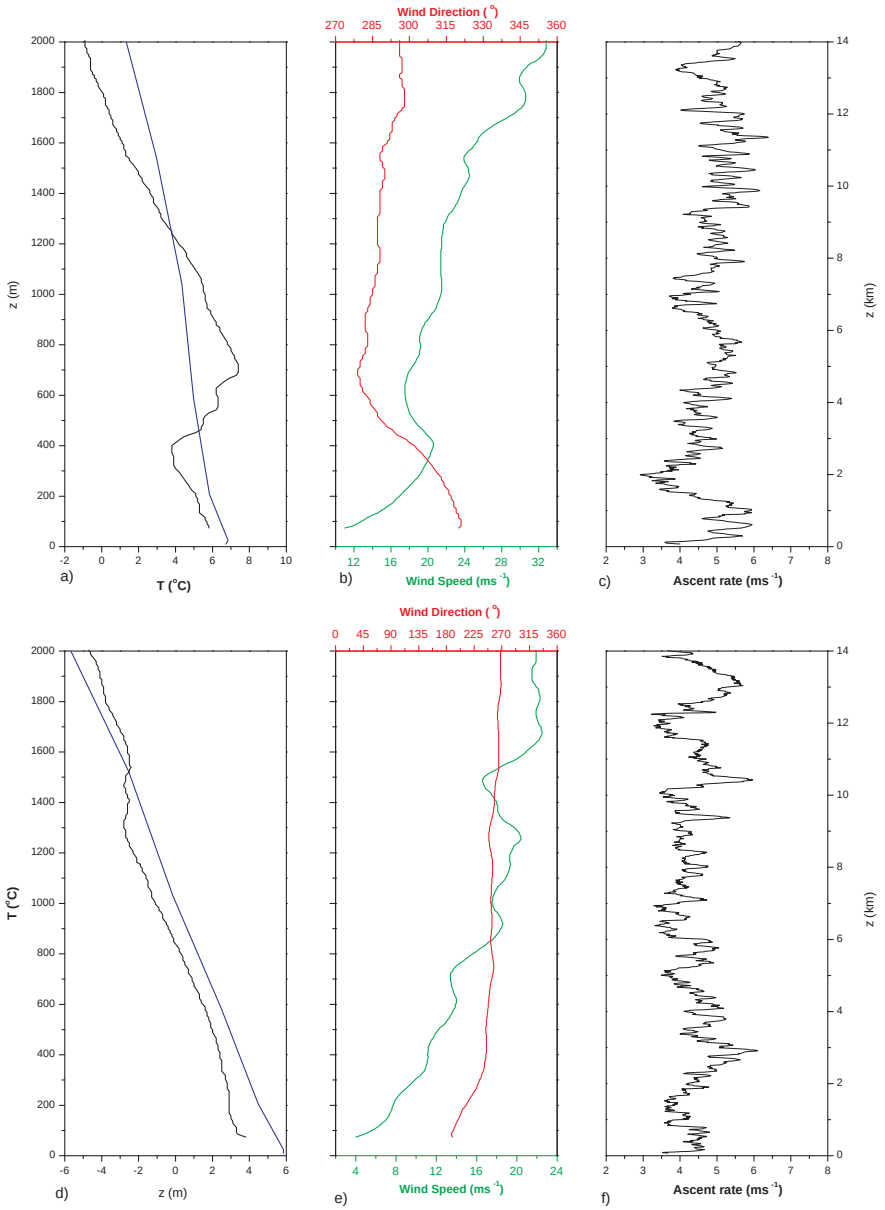

Figure 5.17: MPA radiosonde measurements at $1110Z$ ($T = 219.47$ days) of (a)temperature (black line), (b) wind speed and direction, (c) ascent rate and measured at $2305Z$ ($T = 219.96$ days) of (d) temperature (black line), (e) wind speed and direction, (f) ascent rate for the 7^{th} of August 2001. Met Office temperature forecast for (a) $1200Z$ ($T = 219.5$ days) on the 7^{th} of August and (d) $0000Z$ ($T = 220.0$ days) on the 8^{th} of August (blue line).

indicative of the occurrence of gravity waves (figure 5.17c).

By $2305Z$ ($T = 219.96$ days), the temperature inversion near the surface has disap-

peared, there is just a small inversion at 1300 m (figure 5.17d – black line). As before, there is no inversion in the Met Office forecast (figure 5.17d – blue line). In the radiosonde, the wind has become southerly near the ground veering with height, becoming westerly and the ascent rate just shows small oscillations (figure 5.17 e and f). There is less evidence of gravity waves.

The behaviour of the 2 m wind measured at site 24 (figure 5.18g) can be broken up into three subdivisions in which three different flow types can be observed. In the first, from $T = 219.0$ to $T = 219.1$ days, the wind is northerly and has a low wind speed. It then, turns to north–westerly and remains so up to $T = 219.6$ days (second section). The wind speed during this stage is greater than 8 ms^{-1}. In the final phase (between $T = 219.6$ and $T = 220$ days) the flow becomes westerly.

For the first period, $NH/U > 1.35$ (N is the height average Brunt Väisälä frequency between the ground and 500 m at $2305Z$ on the 6^{th} of August ($T = 218.95$ days) – $N = 0.02$ Hz – and H is the height of Mt. Wickham). Since the horizontal velocity perturbation can by scaled by NH/U a strong wind is expected downstream. This is confirmed by the speed–up (figure 5.19a, b, c and d) which exhibits high values — the wind speed is more than 100% higher than the speed at site 24.

During the second section, $0.6 < NH/U < 1.6$ where U is $8 < U < 16$ ms^{-1} and $0.013 < N < 0.02$ Hz ($N = 0.02$ Hz at $2300Z$ on the 6^{th} ($T = 218.95$ days) and $N = 0.013$ Hz at $1110Z$ on the 7^{th} ($T = 219.47$ days)). As expected, the speed–up is low and in some instances negative.

In the last stage, this kind of scaling is no longer valid — the wind at 24 cannot be considered as a reference any longer.

The gust factors for stations 3, 4, 6 and 8, (figure 5.19e, f, g and h) apart from a few isolated moments, do not deviate greatly from their average value $0.9 < G/G_{ave} < 1.1$. This is also an indication of the low turbulence observed during this day.

A typical example of the flow direction is presented in figure (5.20). The flow in the first and second phase is consistently northerly for all stations. The flow vectors show acceleration downstream of the mountains in the first period and some of the stations show deceleration in the second period. In the third period there is negligible flow over the ridges and the flow's behaviour on each side is different.

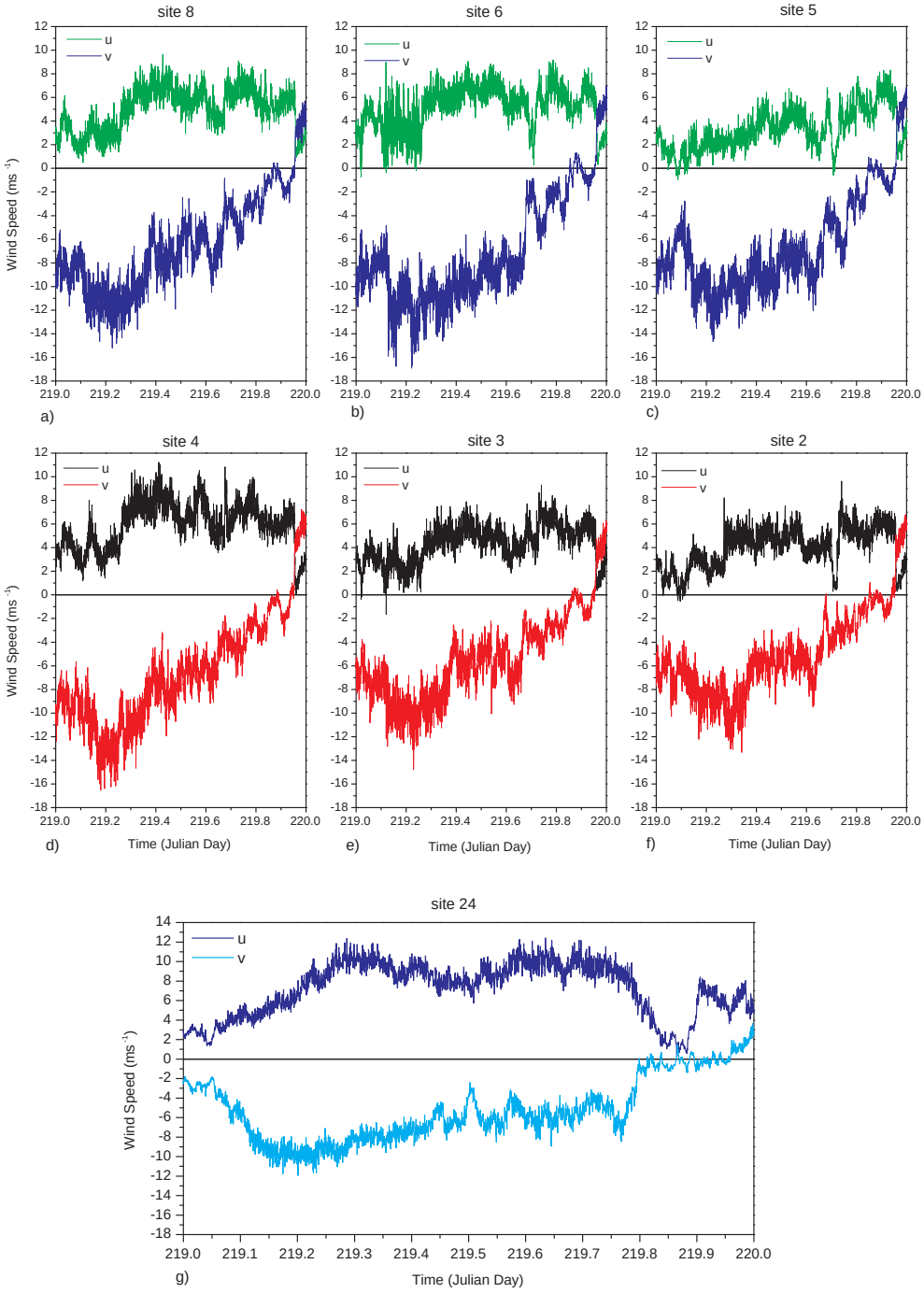

Figure 5.18: 30s wind for stations (a)8, (b)6, (c)5, (d)4, (e)3, (f)2 and (g)24 for the 7^{th} of August 2001.

The temporal or spatial variability of the wind across MPA is very small (figure 5.21).

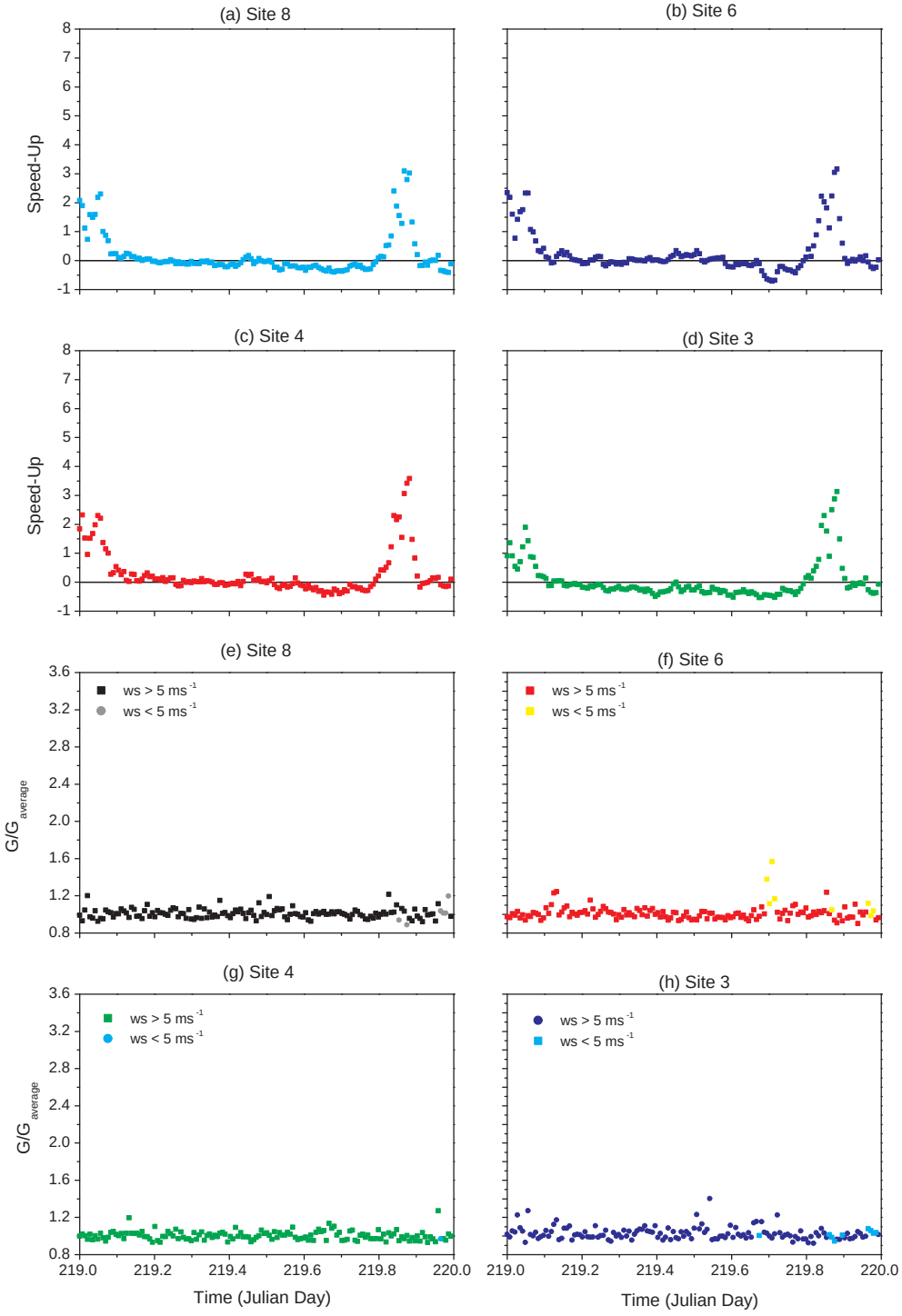

Figure 5.19: Speed–up for stations (a)8, (b)6, (c)4 and (d)3 and gust factors for stations (e)8, (f)6, (g)4 and (h)3 for the 7^{th} of August 2001.

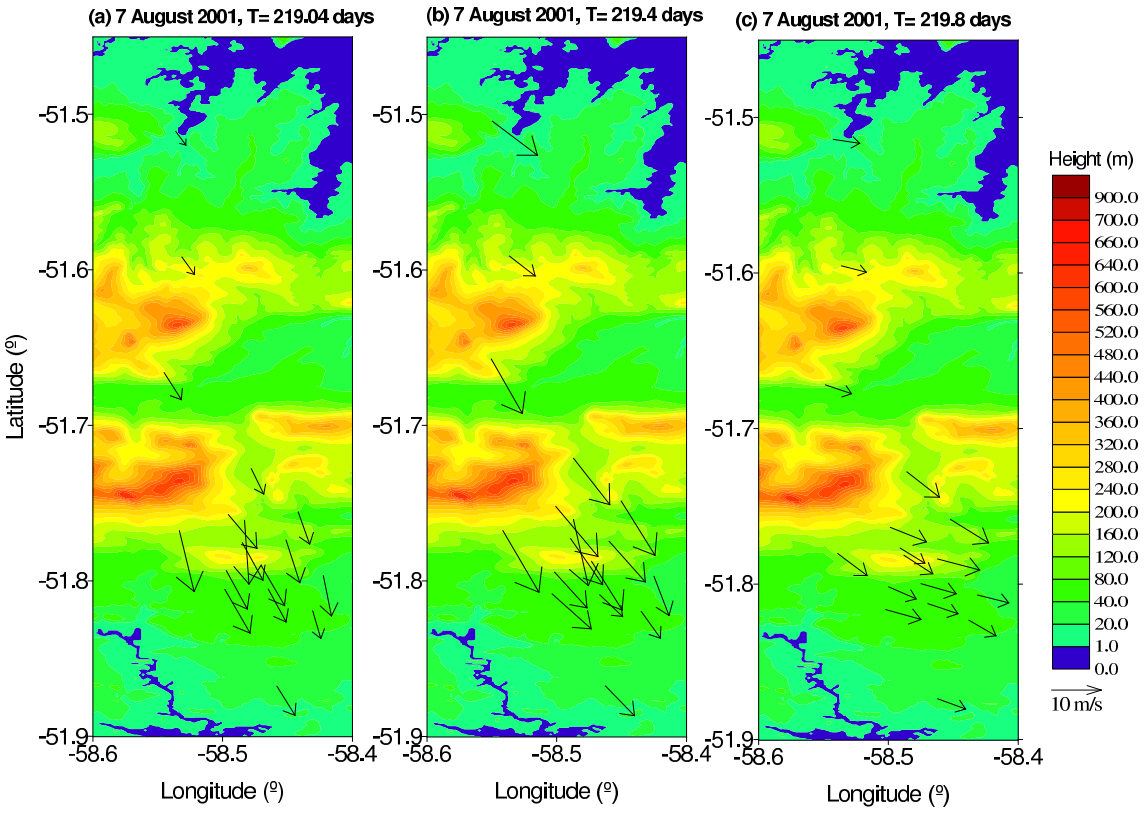

Figure 5.20: The 10 minute average wind field measured at the AWS sites for the 7^{th} of August 2001

The 10 min standard deviation (figure 5.21) oscillates between 1.6 and 0.6 ms^{-1}, which is similar to the 10 min standard deviation for the 17^{th} of May 2001. Only site 6 shows a higher standard deviation between $T = 219.1$ and $T = 219.2$ days when the wind speed is low.

The horizontal standard deviation is between 1 and 3 ms^{-1} and there is a reduction of the standard deviation after $T = 219.8$ days when the wind becomes westerly. Like the previous parameter, this standard deviation does not show any relevant periods either and is not very high.

The ratio between the inversion height (z_i) and the height of Mt. Wickham (H) is $H/z_i = 1.65$ and the Froude number [3] for 1110Z ($T = 219.47$ days) is equal to one.

[3]The Froude number is defined in the usual way for a two–layer shallow water flow: $F = \frac{\overline{U}}{\sqrt{g' z_i}}$, where $g' = g\Delta\theta/\theta_0$ is the reduced gravity acceleration, $\Delta\theta$ is the magnitude of the potential temperature difference across the inversion, θ_0 is a reference potential temperature and the reference wind speed is taken as a two hour average centred on the radiosonde launch of the wind measured

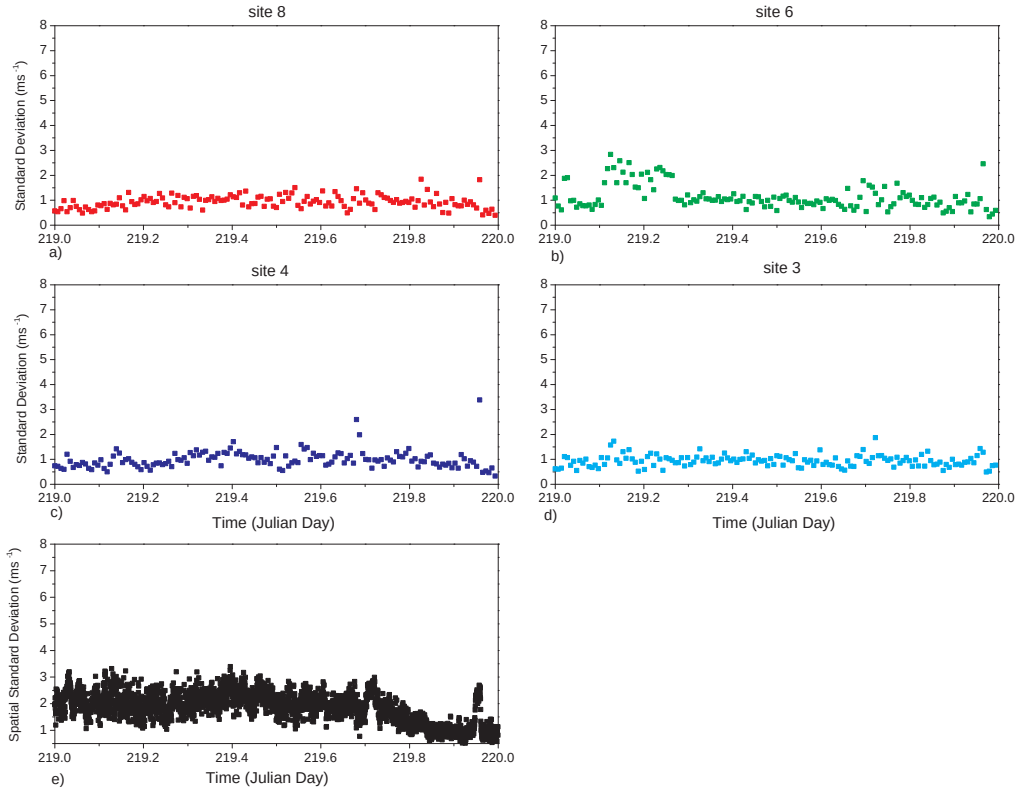

Figure 5.21: 10 min standard deviation for stations (a)8, (b)6, (c)4, (d)3 and (e)horizontal standard deviation for the 7^{th} of August 2001

Although Vosper's (2004) flow

regime diagrams do not extend beyond $H/z_i = 1$ it is easily inferred that the probability of the occurrence of lee waves on the inversion is minute.

The pressure difference between the pressure measured at site 24 and the downstream stations (figure 5.22) is mostly less than 2 hPa with several small oscillations but with no striking periods before $T = 219.7$ days. After $T = 219.7$ days the wind is westerly and there is not a correlation between the flow on the two sides of the ridges any longer. Note that microbarograph at station 3 has a small temporal drift, hence the pressure difference lines do not overlap.

The 2 h spectrum of the pressure signal is illustrated in figure (5.23). The pressure spectrum for the stations at MPA shows two relevant frequencies corresponding to periods of 32 and 16 minutes. The spectrum of station 6 deviates from the others for periods

at station 24

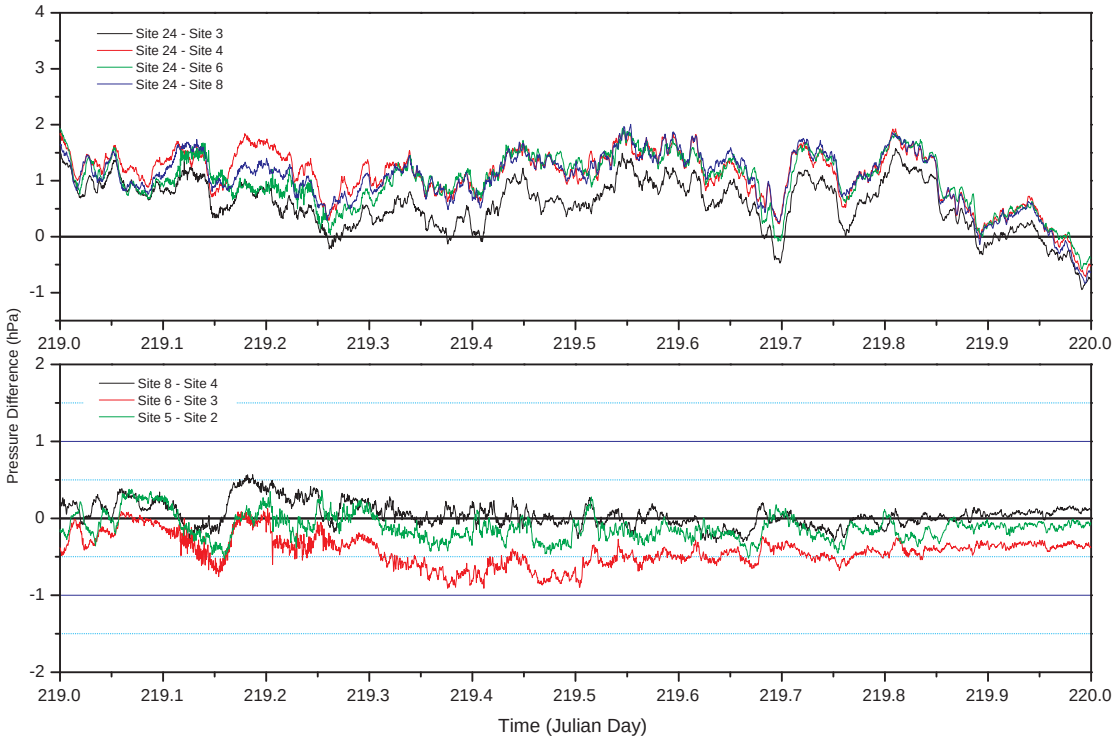

Figure 5.22: The 30s pressure difference between (a) site 24 and 4 stations at MPA and (b) the opposite stations at MPA for the 7^{th} of August 2001

shorter than 4 minutes. The spectrum for station 24 also has a small amplitude and reveals three relevant frequencies which are distinct from the ones at the stations downstream. Upstream, the relevant periods are: 43, 18 and 11 minutes. The longer periods are likely related to the gravity wave.

The difference in potential temperature between station 24 and the downstream stations shows the same three separate periods (figure 5.24). The first ends at $T = 219.2$ days and is a period where the temperature of the downstream stations is significantly higher than at 24 which might be due to the transport of air with higher potential temperature from aloft related to the gravity wave. The second period extends from $T = 219.2$ to $T = 219.56$ days where there is no significant difference between the stations, and in the third period there is warming at MPA. Since the flow in the third period is along the ridges the differences in potential temperature are no longer correlated. The potential temperature differences between stations at MPA are likely due to local cloud cover.

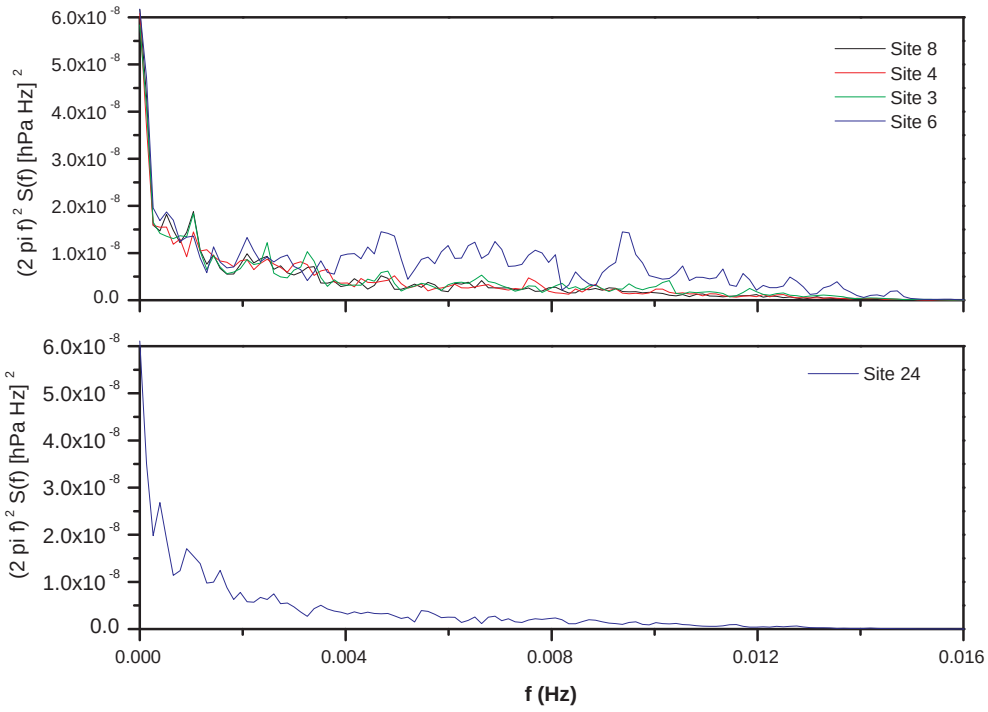

Figure 5.23: 2 h pressure spectrum for stations (a)8, 6, 4 and 3, and (b)24 on the 7^{th} of August.

In summary, for the initial stages of the first period the flow is accelerated downstream and falls into category (*i*). During the second phase the flow has very low variability falling into category (*iii*). Since in the third phase the wind is westerly, this classification no longer applies. The low variability is also confirmed by the Froude number in conjunction with the ratio of the inversion height and the height of Mt. Wickham, i.e., in this parameter space only propagating gravity waves are allowed. The pressure spectrum exhibits two frequencies which are probably related to the gravity wave.

As in the previous case, during the second phase the standard deviations, the speed–up and the gust factors have low values. The pressure and temperature differences are also small.

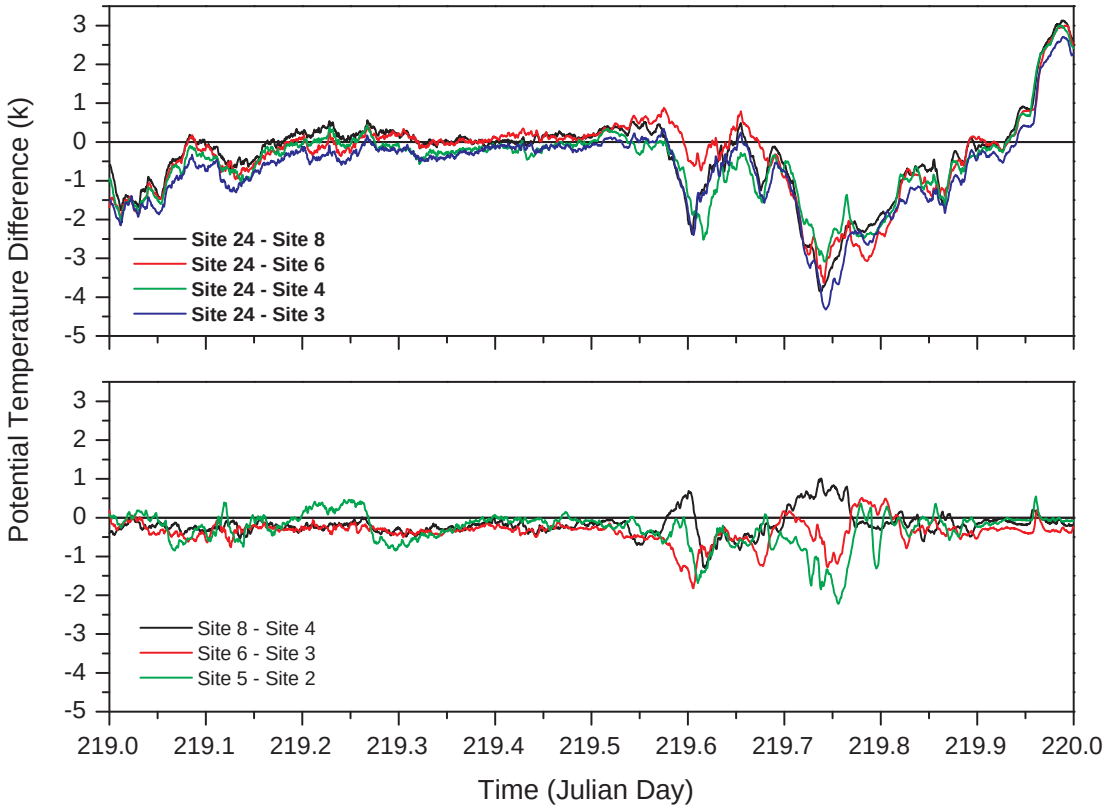

Figure 5.24: The 30s potential temperature difference between (a) site 24 and 4 stations at MPA and (b) the opposite stations at MPA for the 7^{th} of August 2001

5.2.2 Strong Downwind Acceleration

The next cases fall into category (*i*) or category (*ii*). All cases show evidence of the presence of gravity waves, the vertical temperature profile exhibit a temperature inversion in the first hundred meters and the flow at MPA is accelerated in relation to the flow at station 24.

In the first case the accelerated flow is interspersed with decelerated and reversed flow. The flow at MPA displays a high degree of variability and the temperature and pressure time series show significant differences between neighbouring stations. Rotors are said to be observed during this day.

In the second case, reversed decelerated flow is observed at the beginning and end of the phenomenon. In between these two moments the flow is accelerated at MPA and has low variability. There is the possibility of a travelling hydraulic jump at the beginning of the event.

In the third case the flow is accelerated downstream and has low variability. Although the flow acceleration downstream is not particularly very high there are some periods when the speed– up is greater than 1.75, which puts this flow into category (i).

In the last case a decrease in the pressure differences between the upwind station and the stations at MPA is followed by a rapid increase, possibly indicating a hydraulic jump. The stations downstream also show considerable differences in pressure during the same period. The flow is considerably accelerated downstream and there are some periods with high variability. It can be classified as being in category (i) or (ii) depending on the specific period.

9^{th} of February 2001

Except for a short one hour period after $0100Z$ on the 8^{th} of February ($T = 39.042$ days), the wind speed at site 24 is below 2 ms^{-1} from $0000Z$ to $1010Z$ ($T = 39.424$ days). For this period, the wind direction at the station oscillates wildly with no preferred direction.

In the ECMWF ERA 40 analysis the temperature difference between the air temperature and the sea surface temperature (SST) is -0.211 K for $0000Z$ and 2.33 K for $1200Z$ ($T = 39.5$ days), which indicates a presence of warm air North of the Falklands. The temperature difference between the temperature measured at 2 m and the weekly averaged sea surface temperature remains negative until the wind becomes northerly, i.e. after $1010Z$ ($T = 39.424$ days). By $1100Z$ ($T = 39.458$ days) the 2 m air temperature is 1.77 K greater than the SST, suggesting that the advection of warmer air plays a role in the warming of the boundary layer.

The radiosonde profile for $1123Z$ on the 8^{th} of February ($T = 39.474$ days), shows a temperature inversion with an amplitude of 3.1^o C between 246 m and 436 m, which represents a gradient of 0.0163 Km^{-1} (figure 5.25a – black line). This inversion is also present in the Met Office forecast profile albeit its amplitude is considerably smaller – 0.25^o C. The model's atmosphere above the inversion is also warmer than the observed (figure 5.25a – blue line). The wind at MPA is, as in the other cases, northerly and backs with height. The ascent rate of the radiosonde has oscillations of 1 ms^{-1} in the lowest 2000 m and above this height, small fluctuations of 0.5 ms^{-1} are superimposed on a 1.5 ms^{-1} undulation between 2000 m and 12000 m.

At $2316Z$ ($T = 39.969$ days) the inversion becomes lower and increases in strength. The

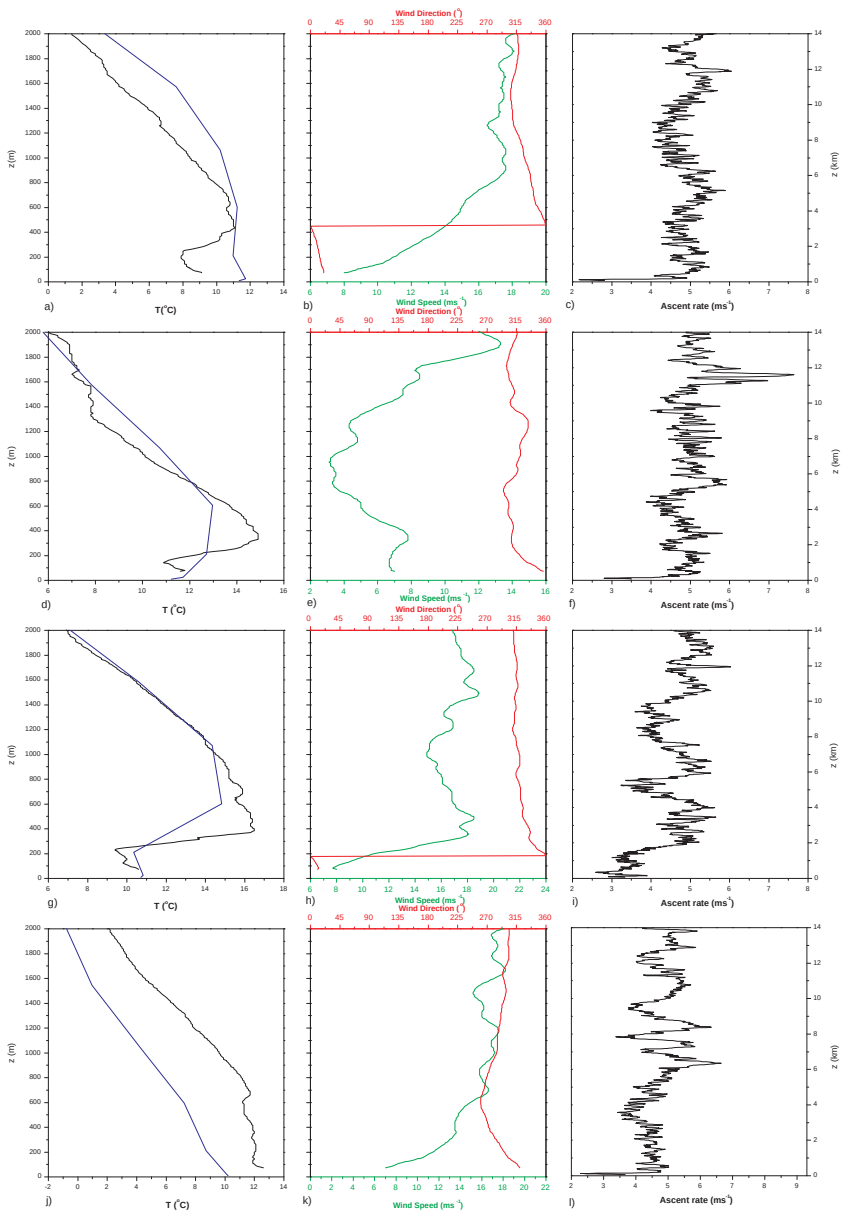

Figure 5.25: MPA radiosonde measurements at: $1123Z$ ($T = 39.474$ days) (a) temperature (black line), (b) wind speed and direction, (c) ascent rate; at $2316Z$ ($T = 39.969$ days) (d) temperature (black line), (e) wind speed and direction, (f) ascent rate for the 8^{th} of February and at $1126Z$ ($T = 40.48$ days) (g) temperature (black line), (h) wind speed and direction, (i) ascent rate; at $2306Z$ ($T = 40.96$ days) (j) temperature (black line), (k) wind speed and direction, (l) ascent rate for the 9^{th} of February. Met Office forecast profile for: (a)$1200Z$ ($T = 39.5$ days) on the 8^{th} of February, (d) $0000Z$ ($T = 40.0$ days), (g) $1200Z$ ($T = 40.5$ days) on the 9^{th} of February and (j) $0000Z$ ($T = 41.0$ days) on the 10^{th} of February – blue line.

temperature increases by about 3.9 K from 145 m to 330 m, i.e, a 0.012 Km^{-1} gradient. The wind direction remains northerly and the ascent rate has peak–to–peak fluctuations of 1.5 ms^{-1}. The depth average Brunt Väisälä based on the difference in potential temperature between 500 m and the ground shows evidence of these rapid increases in temperature. Its values are 0.022 s^{-1} and 0.023 s^{-1} respectively. In the forecast (figure 5.25d – blue line), the inversion starts in the lowest levels and ends at 600 m and the atmosphere above the inversion is still warmer.

By $1126Z$ of the 9^{th} ($T = 40.48$ days), the wind direction remains northerly and the ascent rate shows evidence of gravity waves by exhibiting oscillations with peak–to–peak amplitudes around $2 - 3$ ms^{-1} (figure 5.25h and i). Now, the intensity of the inversion is even bigger, it is approximately 7.1 K with a gradient of 0.0449 Km^{-1}. The Brunt Väisälä frequency reaches a maximum at around 271 m (just above bottom of the inversion), decreasing sharply up to 521 m and continues to decrease from there upwards, up to 2750 m. The Met Office forecast for $1200Z$ ($T = 40.5$ days) shows an inversion between 200 and 600 m with an amplitude of 4.5^o C which is a reasonable upstream profile. The layer between 600 and 1000 m is colder than the observed and it is feasible that the end of the upstream inversion occurs in this layer which is not forecasted due to the low resolution. Now, the forecast is able to determine the temperature profile for the layers above 1000 m.

At $2306Z$ ($T = 40.96$ days) the inversion is replaced by a stable layer. The wind remains northerly and backs with height up to a height around 600 m, by then its direction is westerly. From this height upwards, it veers and becomes northerly once again. The temperature profile in the Met Office is about 2^o C colder.

The pressure difference between site 24 and the sites at MPA is about 1 hPa from $T = 40.0$ to $T = 40.2$ days (figure 5.26). It then increases up to 3 hPa and has two episodes ($T = 40.6$ and $T = 40.8$ days) when the difference is around zero (stations 4 and 8) or slightly negative (stations 3 and 6).

The pressure difference between the stations at MPA does not have a uniform behaviour between the three pairs of stations. This difference between sites 8 and 4 has very sharp oscillations between -1 hPa and 1 hPa and episodes when the pressure at 8 is lower than -1 hPa in relation to the pressure at site 4 which is reversed a few minutes later. These oscillations are not visible in the pairs $3-6$ and $2-5$, but the first pair's behaviour

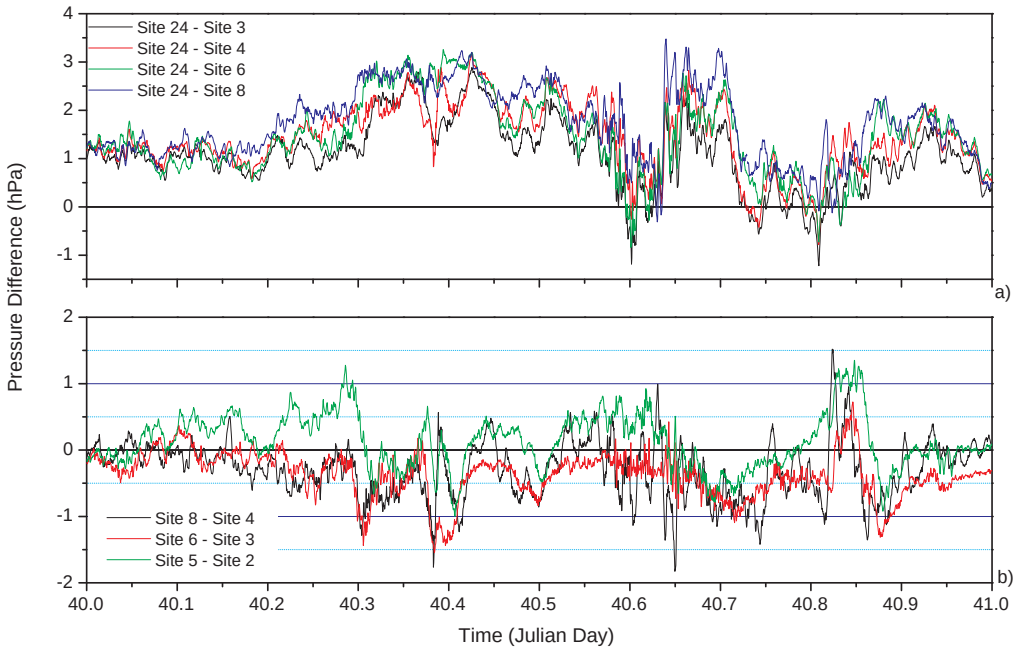

Figure 5.26: The 30s pressure difference between (a) site 24 and 4 stations at MPA and (b) stations 8 and 4, 6 and 3, 5 and 2 (opposing stations at MPA) for the 9^{th} of February 2001.

looks like a smoothed version of the difference between 8 and 4. The behaviour of the second pair is distinct from the others. All this implies high spatial variability across MPA.

The 2 h pressure spectrum for station 24 has significantly higher energy than the one observed for a decelerated flow. It has a maximum for $f = 0.00117$ Hz, which corresponds to a 14 min. period; a 12 min. and a 4 min. period also show significant energy (figure 5.27b).

The downstream stations (stations 3, 4, 6 and 8) have different spectra even for low frequencies. In the first three stations the frequency corresponding to a two hour period has significant energy. The next considerable frequency for site 4 is related to a 18 min period, while for stations 6 and 8 the relevant period is 25.6 min. Between these frequencies and $f = 0.005$ Hz all stations have other significant periods (figure 5.27a).

The spectra density plots (figure 5.28) shows that the high energy for station 24 occurs for $T = 40.65$ days which encompasses the first period when the difference in pressure between this site and the downstream stations is at a minimum and the period when station 8 and 4 oscillates significantly.

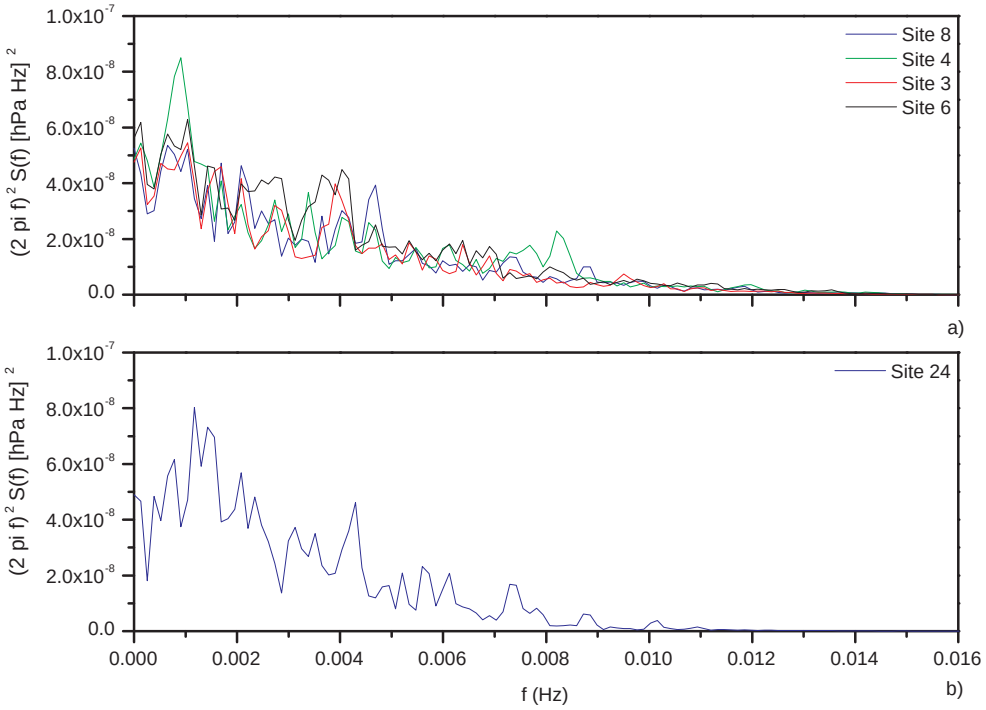

Figure 5.27: 2h spectrum for stations (a)8, 6, 4 and 3, and (b)24 for the 9^{th} of February 2001.

The spectra for all downstream stations shows two relevant periods. The first occurs for $T = 40.375$ days where the highest energy occurs for periods of 8, 6 and 4 minutes. Station 6 is the one which has the highest energy. The second period occurs between $T = 40.75$ and $T = 40.875$ days. For the first part of this period, stations 6 and 3 have a maxima at 12 min and 4 min. The maximum at station 8 is for a period of 21 min while for station 4 it is located at 16 min. In the second part all stations exhibit a maximum at 21 min.

The high energy in the larger frequencies indicates strong turbulence and only occurs in cases where the pressure differences are highly variable, indicating the possible presence of rotors. The different relevant frequencies amongst the stations at MPA are an indication that the flow is highly anisotropic. Note that the energy in the higher frequencies is about four times greater than the energy of turbulence observed in decelerated flows and flows where no rotors are detected. In the lower frequencies it might be an indication of trapped waves.

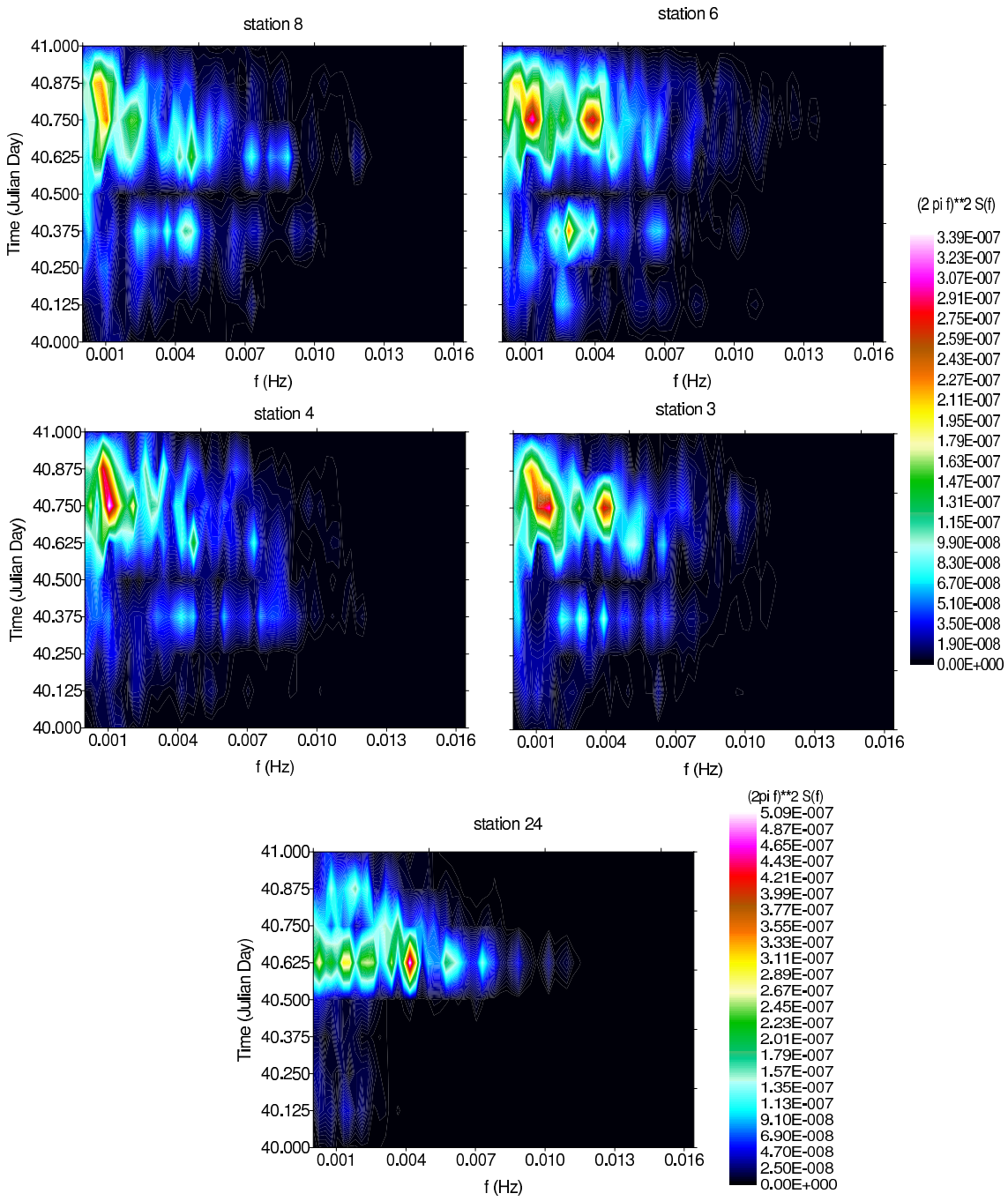

Figure 5.28: Spectrum density for stations 8, 6, 4, 3 and 24 for the 9^{th} of February 2001.

Figure (5.29g) shows the wind at site 24. Its direction remains northerly for the whole of the 9^{th} of February. The wind speed at MPA from $T = 40.2$ days onwards has episodes of weak and reversed flow interspersed in intervals of strong flow with speeds greater than 10 ms^{-1}. These periods of reversed flow are concurrent with the instants of increased pressure difference between the downstream stations. The two occasions when the pressure differ-

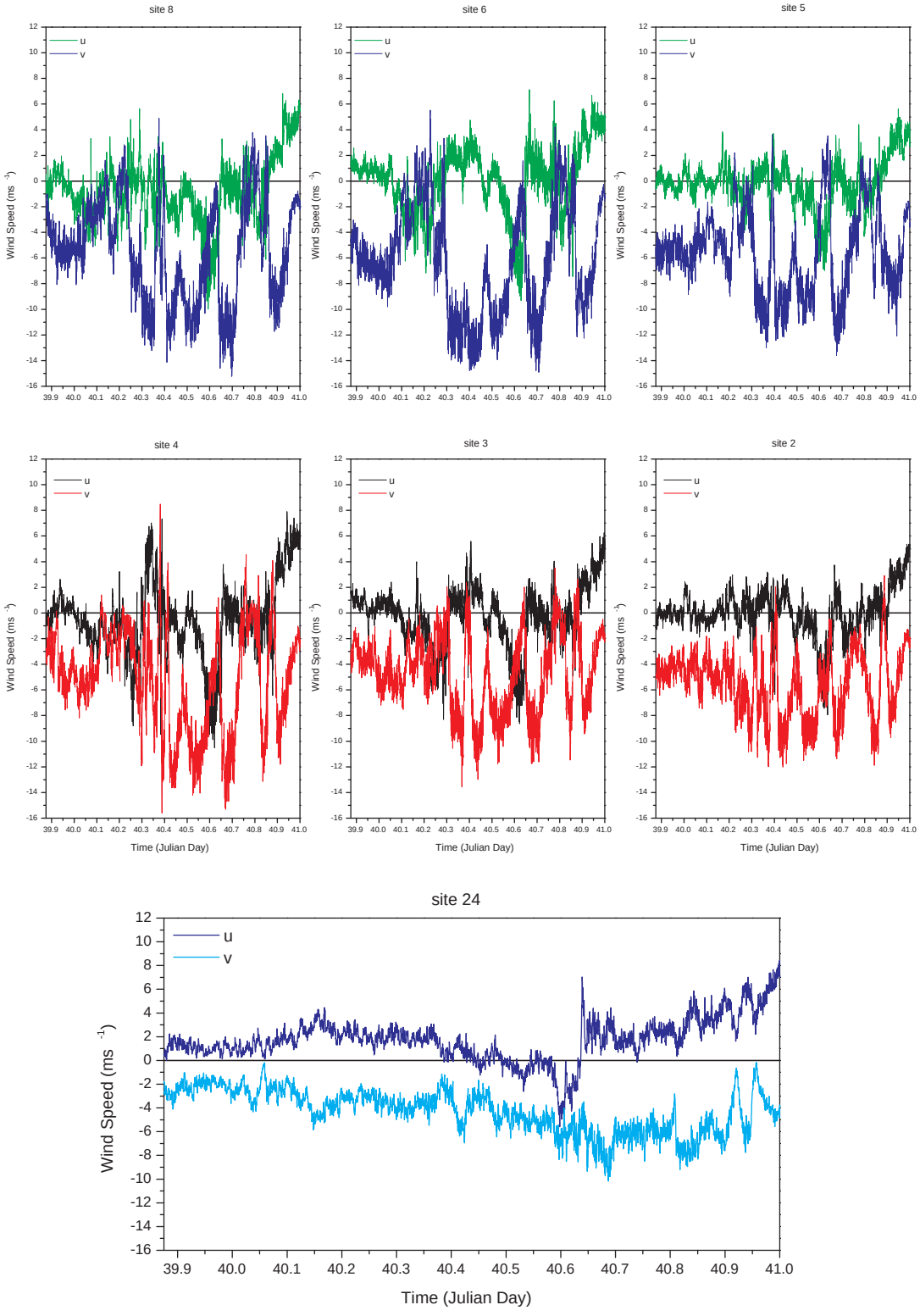

Figure 5.29: 30s wind for stations (a)8, (b)6, (c)5, (d)4, (e)3, (f)2 and (g)24 for the 9^{th} of February 2001.

ence between site 24 and the sites at MPA is very low is also related with the reversed flow. The disturbances take different times to travel downstream between the stations. For $T = 40.375$ days it takes 7.2 min for it to travel the 1535 m between stations 4 and 8, this implies a phase speed of 3.55 ms^{-1}. For $T = 40.394$ days the previous stations are 28.8 min. out of phase, this is reduced to 15 min at $T = 40.627$ days and by $T = 40.856$ days the disturbance takes 32 min. to travel between the stations. Stations 6 and 3 are circa 25 to 34 min out of phase. These long periods which are also found in the pressure spectrum are related to a lee wave which changes wavelength throughout the day. Although, for $T = 40.48$ days the ratio of the height of Mt. Wickham to the inversion height is $H/z_i = 2.69$, which is well above unity and hence not examined in Vosper (2004), the Froude number, $F = 0.48$, is probably low enough to be below the critical value whereof lee waves occur on the inversion.

The strong flow downstream is always greater than the flow upstream which is emphasized by the speed–up (figure 5.30). The strong speed–up is to be expected since $0.96 < NH/U < 8.96$.

In the periods of strong flow, the speed–up can be in excess of 2, i.e, the flow is accelerated more than 200% in relation to the upstream wind speed. On the other hand, when the flow is reversed it suffers a deceleration (the speed–up is negative).The main features of the flow are analogous in all stations, but there are important differences in–between stations. This is highlighted by the spatial standard deviation and 10 minute standard deviation (figure 5.31).

Figure (5.31e) reveals three periods where the standard deviation is always greater than two, which reveals a high spatial variability across MPA. More importantly, the three peaks coincide with the period of reversed or stagnant flow. When the flow is strong, the standard deviation is around two, which is the same as the standard deviation for undisturbed flow.

The 10 minute standard deviation illustrates the different behaviour between the stations. The plots (figure 5.31a, b, c and d) expose two periods ($T = 40.3$–40.4 and $T = 40.8$ days) where the wind speeds at each station deviate notably from the 10 minute average that encompasses all stations. The standard deviations at the second peak ($T = 40.6$ days) are not so high as in the other two intervals.

In the gap between the reversed flow, the wind speed at stations 8 and 6 deviates more from the average than the speed at 4 and 3. These stations also have a greater divergence

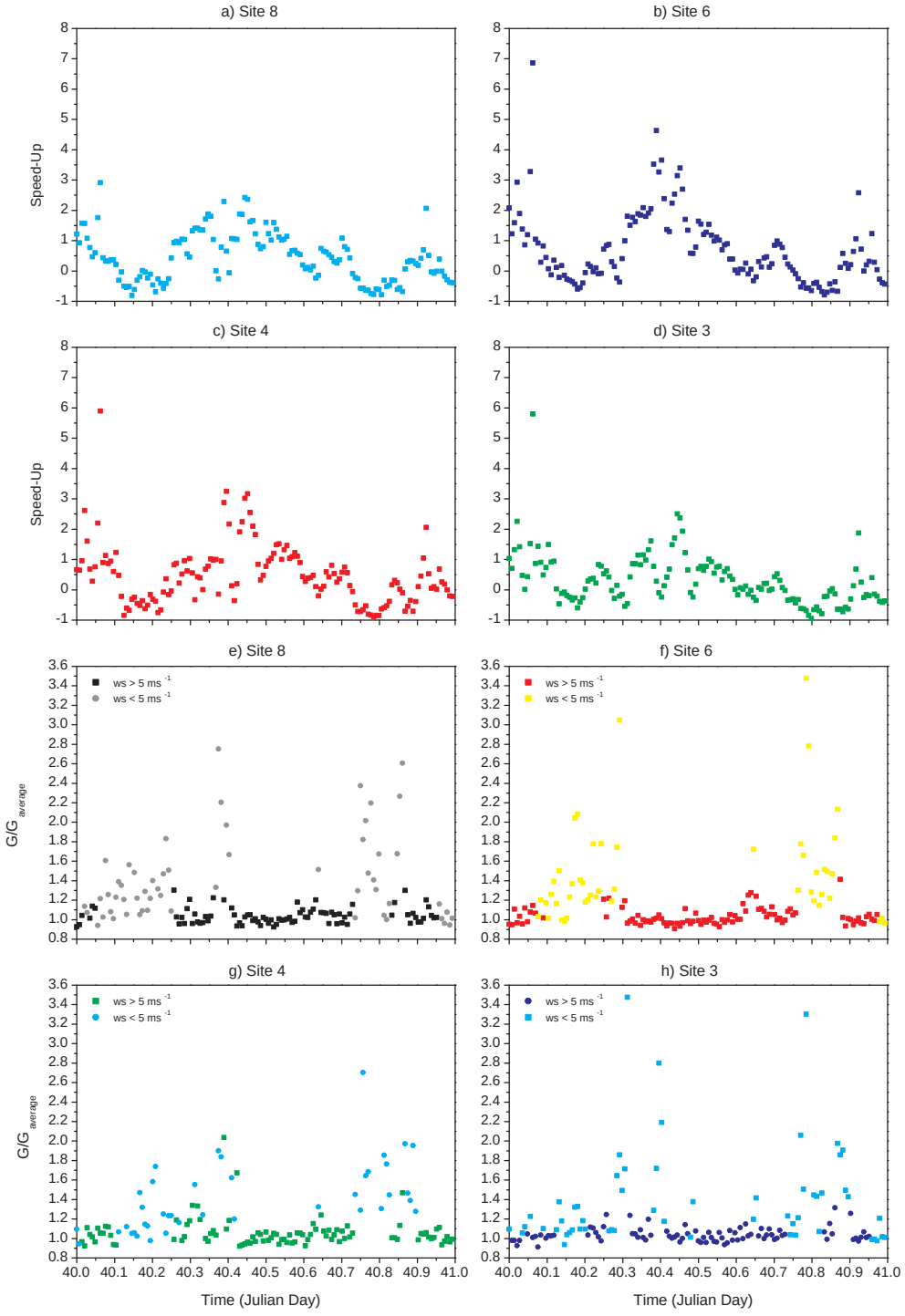

Figure 5.30: Speed–up for stations (a) 8, (b) 6, (c) 4 and (d) 3 and gust factors for stations (e)8, (e)6, (g) 4 and (h) 3 for the 9^{th} of February 2001.

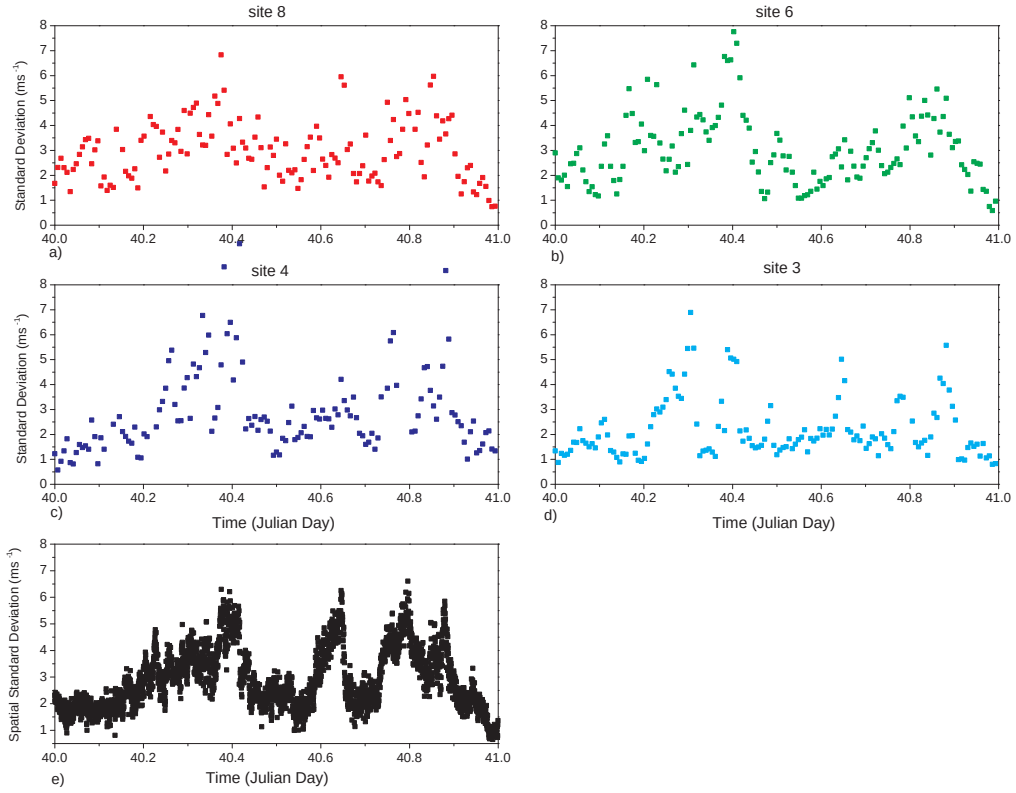

Figure 5.31: 10 min standard deviation for stations (a) 8, (b) 6, (c) 4, (d) 3 and (e) spatial standard deviation for the 9^{th} of February 2001.

from the average at the beginning of the event.

The high flow variability is emphasised by the gust factors (figure 5.30e, f, g and h). During the periods when the flow is reversed or very low, the gusts are more than 20% above the average. For $T = 40.8$ days, all the stations have gusts which are more than twice the average. The same happens for stations 3 and 8 at $T = 40.4$. $T = 40.3$ days also has relevant gusts in stations 3, 4 and 6. For the duration of strong flow the gusts are not above average. It should be emphasised that the wind at site 24 is not negligible.

The temporal and spatial variability is patent in the wind vector plots (figure 5.32). The wind field upstream (at station 24) is relatively week but is always northerly. Downstream the high variability is clearly visible. While for $T = 40.7$ days the wind at MPA is clearly accelerated and relatively uniform for all stations. For $T = 40.23$ days, the flow immediately to the north of the air field is northerly, whereas in stations 8, 6 and 5 the flow is southerly and in stations 4, 3 and 2 the flow is northerly again. At $T = 40.82$

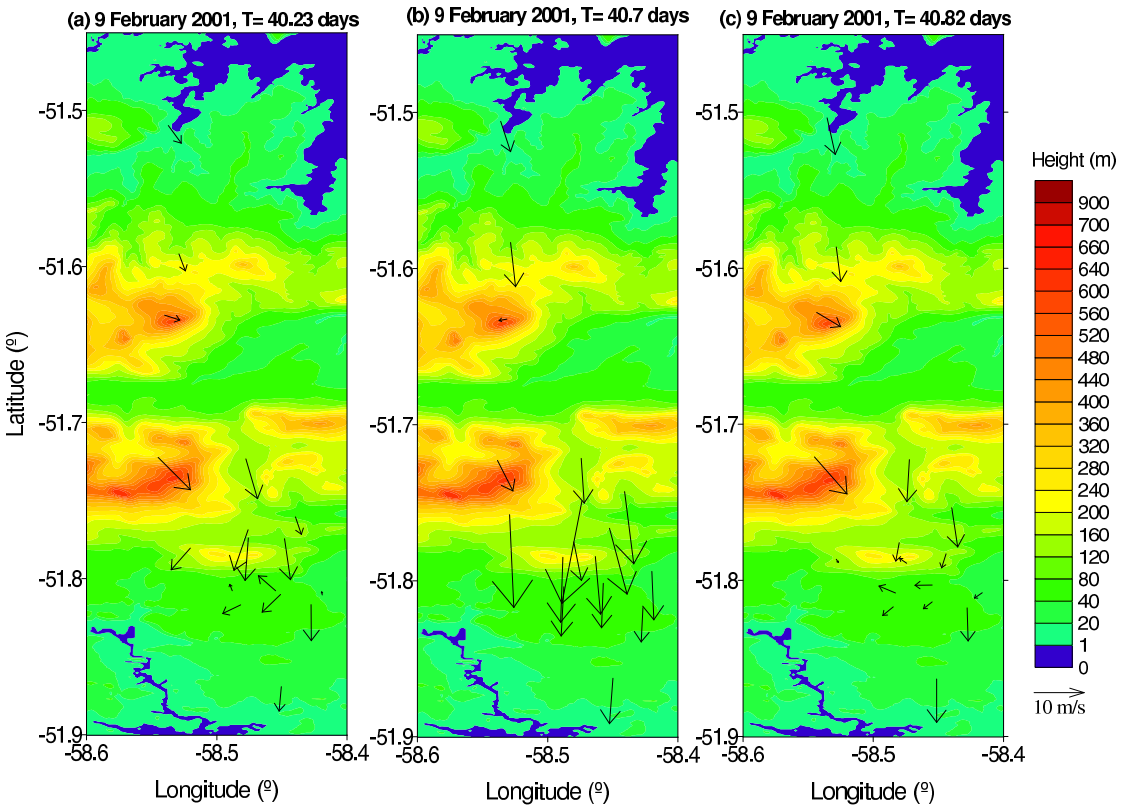

Figure 5.32: The 10 minute average wind field measured at the AWS sites for the (a) beginning, (b) middle and (c) end of the storm for the 9^{th} of February 2001.

days, the reversed flow is observed at stations 9, 7, 6 and 5, while all the others have a northerly flow. The reversed flow implies convergence at the surface and the likelihood of flow separation at the foot of Mt. Pleasant. In fact the 10 min. vertical gradient of the vertical wind component has peaks above 0.005 s^{-1} which represents vertical wind speeds above 1 ms^{-1} at 200 m [4].

All this is consistent with the presence of rotors near the surface which also leave an imprint on the surface potential temperature (figure 5.33). The potential temperature at the surface is increased during the periods of reversed flow, i.e, the temperature difference between station 24 and the stations at MPA is significantly increased. The anisotropy of the flow is also reflected in the differences between the stations at MPA. The spike in the differences between site 4 and sites 24 and 8 is probably related to the advection of warmer air from above when the lee–wave trough touches the ground over the station. For this

[4] The 30 s wind measurements at stations 9 and 13 were used to calculate the east–west gradient in the westerly wind component and stations 12 and 8 to compute the north–south gradient in the southerly component. A 10 min. average of the sum of the two gradients was then determined

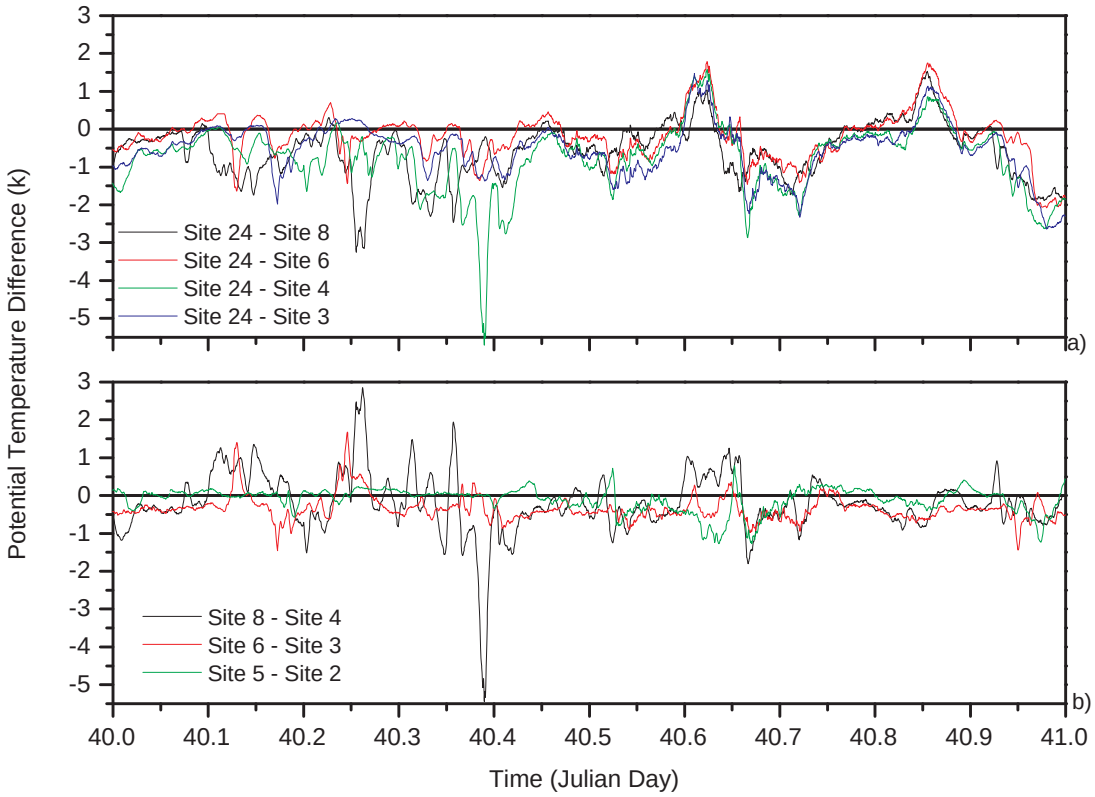

Figure 5.33: The 30s potential temperature difference between (a) site 24 and 4 stations at MPA and (b) the opposite stations at MPA for the 9^{th} of February2001.

moment station 4 also has the highest wind speed.

In summary, when the downstream flow is decelerated relatively to the upstream wind speed it has high spatial and temporal variability. During these periods, the wind component normal to the ridge is very small and, in some occasions, its sign is reversed. The horizontal convergence associated with this local wind reversal indicates that flow separation takes place and is consistent with the presence of rotors.

The rotors are also associated with high pressure and temperature differences across short distances.

20^{th} of January 2001

The vertical profiles of the temperature, wind speed, wind direction and balloon ascent rate deduced from the radiosonde launched at MPA on this day are shown in figure (5.34). At $1112Z$ ($T = 20.47$ days), the wind direction at the surface is northerly and backs with height and there is evidence of gravity–wave motion in the balloon ascent rate, where peak–to–peak amplitudes of around $2 - 3$ ms^{-1} for three oscillations between the ground and 6 km can be observed.

The radiosonde temperature profile (figure 5.34 – black line) shows an inversion with an increase of 1.5^o C from 291 to 334 m, i.e., a temperature gradient of 0.03488 Km^{-1} and above this layer there is an almost neutral layer up to 640 m, with a gradient of 0.003 Km^{-1}. The Brunt Väisälä frequency has a maximum at the base of the inversion ($N = 0.0179$ Hz), is reduced to 0.012 Hz and reaches a minimum at 1200 m.

At $2318Z$ ($T = 20.97$ days) the wind direction is north–easterly and also backs with height. The oscillations in balloon ascent rate have been reduced with peak–to–peak amplitudes around $1 - 2$ ms^{-1}. Now, the temperature profile shows two inversions; the first with a temperature difference of 1.4^o C between 121 and 357m and the second between 826 and 1002 m with an increase of 2.3^o C.

The temperature at the ECMWF ERA 40 reanalysis grid point centred at $301E$ and $-51N$ is higher than the sea surface temperature for the whole day (at $T = 20.5$ days, the air temperature is 3.5 K above the SST). The Met Office forecast for the same grid point shows a 2^o C temperature inversion at $1200Z$ ($T = 20.5$ days) which reflects the downward heat flux. The correlation between the forecast and the radiosonde is very good. At $0000Z$ on the 21^{st}, the correlation between the radiosonde and the forecast is not as good. While the radiosonde probably reflects the effects of the gravity wave, the forecast has just one inversion below 600 m with an amplitude of 2^o C.

The pressure difference between station 24 and four stations downstream figure (5.35a) begins to increase from the beginning of the day reaching a plateau of around 1 hPa that starts at $T = 20.2$ and ends at $T = 20.4$ days when it increases more markedly, reaching a maximum of 3.64 hPa at $T = 20.65$ days and starts to decrease by $T = 20.83$ days to reach a minimum at $T = 20.9$ days. The period of increased pressure difference is another signal of the possible presence of gravity waves.

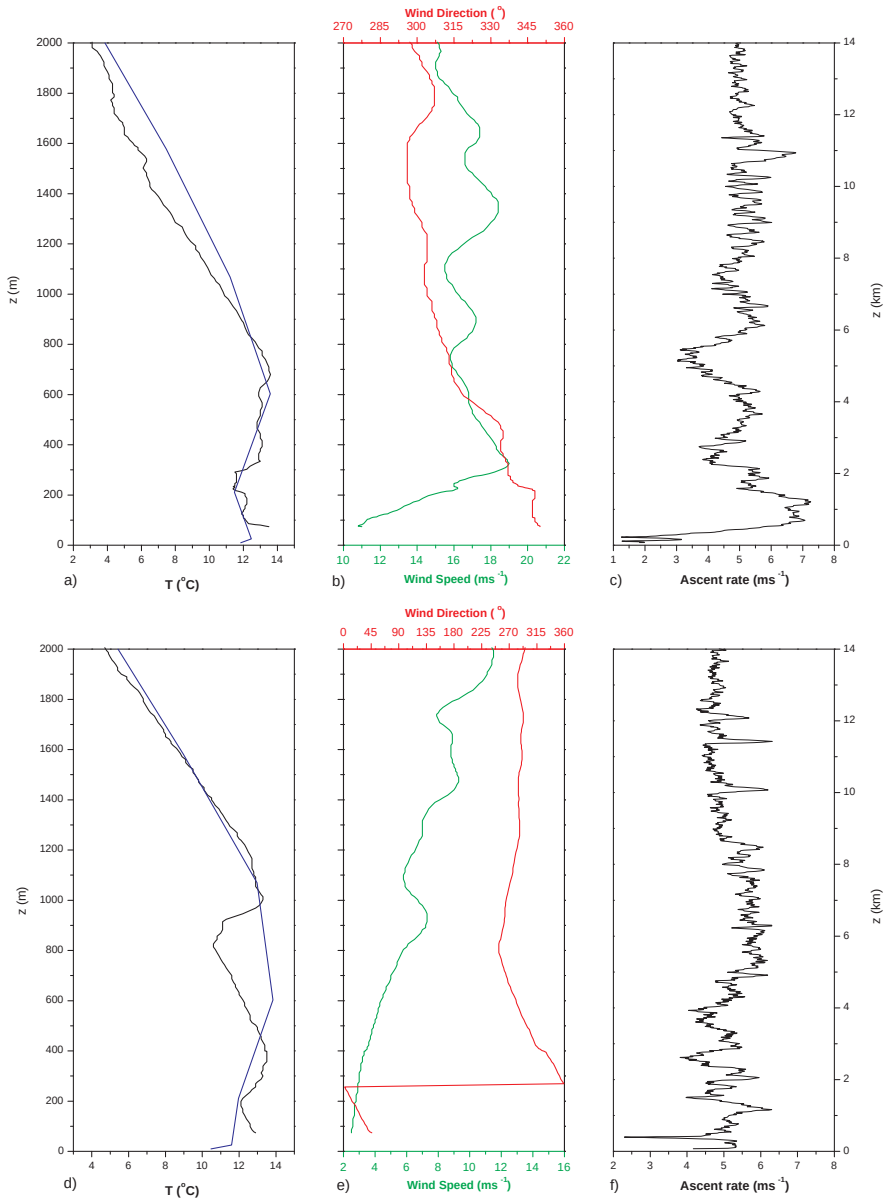

Figure 5.34: MPA radiosonde measurements at $1112Z$ ($T = 20.47$ days) of (a) temperature (black line), (b) wind speed and direction, (c) ascent rate and measured at $2318Z$ ($T = 20.97$ days) of (d) temperature (black line), (e) wind speed and direction, (f) ascent rate for the 20^{th} of January 2001. Met Office forecast for (a) $1200Z$ ($T = 20.5$ days) on the 20^{th} of January and (d) $0000Z$ ($T = 21.0$ days) on the 21^{st} of January – blue line.

Another feature that occurs at the beginning of the event is the different behaviour of the pressure at the stations at MPA. This is enhanced in figure (5.35b) where the difference between the downstream stations is as high as the difference between them and site

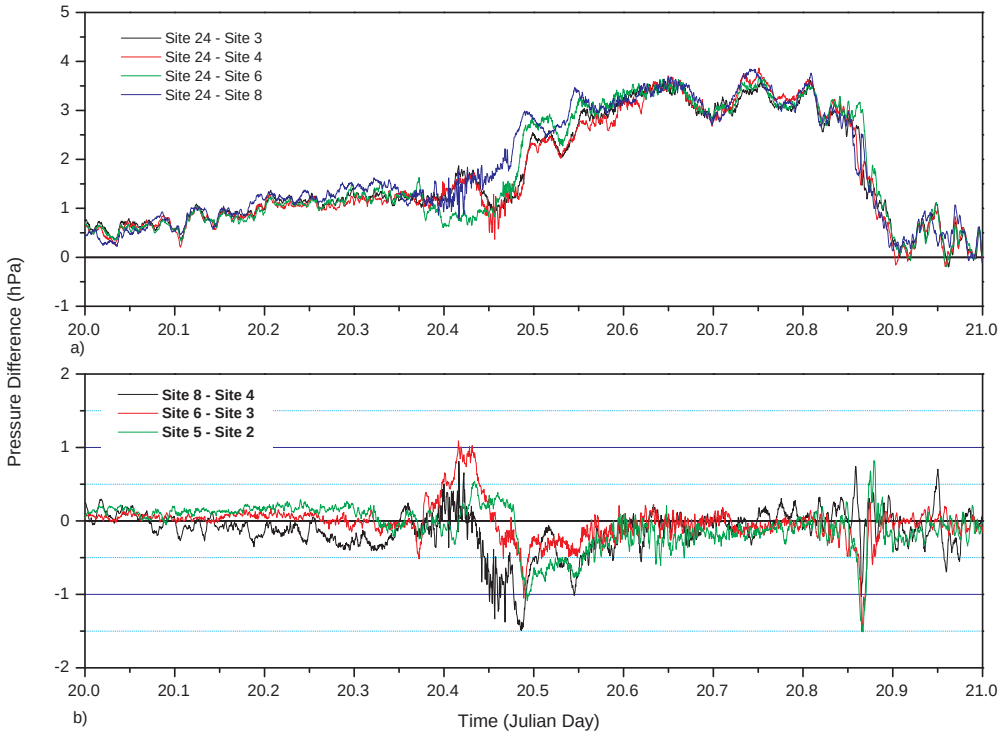

Figure 5.35: The 30s pressure difference between (a) site 24 and 4 stations at MPA and (b) the opposite stations at MPA for the 20^{th} of January 2001.

24 which might be an indication of the presence of a rotor. Note that the behaviour of the three downstream pairs is not the same. At the end of the event there is once again a sharp increase in the pressure difference between the stations downstream, but this time the behaviour of stations 8, 6 and 5 is synchronised as well as the behaviour of stations 4, 3 and 2.

The wind direction at site 24 is between westerly and north–westerly up to 20.3 days, turns to northerly up to 20.9 days and lastly turns gradually to southerly (figure 5.36g). The wind speed before $T = 20.4$ days is low and subsequently increases attaining 8 ms^{-1} by $T = 20.46$ days. Between this time and $T = 20.7$ days the wind speed oscillates between 6 ms^{-1} and 12 ms^{-1}. Finally the speed decreases steadily to 0 ms^{-1}. The behaviour of the flow at the downwind stations is markedly distinct apart from the initial period, when the flow has low speed and is westerly. As the wind upstream turns northerly the northerly wind component at the downwind stations increases and when the

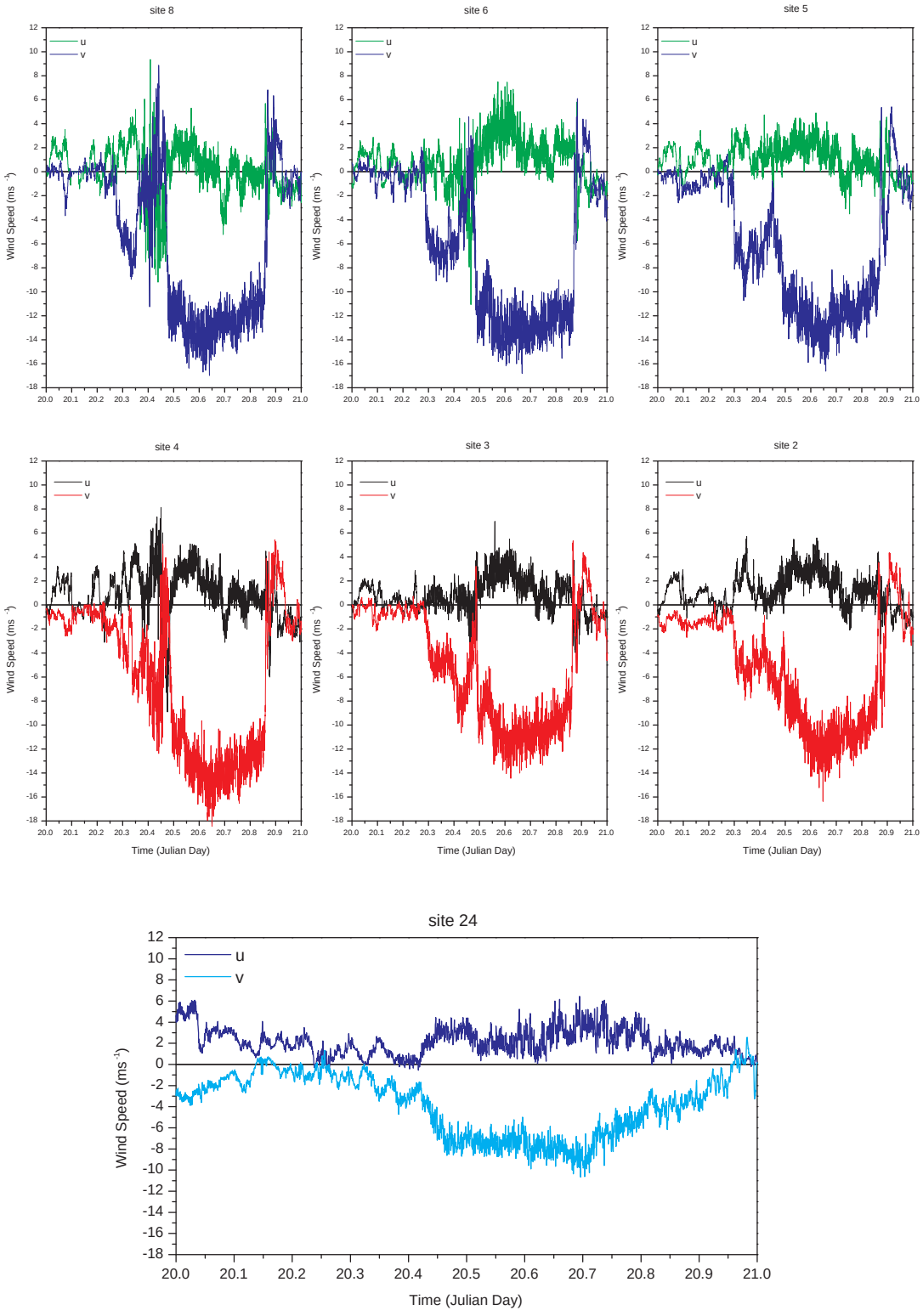

Figure 5.36: 30s wind for stations (a)8, (b)6, (c)5, (d)4, (e)3, (f)2 and (g)24 for the 20^{th} of January 2001.

upstream wind starts to increase the flow downstream stalls and reverses. The reversed flow at station 8 and 6 starts and ends before the reversed flow at stations 4 and 3, i.e, it takes ~ 16 min for the rotor to travel between the stations. This is might be indicative of a travelling hydraulic jump. The Froude number for $T = 20.47$ days is $F = 0.78$ and although $H/z_i = 2.9$ there could be a trapped wave on the inversion with rotors under the crests. By the time the wind upstream reaches 8 ms^{-1} the wind at MPA is once again northerly and its speed is amplified in relation to the speed at 24. When the flow at 24 turns from northerly to southerly ($T = 20.9$ days) the flow at MPA reverses. These two cases of reversed flow coincide with the increased pressure difference between the stations at MPA, suggesting the presence of rotors.

For the period when there is low wind speed at 24 and the flow is northerly there is accelerated flow at all stations downstream although the speed–up has a high variability due to the low speed upstream (figure 5.37). In some instants, this speed is increased by values greater than 200%. For the moments when there is reversed and stalled flow the speed–up is negative. The period between the reversed flow has a more uniform speed–up, with an increase greater than 50% in the wind speed.

The high variability of the flow during the reversed flow is noticeable in the gust factors (figure 5.37e, f, g and h) where gusts can be 240% greater than the average wind speed at the downwind stations.

The ten minute standard deviation (figure 5.38) shows the expected increase for low wind speeds. The different features of flow at the four stations at MPA are now enhanced. Stations 8 and 4 have a high temporal variability around $T = 20.4$ days which is higher than the variability at station 6 and this is reversed at $T = 20.9$ days. Both moments are related to the reversed or stagnated flow at the beginning and end of the event. Stations 4 and 8 have also a smaller peak around $T = 20.7$ days which is related to the change in direction in u, from westerly to easterly. Although station 3 has an increased standard deviation from $T = 20.3$ to $T = 20.9$ days there is moderate variability at the beginning and the end of the event.

The horizontal irregularity of the flow in the initial and final stages of the event is perceptible from the horizontal standard deviation which shows high values at times around $T = 20.4$ and $T = 20.9$ days (figure 5.38d). This is clear in the wind vector plots. At $T = 20.44$ days (figure 5.39a)the flow is reversed station 8 and there is also stagnation at stations 9 and 7. One hour and three quarters later the flow besides being enhanced

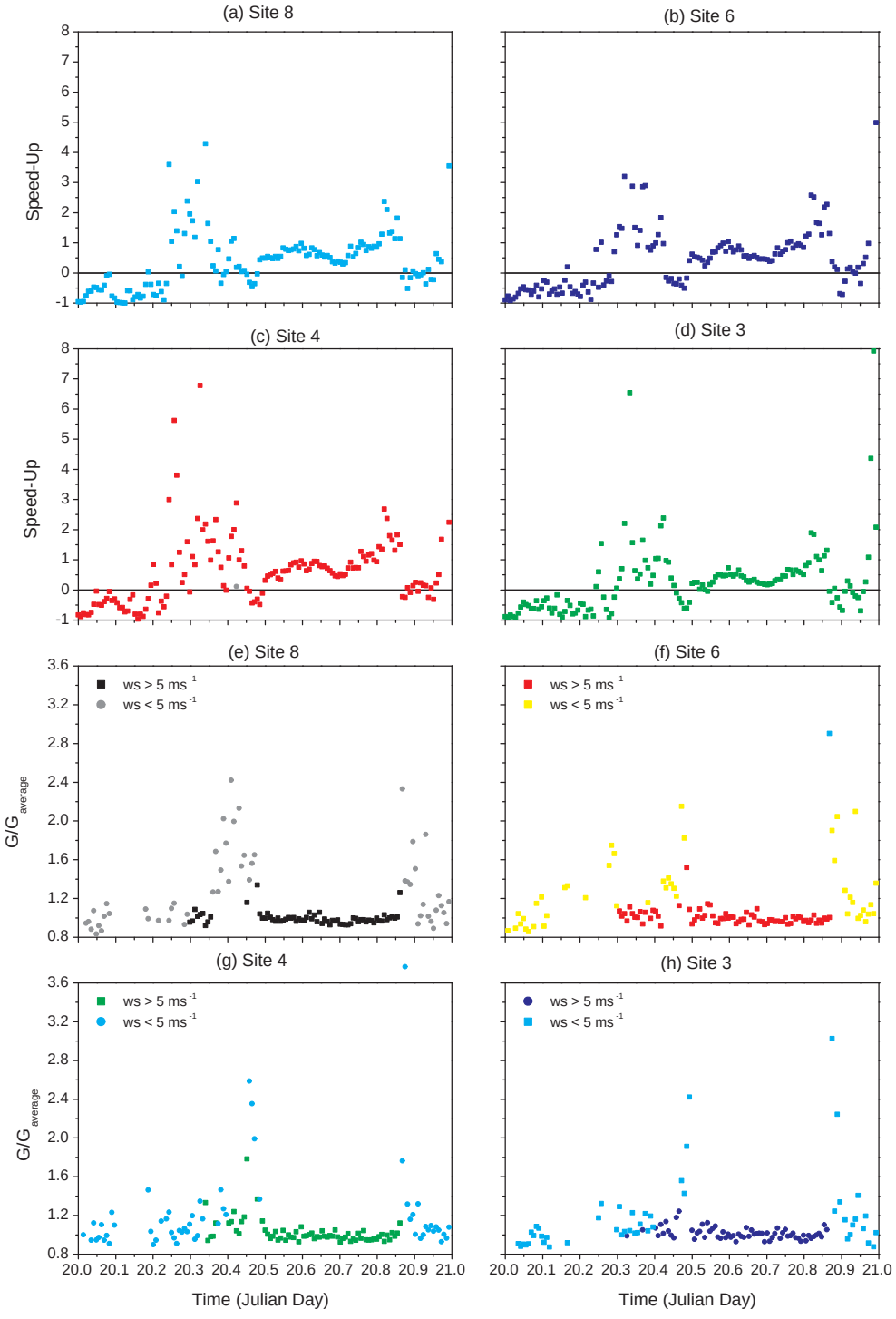

Figure 5.37: Speed–up for stations (a) 8, (b) 6, (c) 4 and (d) 3 and gust factors for stations (e) 8, (e) 6, (g) 4 and (h) 3 for the 20^{th} of January 2001.

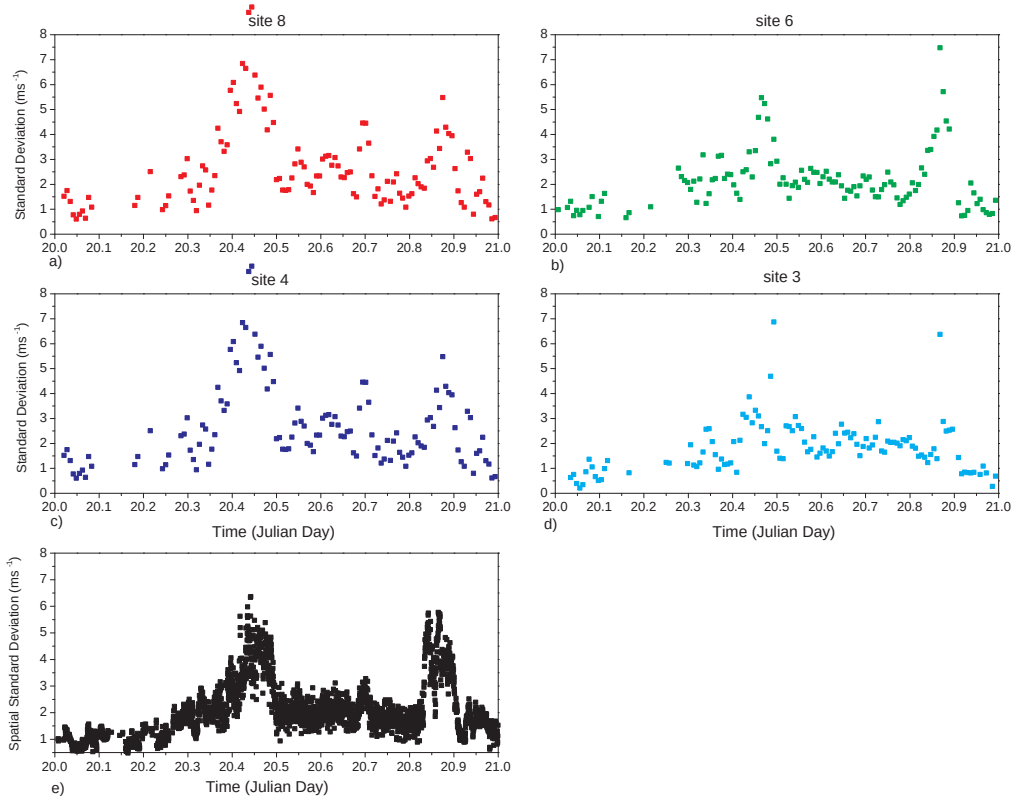

Figure 5.38: 10 min standard deviation for stations(a) 8, (b) 6, (c) 4, (d) 3 and (e) horizontal standard deviation for the 20^{th} of January 2001.

has also similar directions at all downstream stations (figure 5.39b). At the end of the event (figure 5.39c) there is flow reversal at stations 8, 6 and 4 and cross flow at stations 9 and 7. These two patterns at the beginning and end of the event are consistent with convergence along an east west line between station 12 and stations 8 and 6, leading to high vertical wind speeds. In fact, the estimate of the 10 minute average of the vertical gradient of this component exhibits two maxima at time $T = 20.47$ and $T = 20.875$ days with an amplitude of 0.0041 s^{-1} and 0.0045 s^{-1} respectively . This represents a vertical wind speed of 0.82 ms^{-1} and 0.9 ms^{-1} at heights of 200 m. In between these two occasions, the vertical gradient oscillates between 0.001 s^{-1} and 0.002 s^{-1}. All this is consistent with the presence of a rotor at the beginning and end of the event.

The rotors also leave a significant imprint on the temperature. The potential temperature difference between station 24 and four stations downstream (figure 5.40a) is negative for the period between $T = 20.2$ and $T = 20.35$ days. The other relevant features in the

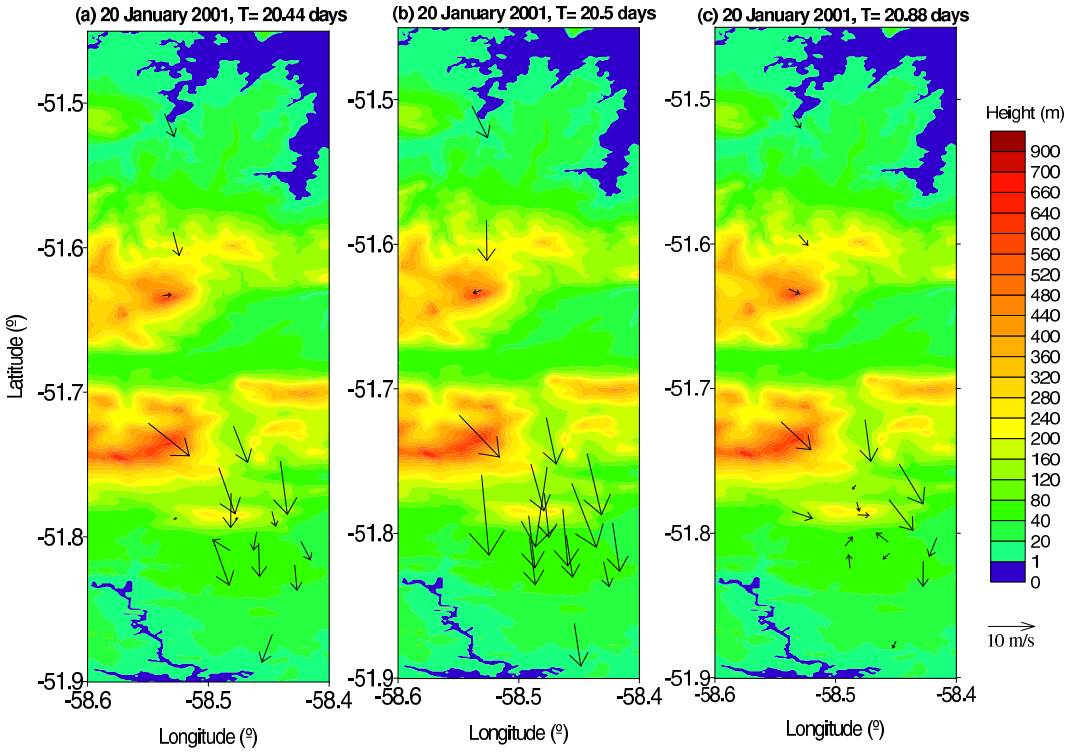

Figure 5.39: The 10 minute average wind field measured at the AWS sites for the (a)beginning, (b)middle and (c)end of the event for the 20^{th} of January 2001.

same plot are the two peaks of relative very warm air during the rotor events. This plot also demonstrates that the three dimensional structure of the first rotor is highly complex. While there is an increase in the temperature at stations 8 and 4, stations 6 and 3 show no significant differentiation although the pressure difference between the same stations exhibit considerable divergence. In the case of the second rotor, all four stations detect the warming. The difference in potential temperature between the stations at MPA (figure 5.40b) also show the influence of the rotor although not so markedly.

During the event, the downstream stations are warmer than station 24 (not so warm as when the rotor was over them), but the difference in temperature between them is insignificant. All these features are supported by (figure 5.41). The arrows indicate the rotors.

For a period of about one hour, the flow at MPA, at the beginning and end of this particular event, is reversed and decelerated relatively to the flow at station 24. In between these two episodes the flow is accelerated and the length of this phase was about eight and a half hours.

As before, the rotors are associated with high pressure and temperature differences

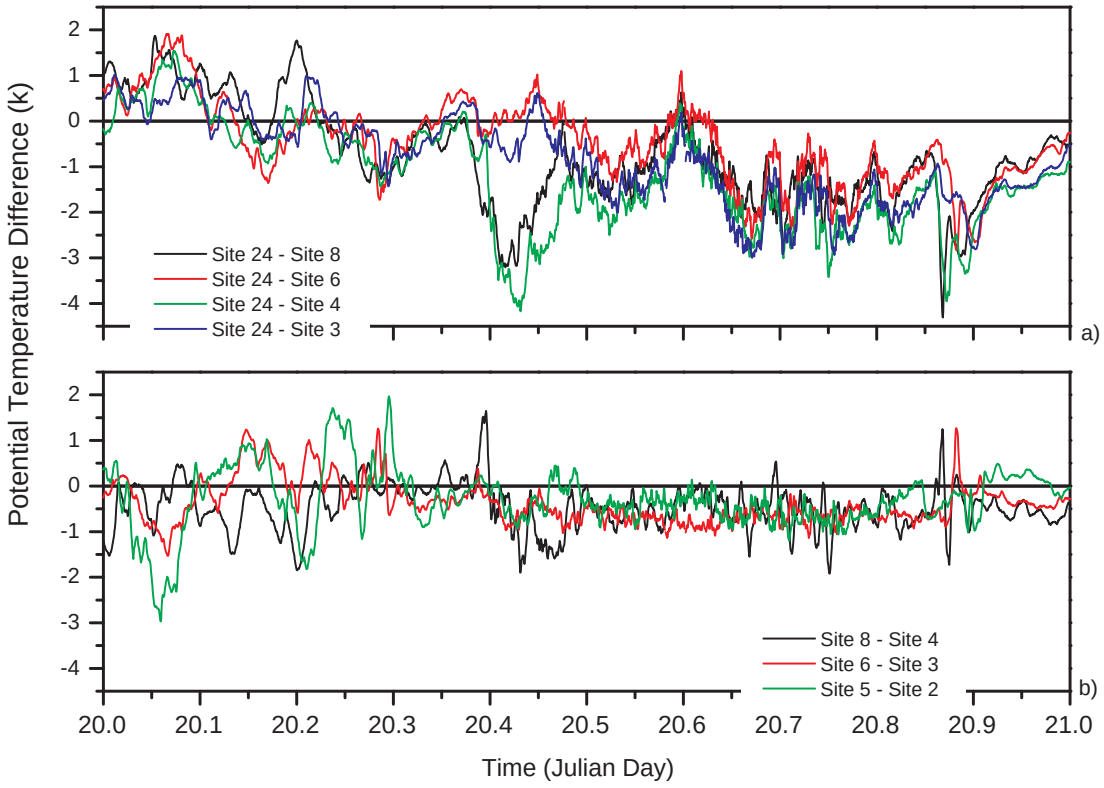

Figure 5.40: The 30sec potential temperature difference between (a) site 24 and 4 stations at MPA and (b) the opposite stations at MPA for the 20^{th} of January 2001.

across short distances, as well as high temporal and spatial variability in the flow downstream.

8^{th} and 9^{th} of April 2001

For the first six hours of the 8^{th} of April the ECMWF analysis yields a sea surface which is warmer than the 2 m air temperature ($T_{2m} - T_{SST} < 0$). By $1200Z$ ($T = 98.5$ days) the temperature difference is reversed but only by 0.7 K and remains positive for the rest of the event. The temperature difference between the measured 2 m temperature and the weekly averaged SST shows a similar pattern.

The radiosonde vertical profile for $1117Z$ ($T = 98.47$ days) reveals a stable layer from the ground up to 1624 m where a small temperature inversion of 3.55^{o} C, can be observed (figure 5.42a – black line). For heights below the inversion the Met Office forecast for $1200Z$ ($T = 88.5$ days) is warmer than the radiosonde temperature profile (figure 5.42a – blue line). The inversion is also absent from the forecast. The wind direction for the bal-

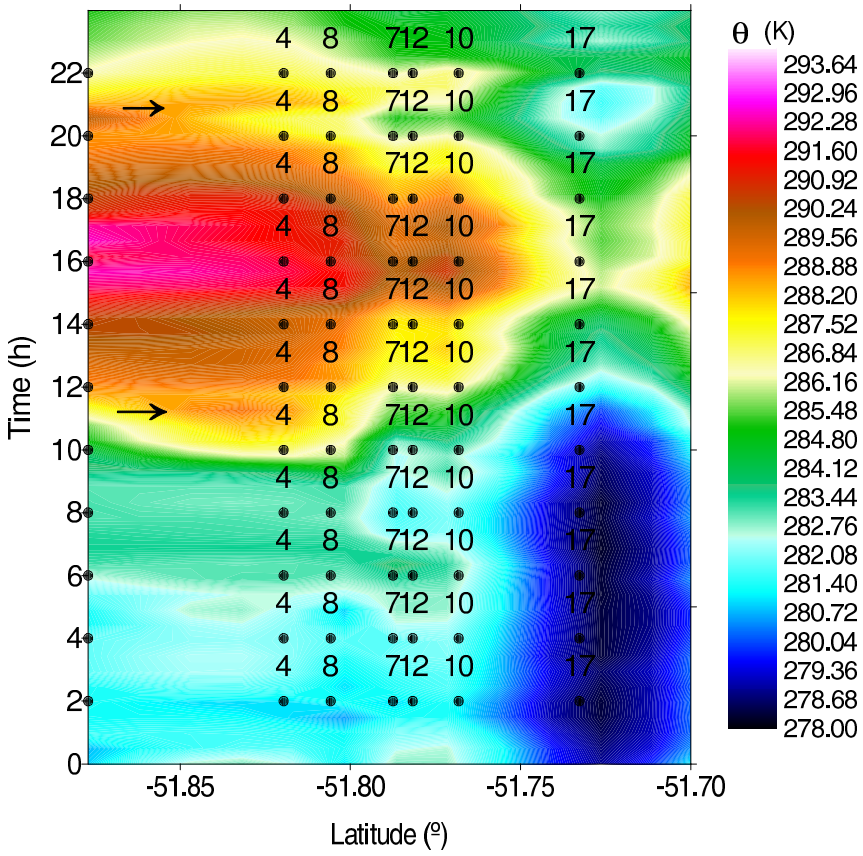

Figure 5.41: Hovemöller of the 30sec potential temperature for a line through stations 1, 4, 8, 7, 12, 10, 17, 20, 23 and 24 for the 20^{th} of January 2001.

loon ascent is south–westerly and its ascent rate does not show any particular oscillation revealing gravity waves (figure 5.42b and c). Unfortunately there was no launch at $2300Z$.

By $0507Z$ ($T = 99.21$ days) the temperature profile exhibits two inversions (figure 5.42d – black line). The first stretches from 341 m to 502 m with a temperature increase of 4.9 K. The second inversion begins at 725 m, ending at 976 m with a temperature difference of 3.4 K (there is a small (less than 100 m in length) stable layer in–between these two levels). The vertical profile of the Brunt Väisälä frequency reflects these features. It shows two peaks; the first has a maximum of 0.026 Hz at 381 m and by 572 m, $N = 0.013$ Hz. From this level onwards the stability increases once again and by 914 m the second maximum is reached ($N = 0.025$ Hz).

The vertical wind profile from the ground, up to the top of the second inversion displays a strong negative curvature. From the ground to the top of the second inversion, the wind direction is northerly and does not change with height. Afterwards the wind direction backs with height (figure 5.42e).

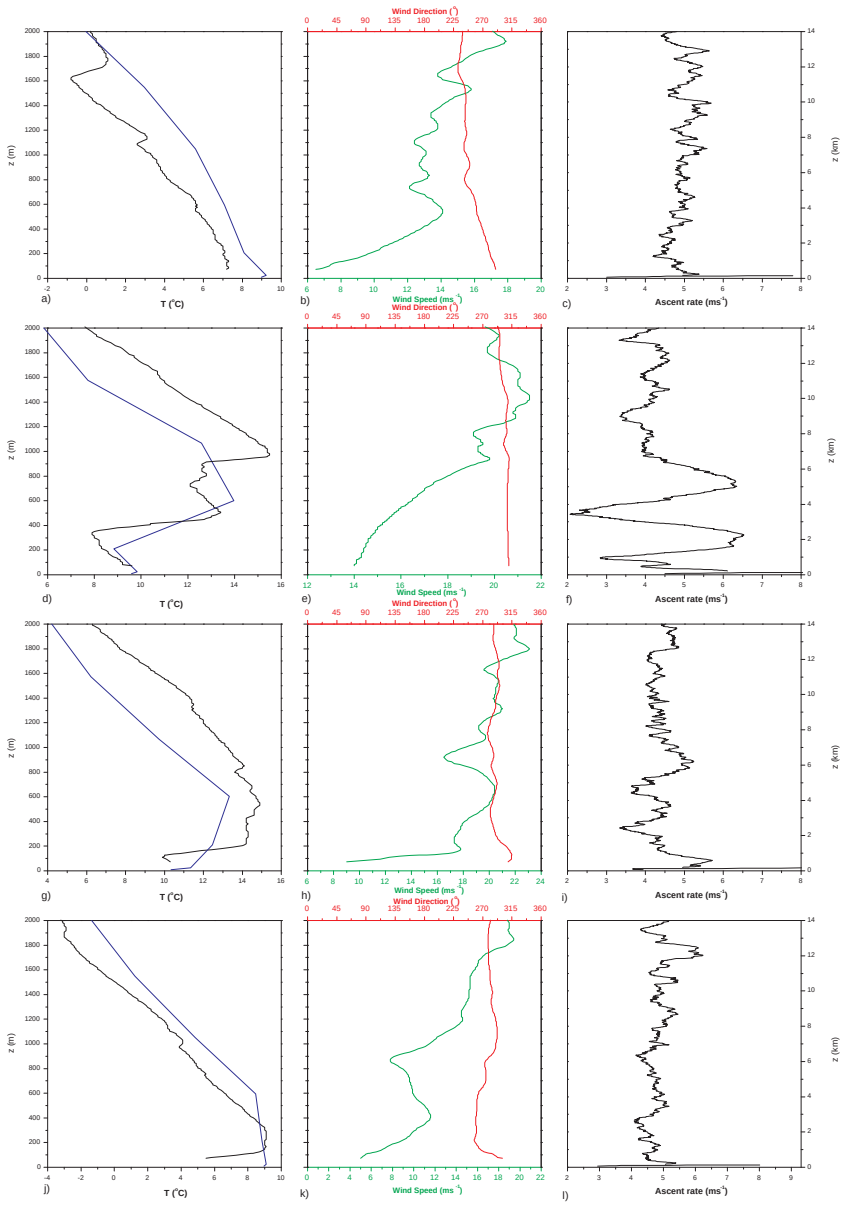

Figure 5.42: MPA radiosonde measurements at: $1117Z$ ($T = 98.47$ days) (a) temperature (black line), (b) wind speed and direction, (c) ascent rate for the 8^{th} of April; at $0507Z$ ($T = 99.21$ days) (d) temperature (black line), (e) wind speed and direction, (f) ascent rate; at $1126Z$ ($T = 99.48$ days) (g) temperature (black line), (h) wind speed and direction, (i) ascent rate and at $2320Z$ ($T = 99.97$ days) (j) temperature (black line), (k) wind speed and direction, (l) ascent rate for the 9^{th} of April. Met Office temperature forecast for (a) $1200Z$ ($T = 88.5$ days) on the 8^{th} of April, (d) $0600Z$ ($T = 89.25$ days), (g) $1200Z$ ($T = 89.5$ days), on the 9^{th} of April and (j) $0000Z$ ($T = 90.0$ days), on the 10^{th} of April (blue line).

The balloon ascent rate shows two large oscillations with amplitudes around 4 ms^{-1} below 5000 m indicating a strong vertical propagating gravity wave (figure 5.42f).

The Met Office temperature forecast for $0600Z$ ($T = 99.25$ days) fails to produce the two inversions, there is just one between 200 and 600 m (figure 5.42d – blue line). Due to lack of resolution, the forecast is unable to determine the height at which the inversion begins. However, the lack of resolution is not enough to explain why the temperature above the inversion and below 2360 m is also lower than the temperature measured by the radiosonde and the inability of the forecast to correctly determine the top of the inversion. The difference in temperature gradient in the inversion is possibly due to the presence of the gravity wave, i.e., the downslope acceleration induced by the wave steepens the gradient downstream. So it is reasonable to assume that the upstream gradient (forecast) is smaller that the downstream (radiosonde).

By $1126Z$ ($T = 99.48$ days) the two inversions have merged and their base is lowered, it starts at 99 m and remains strong (there is a 4.2 K increase for the next 180 m). Above it, there is a 200 m layer with constant temperature (figure 5.42g – black line). The forecast above the inversion and below 3000 m (figure 5.42g – blue line) remains colder than the observed but is able to reasonably capture the height of the top of the inversion. The same reasoning as before applies to the temperature gradient.

The Brunt Väisälä frequency determined from the radiosonde profile reaches its maximum in the lower two hundred meters but wind speed no longer shows the strong negative curvature in this layer.

The wind direction remains northerly and the balloon ascent rate shows oscillations around 1 ms^{-1} in the lower 6000 m (figure 5.42h and i).

By $2320Z$ ($T = 99.97$ days) the temperature profile shows a temperature inversion characteristic of a nocturnal boundary layer (figure 5.42j – black line). The forecast profile is too warm at the surface and due to the low resolution the top of the inversion is too high.

The pressure difference plots (figure 5.43) show that the difference between station 24 and the stations at MPA starts to increase from $T = 98.2$ days. By $T = 98.8$ days the difference is 4.7 hPa and although it remains high there are clear oscillations superimposed. These oscillations have periods between 2.5 and 3 hours and are related to oscillations in pressure at station 24 due to oscillations in the wind direction. The pressure difference starts to decrease by $T = 99.4$ days.

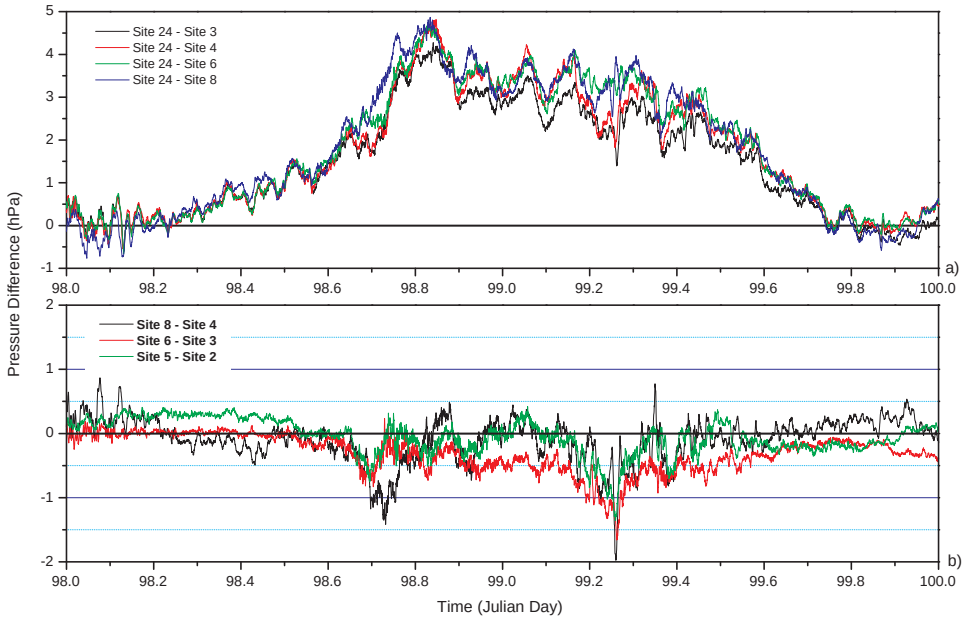

Figure 5.43: The 30s pressure difference between (a) site 24 and 4 stations at MPA and (b) the opposite stations at MPA for the 8^{th} and 9^{th} of April 2001

The pressure difference between the opposing stations at MPA shows two relevant occurrences at $T = 98.7$ and $T = 99.25$ days when there is a pressure difference greater than 1 hPa.

The two hour pressure spectrum for the stations at MPA shows an energy peak for a period of 32 min for both days but which is much stronger for the second day (figure 5.45). For the 8^{th} of April there are also other frequencies with increased energy. The relevant periods are 8 min, 7 min, 4 min and 3 min. In the first three the energy is even higher than the peek for the 32 min period. On the 9^{th}, only the 32 min period is relevant. The spectrum for station 24 has peaks for periods of 43 min and 7 min on the 8^{th} and a peak for 16 min for the 9^{th}.

When the one hour spectrum is performed different features emerge. The half an hour period is only relevant for the first twelve hours of each day and it is not at all relevant in station 4. Site 8, for the second period of day 8 has several peaks for periods less than 8 min and all stations have a small energy peek for a period of 2.7 min. The spectral density plots (figure 5.45) show that the high energy for the longer frequencies is related to the two moments when the pressure difference across the stations at MPA reached a

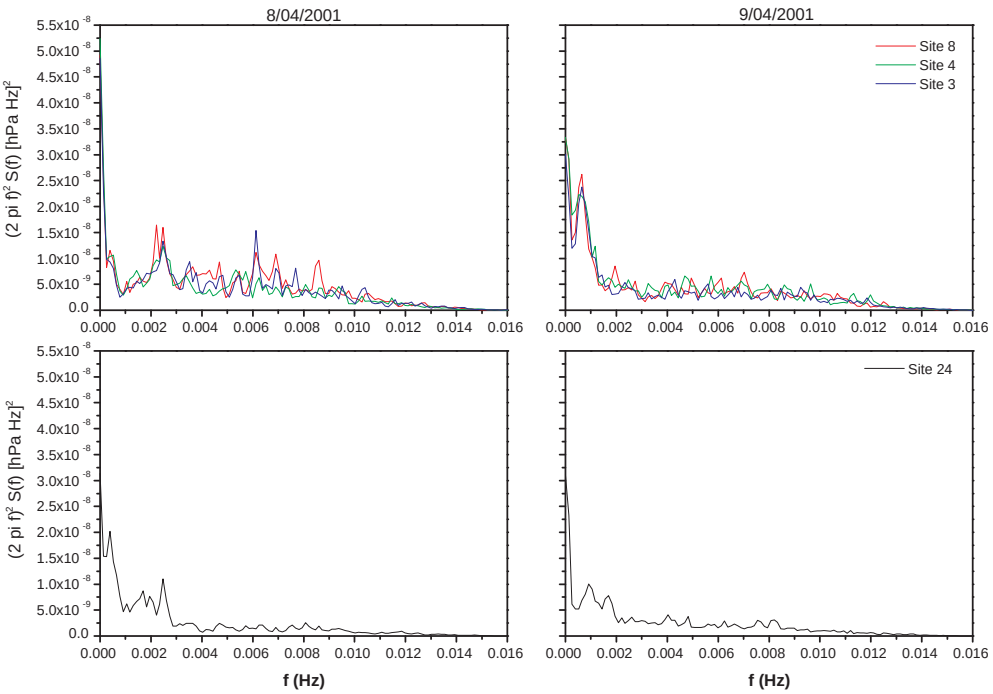

Figure 5.44: Two hour pressure spectrum for the 8^{th} and 9^{th} of April 2001

maximum. The spectrum for station 24 has very little energy for periods greater than 10 min.

The wind direction at station 24 is only north–westerly between 98.5 and 99.5 (figure 5.46) and its speed oscillates between 4 ms^{-1} and 11 ms^{-1}. For this period, $1.5 < NH/U < 4$ and a strong acceleration of the wind speed downstream is observed. Also noteworthy are the two intervals when the wind at stations 3 and 2 is significantly decelerated. These two moments are related to the same intervals when there is maximum pressure difference between the downstream stations. All this, along with the long frequency peaks in the pressure spectrum suggest the presence of rotors where the reversed flow does not reach the surface (see the case study for the 8^{th} and 9^{th} of February 2001). In the $0507Z$ ($T = 99.21$ days) radiosonde $H/z_i = 1.88$ and 0.88 in the first and second inversion respectively and Froude numbers are $F = 0.68$ and $F = 0.52$. According to Vosper (2004) the second inversion should induce a stationary hydraulic jump above the lee slope with a region of overturning and stagnant flow behind the jump. The downstream temperature profile of his figure 8 is very similar to the radiosonde profile. If this is the case the first inversion

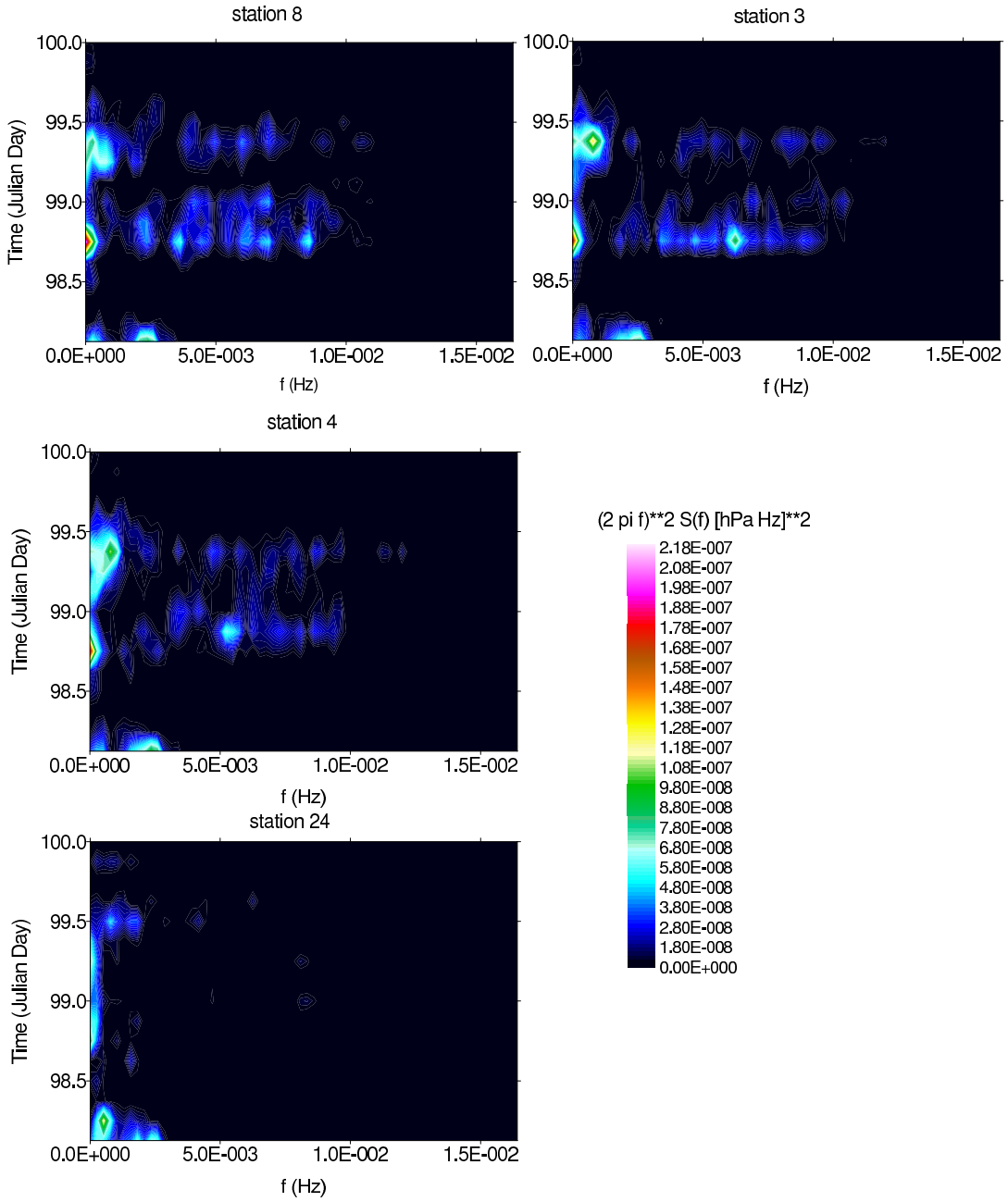

Figure 5.45: One hour pressure spectrum density for the 8^{th} and 9^{th} of April 2001

does not occur in the upstream profile and the inversion in the Met Office forecast is too low. If the forecast is taken as the upstream profile then the second inversion is absent upstream. The first inversion could induce a trapped lee wave on the inversion with rotors underneath the wave crests.

The two intervals mentioned above also have an impact on the speed–up. Figure (5.47a, b, c and d) shows that for these two moments there is deceleration. The strong acceleration

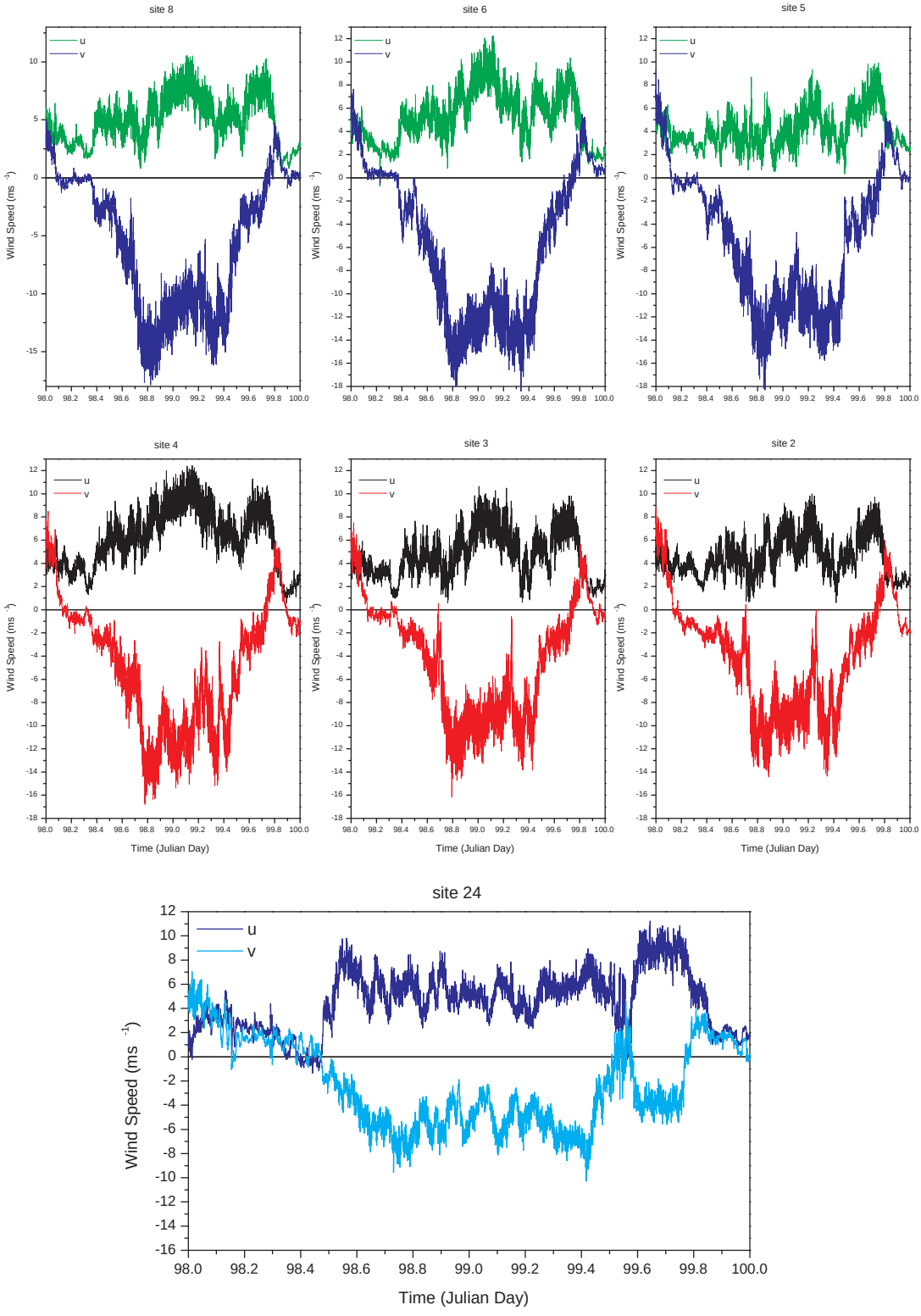

Figure 5.46: 30s wind for stations (a) 8, (b) 6, (c) 5, (d) 4, (e) 3, (f) 2 and (g) 24 for the 8^{th} and 9^{th} of April 2001

predicted with the non dimensional parameter (NH/U) is only observed between these two periods. Although there are oscillations in the speed–up there are $\Delta s > 1.75$ which puts this into category (i).

The horizontal standard deviation is not greater than the same parameter for a simple gravity wave (7^{th} of August), but there is increased variability for the two periods already mentioned. (figure 5.48). The 10 min standard deviation has even less variability and the moments mentioned earlier have no influence on this parameter.

The gust factors (figure 5.47e, f, g and h) are approximately equal to the average, reinforcing the low temporal variability of the phenomenon.

There is no significant difference in the potential temperature between the stations downstream and the upstream and downstream stations.

In summary, for the period when high pressure difference between station 24 and the downstream stations is observed, the flow downstream is strongly accelerated. During this period the flow has low spatial and temporal variability.

There are also two moments when there is increased pressure difference between stations downstream and high energy peaks in the pressure spectrum. Although no wind reversal is observed at the surface (there are just signs of flow deceleration) it is possible that a rotor was formed.

25^{th} and 26^{th} of February 2001

For the first eleven hours on the 25^{th} of February, the wind direction is southerly and the difference between the 2 m air temperature and the SST is negative both in the ECMWF ERA 40 analysis and between station 24 and the weekly averaged sea surface temperature. This is reflected on the atmospheric structure observed at MPA. In the radiosonde for $1118Z$ ($T = 56.47$ days) the vertical temperature for the first 2000 m is of a stable boundary layer with a small temperature inversion of 0.5 K at 733 m (figure 5.49a – black line). The wind is already northerly near the surface and backs with height and the balloon ascent rate is relatively uniform. Although the Met Office temperature forecast for $1200Z$ ($T = 56.5$ days) is warmer than the radiosonde by about 2^o C, it reflects the stable boundary layer in the observed profile (figure 5.49a – blue line). From $1111Z$ ($T = 56.466$

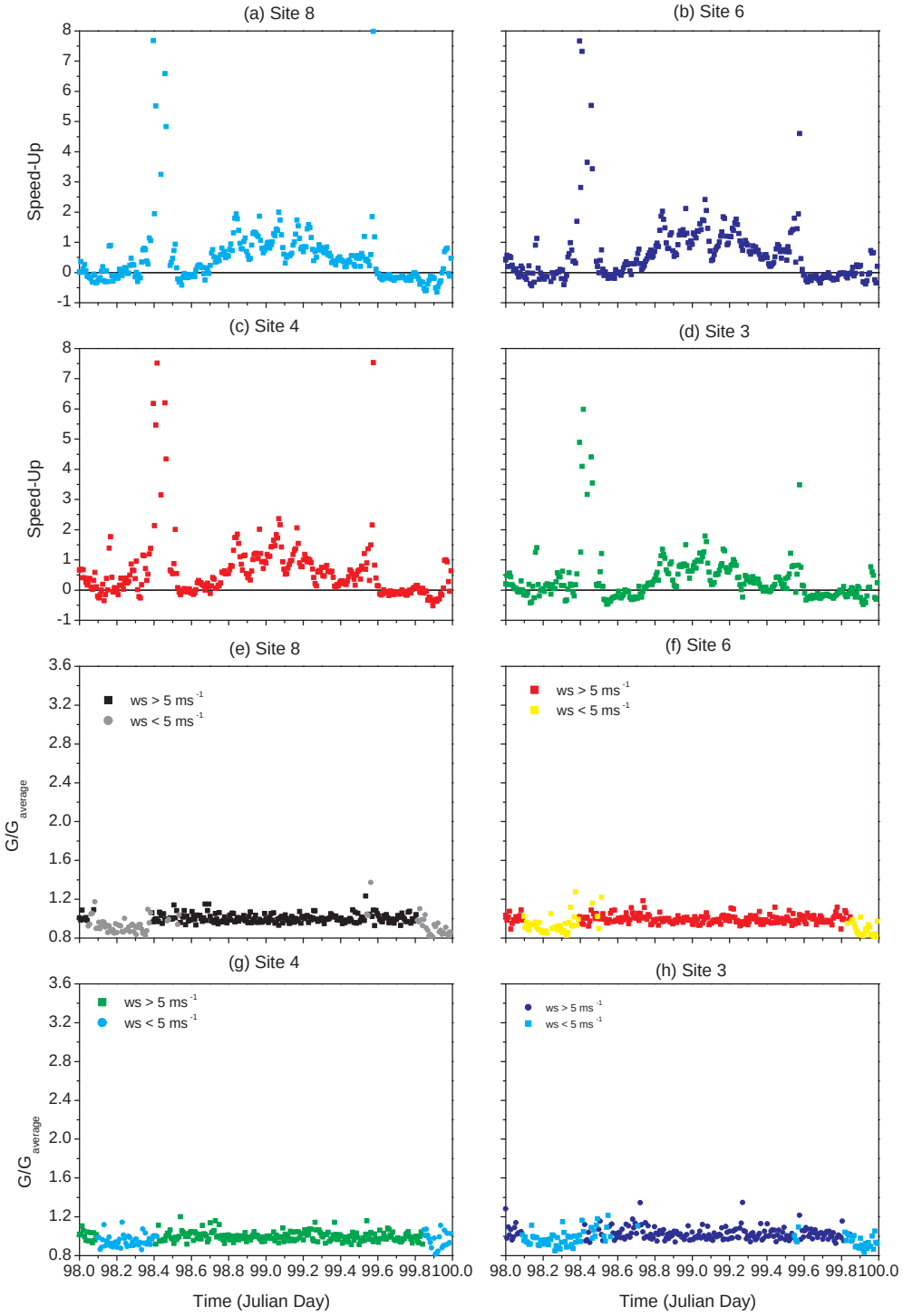

Figure 5.47: Speed–up for stations (a) 8, (b) 6, (c) 4 and (d) 3 and gust factors for stations (e) 8, (f) 6, (g) 4 and (h) 3 for the 8^{th} and 9^{th} of April 2001

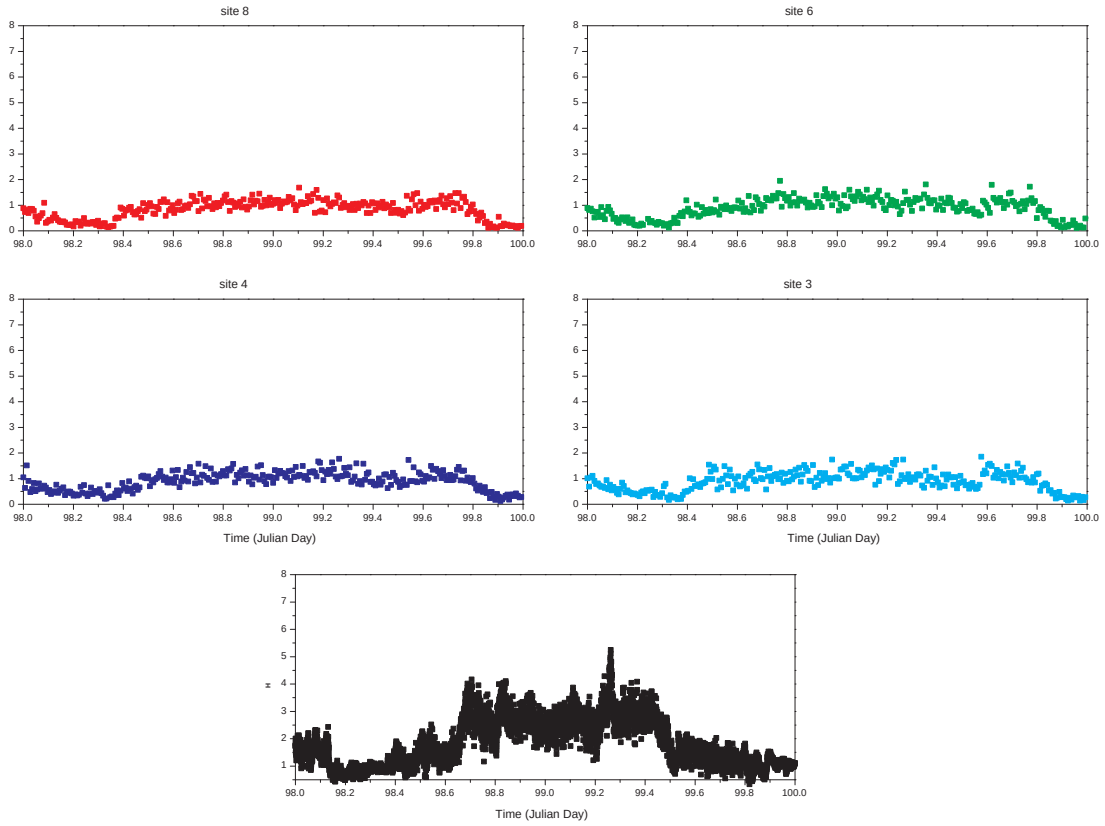

Figure 5.48: 10 min standard deviation for stations (a) 8, (b) 6, (c) 4, (d) 3 and (e)horizontal standard deviation for the 8^{th} and 9^{th} of April 2001

days) onwards the wind at station 24 is (figure 5.51g) and the differences in the temperature between the 2 m air temperature and the SST are positive. Once again, the ECMWF analysis suggests that warm northerly air is being advected north of the Falklands. The emergence of a temperature inversion is now observed in all the radiosonde vertical profiles. At $2315Z$ ($T = 56.97$ days) an increase of 7.3 K can be observed between 374 m and 858 m (this profile is not shown due to the lack of wind data). The balloon ascent rate for this launch displays evidence of the presence gravity waves.

By $0516Z$ ($T = 57.22$ days) the base of the inversion is a hundred metres lower but the top remains approximately at the same height (figure 5.49d – black line). The temperature between these levels increases by 8.7 K but the gradient remains the same, $|\nabla T| = 0.015$ Km^{-1}. As in the previous cases, the Brunt Väisälä frequency reflects this profile. It increases steadily from a value of $N = 0.0083$ Hz at 100 m to a maximum of $N = 0.0249$ Hz at 475 m. Above this height and up to 1200 m, it decreases steadily. Now, although the wind backs with height, it remains northerly in the first 5000 m and the balloon as-

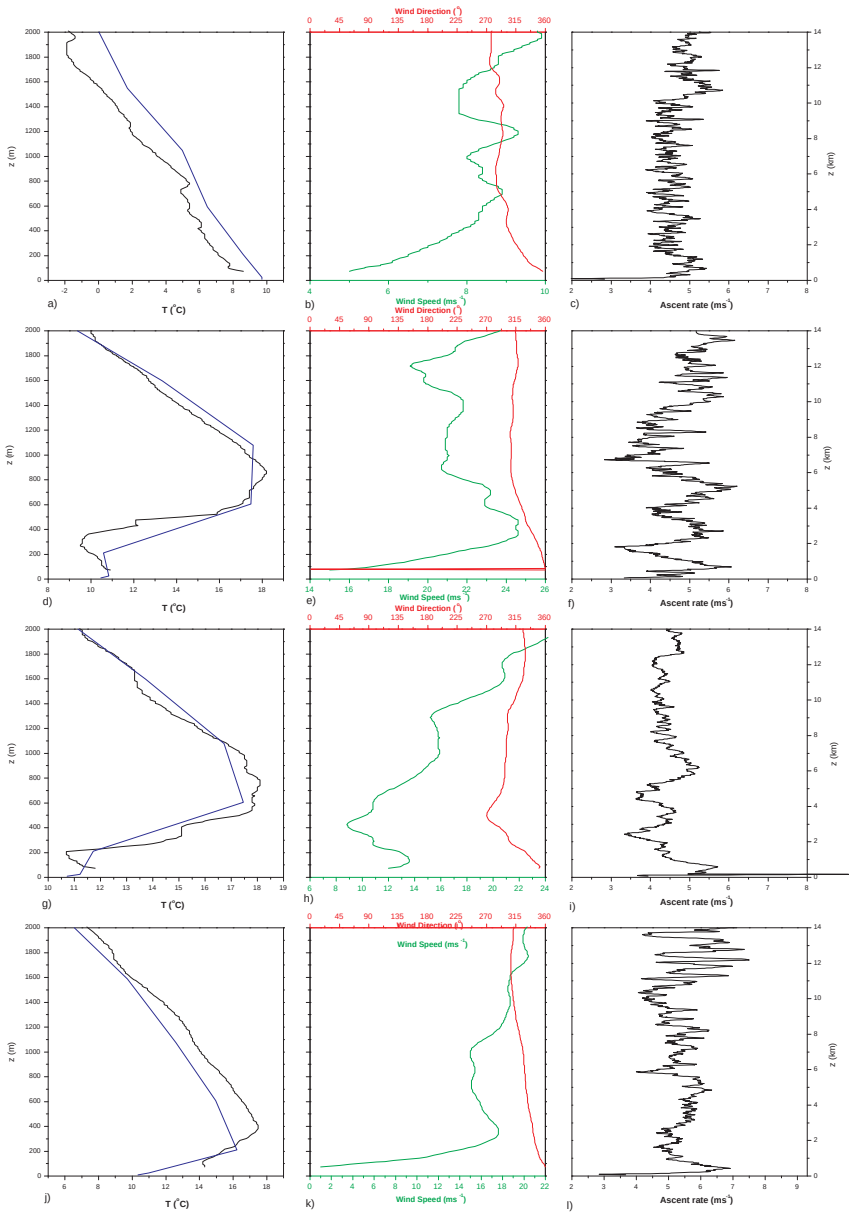

Figure 5.49: MPA radiosonde measurements at: $1118Z$ ($T = 56.47$ days) (a) temperature (black line), (b) wind speed and direction, (c) ascent rate for the 25^{th} of February; at $0516Z$ ($T = 57.22$ days) (d) temperature (black line), (e) wind speed and direction, (f) ascent rate; at $1121Z$ ($T = 57.47$ days) (g) temperature (black line), (h) wind speed and direction, (i) ascent rate; at $2334Z$ ($T = 57.98$ days) (j) temperature (black line), (k) wind speed and direction, (l) ascent rate for the 26^{th} of February. Met Office forecast for (a) $1200Z$ on the 25^{th} of February ($T = 56.5$ days), (d) $0600Z$ ($T = 57.25$ days), (g) $1200Z$ ($T = 57.5$ days) on the 26^{th} of February and (j) $0000Z$ ($T = 58$ days) on the 27^{th} of February (blue line)

cent rate shows oscillations between 2 – 3 ms^{-1} in the first 6000 m, indicating gravity wave activity. The forecast temperature profile for $0600Z$ ($T = 56.25$ days) is very well correlated with the radiosonde's but due to its coarse resolution it is unable to determine the height of the top and base of the inversion. Hence the temperature gradient and the inversion's amplitude are not correctly determined (figure 5.49d – blue line). At $1121Z$ ($T = 57.47$ days) these oscillations are not so pronounced, but the wind remains northerly and a temperature inversion is still observed. The inversion, now, starts at 207 m and its gradient has increased to 0.02 Km^{-1}. The inversion is topped by a near neutral layer of about 200 thick (figure 5.49g – black line). As before, the Met Office's forecast is well correlated to the radiosonde's temperature profile (figure 5.49g – blue line).

The radiosonde profile for the launch at $2334Z$ ($T = 57.98$ days) is a typical profile of a nocturnal boundary layer with a small jet near the surface (figure 5.49j and k). Now, the correlation between the forecast and the radiosonde is considerably reduced.

The pressure difference between station 24 and four of the stations at MPA (figure 5.50) shows a pronounced decrease of ~ 4 hPa from $T = 56.91$ to $T = 57.11$ days followed

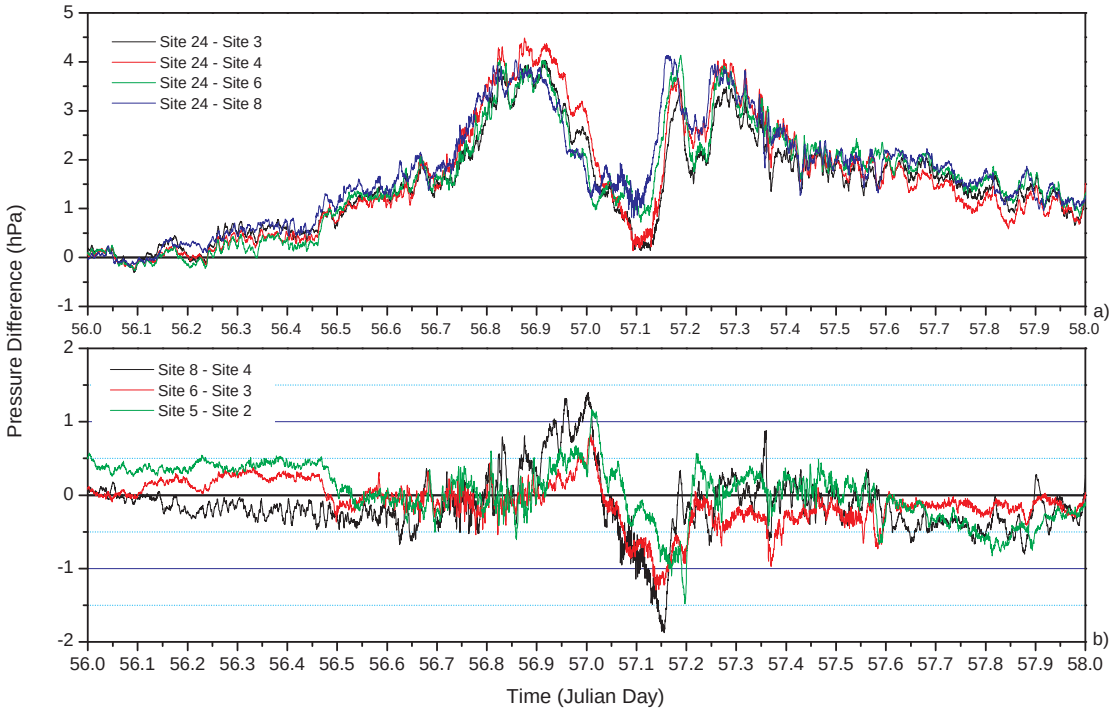

Figure 5.50: The 30s pressure difference between (a) site 24 and 4 stations at MPA and (b) the opposite stations at MPA for the 25^{th} and 26^{th} of February 2001

by a marked increase of ~ 4 hPa from $T = 57.11$ to $T = 57.159$ days. Initially, there is a reduction in the intensity of the wave due to the low wind speeds observed at station 24 (figure 5.51g) – the wind decreases from 8.37 ms^{-1} at $T = 56.86$ days to ~ 3 ms^{-1} at $T = 56.9$ days. The reduction in the wave intensity lasts probably until $T = 57.1$ days when once again an increase in the pressure difference is observed. The decrease in pressure between station 24 and the downstream station is accompanied by an increase in the pressure difference between the stations at MPA.

Before the occurrence of this phenomenon, the usual low pressure is observed downstream, i.e. the pressure difference between station 24 and the stations at MPA is high and positive. When it occurs a rotor is formed and the high pressure is due to the convergence of the flow from the lee slope and from

the reversed flow. As the perturbed flow approaches the stations their pressure increases, hence the decrease in the pressure difference. Note that the flow is very anisotropic; the pressure difference at stations 4 and 3 reaches a minimum two hours after the minimum is reached at stations 8 and 6. By $T = 57.11$ days the phenomenon starts to move away and the pressure at the stations decreases. This sharp pressure signature on the downstream stations could be due to a hydraulic jump or an advection of a trapped wave.

The time series of the wind components (figure 5.51) shows that during this phenomenon the wind component normal to the ridges (v component) decreases and in stations 8 and 4 there are some moments when there is reversed flow. It can also be observed that the decrease in wind speed at stations 5, 6 and 8 starts two hours before the reduction in stations 2, 3 and 4. Figure (5.51) also reveals that the flow in the former stations is more decelerated than in stations 5, 6 and 8, which explains the difference in the pressure between the opposing stations.

A snapshot of the flow for this period is represented in figure (5.52). Initially the flow reverses at station 7 and is northerly in all the other stations, which reveals flow separation at the base of Pleasant Peak. During the phenomenon (figure 5.52b) the flow at stations 3, 4, 6, 8 and 7 has a stronger

easterly component indicating that the disturbance has propagated downstream. Afterwards, the flow is northerly for all stations and is accelerated.

The flow separation along a east–west line at the base of Pleasant Peak is confirmed by the calculation of the divergence horizontal between stations 12 and 8. In fact, the 10 min average of the divergence attains a value of -0.0067 s^{-1} at $T = 57.083$ days which

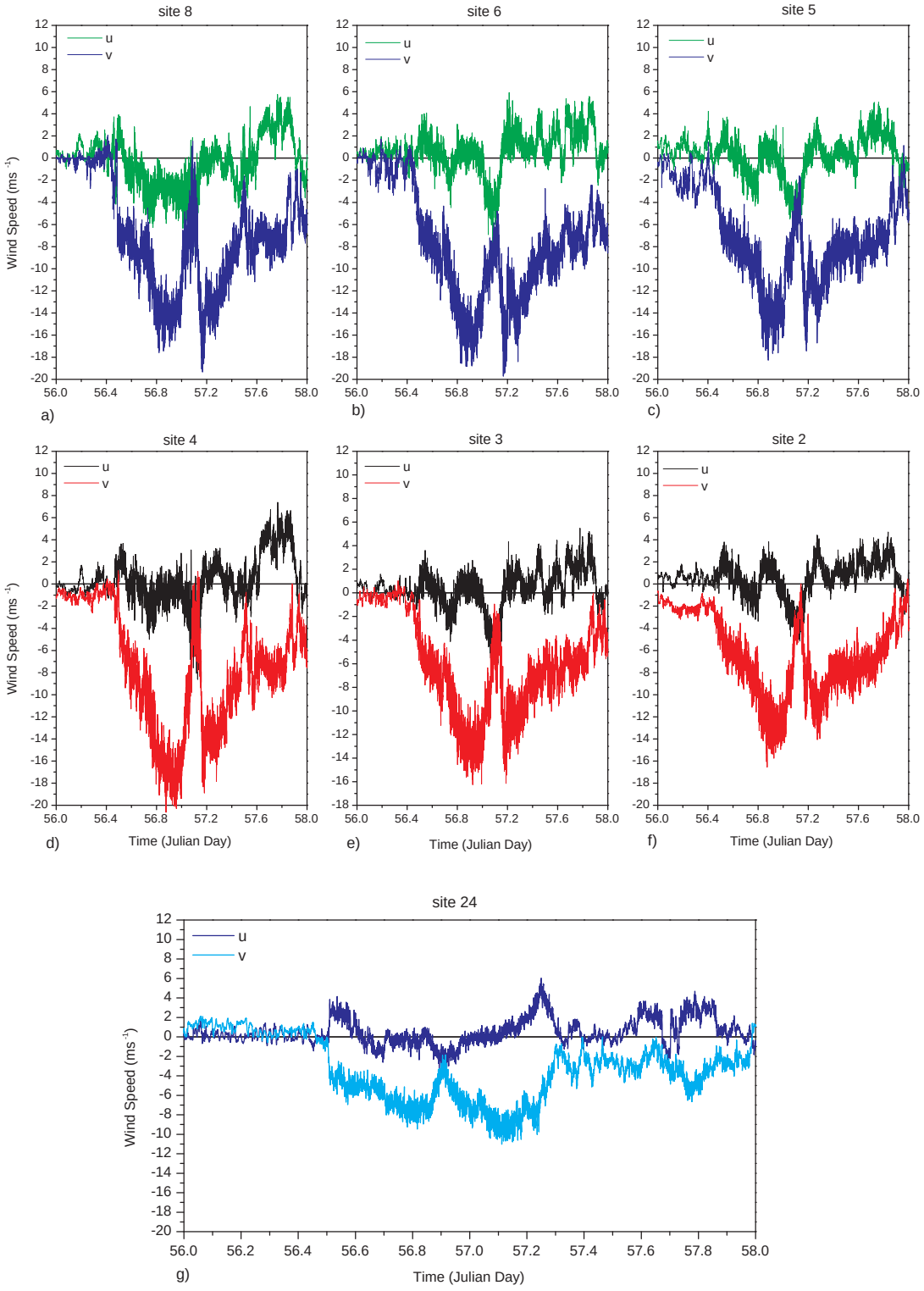

Figure 5.51: 30s wind for stations (a)8, (b)6, (c)5, (d)4, (e)3, (f)2 and (g)24 for the 25^{th} and 26^{th} of February 2001

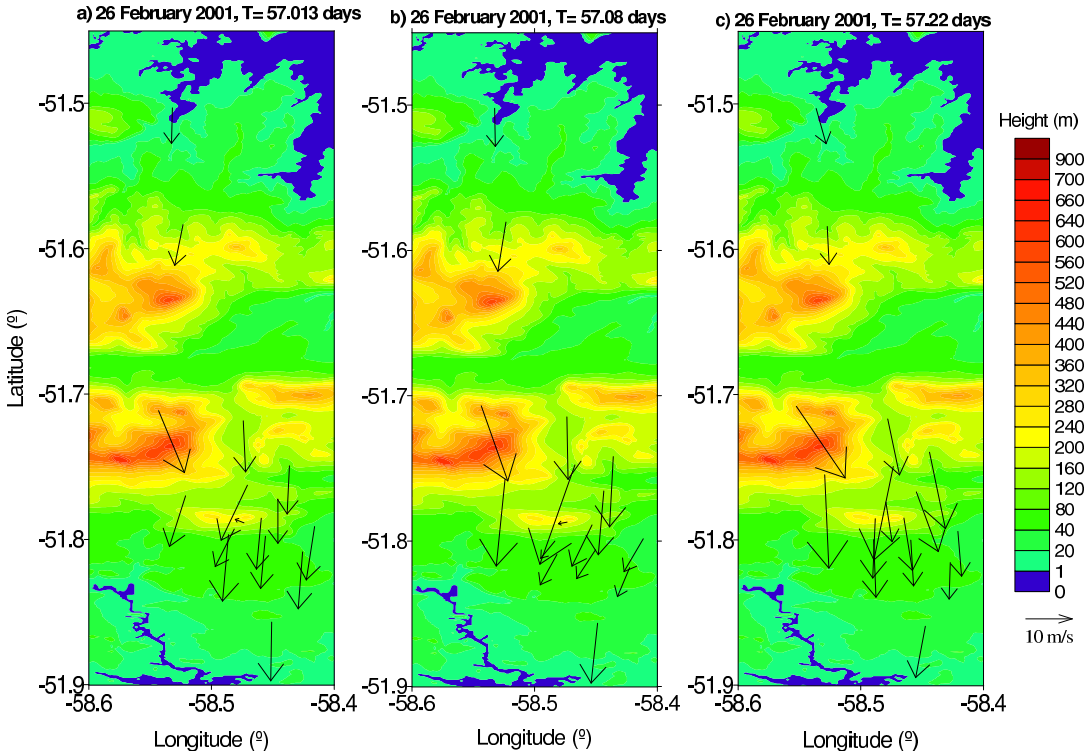

Figure 5.52: The 10 minute average wind field measured at the AWS sites for the (a)beginning, (b)middle and (c)end of the event for the 26^{th} of February 2001.

represents a vertical wind speed of 1.34 ms^{-1} at heights of 200 m. Before the jump there is convergence along the same line with downward wind speed 0.33 ms^{-1}.

The flow acceleration and deceleration is consistent by the values of NH/U. For the radiosonde launch at $2315Z$ on the 25^{th} ($T = 56.969$ days), $NH/U = 1.23$, for the launch at $516Z$ on the 26^{th} ($T = 57.22$ days), $NH/U = 1.31$ and deceleration or small accelerations are expected and observed during these periods. For the $1121Z$ launch $NH/U = 4.78$ and acceleration is expected. In fact, figure (5.53) confirms the assertion that the speed–up increases with an increase in NH/U. From $T = 57.27$days onwards there are several moments when the speed–up is greater than 1.75 (for greater clarity, moments with speed–ups greater than 8 are not shown). As expected, during the period of the reversed flow the speed–up is low and there are also some moments when the flow is decelerated. During the low wind speed phase at station 24, $\Delta s \gg 1$. Note that the speed–up is meaningless for $T < 56.5$, since the flow is southerly during this period.

The standard deviations (figure 5.54) confirm that for the period after the pressure difference increases, when $\Delta s > 1.75$, the flow has low temporal variability. As in the previous cases, during the phase when the flow is decelerated, the temporal variability is

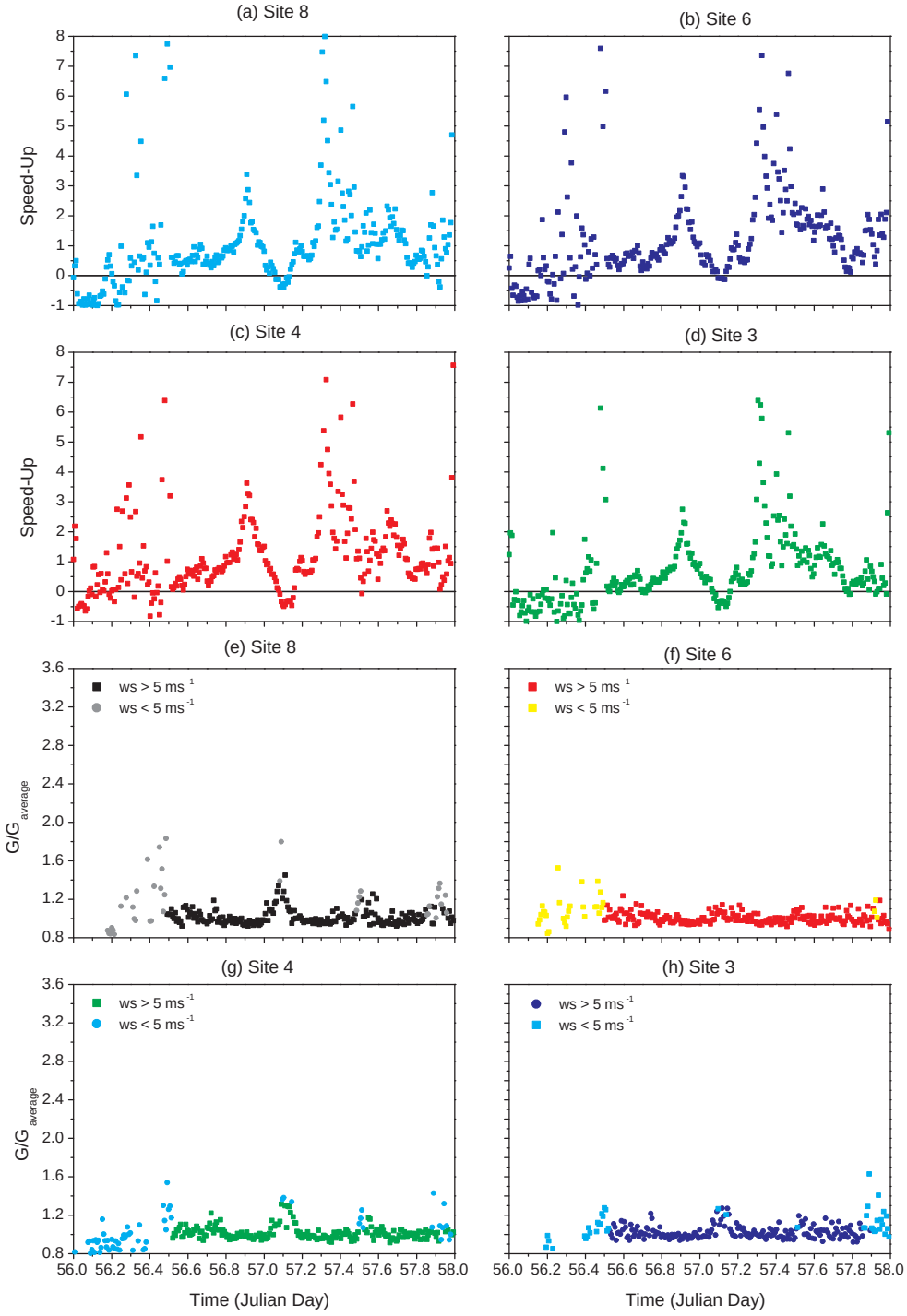

Figure 5.53: Speed–up for stations (a) 8, (b)6, (c) 4 and (d) 3 and gust factors for stations (e) 8, (f) 6, (g) 4 and (h) 3for the 25^{th} and 26^{th} of February 2001.

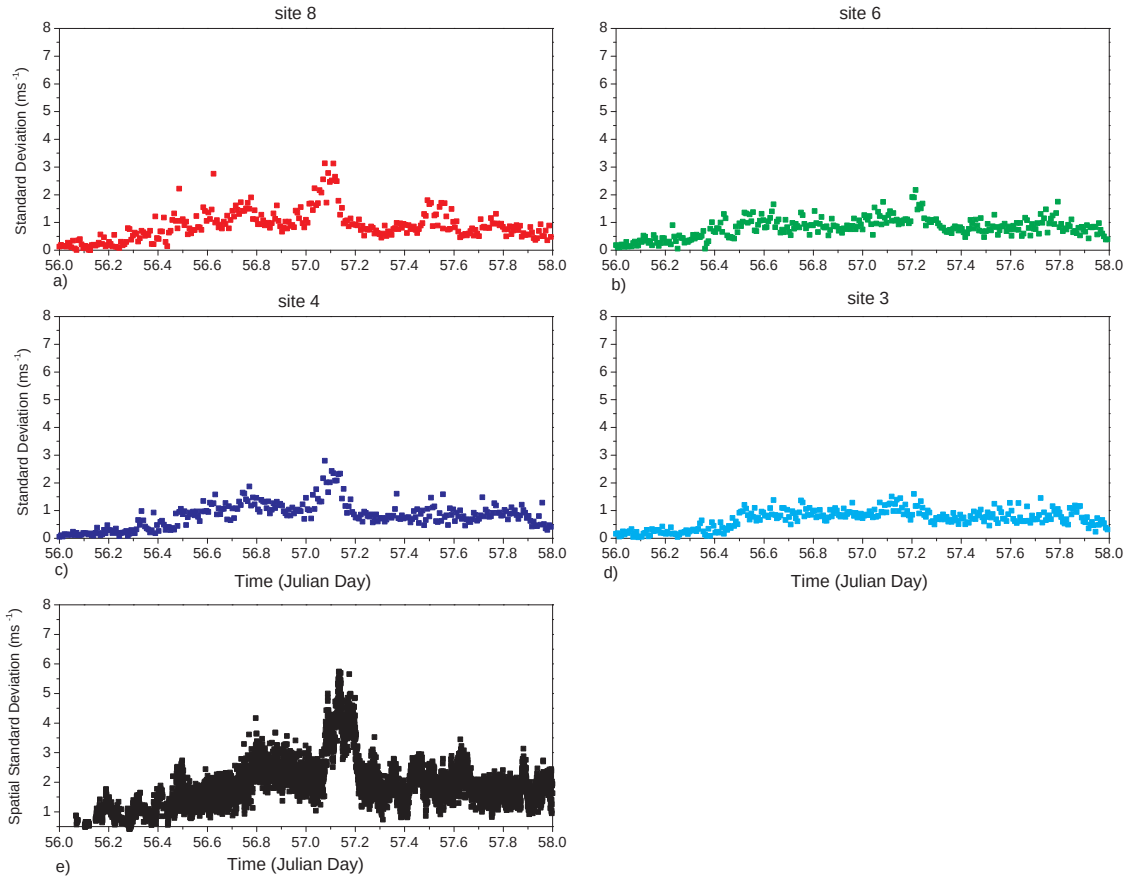

Figure 5.54: 10 min standard deviation for stations (a)8, (b)6, (c)4, (d)3 and (e)horizontal standard deviation for the 25^{th} and 26^{th} of February 2001

increased.

From $T = 57.0$ days onwards the spatial variability is high, there are several periods when $\sigma/U > 0.4$, which puts the flow type into category *ii* for all radiosonde launches. For the twelve hour period of the 25^{th} the spatial variability is low. During this stage $0 < \Delta s < 1.75$ and $\sigma/U < 0.4$, so the flow does not fit into any of the categories.

The gust factors (figure 5.53e, f, g and h) reflect the low temporal variability, since gusts greater than average by more than 20% are observed only during the period of the jump.

In summary, the flow exhibits what could be considered as an hydraulic jump or the advection of a trapped wave. During this period the flow is decelerated and very anisotropic. After, it has a high spatial variability but is not very turbulent (low temporal variability).

5.3 Summary

The wind speeds observed during the campaign are generally not very strong; a high percentage of the wind speed is below 6 ms^{-1}. The highest wind speeds are observed during the summer months. These months also have the highest frequency of northerly winds.

The high frequency of strong lee–side phenomena and temperature inversions on the upwind temperature profiles is related to the consistent higher air temperature relatively to the sea surface and the higher frequency of northerly winds. During these months the reversal of the relationship between the sea surface temperature and the air temperature was only observed for southerly winds.

The winter months are months with the lowest frequency of strong phenomena. On average, the wind speed during these months is the lowest and the frequency of northerly winds is also lower than in the summer months. The sea surface temperature is consistently higher than the air temperature and this is only reversed for northerly flow.

Gustiness and flow acceleration at MPA also revealed a direction dependency. The highest values of both of these parameters are found for northerly flows.

The six case studies can be summarised as follows:

- Downwind deceleration with low spatial and temporal variability: 17^{th} of May and 7^{th} of August;

- Strong downwind acceleration and high spatial and temporal variability: 9^{th} of February and 20^{th} of January;

- Strong downwind acceleration: 8^{th} and 9^{th} of April and 26^{th} of February.

5.4 Appendix: Spectral Analysis

Time series often exhibit a slow varying underlying trend superimposed on higher frequency disturbances under investigation. This trend was removed by differentiating the data with a central difference in time. The Fourier transform pair for a general function $h(t)$ differentiated in time is:

$$\frac{dh(t)}{dt} \quad \Longleftrightarrow \quad -i2\pi f H(f). \tag{5.8}$$

Thus, the Fourier transform pair for the power spectral density becomes:

$$P\left[\frac{dh(t)}{dt}\right] \quad \Longleftrightarrow \quad (2\pi f)^2 S(f). \tag{5.9}$$

Therefore, the power spectral density is not distorted by the detrending procedure.

The spectrum of a discrete and finite time series is merely an estimation of the true spectrum for a continuous set of frequencies. Each of the discrete frequencies is representative of the continuous frequencies in the interval extending halfway from the previous discrete frequency to halfway to the next one. The spectrum is in fact an average of the continuous spectrum over a narrow window centred on each discrete frequency. This leads to significant leakage from one frequency to another.

The reduction of the leakage is obtained by convoluting the fast Fourier transform of the data by the fast Fourier transform of a *window* which is zero for all frequencies except the frequency which is being analysed, i.e., multiplying the data by a window which is one for the period under analysis and zero elsewhere. Six different types of windows where studied:

Bartlett window

$$w_j = 1 - \left|\frac{j - \frac{1}{2}N}{\frac{1}{2}N}\right|, \tag{5.10}$$

Hann window

$$w_j = \frac{1}{2}\left[1 - \cos\left(\frac{2\pi j}{N}\right)\right], \tag{5.11}$$

Welch window

$$w_j = 1 - \left(\frac{j - \frac{1}{2}N}{\frac{1}{2}N}\right)^2, \tag{5.12}$$

Tappered window

$$w_j = \begin{cases} \frac{1}{2}\left[1 - \cos\left(\frac{10\pi j}{N}\right)\right], & \text{for } 0 \le j \le N/10 \\ 1, & \text{for } N/10 < j < 9N/10 \\ \frac{1}{2}\left[1 + \cos\left(\frac{10\pi(j-9N)/10}{N}\right)\right], & \text{for } 9N/10 \le j \le N \end{cases} \tag{5.13}$$

and *Hanning window*

$$w_j = \frac{1}{2}\left[1 + \cos\left(\frac{2\pi j}{N}\right)\right], \tag{5.14}$$

where N is the number of points under analysis which is a power of 2.

Figure (5.55) shows a two hour pressure spectrum (the procedure used to determine

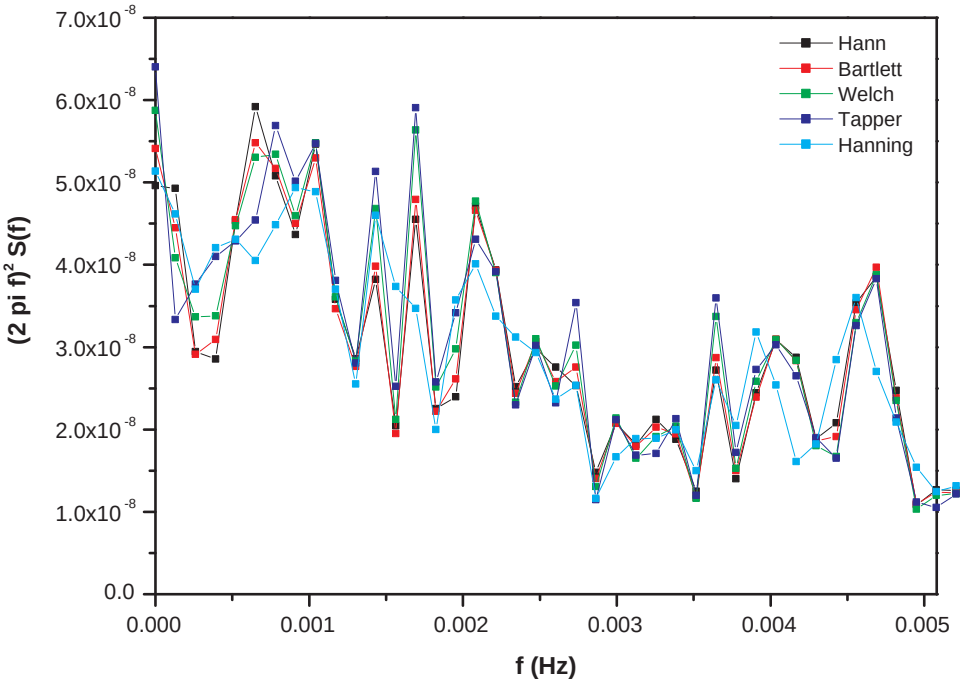

Figure 5.55: 2 hour pressure spectrum determined by applying the five different windows

the spectrum is described in the next paragraph) determined by multiplying the data by each of the previous windows. The last two windows smooth considerably the lower frequencies and the later even identifies peaks which the other windows do not. The first three have very similar behaviour. Following the recommendation from Press *et al.* the Bartlett window was chosen to be used in the spectral analysis.

An estimate of the power spectrum is obtained through the computation of an estimator which is historically called periodogram. Each data section is divided into K segments with $2M = N$ data points which overlap by one half of their length. Each seg-

ment is FFT'd and the K periodograms are then averaged together to produce a power spectrum estimate at $M + 1$ frequencies. The overlapping of the data segments is done in order to obtain the smallest spectral variance per data point from the section of data under analysis. The total number of points in the data set has to be $(2K + 1)M$.

There needs to be some care in the averaging process because when too many sections are used, there is the risk that the energy at relevant frequencies may be smoothed. There is not, though, a consensus about the number of K segments needed to produce a spectrum which is a true measure of the continuous spectrum. Chatfield (2003) suggests that the number of segments should be $N/40$ but also reveals that $\sqrt{2}N$ is probably a better limiting value.

The pressure spectrums were determined from the 30 s data so for a two hour spectral analysis each of the K segments is composed by 256 points and a one hour spectrum needs 128 points (the number of points to be FFT'd has to be a power of two). For a two hour spectrum 11 averaging sections can be obtained from a 24 hour period [5] although this is below the top limit it is well above the lower limit.

The highest limit is only achieved when a one hour spectrum is performed. In this case, a day can be separated into two, twelve hour, subsets from which 11 averaging sections are used to determine the one hour power spectrum. The lower averaging limit implies the need for four averaging sections. With this in mind, each day was split into eight three hour subsets and the one hour power spectrum was determined for each subset. The spectral density plots are constructed from the time series of isopleths of spectral densities, $(2\pi f)^2 S(f)$, determined from the eight power spectrums.

[5] Since the number of points has to be $(2K + 1)M$ and a power of two, the data series starts at 23:44 of the previous day and ends at 15:30 of the next day.

6. 1-D Simulations

In the previous test case analysis, the lack of an upstream radiosonde profile and the inability of the forecast model to produce temperature inversions with the correct strength and at the appropriate height constrains the capability of the forecast in predicting these strong events and any subsequent modelling. The one dimensional model described in chapter 3 was developed with the aim of providing an approximate upstream profile which would aid the forecasting of these events. The model was run for the test cases of the preceding chapter and for two other cases where the Met Office forecast departs form the radiosonde profile.

In chapter 5 it is suggested that the advection of warm northerly air over a colder ocean surface is responsible for the development of the inversion in the first 500 m therefore, it is expected that thermal advection rather than the surface heat flux will be the primary driving force in the boundary layer. In the 1–D model, the thermal advection is determined through the thermal wind equations thus, the geostrophic wind is evaluated before each run.

The geostrophic wind was calculated using the ECMWF ERA40 analysis through the following formula:

$$\frac{\partial \vec{v_g}}{\partial p} = -\frac{R}{fp}\vec{i} \times \nabla T. \tag{6.1}$$

This can be vertically integrated between two levels (level 1 —higher level — and level 2 — lower level) through the following procedure:

$$\int_{p_1}^{p_2} \frac{\partial \vec{v_g}}{\partial p}\, dp = -\int_{p_1}^{p_2} \frac{R}{fp}\vec{i} \times (\nabla T)_p\, dp. \tag{6.2}$$

The approximation $\frac{\partial \vec{v_g}}{\partial p} dp \approx d\vec{v_g}$ is used. It is also assumed that the temperature is constant over the pressure interval, which is a good approximation if the temperature is averaged over that interval. Then,

$$\int_{p_1}^{p_2} d\vec{v_g} = -\frac{R}{f}\vec{i} \times \nabla \overline{T} \int_{p_1}^{p_2} \frac{dp}{p} \tag{6.3}$$

or

$$\vec{v_{g1}} - \vec{v_{g2}} = -\frac{R}{f}\vec{i} \times \nabla\overline{T} \ln \frac{p_1}{p_2}. \tag{6.4}$$

The surface geostrophic wind is used as the lower boundary condition and the surface horizontal pressure gradient was obtained by averaging five adjacent pressure gradients between two grid points five degrees apart. The geostrophic wind profile was determined every six hours and was interpolated into a time series with a $\Delta t = 20$ s.

The lower boundary conditions for temperature and pressure were obtained from the ECMWF's ERA40 analysis and the specific humidity was obtained from the Met Office forecast. The first two variables were available with an interval of six hours and the third was obtainable at three hour intervals. The use of different sources is due to the lack of surface specific humidity in the ERA 40 analysis or the lack of 2 m forecast values for the temperature and of surface pressure. A time series with the same Δt was also obtained for each parameter.

Note that, since the geostrophic wind can only be obtained every six hours, the model runs were started at either 0000 Z, 0600 Z, 1200Z and 1800 Z, in an attempt to improve accuracy.

6.1 1-D Simulations of the Test Cases

A summary of the relevant features of the test cases is given in table 6.1.

6.1.1 9^{th} of February 2001

As previously described, a temperature inversion is observed as early as the $1123Z$ radiosonde of the 8^{th} of February and since the radiosonde at $2323Z$ on the 7^{th} shows a very weak and small inversion at $\sim$ 900 m, the one dimensional model was started with the Met Office forecast profile for $0000Z$ for the 8^{th} of February. The model run ended at $1200Z$ on the 9^{th} of February.

Figure (6.1) shows the initial profile. The temperature has a neutral layer between 1000 m and 1500 m, but otherwise decreases with height and the wind is westerly and veers with height.

The model develops a small inversion near the surface in the first hours and by $1123Z$

Date	Time	Inversion Height (m)		ΔT (K)	Comments
		Base	Top		
09/02/2001	$1126Z$	232	393	7.1	Accelerated flow interspersed with very turbulent decelerated flow. Rotors observed near the surface.
20/01/2001	$1112Z$	291	334	1.5	Accelerated flow with decelerated flow at the beginning and end of the event.
8 and 9/04/2001	$0507Z$	341 725	502 976	4.9 3.4	Small downslope windstorm.
25 and 26/02/2001	$2315Z$	374	858	7.3	Downslope windstorm with possibly an hydraulic jump or travelling trapped wave in the middle of the event.

Table 6.1: Summary description of the test cases with accelerated flow from the previous chapter

the potential temperature vertical profile is almost coincidental with the radiosonde's (figure 6.2a — black line). Although the model runs are meant to represent the upstream profiles this is not surprising since the 2 m wind at site 24 has very low speed and its direction oscillates wildly up to one hour before the radiosonde launch. The geostrophic wind direction in the profiles obtained for $0000Z$ and $0600Z$ is westerly so there is very limited flow across the two ridges and is conceivable that the vertical temperature profiles are reasonably correlated. In the hour that precedes the launch; the wind strengthens and turns northerly but probably the small oscillations of the balloon ascent rate could

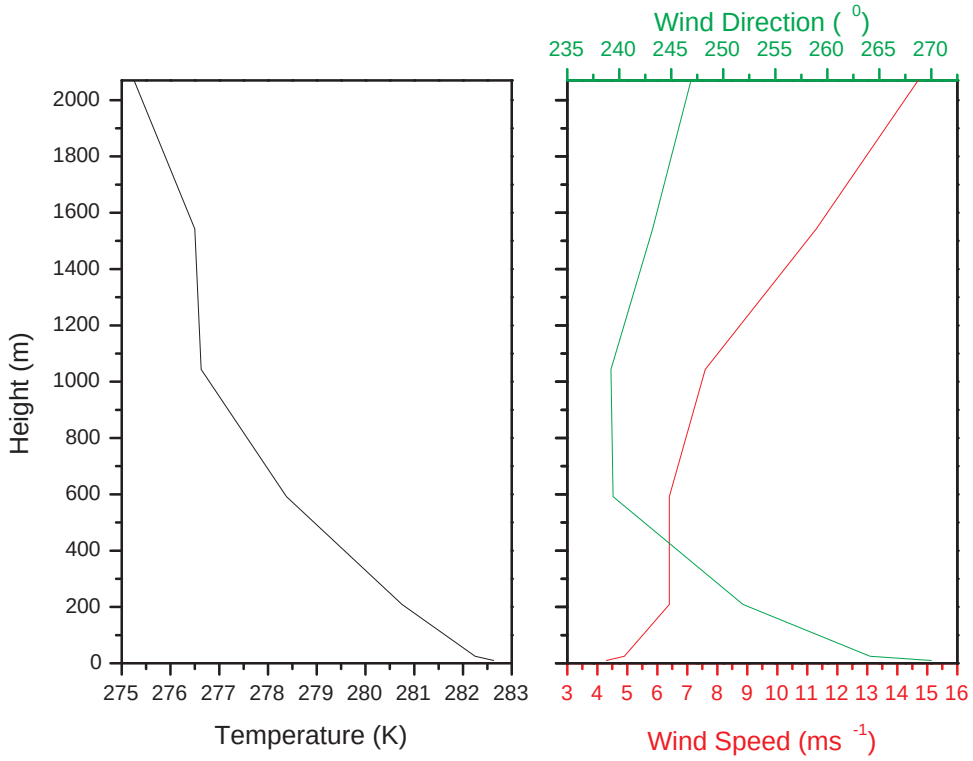

Figure 6.1: Met Office forecast vertical profile for temperature and wind speed and direction for $0000Z$ on the 8^{th} of February 2001.

be taken as an indication that the atmosphere at MPA is not very much disturbed by the flow across the ridges. The Met Office forecast (in blue) is unable to reproduce this structure and its atmosphere is warmer than the observed.

By $2320Z$, (figure 6.2b — black line) the correlation between the model and the radiosonde is greatly reduced. The model and radiosonde profiles concur above 1600 m, i.e., above the boundary layer and the base of the inversion in both profiles differs only by 40 m. The top of the inversion in the model is well above the height of Mt. Wickham and is considerably higher than the radiosonde's, by about 400 m. It is reasonable to assume that between 671 m (where the model's profile intersects the radiosonde's profile) and 1600 m the model is too warm. In Vosper (2004) the propagation of the trapped gravity waves is at the height of the inversion and above it the vertical temperature profiles are concurrent. Below the temperature inversion and in its vicinity the downstream temperature profile should be warmer than the upstream as a result of the contraction of the isentropes due

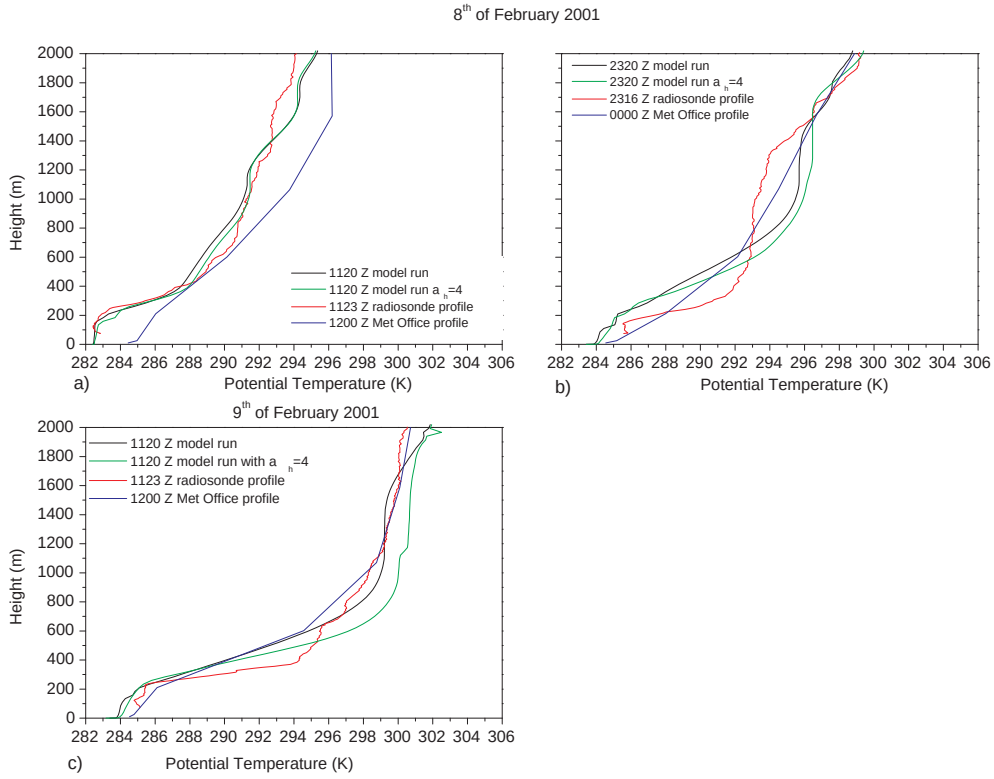

Figure 6.2: 1–D model potential temperature vertical profiles 8^{th} and 9^{th} of February 2001. The radiosonde potential temperature is shown in red for comparison. The Met Office forecast is shown in blue. The green line represents a model run with α_h and $\alpha_q = 4$. (a) $1123Z$ on the 8^{th} of February, (b) $2320Z$ on the 8^{th} of February and c) $1120Z$ on the 9^{th} of February

to the downslope flow. So, the higher temperatures in the model are a result of a incorrect e valuation of the temperature advection. In the results presented here, the geostrophic wind was given for three levels (surface, $\sim$ 1100 m and $\sim$ 2200 m) but in another run with fourteen levels (not shown) the model's temperature increases even more, which is even more unrealistic. The correlation between the Met Office forecast and the radiosonde is not much better. Not only is the forecast unable to produce an inversion, it is also too warm between 700 and 1600 m.

At $1120Z$ on the 9^{th}, the correlation is improved. Once again the temperature inversion's top is above Mt. Wickham's summit and the model's profile above 1600 m is too warm. The correlation between this profile and the Met Office forecast is very good. Nevertheless the lack of resolution of the former implies that the height of the top of the

inversion and its amplitude is not correctly determined.

In an attempt to produce more reasonable profiles the model's α_h and α_q were reduced form 10 to 4 (figure 6.2 — green line). Note that these parameters were obtained through the sensitivity analysis of the Wangara experiment. The results were not significantly different; in fact the results are slightly worse. Other attempts were also made by changing the geostrophic wind calculation procedure. No significant changes were found, the only possible conclusion is that the ECMWF's analysis overestimates the temperature advection in the boundary layer layers above the inversion.

6.1.2 20^{th} of January 2001

The $1100Z$ radiosonde profile for the 19^{th} of January is the first that reflects a stable boundary layer. It shows just a small temperature inversion above 1400 m. Hence, the model was initialised at $1200Z$ on the 19^{th} and was run for 24 hours until $1200Z$ on the 20^{th} of January.

From $1200Z$ on the 19^{th} up to $0000Z$ on the 20^{th}, the geostrophic wind direction is westerly, and becomes northerly afterwards. During the period of westerly wind the model's atmosphere develops a convective boundary layer below 1300 m. It is worth noting that the surface temperature is considerably warmer than the forecast's first level (black line in figure (6.3)). At $2200Z$ (two hours before sunset) an incipient stable boundary layer can be observed near the surface which grows and by $0800Z$ (sunrise) it has a depth of 300 m. Above it, there are two other layers: residual layer is observed between the top of the former convective boundary layer ($z = 900$ to $z = 1300$ m) and a layer which cools more slowly than the stable layer and remains well mixed. At $0600Z$ the warming effect of the northerly flow becomes apparent since the temperature inversion between the two layers steepens.

In figures (6.3c and d) the model results are compared with the radiosonde profiles. At $2300Z$ the model's stable layer is thinner than the one observed at MPA and the model's surface temperature is clearly warmer than the observed (black line). Nevertheless, model manages to reproduce reasonably well the height of the mixed layer but is incapable to replicate the potential temperature gradient of the free atmosphere. The smaller temperature gradient of the free atmosphere could be due to an inappropriate top boundary condition which is used in the radiation model to determine the radiation fluxes or to not

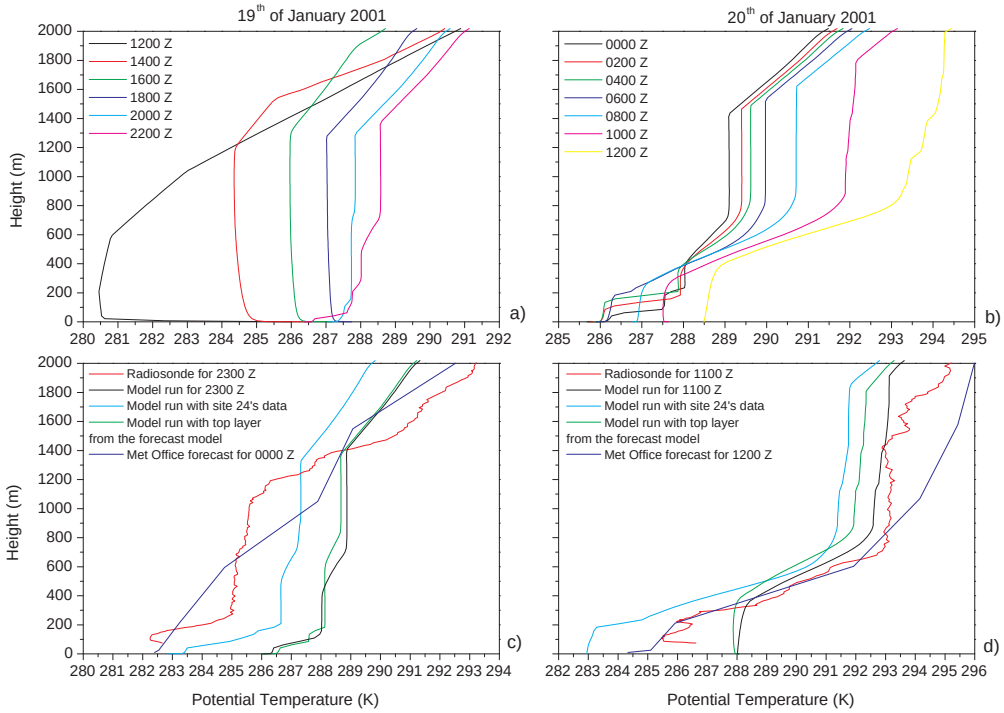

Figure 6.3: 1–D model potential temperature vertical profiles a)19^{th} and b)20^{th} of January 2001. c) Potential temperature profiles for the 1–D model with ECMWF's ERA40 2 m temperature and surface pressure (black line), 2 m temperature and surface pressure from site 24 (blue line) and top boundary condition for the radiation model forced by the forecast profiles (green line). The radiosonde potential temperature is shown in red for comparison. The blue line represents the Met Office forecast. Profiles for the 19^{th} at $2300Z$. d) As in c) but for the 20^{th} at $1100Z$.

enough temperature advection (related to the strength of the geostrophic wind). To assess the first problem the top boundary condition for the radiation scheme was changed.

The atmosphere above the model's top layer was assumed to be in hydrostatic balance and the temperature decreased with height according to the dry adiabatic lapse rate. Five layers, each 1 km apart, were added and the temperature and pressure of each layer are determined by:

$$T(z) = T(nz) - 0.0065\Delta z, \tag{6.5}$$

$$p(z) = p(nz)\left[\frac{T(z)}{T(nz)}\right]^{\left(\frac{g}{0.0065R_d}\right)}. \tag{6.6}$$

The water vapour is assumed to be equal to the water vapour at the top of the model. Note that these layers are only part of the radiation scheme.

The previous profile was replaced by 8 layers with temperature, pressure and humidity obtained from the forecast model. The results at the top of the model do not differ from each other; the differences appear at the height of the inversion (green line).

Different geostrophic wind profiles were also used but with no success. There is not enough heating at this height.

The potential temperature difference between site 24 and the stations at MPA was around 1 K for $T = 2300Z$ so, a ~ 4 K difference between the model's results and the observed seems excessive. To address this discrepancy the surface boundary conditions for temperature and pressure were replaced by the one hour average of these two variables observed at site 24 (blue line). The model's profile is parallel to the previous ones and shows a better agreement at the surface.

Although the Met Office forecast has a reasonable surface temperature it is unable to reproduce the stable layer near the surface as well as the mixed layer above it and the potential temperature gradient of the free atmosphere. Its correlation with any of the previous profiles is very poor.

At $1100Z$ the agreement between the model's results and the radiosonde profile for the layers above the surface mixed layer is very good. The temperature inversion in the model is higher and smaller than the observed at MPA. It is to be expected that the tightening of the isentropes due to the downslope flow would lead to an inversion which is lower and larger than the one observed upstream. The difference in the surface temperatures might once again be due to an overestimation of the 2 m air temperature by the ECMWF. The profile obtained with site 24's temperature and pressure does not seem reasonable since the top of the inversion upstream is lower than the observed at MPA. Now, the correlation between the Met Office forecast and the radiosonde profile is very good for the layers below the top of the inversion, but once again, the lack of resolution implies that the top of the inversion and its amplitude is not very well determined. The forecast also has an atmosphere above the inversion which is warmer than the observed.

6.1.3 8^{th} and 9^{th} of April 2001

The radiosonde launch at $1117Z$ on the 8^{th} of April reveals a stable boundary from the ground up to 1624 m where an inversion can be observed and there are no oscillations in the balloon ascent rate that would indicate the presence of a gravity wave. Thus, the model run was initialised with the forecast profile for $0000Z$ (figure 6.4a and b).

The initial wind direction is south–westerly which concurs with the wind direction

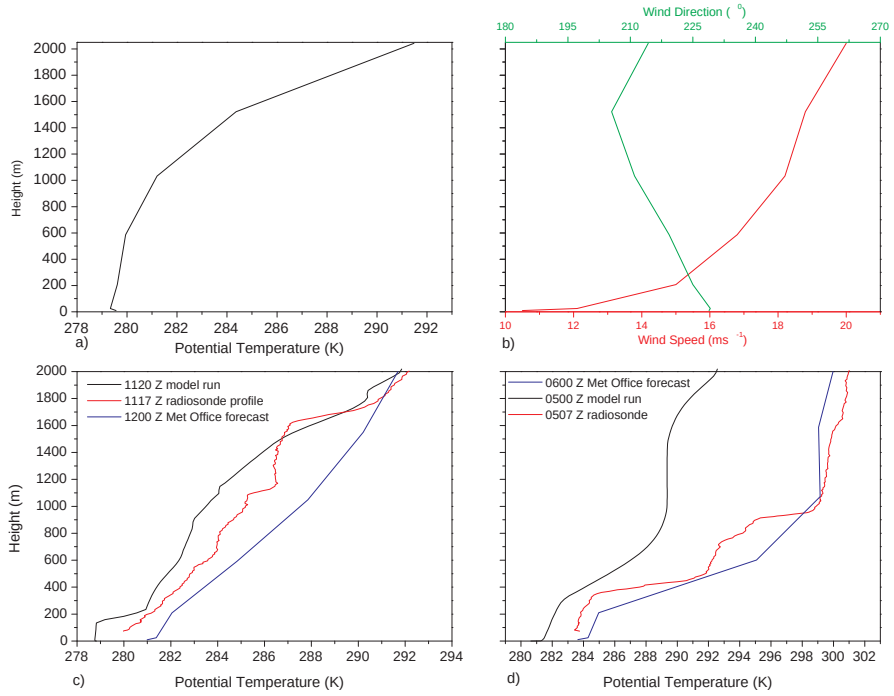

Figure 6.4: Met Office $0000Z$ forecast vertical profile for: (a) potential temperature, (b) wind speed and direction for the 8^{th} of April 2001. 1–D model potential temperature vertical profiles for: (c) $1120Z$ for the same day and (d) $0500Z$ for the 9^{th} of April 2001. The radiosonde potential temperature is shown in red for comparison. The Met Office forecast is shown in blue.

measured at site 24 and the geostrophic wind direction is also south–westerly.

By $1120Z$ the model results agree reasonably well with the radiosonde profile except for the first 200 m where the model exhibits a neutral layer topped by a small inversion. Since the surface temperature is the model is colder than the observed this small inversion could be due to the incorrect evaluation of the 2 m temperature in the ECMWF ERA 40 analysis. From 500 m upwards the model's profile has kept the shape of the forecasts'

profile, thus an improvement in the forecasts resolution would improve the correlation between the two profiles. The forecast profile for $1200Z$ does not show the temperature inversion near the surface and its too warm. It is, nevertheless, a reasonable upstream profile.

At $0500Z$ on the 9^{th}, the two profiles differ significantly. The model produces a temperature inversion from 360 m up to 940 m which is approximately the height of the base of the second inversion in the radiosonde. The radiosonde balloon ascent rate shows evidence of a very strong gravity wave below 5000 m so the downslope wind may be responsible for the lowering of the top of the inversion and if wave breaking occurs the entrainment of warmer air from above may induce the second one. Hence, this higher inversion would never occur in an upstream profile and the potential temperature above it would be lower. The Met Office profile for $0600Z$, also seams reasonable since its inversion envelops both of the radiosonde's inversions and the temperature profile above them is well correlated with the observed. This agreement could also be the result of the influence of the $0500Z$ radiosonde in the model run.

6.1.4 25^{th} and 26^{th} of February 2001

A stable boundary layer is observed between $2300Z$ on the 24^{th} and the $1111Z$ on the $25th$ of February. Thus, the model was initialised with the $0600Z$ forecast profile.
Figure (6.5) illustrates the potential temperature profiles for the radiosonde launches at $1116Z$ (figure 6.5a) and $2320Z$ (figure 6.5b) on the 25^{th} of February and $520Z$ on the 26^{th} of February (figure 6.5c). At $1116Z$, the model reproduces reasonably well the stable profile except for the first 200 m where a small temperature inversion can be observed. This is probably due to the incorrect 2 m temperature in the ECMWF analysis. At $2320Z$ the model's temperature inversion is visibly lower than the inversion captured by the radiosonde, there is too much temperature advection below 680 m. According to the model, the temperature inversion is below the height of Mt. Wickham. Since the temperature inversion at MPA is higher than the model's (i.e., the temperature at MPA is colder than the model's), the model results are not reasonable. By $0520Z$ the model results above 500 m are well correlated with the radiosonde profile and could be taken as an approximation of an upstream profile. Be low 500 m, the model's boundary layer is warmer than the observed. An attempt to run the model with the temperature and pressure at site

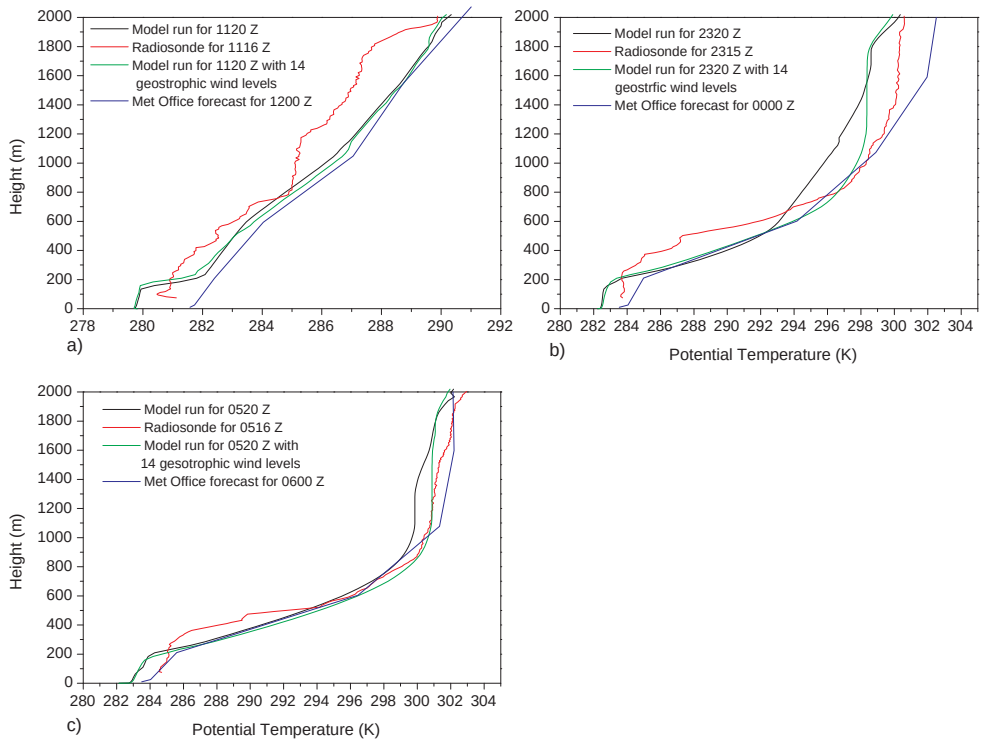

Figure 6.5: 1–D model potential temperature vertical profiles for the 25^{th} and 26^{th} of February 2001. The radiosonde potential temperature is shown in red for comparison. The green line represents a model run with 14 levels in the geostrophic wind profiles. The Met Office forecast profiles are shown in blue. (a) $1116Z$ and (b) $2320Z$ on the 25^{th} of February and $0520Z$ on the 26^{th} of February

24 was made but the model was unstable. A model run with increased resolution in the geostrophic wind profile is represented in figure (6.5), green line. The differences between the runs is more obvious in the $2320Z$ profiles. The correlation between the model results and the radiosonde between 680 m and 1500 m is visibly improved, but overall the temperature inversion is still lower than the observed. Nevertheless, the top of the inversion is nearer the observed and is above Mt. Wickham's height. The Met Office forecast for $1200Z$ on the 25^{th} and for $0000Z$ and $0600Z$ on the 26^{th} is very well correlate with the model's profiles.

6.2 Two Extra Cases

In this section the 1–D model was run for two cases where the Met Office forecast departs significantly from the radiosonde profile.

6.2.1 20^{th} and 21^{st} of August 2001

This event is very similar to the event that occurred between the 25^{th} and 26^{th} of February 2001. As in that case, the flow downstream is considerably accelerated and a high pressure difference between station 24 and the downstream stations is observed. On $0000Z$ of the 21^{st} this pressure difference decreases significantly while the pressure difference between the downstream stations increases.

A 5^{o} C temperature inversion is observed on the $1112Z$ ($T = 232.47$ days) radiosonde profile for the 20^{th} of August, hence the one dimensional model was initialised with the Met Office forecast for $0000Z$ on the 20^{th} of August.

At $1112Z$ the correlation between the model and the radiosonde is not very good. The model's surface temperature is 4 K warmer than the radiosonde's (figure 6.6). This is due to differences between the 2m temperature in the ECMWF ERA 40 analysis and the Met Office temperature profile. The temperature inversion in the model starts at the same height as in the radiosonde, but the temperature gradient of the former is considerably greater. The temperature inversion in the radiosonde ends at 377 m while it ends at 858 m in the model. The inversion amplitude in the model is also smaller, thus the subsequent temperature profile is colder.

The correlation between the radiosonde and the Met Office is considerably better.

By $2312Z$ the correlation between the forecast and the radiosonde is considerably reduced. Due to the low resolution the height of the inversion is not correctly determined. Since a strong oscillation is observed in radiosonde ascent rate and there is a large pressure difference between station 24 and the downstream stations it is reasonable to assume that the strong temperature gradient in the inversion is due to the downslope flow. Hence this should not be mirrored in the upstream profile.

The surface temperature difference between boundary layer model and the radiosonde is now reduced to 1 K. The height of the inversion is also well determined but the temperature profile above the inversion is significantly colder. In an attempt to produce a more reasonable profile different procedures were used to determine the geostrophic wind but

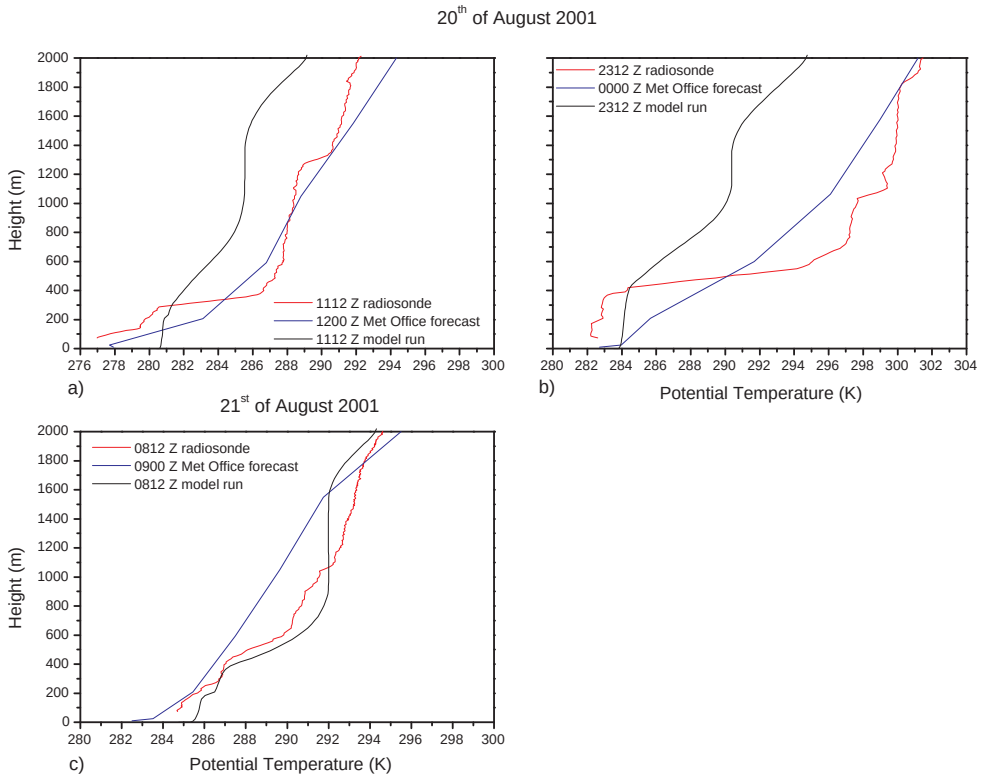

Figure 6.6: 1–D model potential temperature vertical profiles for the 20^{th} and 21^{st} of August 2001. The radiosonde potential temperature is shown in red for comparison. The blue line represents the Met Office forecast. (a) $1112Z$ and (b) $2312Z$ on the 20^{th} of August and $0810Z$ on the 21^{st} of August

no significant changes were found. The possible conclusions are that either the ECMWF's analysis underestimates the temperature advection above the inversion or the wave activity is responsible for that warming. Note that a hydraulic jump or some strong wave activity starts around this time.

At $0812Z$ the correlation between the boundary layer model and the radiosonde is very good. The temperature inversion in the model is slightly lower than the one in the radiosonde and its amplitude is also greater. Now, the correlation between the Met Office forecast and the radiosonde is smaller, in fact, the temperature inversion is absent from the profile.

6.2.2 27^{th} of January 2001

A strong downslope windstorm is observed during the first half of the day and the radiosonde temperature profile for $1118Z$ has a 3.5^{o} C inversion which starts at 100 m.

The radiosonde launch for $1113Z$ the 26^{th} of January reveals a stable boundary layer

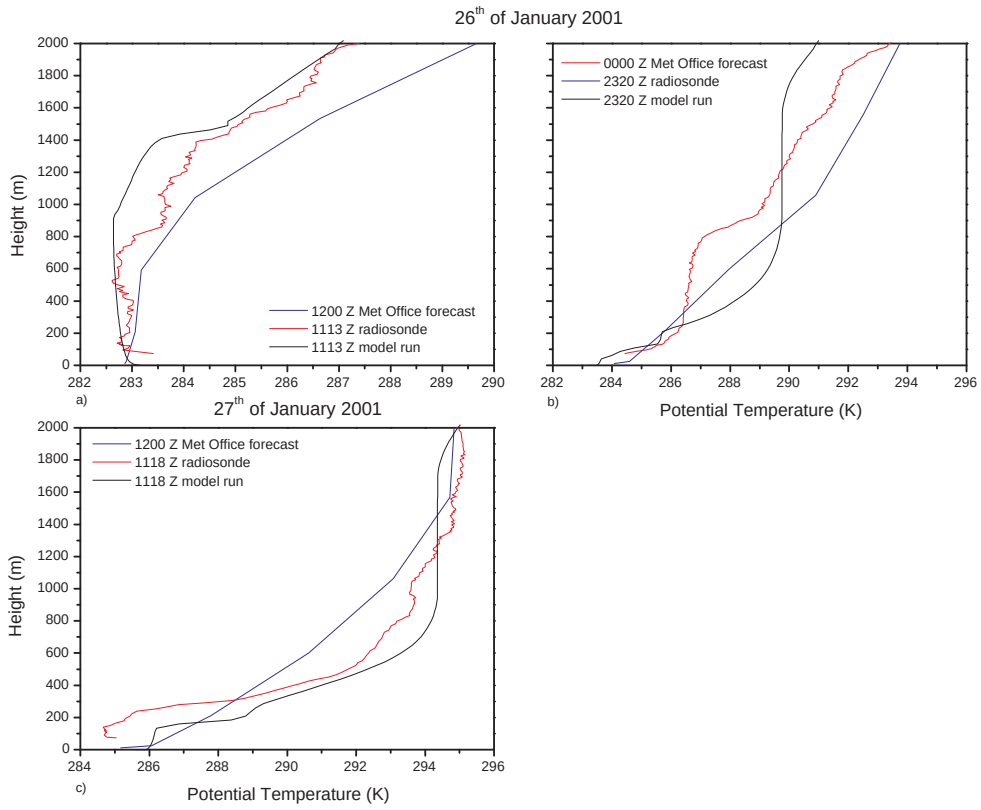

Figure 6.7: 1–D model potential temperature vertical profiles for the 26^{th} and 27^{th} of January 2001. The radiosonde potential temperature is shown in red for comparison. The blue line represents the Met Office forecast. (a) $1113Z$ and (b) $2320Z$ on the 26^{th} of January and $1118Z$ on the 27^{th} of January

from the surface to 2000 m, hence the model was initialised with the $0600Z$ Met Office forecast.

The model is able to reproduce the radiosonde's $1113Z$ temperature profile (figure 6.7a). Since the wind for the layers below 2000 m is westerly it is reasonable to assume that the profiles on either side of the ridge would be similar.

Figure (6.7a) also shows that the Met Office forecast is able to correctly forecast the

temperature profile for the layers below 1000 m. However the forecast is too warm for the levels above 1000 m.

By $2320Z$ the wind at the surface has become northerly and it veers with height and the wind speed for the layer below the temperature inversion (figure 6.7b) is between 2 and 4 ms^{-1}. The model's profile and the forecast are not able to reproduce the inversion which could be the result of a local phenomenon. The correlation between both profiles and the radiosonde is poor.

The correlation between the $1118Z$ radiosonde and the model run is good. Although the model's temperature for the layers below 1200 m is higher than the observed in the radiosonde, the top of the inversion is above Mt. Wickham's summit (700 m). The Met Office forecast profile is not as well correlated; in fact, the inversion is absent from this profile. Since the wind is northerly and the air temperature is greater than the SST it is reasonable to assume that an inversion should be present in the upstream profile.

6.3 Summary

The model predicts that the top of the temperature inversion is above Mt. Wickham's summit for all cases. For the cases in February the model results exhibit a boundary layer which is probably warmer than the one that would be observed upstream. This is related to the temperature advection and suggests that the ERA40 analysis is overestimating the temperature advection for those days. In the January test case, the model results are in good agreement with the observed profiles, apart from the surface temperature which is overestimated. Apart from the $2300Z$ profile the second January case is also well modelled. The April case seems to also be well modelled as well as the August case. In both cases the strong wave activity changes the downstream potential temperature significantly.

An improvement in accuracy of the temperature advection would significantly improve the accuracy of the model's results as well as in the Met Office forecast.

Due to the coarse resolution the Met Office forecast has difficulty in determining the inversions amplitude and heights.

7. A 2–D Approach to the Effects of Inversions on Flow Over Ridges

An ubiquitous feature of the flow of the preceding chapters, was the presence of a temperature inversion. The influence of such an inversion on flow over a ridge has already been approached by Vosper (2004). In his work, simulations of flow over an isolated two–dimensional ridge were conducted for a range of inversion strengths and heights above the mountain top.

Although the inversions simulated in the previous chapter reach heights which are above 640 m (altitude of Mt. Wickham), they start well below the mountain top. The lack of literature on the influence of such inversions in the development of strong downslope winds, the formation of rotors and low–level turbulence, lead to the implementation of simulations in which the inversions are below the mountain top.

Grisogono *et al.* (1993) found that the mountain wave drag (MWD) exerted by linear hydrostatic waves on two ridges is not just the sum of MWD for each individual ridge; there is a third component which is the order of the product of the heights of the two mountains. They also show that the MWD is also dependent on the spacing between the ridges. Vosper (1996) expanded this work and determined that the interference between the waves generated by the two mountains was most dramatic when the waves are trapped in the lower layers of the atmosphere. Since the Falklands topography is composed by two ridges, the effects of such interference in the type of flows of the preceding paragraph will also be examined in this chapter.

The aim of this chapter is to extend Vosper's (2004) work to inversions below the summit and to flow over two ridges. A simulation of the case study for the 9^{th} of February 2001 will also be presented. The one dimensional profile obtained from the boundary layer model will be used to initialise the simulation.

7.1 Configuration of the simulations

The simulations were performed with the Met Office BLASIUS code (Wood and Mason, 1993), which has been extensively used for studies on flow over hills and boundary layer problems (Brown *et al.*, 2003; Vosper, 2003; Ross and Vosper 2003). The model solves the Bousinesq equations in a terrain following coordinate system (Gal-Chen and Somerville, 1975).

$$\frac{DU}{Dt} - fV = -\frac{1}{\rho}\frac{\partial p'}{\partial x} + \frac{1}{\rho}\left(\frac{\partial \tau_{11}}{\partial x} + \frac{\partial \tau_{12}}{\partial y} + \frac{\partial \tau_{13}}{\partial z}\right) \tag{7.1}$$

$$\frac{DV}{Dt} + fU = -\frac{1}{\rho}\frac{\partial p'}{\partial y} + \frac{1}{\rho}\left(\frac{\partial \tau_{21}}{\partial x} + \frac{\partial \tau_{22}}{\partial y} + \frac{\partial \tau_{23}}{\partial z}\right) \tag{7.2}$$

$$\frac{DW}{Dt} = -\frac{1}{\rho}\frac{\partial p'}{\partial z} + \frac{1}{\rho} + g\frac{\theta'_v}{\theta_{vr}} - g\frac{p'}{c^2\rho}\left(\frac{\partial \tau_{31}}{\partial x} + \frac{\partial \tau_{32}}{\partial y} + \frac{\partial \tau_{33}}{\partial z}\right) \tag{7.3}$$

$$\frac{\partial(\rho U)}{\partial x} + \frac{\partial(\rho V)}{\partial v} + \frac{\partial(\rho W)}{\partial z} = 0 \tag{7.4}$$

$$\rho\frac{D\theta}{Dt} = \frac{\partial H_x}{\partial x} + \frac{\partial H_y}{\partial y} + \frac{\partial H_z}{\partial z} \tag{7.5}$$

where τ represents the Reynolds stress tensor and H_i represents the turbulent flux of potential temperature in the i^{th} direction. The equations are discretised using finite differences with a second–order scheme for the advection of velocity (Piacsek and Williams, 1970) and the Ultimate–Quickest scheme for the advection of potential temperature (Leonard *et al.*, 1993).

The lower boundary condition used in these simulations was a no–slip condition obtained by a similarity condition for the surface stress and using a constant roughness length of 0.05 m. The turbulence closure was a first–order Richardson number dependent mixing length closure scheme.

All the simulations were run with 1024 grid points in the horizontal, with a $\Delta x = 150$ m, and 60 grid points in the vertical (see appendix at the end of the chapter for the influence of resolution on the results). Periodic boundary conditions were applied in the horizontal and the top of the model was considered to be a rigid lid. Rayleigh damping layers were placed above 15 km and in the first and last 8 km of the horizontal domain. These layers, along with a fourth order smoothing applied in the horizontal to the perturbation velocity and potential temperature are effective in removing wrap–around effects and grid–scale noise.

The idealised ridge used in the simulations with just one mountain had the form:

$$h(x) = \begin{cases} H_1\{1 + cos(Kx)\}/2 & \text{for} |x| \leq \pi/K \\ 0 & \text{for} |x| > \pi/K, \end{cases} \tag{7.6}$$

where $x = 0$ is the centre of the model domain, $H_1 = 617$ m (height of Mt. Simon), $K = 2\pi/L$ and $L = 28000$ m, which is an approximate span of the two ridges in East Falkland. For the simulations with two ridges the following equation was used:

$$h(x) = \begin{cases} 0 & \text{for } x < -(a+b) \\ H_1\{1 - cos((\pi/a)(x - a + b))\} & \text{for } -(a+b) \leq x < -b \\ H_1\{1 - cos((\pi/b)x)\} & \text{for } -b \leq x < 0 \\ H_2\{1 - cos((\pi/c)x)\} & \text{for} 0 \leq x < c \\ H_2\{1 - cos((\pi/d)(x + d - c))\} & \text{for} c \leq x < c + d \\ 0 & \text{for} x > c + d, \end{cases} \tag{7.7}$$

where, as before, $x = 0$ is the centre of the model domain; $H_1 = 617$ m (height of Mt. Simon); $H_2 = 640$ m (height of Mt. Wickham); $a = 9000$ m and $b = 5800$ m (lengths of Mt. Simon); $c = 5500$ m and $d = 7500$ m (lengths of Mt. Wickham). The total length of the ridges is equal to $L = 27800$ m.

The initial wind speed profile was for a constant westerly wind of $\overline{U} = 8$ ms^{-1}. Given that the simulations included friction and Coriolis force, ($f = 10^{-4}$ s^{-1}) the wind in the boundary layer turns with height. Since the Rossby number ($R_0 = \overline{U}/fL$) for the cases considered was $R_0 >> 1$, the impact of rotation on the flow will be very small.

The atmosphere which was simulated consisted of two layers with different values of Brunt Väisälä frequency. The first layer was a neutral layer with a constant potential temperature of 276.58 K and the second layer with $N = 0.00625$ Hz. At the interface between the two layers a discontinuity in potential temperature is imposed.

The non-dimensional numbers which control the flow, relevant to the simulations are:

- The Froude number, $F = \overline{U}/\sqrt{g' z_i}$, where $g' = g\Delta\theta/\theta_0$ is the reduced gravity acceleration. It represents the ratio of the flow speed to the speed of long–wavelength gravity waves travelling on a stationary fluid of depth z_i (Baines, 1995);

- $\overline{U}/NL$ which represents the ratio of the vertical wavelength of a hydrostatic wave ($\overline{U}/N$) to the horizontal scale of the mountain. According to Smith (1980), the hydrostatic approximation is valid when the horizontal scale of the of the mountain

is much larger than the distance an air particle travels downstream during a buoyancy oscillation, i.e $\overline{U}/NL << 1$;

- $S = H/L$, the ratio of the height of the mountain to its length;
- $Z = Nz_i/\overline{U}$, which relates the inversion height to the vertical wavelength of a hydrostatic wave in the upper layer.

The previous parameters can be combined to form two other useful non–dimensional parameters: $NH/\overline{U}$ and H/z_i. The later relates the height of the inversion to the height of the mountain and the first is the ratio of the mountain height to the wavelength of a hydrostatic mountain wave. It is a measurement of linearity, i.e., the flow is considered linear when the vertical motion of an air particle in a buoyancy oscillation is much greater than the height of the mountain ($NH/\overline{U} << 1$).

Here, three different inversion heights (z_i) were studied: 637.057 m, 548.56 m and 469.95 m. Which makes the ratio of the hill height to the inversion height equal to $H/z_i = 1$; 1.167; 1.36 for each inversion respectively. The jump across the discontinuity depended on the grid spacing and was 99 m for the first height, 88.4 m for the second and 79.7 m for the third.

For all the simulations the non–dimensional parameters $NH/\overline{U}$, $\overline{U}/NL$ and $S = H/L$ are kept fixed at 0.5, 0.046 and 0.02 respectively, so the flow will be linear and hydrostatic in the layer above the inversion. The Froude number ($F = \overline{U}/\sqrt{g'z_i}$, where $g' = g\Delta\theta/\theta_0$ is the reduced gravity acceleration) is changed through changes in $\Delta\theta$.

A summary of the different simulations performed, is given in table 7.1.

All the simulations were performed for one or two ridges with the exception of $F05_{Hz_{i1}}$ which was executed for two ridges only.

7.2 Model Results

In this section the model results for the simulations outlined in the previous section are displayed. The results are presented in terms of Froude number, the ratio of the mountain height to inversion height upstream and the number of ridges in the model. All the results will be presented at time $t = 26L/\overline{U}$ (91000 s), where $L = 28000$ m.

Exp.	H/z_i	F	$\Delta\theta$ (K)
$F12_{Hz_{i1}}$	1.0	1.25	1.81
$F09_{Hz_{i1}}$	1.0	0.9	3.69
$F07_{Hz_{i1}}$	1.0	0.75	5.02
$F06_{Hz_{i1}}$	1.0	0.6	7.23
$F05_{Hz_{i1}}$	1.0	0.5	11.30
$F12_{Hz_{i11}}$	1.16	1.25	2.10
$F1_{Hz_{i11}}$	1.16	1.1	2.59
$F09_{Hz_{i11}}$	1.16	0.9	4.29
$F07_{Hz_{i11}}$	1.16	0.75	5.83
$F06_{Hz_{i11}}$	1.16	0.6	8.40
$F05_{Hz_{i11}}$	1.16	0.5	13.12
$F09_{Hz_{i13}}$	1.36	0.9	5.00

Table 7.1: Summary description of the simulations performed.

When appropriate, the wind speed at 2 m, height of the inversion, speed–up at the surface will be given for the approximate location of stations 8 and 4, i.e., for $x = 16600$ and 18100 m respectively. The flow will be categorised according to the characteristics of the simulations for one ridge.

7.2.1 Vertically Propagating Mountain Waves: $F > 1.0$

Figure (7.1a) shows the steady state flow field ($t = 26L/\overline{U}$) resulting from a simulation with a temperature inversion which starts at 637.057 m and has a $\Delta\theta = 1.81$ K. A vertically propagating gravity wave with a vertical wavelength of approximately $2\pi U/N$, can be observed above the mountain top. This wavelength is to be expected since $NH/U << 1$ and linear gravity wave theory is applicable in this parameter space. Although Lin and Wang's (1996) simulations do not include a temperature inversion, their results support the applicability of linear theory for $NH/U = 0.5$. According to them, linear theory is applicable when $NH/U \leq 0.89$. Note that the amplitude of the wave is not sufficient to produce wave breaking above the ridge, this is consistent with the results of Vosper (2004).

The flow downstream is moderately accelerated and the speed up is 0.55 for station 4

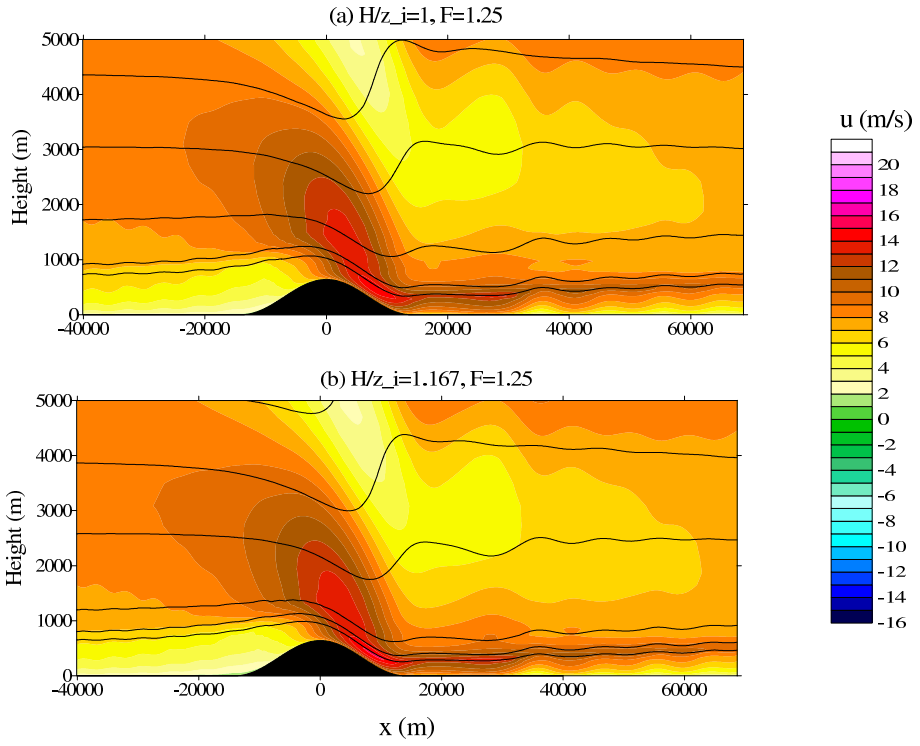

Figure 7.1: Flow field for $F = 1.25$, after an integration time of $t = 26L/\overline{U}$ (91000 s). Line contours represent potential temperature with 277 K as the lowest contour (1 K intervals). x velocity component is shown in coloured contours (1 ms^{-1} intervals). Inversion at (a) 637.057 m (approximate mountain height, $H/z_i = 1$), (b) 548.56 m.

and 0.53 for station 8.

The figure also illustrates the lowering and strengthening of the temperature inversion due to the downslope flow. The inversion has been lowered to 233 m, i.e. it is at $0.365z_i$, and has been increased in strength by 34% ($\Delta\theta = 2.429$ K).

The lowering of the upstream inversion (figure 7.1b) has the effect of strengthening the gravity wave, but the flow is very similar to the described previously. The inversion downstream is lowered to the same height as in the previous simulation and its strength is only increased by 14%. The speed up is increased to 0.66 at both stations; this is the result of slightly lower wind speed near the surface and increased acceleration downstream (the wind speed at these sites is greater than in the previous simulation).

The simulation for flow over two mountains is shown in figure (7.2) for three adimensional times, $t = 22L/\overline{U}$ (77000 s), $t = 24L/\overline{U}$ (84000 s) and $t = 26L/\overline{U}$ (91000 s),

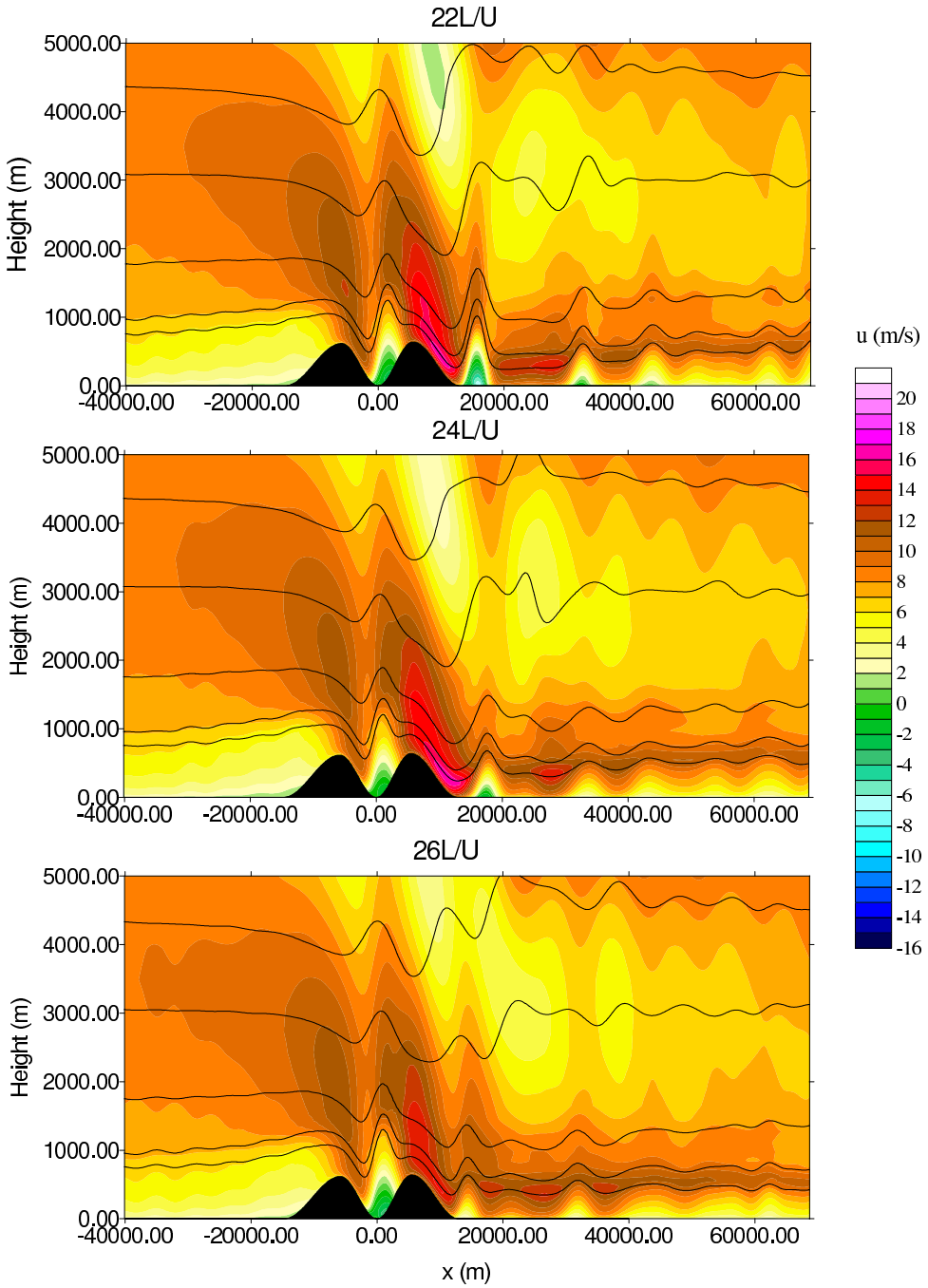

Figure 7.2: Flow over two ridges with the inversion at 637.057 m. Line contours represent potential temperature with 277 K as the lowest contour (1 K intervals). x velocity component is shown in coloured contours (1 ms^{-1} intervals). Flow field after an integration time of (a) $t = 22L/\overline{U}$ (77000 s), (b)$t = 24L/\overline{U}$ (84000 s), (c)$t = 26L/\overline{U}$ (91000 s).

since the flow never becomes steady. Above each ridge a propagating gravity wave can be observed and as before, its vertical wavelength is approximately $2\pi U/N$.

The flow below the inversion is significantly altered by the two ridges. The proximity of

the second ridge changes extensively the downslope flow from the first and between them; a rotor is formed with downslope flow on the slope of the second ridge. The temperature inversion at $x = 75$ m (lowest point in the valley) has increased in strength from 1.81 to 2.141 K and is located at 973.4 m. Hence the flow over the second ridge has no longer a Froude number of 1.25, in fact, its Froude number has changed to 0.93. According to Vosper (2004) a rotor should form on the lee slope of the second ridge. In fact, another rotor can be observed at the foot of the lee slope of the second ridge but does not remain stationary, it propagates downstream. The height of the inversion, now, depends on the location of the rotor. For $t = 26L/\overline{U}$, the height of the inversion at station 4 or 8 is the same as in the previous simulations, 233 m and its strength is 2.459 K. At $t = 24L/\overline{U}$ the inversion height for station 8 and 4 was 400 and 470 m respectively. Its strength is unaltered. The speed–up for $t = 26L/\overline{U}$ is similar to what was found in the previous simulations.

When the inversion upstream is lowered to 548.56 m the vertically propagating gravity waves are stronger. The flow is unsteady, as before, and rotors form on the lee slopes of the ridges.

7.2.2 Lee–Wave Rotors

According to Vosper (2004), when the inversion height is at the height of the mountain rotors can be found for Froude numbers between 0.6 and 1 (excluding this last value). Figure (7.3) shows the flow field for three Froude numbers, $F = 0.6$, $F = 0.75$ and $F = 0.9$.

From the observation of figure (7.3) it is evident that closed circulations associated to reversed flow (rotors) are present underneath the lee waves and that as the Froude number increases, the distance of the first jump (which generates the first lee wave) to the lee slope also increases. Also visible, is that, as the Froude number increases, the region of the strongest surface wind migrates down the lee slope. According to Turner (1973), when stationary waves appear downstream, longer waves can propagate upstream and when their amplitude is large enough that the frequency dispersion can no longer balance the steepening effect, hydraulic jumps or wave breaking can occur. So, the position of the jump is intimately linked to the strength of the vertical propagating gravity wave. This can also be inferred from figure (7.3) were the strength of the propagating wave increases

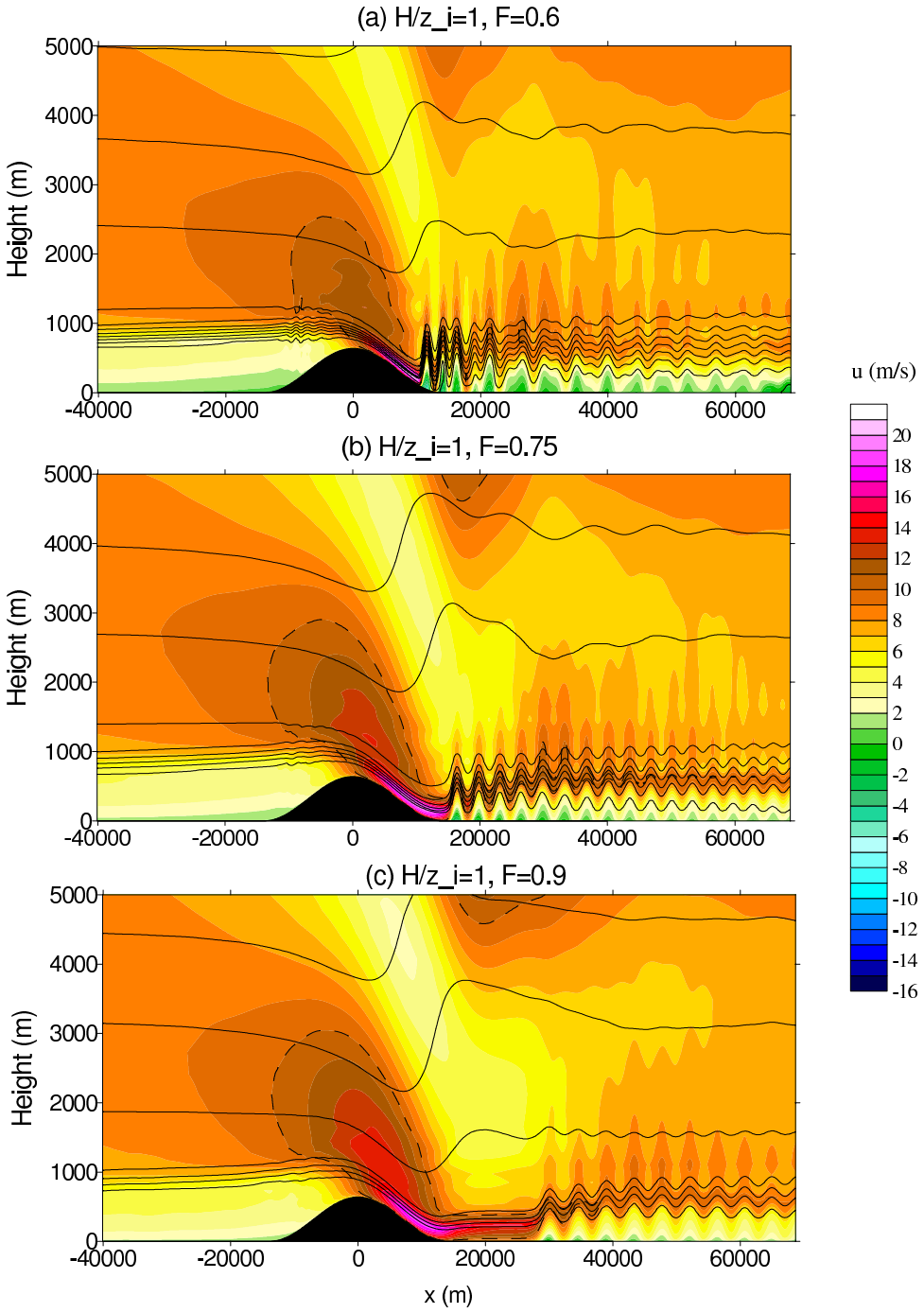

Figure 7.3: Flow over one ridge with the inversion at 637.057 m. Line contours represent potential temperature with 277 K as the lowest contour (1 K intervals). x velocity component is shown in coloured contours (1 ms^{-1} intervals). The dashed line follows 10 ms^{-1} contour. Flow field for (a) $F = 0.6$, (b) $F = 0.75$ and (c) $F = 0.9$.

as the Froude number increases.

The centre of the first rotor for $F = 0.9$ is located at $x = 29700$ m and the reversed

flow reaches a height of 31.8 m. The maximum strength of the reversed flow is -0.926 ms^{-1}. This closed circulation is associated with high positive cross stream component of vorticity (figure 7.4a). A thin layer of positive vorticity is present close to the lee slope due

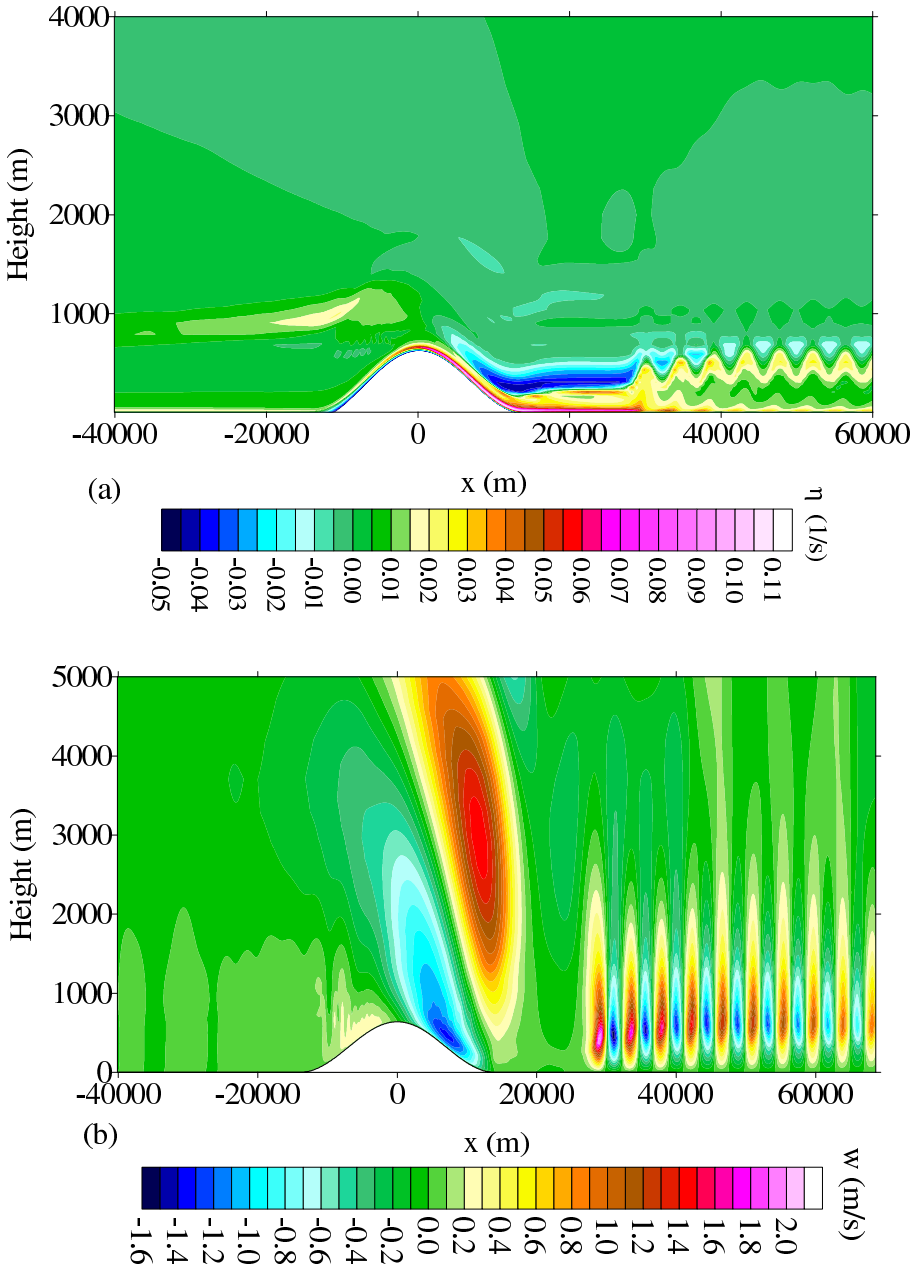

Figure 7.4: (a) Cross–stream vorticity component (shaded contours every 0.005 s^{-1}), (b) vertical component of the wind speed (shaded contours every 0.1 ms^{-1}) for flow with an inversion at the mountain height and $F = 0.9$.

to the friction at the ground and as in Doyle and Durran (2002) and Vosper (2004) this thin layer is advected upwards into the first rotor as the flow separates underneath the

first lee–wave. In the upper portions of the rotor the y component of the vorticity attains a maximum value of 0.033 s^{-1} at 434 m.

Underneath the first lee–wave trough, a new region of positive cross flow component of vorticity is formed as a consequence of the accelerated flow. This continues further downstream but the strength of the vorticity sheet weakens as the distance from the slope increases. This was also found by Doyle and Durran (2002).

The upstream edge of the first rotor is also associated to positive vertical velocity (figure 7.4b) and as noted in both Doyle and Durran (2002) and Vosper (2004) to a positive maximum in the mountain induced pressure gradient which is not associated to the mountain slope. In the downstream edge the reverse occurs.

The inversion height above the approximate location of stations 4 and 8 is the same (188.8 m) since the rotors are advected downstream. Above the first rotor the vertical transport has lifted it to 400 m and the inversion strength in the three locations is around 4 K.

Vosper (2004) determined, from the linearised equations for a two layer atmosphere, an approximate expression for the resonant wave number,

$$|k|z_i \approx \frac{1}{2}\left(\frac{1}{F^2} + Z^2F^2\right) \tag{7.8}$$

where $Z = Nz_i/\overline{U}$ is a non–dimensional mountain height. By applying this equation to the parameter spaced used here; for $F = 0.9$, $|k|z_i = 0.74$. The wavelength obtained, at the inversion height, from the simulation is 4350 m, which implies a $|k|z_i = 0.92$. Although this value is greater than the predicted by the approximation, it is in line with Vosper's results. In his figure (11b) it can be seen that his results overestimate the true value of $|k|z_i$.

For $F = 0.75$, the first rotor is located at $x = 16350$ m and is considerably stronger than the one observed for $F = 0.9$, the maximum reversed wind speed is now -3.37 ms^{-1}, with a -0.67 ms^{-1} speed at $2m$. The height of the reversed flow has also increased to 130 m and although the maximum vorticity is attained at 434 m as before, its value is now 0.052 s^{-1}.

Now, there are differences between stations 8 and 4, while the first lies underneath the lee–wave crest, the other is under its trough. The flow at station 8 is reversed with a 2 m wind speed of -0.56 ms^{-1} and at station 4 has a 1.58 ms^{-1} speed. The inversion height above the stations is also different; while it is 0.627 of the initial inversion height at station

8, at station 4 it is significantly lower ($h/z_i = 0.13$, where h denotes the inversion height). The wavelength, of the lee–wave, has decreased to 3300 m.

The flow for $F = 0.6$ is in a transition stage between a flow with a single hydraulic jump and steady lee–waves. The location of the first rotor is on the lee slope but after three wavelengths the flow is not as uniform as before. The wavelength, of the first three lee–waves, has decreased to 2550 m and now, the maximum reversed speed is attained on the lee slope with a maximum upslope speed of 5.27 ms^{-1} at $x = 11700$ m.

Stations 4 and 8 are located underneath the last lee–wave and while reversed flow is observed at station 8 ($u = -0.233$ ms^{-1}), at station 4 a westerly wind speed of $1,29$ ms^{-1} is observed. The inversion height for each station is $h = 176.645$ m and 56.371 m respectively.

The relationship between the inversion height and the Froude number will be examined with more detail in the next section.

When the inversion upstream is lowered to 548.65 m, the flow maintains its characteristics although the wavelength of the lee–waves is reduced. For $F = 0.9$, $\lambda = 4050$ m (a reduction of 300 m); for $F = 0.75$, $\lambda = 3150$ m which is a reduction of just 150 m and for $F = 0.6$, $\lambda = 2100$ m.

The flow field with an inversion at the height of the mountain, for flow over two ridges is illustrated in figure (7.5). As for the flow for $F = 1.25$ (figure 7.2), the flow is not steady. For $F = 0.9$, two wave crests can be observed in the valley between the ridges and the trough between the crests is almost centred with the valley floor. Rotors are also present beneath the crests of the waves and on either slope.

The interaction of the flow between the two ridges with the westerly reference flow leads to a dramatic change in the flow downstream. The first downstream rotor is now located on the lee slope and the wavelength of the trapped lee–waves is not uniform. The first two waves are distinctive from the remaining. In the first two troughs, the inversion is transported downwards towards the surface and the wind speed near the surface is also enhanced. While the speed–up, at the surface, after the second trough is less than one, below the first two it is greater than one, in fact in the first trough it attains a maximum of 1.9.

The y component of the vorticity in this area is considerably enhanced when compared to the vorticity for the other waves. The features of the trapped lee waves for the remainder of the domain are very similar to the ones observed for flow over just one ridge. When

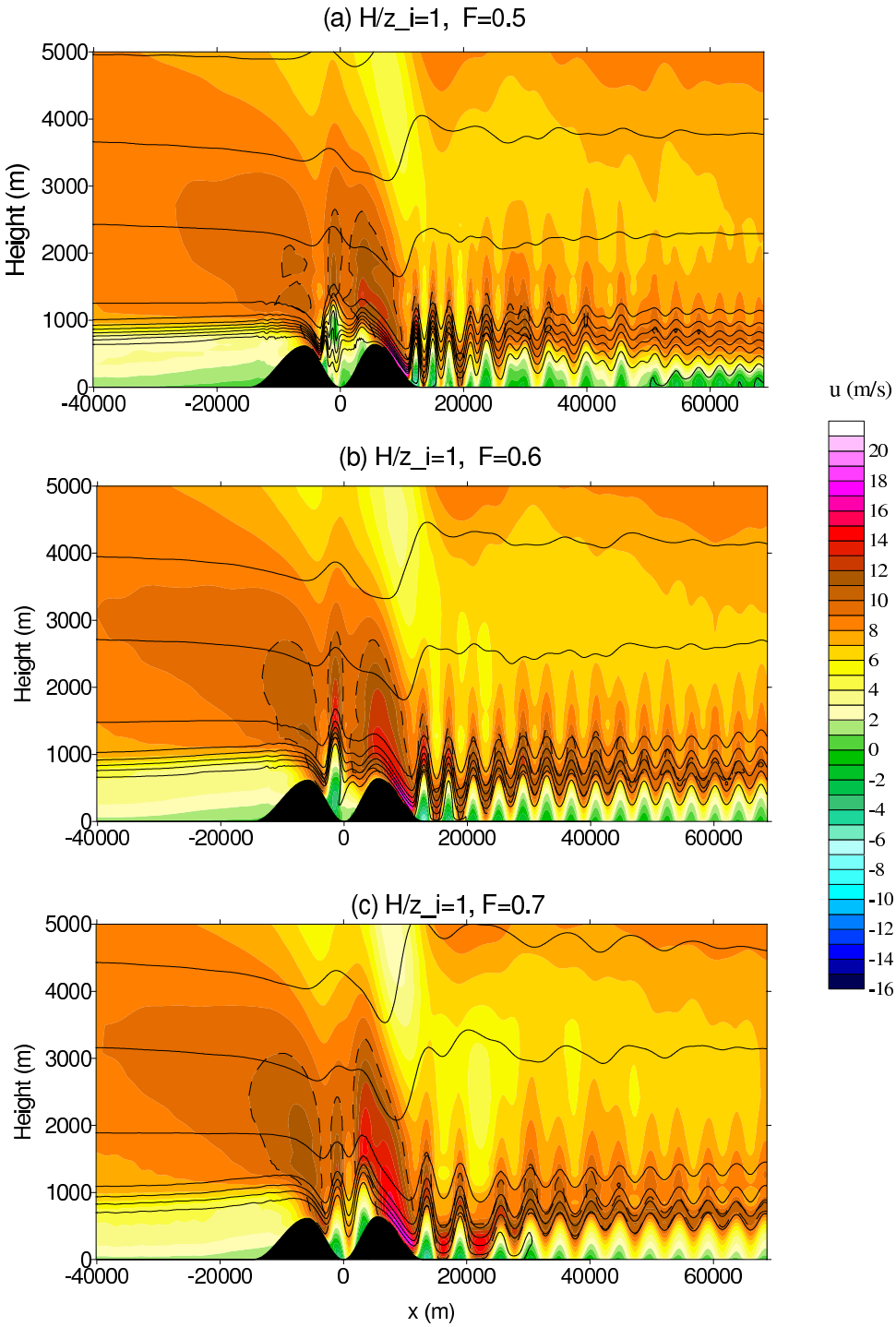

Figure 7.5: Flow over two ridges with the inversion at 637.057 m. Line contours represent potential temperature with 277 K as the lowest contour (1 K intervals). x velocity component is shown in coloured contours (1 ms^{-1} intervals). The dashed line follows 10 ms^{-1} contour. Flow field for (a) $F = 0.6$, (b) $F = 0.75$ and (c) $F = 0.9$.

a superposition of the isentropes for the flow over one ridge and two ridges is made, it becomes apparent that the first three troughs are located in the region of the shooting lee flow in the one ridge case and that the location of the fourth crest overlaps the location of the first crest in the flow over one ridge. The effects of two ridges on the flow downstream is to superimpose a trapped wave on the shooting flow generated by the vertical propagating long wave, i.e., while the supercritical flow extends well beyond the lee slope when there is just one ridge in the domain, for a domain with two ridges, the transition from supercritical to subcritical occurs on the lee slope.

For $F = 0.75$ (figure 7.5), just one wave forms in the valley between the ridges. As with $F = 0.9$, the first wave crest on the lee side has moved up the lee slope; the two ridges have a similar effect on the lee flow. In this case, since the shooting flow is weaker than the shooting flow for $F = 0.9$, the leading edge of the wave is higher. The first two wavelengths are also larger than the subsequent wavelengths and here, the inversion is also transported to the ground below the troughs. As before, the strength of the rotor for $F = 0.75$ is greater than for $F = 0.9$.

For $F = 0.6$, a single hydraulic jump with a region of reversed flow aloft, is observed between the two ridges. Rotors are also observed on either slope in the valley.

The flow on the lee side is stronger than the flow over just one ridge. The reasoning is similar to the previous.

When the inversion height is lowered so that its relation to the height of the ridges is corresponds to $H/z_i = 1.167$ the flow speed upstream is reduced (similar to what was found in the other cases for the same H/z_i). The intensity of the flow downstream and the rotors in the valley are also reduced. For $F = 0.6$, the flow over the first ridge produces a very small hydraulic jump which does no disturb significantly the valley floor. In this case, a stagnation zone occurs in the middle of the valley with a small upslope layer on either ridge.

7.2.3 Hydraulic Jump, $F = 0.5$

Figure (7.6) shows the flow field for $t = 26L/\overline{U}$ in an atmosphere with an inversion at 548.56 m ($H/z_i = 1.167$). On the lee slope a stationary hydraulic jump is observed at $x = 8400$ m (233.7 m high). In the vicinity of the jump, a vertical wind speed of 6.8 ms^{-1} is observed. Behind the jump, the temperature inversion is broadened, it starts at 188.21

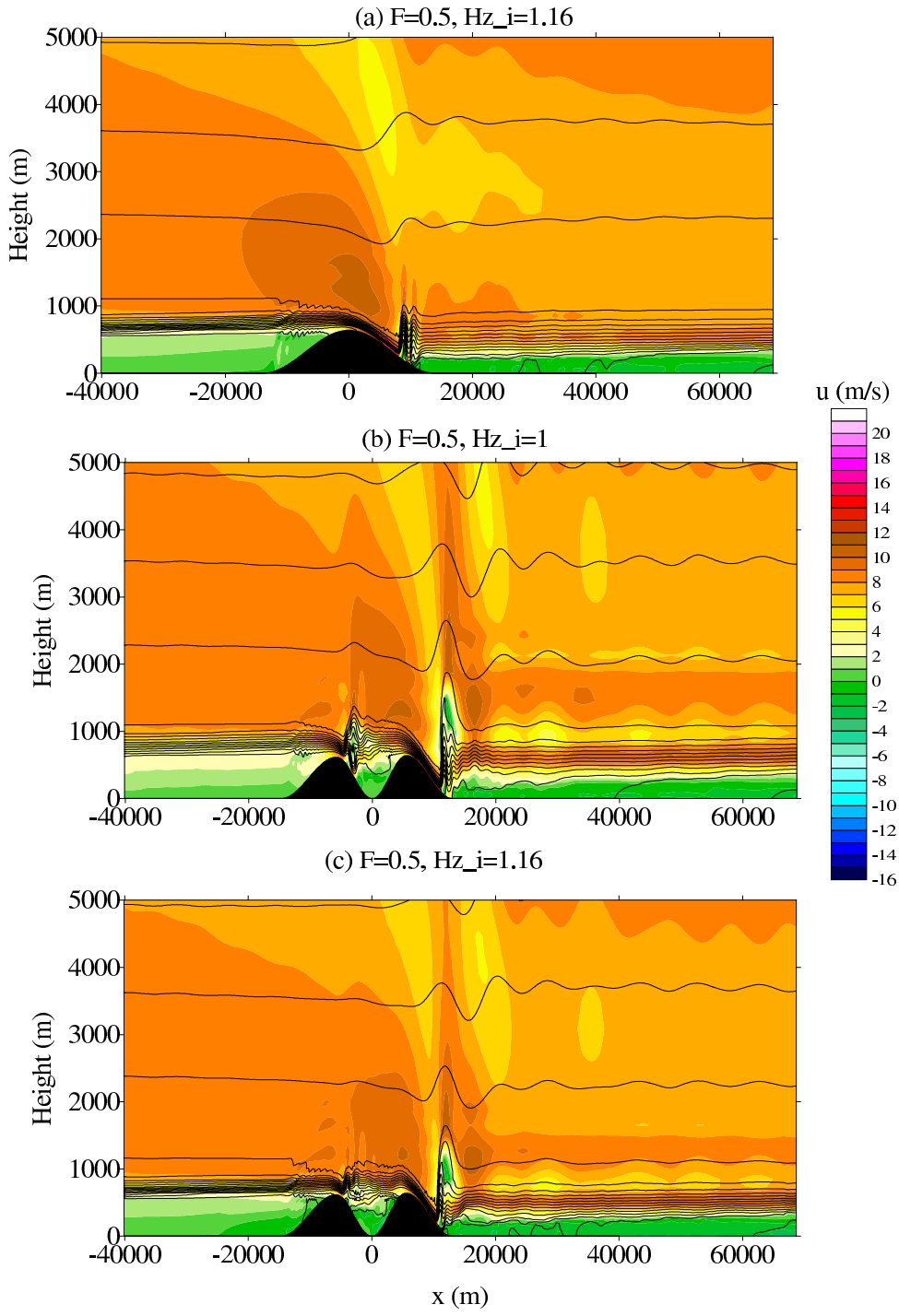

Figure 7.6: Flow field for $F = 0.5$ (a) one mountain with $Hz_i = 1.167$, (b) two ridges with $Hz_i = 1$ and (c) two ridges with $Hz_i = 1.167$. Line contours represent potential temperature with 277 K as the lowest contour (1 K intervals). x velocity component is shown in coloured contours (1 ms^{-1} intervals).

m and ends at 973.43 m and below it the flow is reversed throughout the remainder of the domain. Before the jump, the flow is accelerated to about 270% of the upstream wind

speed, but after the jump the flow suffers an increase of only 50% relative to the upwind wind speed.

A propagating gravity wave can still be seen above the mountain top.

When the flow is over two ridges a hydraulic jump can be observed on both ridges for $H/z_i = 1$, and only on the second ridge for $H/z_i = 1.167$. The gravity wave which was over the first ridge for the other Froude numbers is no longer excited. The hydraulic jump on the second ridge is significantly stronger than when the flow was just one ridge and a stagnation area with flow reversal is also found aloft indicating wave breaking.

7.3 Flow Regimes

In this section, a comparison between the different flow regimes is attempted. In figure (7.7a and b) the minimum height of the lower boundary of the inversion downstream is compared with the same parameter for the upstream inversion. From this, it can be concluded that this parameter is highly dependant on the location of the rotors, i.e., when a rotor is over the station the inversion is transported aloft and an increase in this parameter can be found. For $F = 1.25$, the only difference occurs due to the change in height in the upstream flow, i.e., flows with inversion upstream which are above the summit of the ridge produce stronger downwind disturbances hence their inversions downstream are lowered more pronouncedly. For $F = 0.9$ the enhancement of the flow downstream due to the presence of two ridges lowers the inversion height to the surface. For $F = 0.75$, a rotor is over station 8 when there is just one ridge in the domain, hence the increase in the inversion height. The reverse happens when there are two ridges in the domain. For all the flows and stations the inversion's lowest boundary is always lower than the one for the reference state.

The change in inversion strength (as measured by a change in $\Delta\theta$) is depicted in figure (7.7c and d). In station 8, the reduction of the inversion strength downstream is more pronounced when the inversion height is below the summit. The differences in the strength of the inversion when there are one or two ridges in the domain are not very significant. For flows with $F > 0.75$ the ratio of the strength of the inversion is always greater than one, i.e, the inversion downstream is greater than the upstream. This is also true for flows, with $F = 0.75$, over one ridge and over two ridges when $H/z_i = 1$. For $F = 0.6$, when the

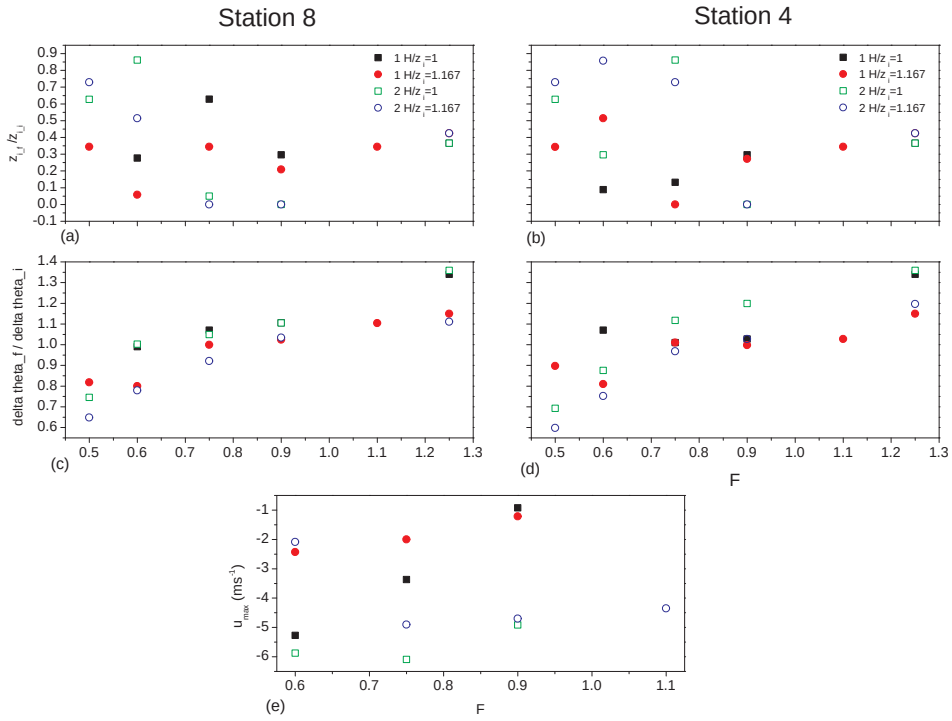

Figure 7.7: Flow regimes for flows over one or two ridges and two inversion heights. (a) Ratio of the inversion height at station 8 and the inversion height for the reference profile, (b) as in (a) but for station 4. (c) Ratio of the inversion strength ($\Delta\theta$) at station 8 and in the reference profile, (d) as in (c) but for station 4. (d) Maximum reversed flow in the first rotor.

inversion is at the height of the summit the downwind inversion has the same strength as the upstream, but when the upstream inversion is bellow the summit, the inversion downstream is weaker. When $F = 0.5$, the inversion downstream is always weaker.

In station 4, the same relationships apply. The most significant differences are found for flow over one ridge and $F = 0.75$, 0.9 since in the first case a rotor is over station 8 and in the second case station 4 is closer to the first rotor.

Figure (7.7e) shows the maximum speed of the reversed flow. When the flow is over one ridge, the maximum reversed flow in the first rotor increases as the Froude number decreases. In the flow over two ridges the flow is more complex. The rotors for $F = 0.6$ are weaker than the rotors for $F = 0.75$. For $F > 0.75$, the strength of the rotors decreases with increasing Froude number.

In all flows, for Froude numbers less than 0.9 the reversed flow for an inversion below

the summit of the ridge is less than when the inversion is above the summit. For $F = 0.9$ the inversion above the ridge produces a weaker rotor.

7.4 2–D Simulations of the 9^{th} of February 2001 Case Study

In this section, the one–dimensional temperature and wind profiles obtained from the boundary layer model are used as the reference profile for two–dimensional simulations performed with BLASIUS.

The idealised two ridge equation was used as the model's orography. The grid resolution in both directions was the same as before. The Coriolis parameter was changed to $f = -11 \times 10^{-4}$ s^{-1}, which is the appropriate parameter for the Falklands. Nevertheless, the impact of the Earth's rotation is not expected to be significant since the Rossby number is still greater than one.

Due to the upstream flow observed in the simulations and the ensuing wrap–effects, the horizontal damping layers had to be increased to 12 km.

The initial profiles for potential temperature and wind speed are obtained from the 1–D simulation (figure 6.2). The first profile used in the simulations was the potential temperature and wind profiles for $2300Z$ on the 8^{th} of February. The initial profiles are represented in figure (7.8). Note that the wind speed from 2000 m up to 20 km is the 1–D model's 2000 m speed. The Brunt Väisälä frequency is determined from the potential profile. The atmosphere is neutral from the surface to 208.4 m, $N = 0.023$ s$^-1$ from the previous level up to 884 m and $N = 0.003$ s$^-1$ for the remaining of the atmosphere. For this simulation $Nh/U = 0.2$, $Na/U = 39$ and $F = 1.06$.

The evolution of the flow for $tL/\overline{U} = 22$, 24 and 26, where $L = 27800$ m is shown in figure (7.9). In it, a vertical propagating gravity can be observed above the ridges.

As in the idealised simulations, a rotor is observed on the upslope of the second ridge and on the downslope of the first. In this case, the rotor on the upslope flow is stronger than the one on the downslope.

On the lee of the second ridge a stationary rotor is also observed with a maximum reversed speed of 7.5 ms^{-1}. The 2 m wind speed for the approximate location of site 8 is 0.1 ms^{-1} for $t = 24L/\overline{U}$ and for $t = 26L/\overline{U}$ the wind speed is 0.18 ms^{-1}.

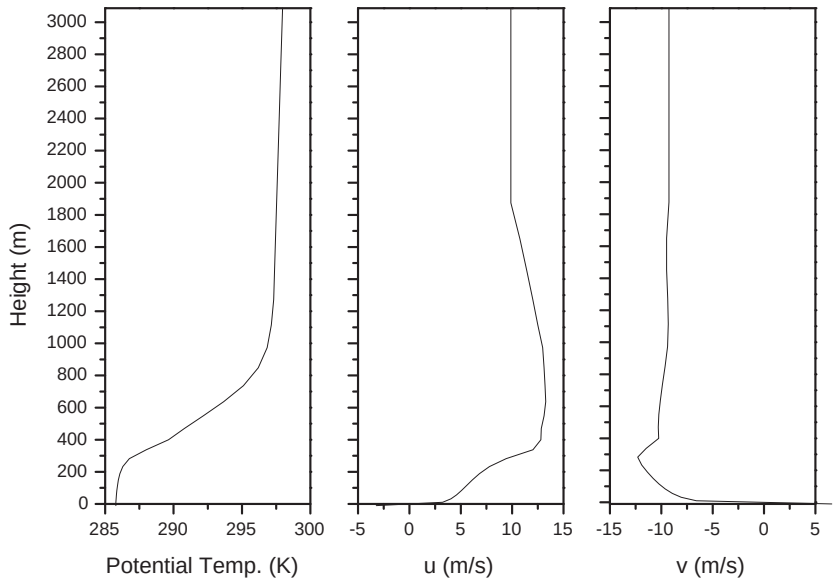

Figure 7.8: Initial potential temperature and wind speed vertical profiles for the $2300Z$ radiosonde launch on the 8^{th} of February 2001.

Figure (5.29) shows that the start of the rotor event is at 40.2 days when flow reversal is observed at station 8 and figure (5.26) shows that the first increase in the pressure difference between station 8 and 4 occurs at 40.3 days. This implies that rotors are only observed six hours after the $2300Z$ radiosonde. Hence rotors should not have developed in this 2–D simulation. By comparing the parameter space (the Froude number, Nh/U and Na/U) of this simulation with the parameter space of the idealised simulations the development of the rotor should be expected. Note that in 1–D simulation there is an incorrect evaluation of the temperature advection, thus the $2300Z$ potential temperature profile is not the appropriate upstream profile.

A second simulation which uses the $0600Z$ ($T = 40.25$ days) profiles to initialise BLASIUS was performed (figure 7.10). As before, the wind speed from 2000 m up to 20 km is the 1–D model's 2000 m speed. The atmosphere is neutral from the surface to 208.4 m, $N = 0.023$ s$^{-}1$ from the previous level up to 884 m and $N = 0.003$ s$^{-}1$ for the remaining of the atmosphere. For this simulation $Nh/U = 1.48$, $Na/U = 32$ and $F = 1.17$.

The evolution of the flow for $tL/\overline{U} = 16$, 20 and 30, where $L = 27800$ m is shown in

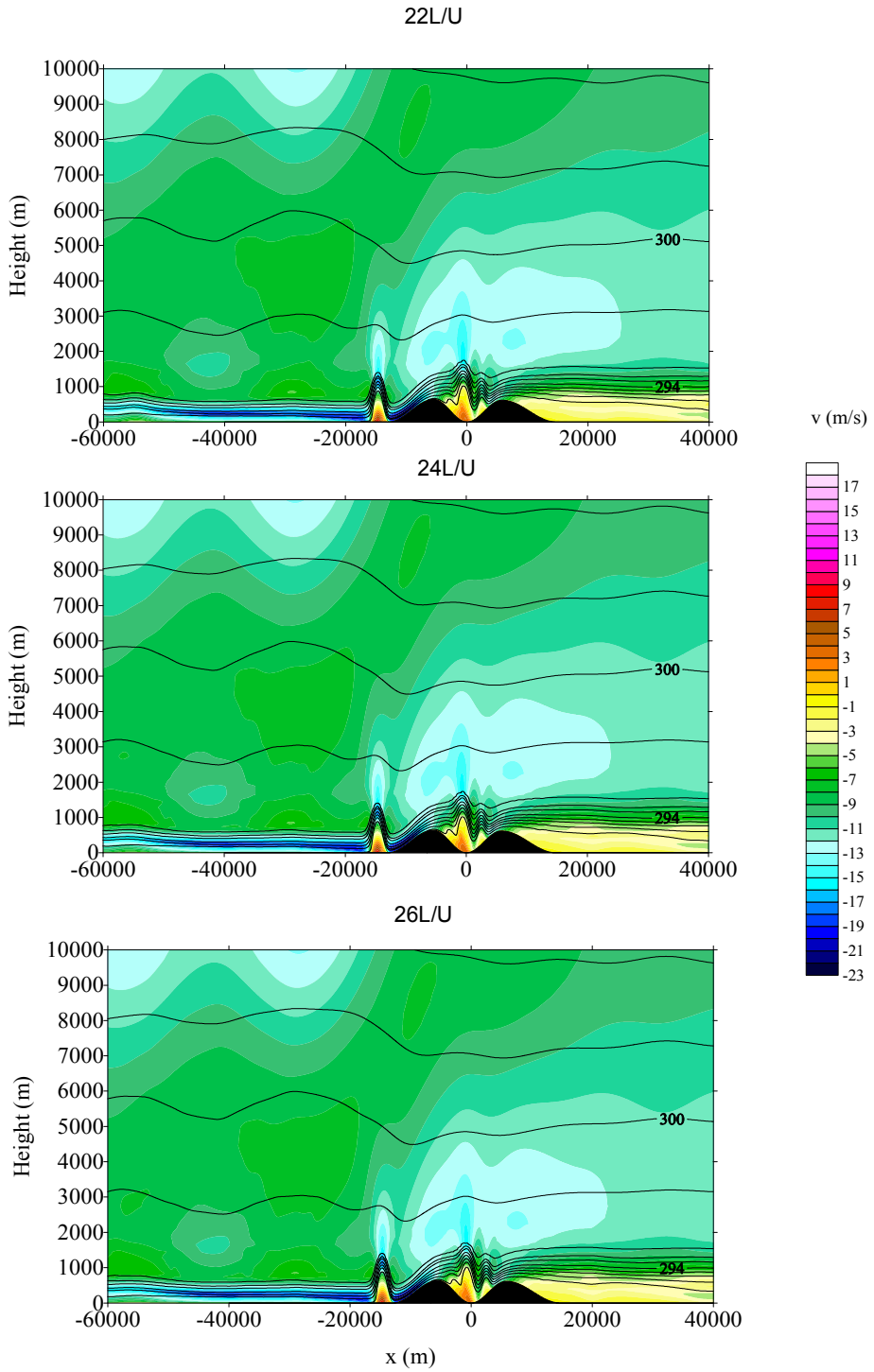

Figure 7.9: Flow field at $tL/\overline{U} = 22, 24$ and 26 for the 8^{th} of February 2001. Line contours represent potential temperature with 284 K as the lowest contour (2 K interval). y velocity component is shown in coloured contours (1 ms^{-1} intervals). Note that the flow is from right to left.

figure (7.11).

In the initial stages of the simulation a rotor develops between the two ridges and it

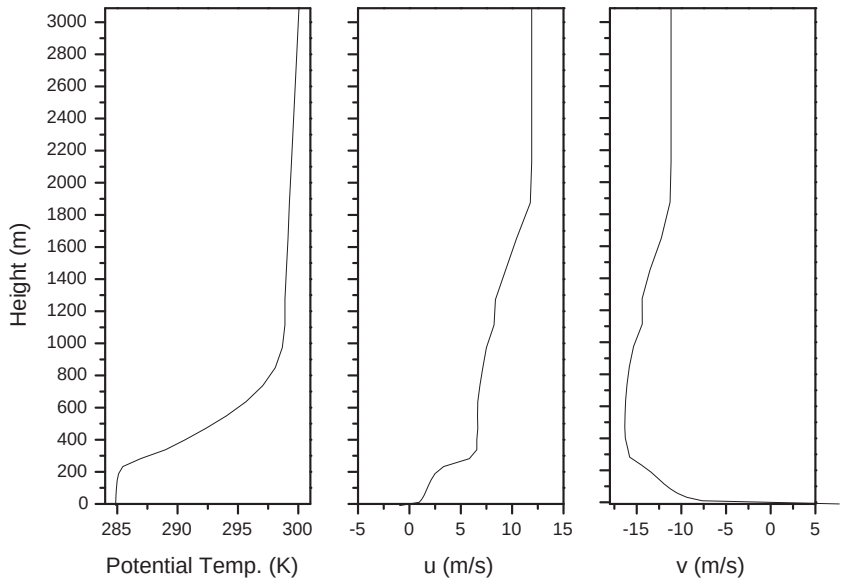

Figure 7.10: Initial potential temperature and wind speed vertical profiles for the $0600Z$ radiosonde launch on the 9^{th} of February 2001.

remains there until the simulation stabilises. Rotors also develop downstream of the second ridge but these are advected downstream and have disappeared by $tL/\overline{U} = 26$. The flow stabilises as a downslope wind storm. Above the inversion a gravity wave is observed.

Figure (7.12) shows the potential temperature profiles for the adimensional times previously mentioned and for the approximate locations of station 4 and 8. The modelled surface temperature and inversion height agrees well with the observed in the radiosondes. The top of the inversion is located above the inversion on $1100Z$ but it is colder than the observed. The atmosphere above the inversion is also colder.

The speed–up for the same moments and at the approximate location of station 4 is 0.98 and it is 1.1 for station 8. The speed–up at these stations around $T = 40.25$ days is between 1 and 0.89 in station 8 and around 0.87 in station 4 (figure 5.30).

The pressure difference between sites 4 and 8 is around 0.12 hPa which is about one third of the observed for $T = 40.25$ days (figure 7.13).

A third and last simulation with the $1100Z$ ($T = 40.47$ days) profiles was performed. In this case, the atmosphere is neutral from the surface to 208 m, $N = 0.026$ s$^{-}1$ from the

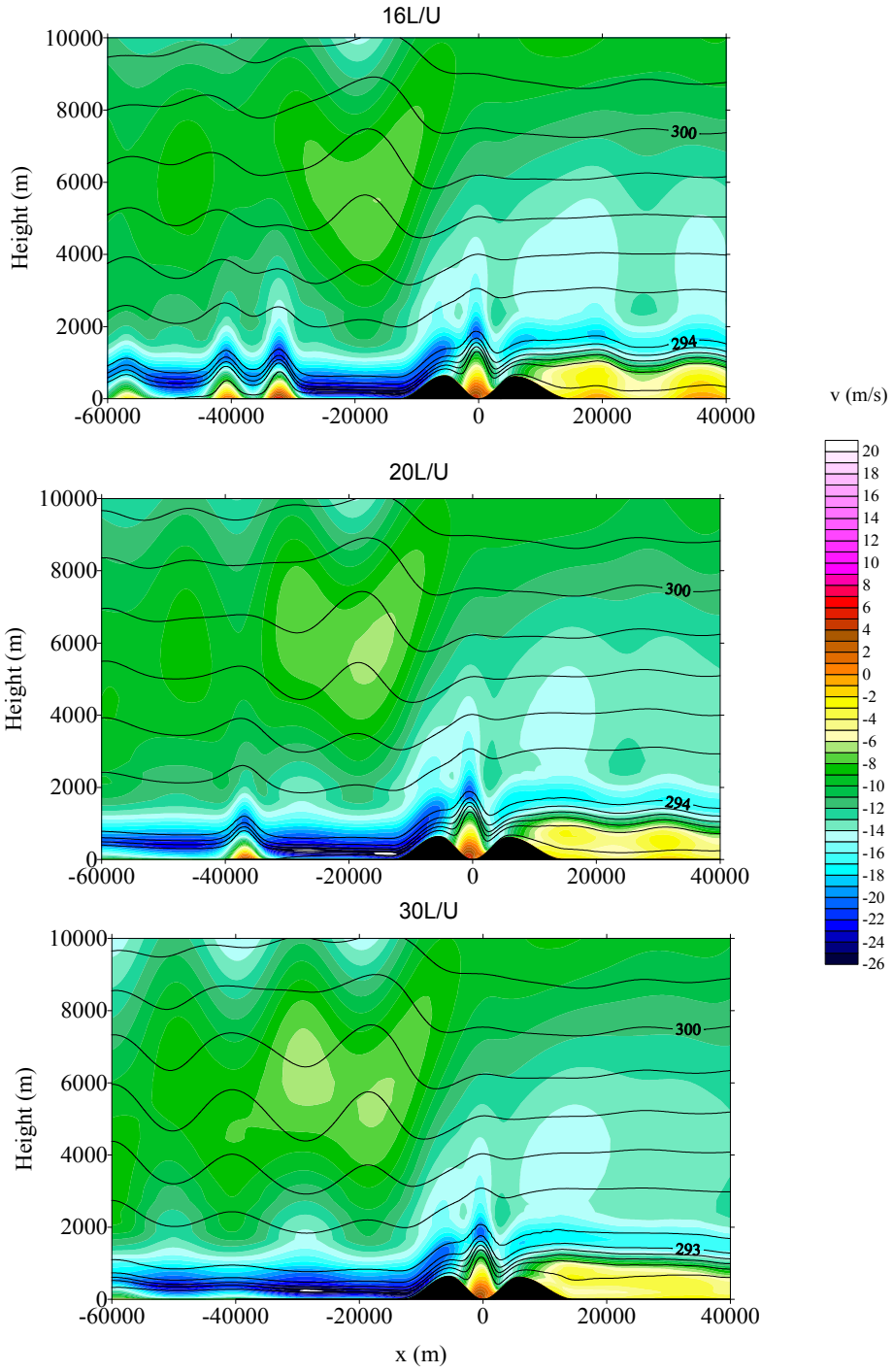

Figure 7.11: Flow field at $tL/\overline{U} = 16$, 20 and 30 for $0600Z$ on the 9^{th} of February 2001. Line contours represent potential temperature with 284 K as the lowest contour (2 K interval). y velocity component is shown in coloured contours (1 ms^{-1} intervals). Note that the flow is from right to left.

previous level up to 884 m and $N = 0.007$ $s^{-}1$ for the remaining of the atmosphere (figure 7.14). For this simulation $Nh/U = 1.23$, $Na/U = 27$ and $F = 1.35$.

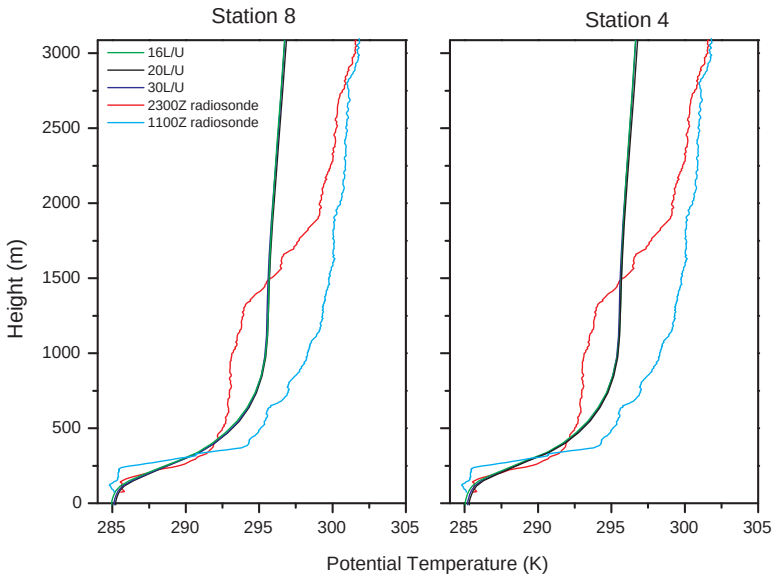

Figure 7.12: Potential temperature at $tL/\overline{U} = 16$, 20 and 30 for $0600Z$ on the 9^{th} of February 2001. The radiosonde profiles for $2300Z$ on the 8^{th} and on the 9^{th} is shown for comparison.

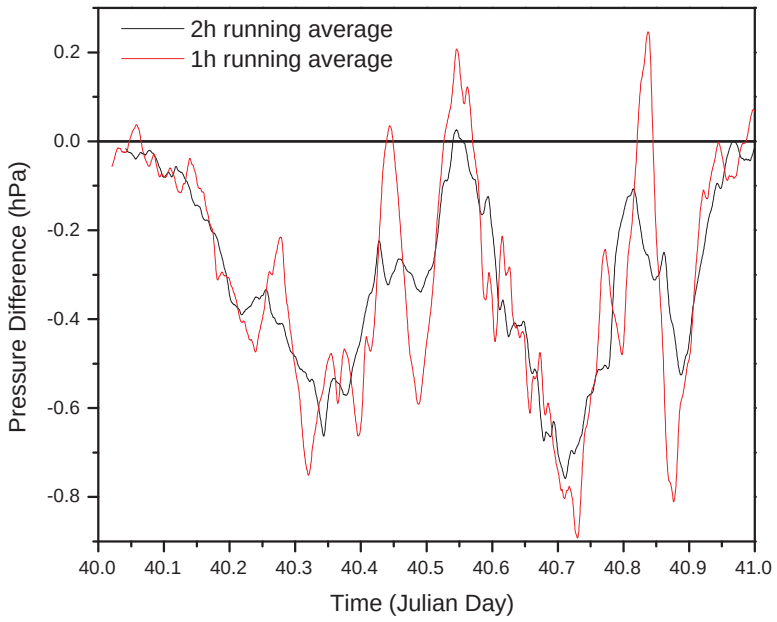

Figure 7.13: One and two hours running average of the pressure difference observed between stations 8 and 4 on the 9^{th} of February 2001.

Figure (7.15) shows the flow for $tL/\overline{U} = 22$, 24 and 25.

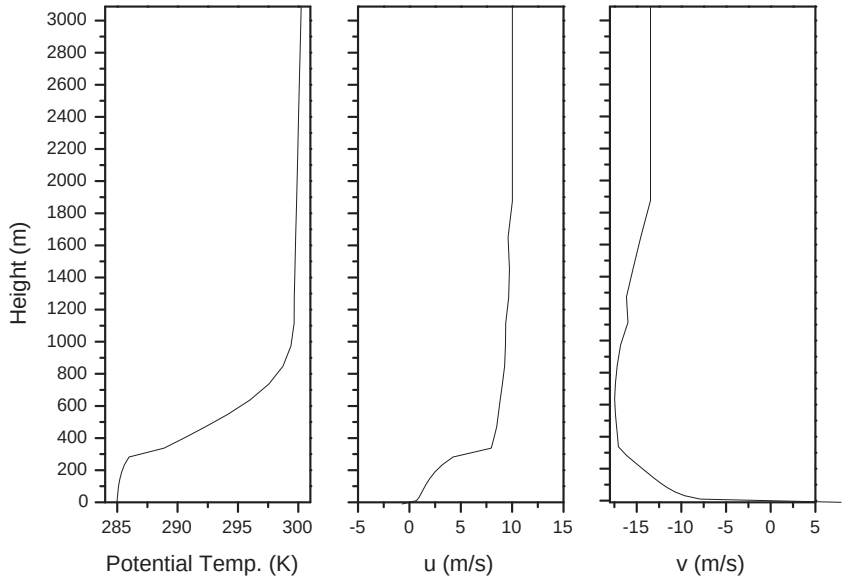

Figure 7.14: Initial potential temperature and wind speed vertical profiles for the $1100Z$ radiosonde launch on the 9^{th} of February 2001.

As before, a vertical propagating gravity wave can be observed above the two ridges as well as a rotor in the valley between them and the upstream flow beneath the inversion is blocked. Although $Nh/U = 1.23$, no wave breaking is observed.On the lee of the second ridge rotors which are advected downstream are also observed. The strength of these rotors is increased with the increase in the strength of the propagating gravity wave. The maximum reverse speed for $tL/\overline{U} = 22$ is 6.29 ms$^-$1, it increases to 8.03 ms$^-$1 for $tL/\overline{U} = 24$ and to 9.36 ms$^-$1for $tL/\overline{U} = 25$. The 2 m wind speed for the approximate location of station 8 is -0.78 ms$^-$1, -1.6 ms$^-$1 and 0.47 ms$^-$1 for the same adimensional times (note that the flow is reversed when the wind speed is positive). At the approximate location of station 4 the wind speeds are 0.38 ms$^-$1, 0.4 ms$^-$1 and 0.35 ms$^-$1 respectively. A rotor is always over that location. These values are similar to those observed at MPA when a rotor is over the stations, see figure (5.29) for $T = 40.38$, 40.62 or 40.78 days. The speed–up at these locations is negative with values comparable to the observed.

Figure (**??**) shows the potential temperature profiles for the same adimensional times.

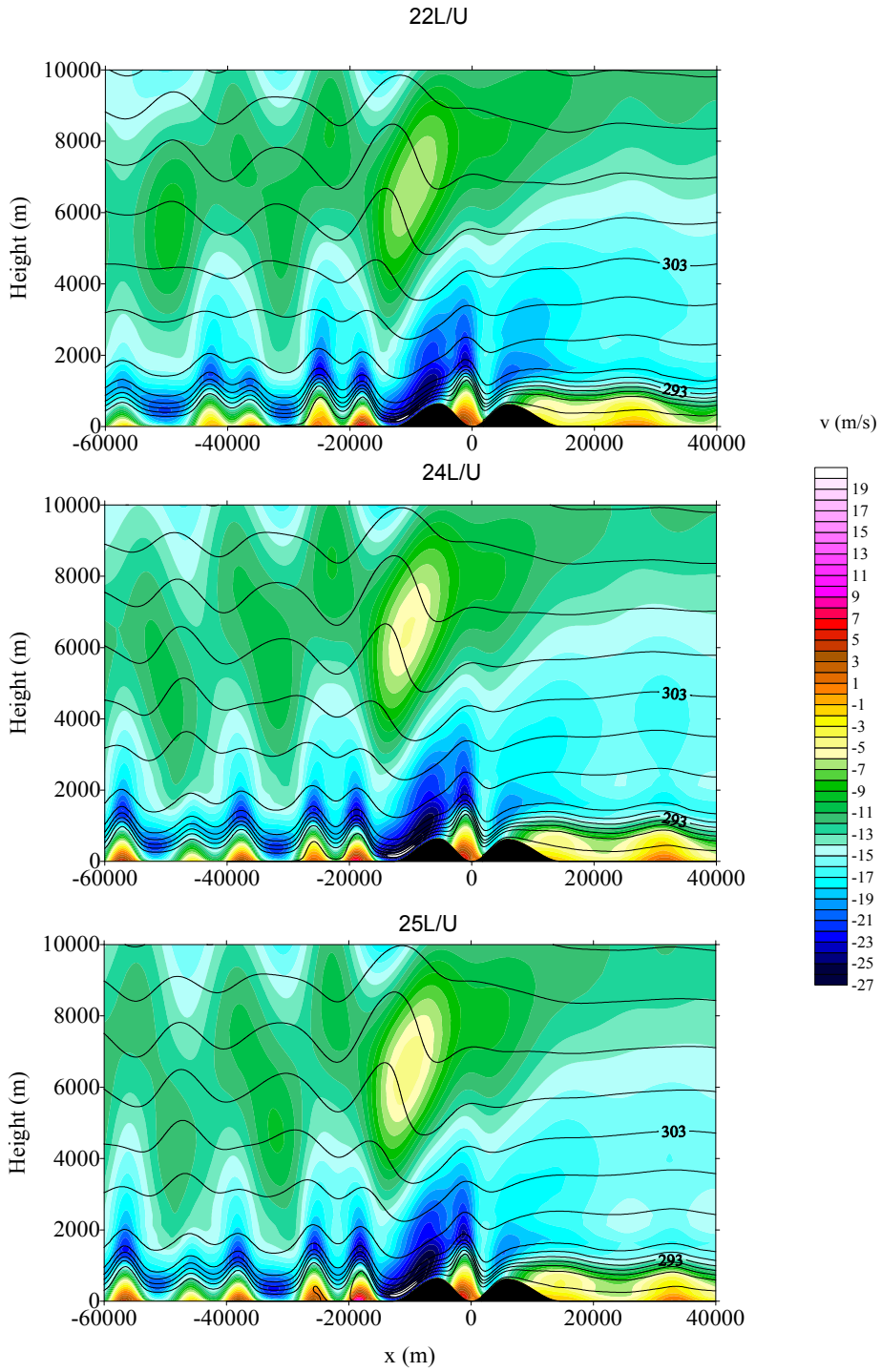

Figure 7.15: Flow field at $tL/\overline{U} = 22$, 24 and 25 for $1100Z$ on the 9^{th} of February 2001. Line contours represent potential temperature with 284 K as the lowest contour (2 K interval). y velocity component is shown in coloured contours (1 ms^{-1} intervals). Note that the flow is from right to left.

The surface potential temperature in both stations is about 1 K higher than the observed,

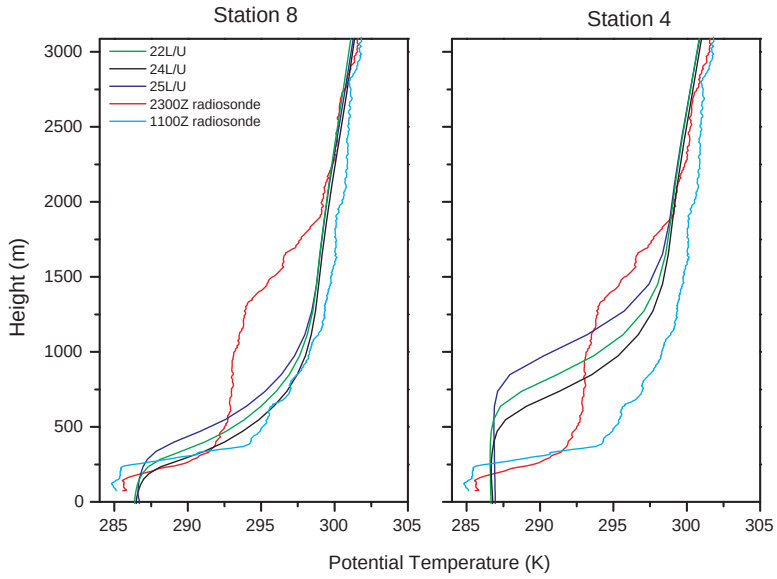

Figure 7.16: Potential temperature at $tL/\overline{U} = 22$, 24 and 25 for the 9^{th} of February 2001. The radiosonde profiles for $2300Z$ on the 8^{th} and on the 9^{th} is shown for comparison.

but the atmosphere above the inversion is correctly simulated. As in the idealised simulations, the lower height of the temperature inversion is dependant on the location of the rotors. Since station 8 is on the edge of the rotor the potential temperature profiles are very similar to the observed, especially on $tL/\overline{U} = 24$ when there is no reversed flow over the station. On the other hand, station 4 is always under the influence of the rotor and the height of the inversion is considerably higher than the observed. The amplitude of the inversion is also reduced by 2 K.

The pressure difference between stations 8 and 4 starts at -0.11 hPa for $tL/\overline{U} = 20$, it is -0.27 hPa at $tL/\overline{U} = 22$, increases to -0.65 hPa by $tL/\overline{U} = 24$ and is -0.007 hPa at $tL/\overline{U} = 25$. The one hour pressure running average of figure (7.13) has a minimum of -0.59 hPa for $T = 40.48$ days. For $T = 40.455$ days the pressure difference is -0.11 hPa and at $T = 40.52 days$ it is 0.01 hPa.

The different features of the flow around $1100Z$ ($T = 40.47$ days) are well simulated by the model.

7.5 Summary

Inversions in the upstream profile which are below the summit of the ridges are able to produce trapped waves with rotors and hydraulic jumps. Since the flow is weaker than when the inversion is above the summit the upper limit for the generation of trapped waves with rotors is lowered in flows over just one ridge.

The introduction of two ridges in the flow increases the strength of the downstream disturbance. The upper limit for the production of trapped waves with rotors is increased to $F = 1.25$. In these flows, the emergence of the trapped waves moves upstream and up the lee slope. In flows with $F = 0.5$ a hydraulic jump associated to gravity wave breaking can be observed.

The strength of the rotors increases with the decrease in the Froude number for flows over one ridge. For flows over two ridges this is also true for $F > 0.75$.

When hydraulic jumps are present the strength of the inversion is reduced in relation to the inversion upstream, otherwise it is always stronger. There is a decrease in the inversion strength with a decrease in the Froude number.

The height of the inversion downstream is dependant on the presence or not of rotors.

The simulation of the case study for the 9^{th} of February shows that the 1–D simulated upstream potential temperature profile for $2300Z$ is not correct. The simulation for $0600Z$ produces a downslope wind storm in the lee of the second ridge which is in agreement with the surface data collected during the campaign. The $1100Z$ simulation produces downstream rotors with similar features as the ones observed during the campaign. The two previous simulations confirm that the strong inversion observed in the downstream temperature profile is also present in the upstream profile.

7.6 Appendix: Resolution

The horizontal dimensions of the simulation domain should be large enough so that the perturbations generated by the mountains at the centre are allowed to propagate for long enough before they reach the boundaries and so that the boundaries do not affect the flow considerably. Equilibrium between the number of grid points in the domain and the resolution must be reached. The resolution of the domain should be large enough as to be able to reproduce the phenomena correctly and small enough as to keep the number of

grid points at a reasonable number. The same applies to the vertical domain.

The resolution of the vertical domain was chosen so that a grid point was located at roughly the mountain height and that the distance from this point to the grid points immediately above was approximately 100 m. The remaining resolution up to top of the domain was chosen so that the top would be located at 20 km.

The horizontal resolution employed by Vosper (2004) implied that, even with 1024 grid points, the domain with a mountain width of 28 km was too small. Initially simulation with $F = 0.75$ and a horizontal resolution of 300 m was tested on a domain with two mountains which means that only 43 grid points span the width of the mountain. This is about half the resolution used in Vosper (200) and no rotors were found. To obtain a number of grid points per mountain width similar to Vosper (2004) a resolution of 150 m was chosen.

Figure (7.17) shows two simulations for two different resolutions, $\Delta x = 200$ m and

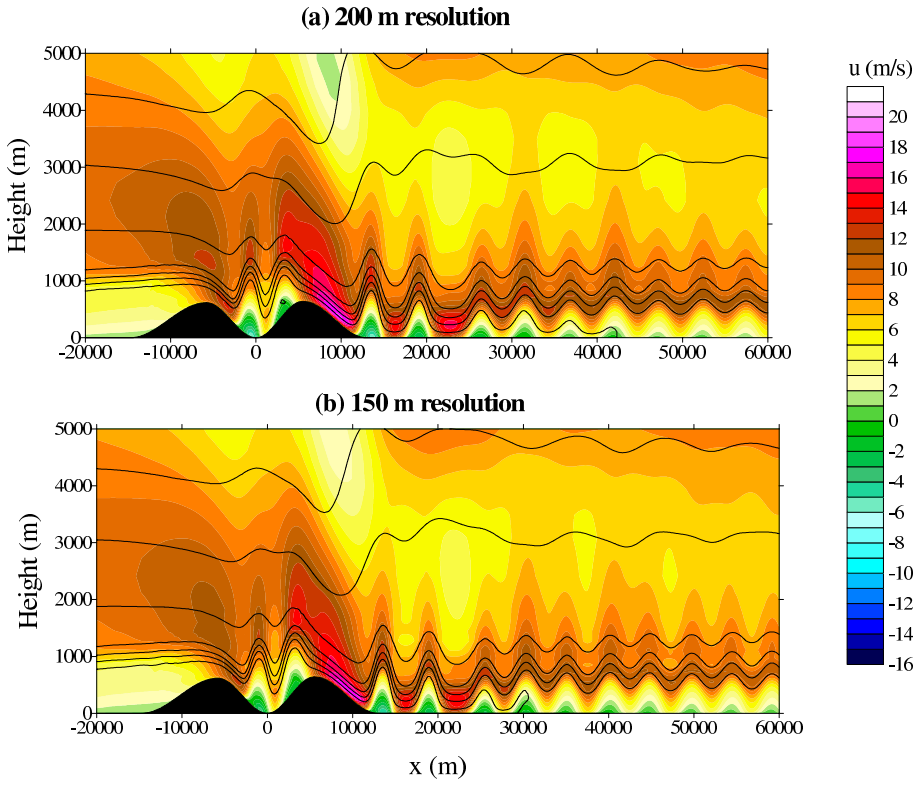

Figure 7.17: Flow over two ridges for two resolutions and $F = 0.75$. (a) $\Delta x = 200$ m and (b) $\Delta x = 150$ m

$\Delta x = 150$ m. The inversion height and strength downstream a not affected by the changes in resolution. The decrease in resolution leads to an increase in wavelength, were the

simulation with $\Delta x = 150$ m shows 10 wave crests while there are only 9 in the simulation with $\Delta x = 200$ m. Vosper (2004), found that linear theory could be used to diagnose the wavelength of the trapped waves downstream so, an increase in wavelength suggests that the simulation with $\Delta x = 200$ m is not resolving all of the wavelengths triggered by the ridges.

The reduction in resolution also leads to an increase in the strength of the first rotor, i.e. the maximum reversed flow speed is -5.58 ms^{-1} whereas the same parameter for a $\Delta x = 150$ m resolution is -4.92 ms^{-1}. The vertical propagating gravity wave is also affected by the resolution; i.e., the wave in the simulation with $\Delta x = 200$ m is steeper than the wave in the simulation with $\Delta x = 150$ m.

Although the domain's boundaries are further away from the mountain in a $\Delta x = 200$ m simulation, the simulation with a resolution of 150 m is a good compromise between the distance of the boundaries to the mountain and the wavelengths resolved by the model.

8. Summary and Conclusions

The central issue in this thesis has been the study of the effects of a low–level temperature inversion on the flow over ridges via data analysis of the Falklands campaign, one–dimensional marine boundary layer simulations of the upwind profile and a series of two–dimensional idealised numerical model simulations.

A climatological analysis of the Falklands campaign data established a correlation between the seasonal occurrence of strong downslope and lee phenomena and the difference in air and sea surface temperatures and wind direction. The main results from this analysis can be summarised as follows:

- The summer months have the highest frequency of northerly winds and the air temperature is consistently higher than the sea surface, hence the higher frequency of occurrence of strong phenomena and of temperature inversions on the upwind temperature profiles. During these months the reversal of the relationship between the sea surface temperature and the air temperature was only observed for southerly winds;

- The winter months are months with the lowest frequency of strong phenomena. On average, the wind speed during these months is the lowest and the frequency of northerly winds is also lower than in the summer months. The sea surface temperature is consistently higher than the air temperature and this is only reversed for northerly flow;

- Gustiness and flow acceleration at MPA also revealed a direction dependency. The highest values of both of these parameters are found for northerly flows.

Six case studies were chosen to depict the types of flow observed at MPA under northerly conditions. They represent the three categories identified in Mobbs *et al.* (2004).

For the two cases with downwind deceleration the pressure spectrum has a lower amplitude when compared with the spectrum of the accelerated flows. Decelerated flow has low spatial and temporal variability as well as small gusts. The pressure differences between the stations at MPA are also very small.

For the four cases with strong downwind acceleration two types of flow can be identified:

- Accelerated flow interspersed with reversed flow. When the wind downstream exhibits some reversal then, for those periods, the flow is decelerated and exhibits high temporal and spatial variability. High gusts also occur during these periods, with gust factors well above average. The horizontal convergence associated with the local wind reversal is indicative of flow separation and of the presence of rotors. Pressure and temperature differences across short distances (between the stations at MPA) are also high.

  The pressure spectrum for the periods when the flow is reversed exhibits peaks of high amplitude for long frequencies, which are associated with turbulence;

- When the flow is simply accelerated, it has low spatial and temporal variability and the gustiness is also low. The pressure and temperature differences across small distances are smaller.

  The pressure spectrum no longer exhibits the high amplitude peaks for high frequencies.

Except for the first case of decelerated flow, a temperature inversion was found in the radiosonde profiles and was associated with the advection of warm air from the north of the Falklands. The temperature differences between the air temperature and the sea surface temperature revealed that the air is always warmer than the sea before the event starts.

In order to simulate the marine boundary layer north of the Falklands and to obtain a reasonable approximation of the temperature profile a one–dimensional boundary layer model was developed. The model has a 1.5 closure turbulence scheme and includes water

radiation parameterisations. The sensitivity tests with day 33 of the Wangara experiment revealed that the model is able to simulate both the diurnal mixed layer and the stable nocturnal boundary layer reasonably well as long as the lowest grid levels are well resolved. The resolution of the lower levels is particularly important for the adequate representation of the development of the nocturnal stable boundary layer.

The results from the model are comparable with published results for a 1.5 order closure model of Mailhot and Benoit (1982) and Yamada's *et al.* (1975) second–order model, as long as a stretched grid is used.

The differences in stability due to changes in the weighting coefficient of the time discretisation scheme are not significant for values of $0.75 \leq \mu \leq 1$.

The turbulence coefficients for the eddy diffusivity parameterisation determined during the sensitivity analysis were also valid when applied to the simulation of the marine boundary layer. When the model was used to simulate the boundary layer north of the Falklands for the strong wind case studies, it generated a temperature inversion at the height of the ridges. In the model runs, the top of the inversion is always above Mt. Wickham's summit for all cases. The temperature advection plays an important role in the development of the temperature inversion and an improvement in the accuracy of the temperature advection would significantly improve the accuracy of the model.

The 2–D simulations with the BLASIUS model determined that a temperature inversion which is entirely below the summit of the ridge, is also able to generate, downstream, similar disturbances to the ones observed when the inversion is located above the summit. The results also show that the downstream phenomena are weakened as the inversion height is lowered. Flows over two ridges are significantly different from flows over just one ridge. The transition from supercritical to subcritical in flows over one ridge is dependant on the strength of the vertical propagating gravity wave while, when the domain has two ridges the transition from supercritical to subcritical flow occurs over the lee of the second ridge independent of the strength of the propagating gravity wave.

The simulations also show that the height of the inversion downstream is dependent on the presence or not of rotors.

The 2–D simulation of the case study for the 9^{th} of February 2001 was able to capture the observed features at MPA. This confirms the supposition that a temperature inversion

was present upstream. Through the assumptions behind the 1–D model, it is reasonable to conclude that the advection of warm air from north of the Falklands which is responsible for the generation of such inversion.

From the analysis of the data and the simulations performed throughout the thesis it is reasonable to infer that if the resolution of the lower levels in the forecasting models is improved then they would be able to better reproduce the temperature inversions that lead to the generation of such strong lee–side phenomena. A more accurate forecast of such hazards could be achieved. An improvement of the temperature advection would also contribute to more accurate forecasts.

Future Work Since stations 8 and 4 always exhibit a stronger perturbation and the characteristics of the lee–side phenomena are clearly three–dimensional, a campaign where a greater number of stations would be deployed in the vicinity of MPA would be useful capture the different flow features and their evolution. The deployment of remote sensing instruments, like lidars, radar wind profilers or radio acoustic sounding systems would greatly facilitate the three–dimensional structure of the phenomena.

For that campaign the launch of radiosondes upstream should also be attempted since one of the problems encountered during the data analysis was the lack of such soundings.

A natural progression of the idealised $2-D$ simulations would be to extend them to three dimensions and to real orography.

Extending the simulations of the case studies to $3-D$ simulations with real orography would provide greater insight into the three dimensional characteristics of the flow.

References

Augustsson, H. and Olafsson, H., 2003: Gust factors. Personal com.

Baines, P.G., 1995: Topographic effects in stratified flow. Cambridge University Press, 482 pp.

Baines, P.G. and Hoinka, K.P., 1985: Stratified flow over two–dimensional in fluid of infinite depth: A laboratory simulation. *J. Atmos. Sci.*, 42, 1614–1630.

Bechtold, P., C. Fravalo and J. P. Pinty, 1992: A model of marine boundary-layer cloudiness for mesoscale applications. *J. Atmos. Sci.*, 49, 1723 – 1744.

Bechtold, P., Cuijpers, J.W.M., Mascart, P. and Trouilhet, 1995: Modelling of trade wind cumuli with a low–order turbulence model: toward a unified description of Cu and Sc clouds in meteorological models. *J. Atmos. Sci.*, 52, 455–463.

Bougeault, P., 1981: Modeling the trade–wind cumulus boundary layer. Part I: Testing the ensemble cloud relations against numerical data. *J. Atmos. Sci.*, 38, 2414–2428.

Brasseur, O., Gallee, H., Schayes, G., Tricot, C. and Ridder, K., 1998: Impact of turbulence closures on diurnal temperature evolution for clear sky situations over Belgium. *Bound.–Layer Meteor.*, 87, 163–193.

Businger, J. A., Wyngaard, J. C., Izumi, Y., and Bradley, E. F., 1971: Flux profile relationships in the atmospheric surface layer. *J. Atmos. Sci.*, 28, 181–189.

Chaboureau, J.– P. and P. Bechtold., 2002: A simple cloud parameterization derived from cloud resolving model data: diagnostic and prognostic applications. *J. Atmos. Sci.*, 59, 2362 – 2372.

Chapman, S. and Lindzen, R.S., 1970: Atmospheric tides. D. Reidel. Dodrecht, Holland.

Chatfield, C., 2003: The analysis of time series. An introduction. Chapman and Hall, sixth edition, pp 327

Clark, R. H. *et al*, 1971: The Wangara Experiment: boundary layer data. Division of Meteorological Physics Technical Paper n 19. Research Organization, Australia.

Cuijpers, J. W. M., and P. Bechtold, 1995: A simple parameterization of cloud water related variables for use in boundary layer models. *J. Atmos. Sci.*, 52, 2486–2490.

Davies, H.C. and Phillips, P.D., 1985: Mountain drag along the Gotthard section during ALPEX. *J. Atmos. Sci.*, 42, 2093–2109.

Deardorff, J. W., 1971: Rate of growth of the nocturnal boundary layer. Proc. Symp. Air Polution, Turbulence and Diffusion, Las Cruces, NM, H. W. Church and R. C. Luna, Eds., Sandia Laboratories, NM, 183–190.

Deardorff, J. W., 1976: On the entrainment rate of stratocumulus capped mixed layer. *Quart. J. Roy. Meteor. Soc.*, 102, 563–582.

Deardorff, J. W., 1977: A boundary–layer parameterization for a GCM with good vertical resolution. National Center for Atmospheric Research, Boulder, CO.

Doyle, J.D. and Durran, D.R. 2002: The dynamics of mountain–wave–induced rotors. *J. Atmos. Sci.*, 59, 186–201.

Doyle, J.D. and Durran, D.R. 2004: Recent developments in the theory of atmospheric rotors. *Bull. of Amer. Meteo. Soc.*, 85, 337–342.

Durran, D.R. 1986: Another look at downslope windstorms. Part I: The development of analogs to supercritical Flow in an infinitely deep, continuously stratified fluid. *J. Atmos. Sci.*, 43, 2527–2543.

Frei, Ch., Davies, C.H., 1993: Anomaly in the alpine diurnal pressure signal: observa-

tions and theory. *Quart. J. Roy. Meteor. Soc.*, 119, 1296–1289.

Fu, Q., 1996: An accurate parameterization of solar radiative properties of cirrus clouds for climate models. *J. Climate*, 9, 2058–2082.

Fu, Q., P. Yang, and W. B. Sun, 1998: An accurate parameterization of the infrared radiative properties of cirrus clouds for climate models. *J. Climate*, 11, 2223–2337.

Fu, Q. and K.-N. Liou, 1992: On the correlated k-distribution method for radiative transfer in non-homogeneous atmospheres. *J. Atmos. Sci.*, 49, 2139–2156.

Fu, Q. and K.-N. Liou, 1993: Parameterization of the radiative properties of cirrus clouds. *J. Atmos. Sci.*, 50, 2008–2025.

Gill, A. E., 1982: Atmosphere–Ocean dynamics. Academic Press, International geophysics Series, Vol. 30, 662pp.

Grachev, A.A., Fairall, C.W., Bradley,E.F., 2000 Convective profile constants revisited. *Bound.–Layer Meteor.*, 94, 495–515.

Haurwitz, B. and Cowley, A.D., 1973: The diurnal and semi–diurnal barometric oscillations: Gobal distribution and annual variation. *Pageoph.*, 102, 193–122.

Holmboe, J. and Klieforth, H. 1957: Investigation of mountain lee waves and the air flow over the Sierra Nevada. Final Report. Contract No. AF19(604)–728, University of California ADNo. 133606, Dept. of Meteorology, University of California, Los Angeles, 290 pp.

Holton, J.R., 1992: An introduction to dynamical meteorology. Third Edition, Academic Press, 511 pp.

Horlacher, V., 2004: Gravity waves and turbulent flow over orography. PhD thesis, University of Leeds.

Hunt, J., and W. Snyder, 1980: Experiments on stably and neutrally stratified flow over a model three–dimensional hill. *J. Fluid Mech.*, 96, 671–704.

Izumi, Y. and Barad, M., 1963: Wind and temperature variations during development of a low–jet. *J. Appl. Meteor.*, 2, 668–673.

Klemp, J.B. and Lilly, D.K., 1975: The dynamics of wave–induced downslope winds. *J. Atmos. Sci.*, 32, 320–339.

Kuettner, J., 1939: Zur entstehung der föhnwalle. Beitr. *Phys. Frei Atmos.*, 25, 251–299.

Lester, P. F., and W. A. Fingerhut, 1974: Lower turbulent zones associated with mountain lee waves. *J. Appl. Meteor.*, 13, 54–61.

Lilly, D.K. and Klemp, J.B., 1979: The effects of terrain shape on non–linear hydrostatic mountain waves. *J. Fluid Mech.*, 95, 241–261.

Lindzen, R.S., 1967: Thermally driven diurnal tide in the atmosphere. *Quart. J. Roy. Meteor. Soc.*, 93, 18–42.

Long, R. R., 1953: Some aspects of the flow of stratified fluids: Part I. A theoretical investigation. *Tellus*, 5, 42–58.

Lyra, G., 1943: Theorie der Stationaren Leewellenstromung in freier Atmosphäre. *Z. Angew. Math. Mech.*, 23, 1–28.

Mahrt, L., 1985: Vertical structure and turbulence in the very stable boundary layer. *J. Atmos. Sci.*, 42, 2333–2349.

Mailhot, J., Benoit, R., 1982: A finite–element model of the atmospheric boundary layer suitable for use with numerical weather prediction models. *J. Atmos. Sci.*, 39, 2249–2266.

Manley, G., 1945: The helm wind of Crossfell. *Quart. J. Roy. Meteor. Soc.*, 71, 197–219.

Mellor, G. L., 1977: The Gaussian cloud model relations. *J. Atmos. Sci.*, 34, 356–358.

Miller, P.P.; Durran, D.R. 1991: On the sensitivity of downslope windstorms to the asymmetry of the mountain profile. *J. Atmos. Sci.* , 48, 1457–1473.

Mobbs, S. D., Vosper, S. B., Sheridan, P. F., Cardoso, R., Burton, R. R., Arnold, S. J., Hill, M. K., Horlacher, V. and Gadian, A. M., 2005: Observations of downslope winds and rotors in the Falkland Islands. *Quart. J. Roy. Meteor. Soc.*, 131, 329–351

New, M., Lister, D., Hulme, M., Makin, I., 2002: A high–resolution data set of surface climate over global land areas. *Clim. Res.*, 21, 1–25.

Ozawa, H., Goto–Azuma, K., Iwanami, K., Koerner, R.M., 1998: Cirriform rotor cloud observed on a Canadian artic ice cap. *Mon. Wea. Rev.*, 126, 1741–1745.

Pratt, L. J., 1984: Nonlinear flow with multiple obstructions. *J. Atmos. Sci.*, 41, 1214 – 1225.

Press, H., Flannery, B.P., Teukolsky, S.A., Vetterling, W.T., 2001: Numerical recipes. The art of scientific computing. Cambridge University Press, pp 818.

Queney, P., 1948: The problem of airflow over mountains: a Summary of theoretical studies. *Bull. of Amer. Meteo. Soc.*, 29, 16–26.

Queney, P., G. Corby, N. Gerbier, H. Koschmieder, and J. Zierep, 1960: The airflow over mountains. World Meteorological Organization Tech. Note 34, 135 pp.

Ralph, F.M., Neiman, P.J., Keller, T.L., Levinson, D. and Fedor, L., 1997: Observations, simulations and analysis of nonstationary trapped lee waves. *J. Atmos. Sci.*, 54, 1308–1333.

Reynolds, R.W. and Smith, T.M., 1994: Improved global sea surface temperature anal-

yses using optimum interpolation. *J. Climate*, 7, 929–948.

Scorer, R. S., 1949: Theory of lee waves of mountains. *Quart. J. Roy. Meteor. Soc.*, 75, 41-56.

Smith, R. B., 1980: Linear theory of stratified hydrostatic flow past an isolated mountain. *Tellus*, 32, 348–364.

Smith, R.B., 1989: Hydrostatic airflow over mountains. *Adv. Geophys.*, 31, 1–41.

Sommeria, G., and J. W. Deardorff, 1977: Subgrid–scale condensation in models of nonprecipitating clouds. *J. Atmos. Sci.*, 34, 344–355.

Sun, W.-Y. and Ogura, Y., 1980: Modeling the evolution of the convective planetary boundary layer. *J. Atmos. Sci.*, 37, 1558–1572.

Therry, G., LaCarrere, P., 1983: Improving the eddy kinetic energy model for planetary boundary layer description. *Bound.–Layer Meteor.*, 25, 63–88.

Turner, J.S., 1973: Buoyancy effects in fluids. Cambridge University Press.

Vosper, S.B., 1996: Gravity–wave drag on two mountains. *Quart. J. Roy. Meteor. Soc.*, 22, 993 –999.

Vosper, S.B., 2004: Inversion effects on mountain lee waves. *Quart. J. Ror. Meteor. Soc.*, 130, 1723 –1748.

Vosper, S.B. and Mobbs, S.D., 1997: Measurement of the pressure field on a mountain. *Quart. J. Roy. Meteor. Soc.*, 123, 129 –144.

Wang, T.A. and Lin, Y.L., 2000: Effects of shear and sharp gradients in static stability on two–dimensional flow over an isolated mountain ridge. *Meteorol. Atmos. Phys.*, 75, 69–99.

Yamada, T., Mellor, G., 1975: A simulation of the Wangara atmospheric boundary layer data. *J. Atmos. Sci.*, 32, 2309–2329.